The Design of an Intense Accelerator–Based Epithermal Neutron Beam Prototype for BNCT Using Near–Threshold Reactions

by

Charles L. Lee

Submitted to the Department of Nuclear Engineering
in partial fulfillment of the requirements for the degree of

Doctor of Philosophy in Nuclear Engineering

at the

MASSACHUSETTS INSTITUTE OF TECHNOLOGY

August 1998
[September 1998]

Author .....
Department of Nuclear Engineering
August 7, 1998

Certified by .....
Xiao–Lin Zhou
Assistant Professor
Thesis Supervisor

Read by .....
Sow–Hsin Chen
Professor
Thesis Reader

Accepted by .....
Sow–Hsin Chen
Chairman, Department Committee on Graduate Students

The Design of an Intense Accelerator–Based Epithermal Neutron Beam Prototype for BNCT Using Near–Threshold Reactions

by

Charles L. Lee

Submitted to the Department of Nuclear Engineering
on August 7, 1998, in partial fulfillment of the
requirements for the degree of
Doctor of Philosophy in Nuclear Engineering

Abstract

Near–threshold boron neutron capture therapy (BNCT) uses proton energies only tens of keV above the (p,n) reaction threshold in lithium in order to reduce the moderation requirements of the neutron source. The goals of this research were to prove the feasibility of this near–threshold concept for BNCT applications, using both calculation and experiment, and design a compact neutron source prototype from these results. This required a multidisciplinary development of methods for calculation of neutron yields, head phantom dosimetry, and accelerator target heat removal. First, a method was developed to accurately calculate thick target neutron yields for both near–threshold and higher energy proton beams, in lithium metal as well as lithium compounds. After these yields were experimentally verified, they were used as neutron sources for Monte Carlo (MCNP) simulations of neutron and photon transport in head phantoms. The theoretical and experimental determination of heat removal from a target backing with multiple fins, as well as numerical calculations of heat deposition profiles based on proton energy loss in target and backing materials, demonstrated that lithium integrity can be maintained for proton beam currents up to 2.5 mA. The final design uses a proton beam energy of 1.95 MeV and has a centerline epithermal neutron flux of 2.2×10^8 n/cm^2-sec/mA, an advantage depth of 5.7 cm, an advantage ratio of 4.3, and an advantage depth dose rate of 6.7 RBE-cGy/min/mA, corresponding to an irradiation time of 38 minutes with a 5 mA beam. Moderator, reflector, and shielding weigh substantially less than other accelerator BNCT designs based on higher proton energies, e.g. 2.5 MeV. The near–threshold concept is useful as a portable neutron source for hospital settings, with applications ranging from glioblastomas to melanomas and synovectomy.

Thesis Supervisor: Xiao–Lin Zhou
Title: Assistant Professor

Acknowledgments

This thesis is the culmination of many years of hard work. However, this effort would not have been possible without the support of many important persons. I want to thank the following people for their help over the past eleven years:

My teacher and advisor, Xiao–Lin Zhou, has given guidance and support in helping me attain this degree. He has provided me with knowledge and experience that will be invaluable over the course of my professional career.

Professors Sow–Hsin Chen, Otto Harling, and Sidney Yip of MIT have given wonderful advice over the years, pertaining to my classes, thesis, and all scientific endeavors. Thank you for the benefit of your experience. In addition, Professor Jacquelyn Yanch has provided me with especially useful suggestions regarding my research. Her expertise in the field of accelerator BNCT is truly remarkable, and allowing me to attend her research group's weekly meetings provided excellent feedback on my own studies.

Emanuella Binello, Brandon Blackburn, Cynthia Chuang, David Gierga, Tim Goorley, Stead Kiger, Kent Riley, Haijun Song, and Susan White — the excellent group of doctoral candidates in the area of BNCT with whom I have worked over the last four years — have provided great intellectual support and friendship. I feel a special bond with all of these comrades–in–arms, the most impressive collection of students I've ever known.

Professor Frank Harmon of Idaho State University has been a terrific boss during my year working in Idaho, always making time if I needed to discuss anything. He has gone far above and beyond the call of duty in helping me over the past year. Dr. Yale Harker of the Idaho National Environmental and Engineering Laboratory (INEEL) has been my mentor in Idaho. He is a brilliant, creative, and supportive person who has really helped prepare me for the road ahead.

Dr. Rajat Kudchadker is a wonderful friend and a damn fine researcher, a truly giving person. Thanks especially for the room last summer and the curries that make my eyes water, even if you did start the whole "Larry" thing.

Roger Bartholomay, you beat me to finishing our degrees, but I guess I can let that slide. It is no exaggeration to say that my experiments would not have happened without your help. Wade Scates is an honest and positive person, always helping with and contributing to the many experiments of the past months. Good luck in your own degree, and remember, "Shake it baby, shake it!" Jim, Lane, and Brett of ISU have been incredibly helpful over the past year, making all the experiments work, even when I was certain they couldn't. You are a terrific group of guys, and I never could have finished this without your help.

Dawn May has been a wonderful friend and roommate in Idaho, a person whose laugh is one of the nicest things I can think of — I always want to join in. You are so loving and supportive, I'll never forget it. Extra thanks to Shep, Pepito, and Spaz.

Doug Denison has been my great friend and roommate in Boston. You are an intellectual powerhouse with a killer wit that is all the more wonderful because of its subtlety. Always remember, "No moleste el gato spectacularrrrr."

Heather Blasdell is my soul mate and the most exciting person I know. Heather is cool beyond words, and I certainly wouldn't be where I am now without her help.

Anne Moulton, my "honey–fritter", will always have a very special place in my heart. Besides a being a wonderful friend, her strength and love were instrumental in helping me recognize and value my gifts.

Mike Jeffery, randomly assigned as my roommate freshman year of college, is truly one of my friends for life. He is honorable and caring, and I really miss being able to spend time together like we used to. You know, if Tom Hanks and Data had a son...

Dana Nelson, my movie partner for so many Fridays over the years, has a smile that is unforgettable. She is a superb friend and confidante.

Mom and Dad, you have been unfaltering in your love and support of me, and I thank you for it all. You are the reason behind everything I've been able to achieve. Last but certainly not least, my sisters, Heather and Anna, are amazing. Spending time with you becomes a greater joy with every passing year. You have unlimited potential, and I have great faith in what your lives have in store.

Chad

Contents

1 Introduction **19**

1.1 An Overview of BNCT 19

1.2 Neutron Beam Requirements for BNCT 21

1.2.1 Neutron Energy Requirements 21

1.2.2 Beam Contamination Components 21

1.2.3 RBE Effects 23

1.3 Accelerator–Based BNCT 24

1.4 Research Goals and Thesis Summary 27

2 Thick Target Neutron Yields **29**

2.1 Theory 30

2.1.1 Near-Threshold Kinematics 30

2.1.2 Near–Threshold (p,n) Cross Sections 35

2.2 Calculated and Experimental Results 38

2.2.1 Thick Target Neutron Yield Surface 38

2.2.2 Thick Target Energy Spectra and Angular Distributions . . . 40

2.2.3 Thick Target Total Neutron Yields 44

2.2.4 Application to Lithium Compounds 46

2.2.5 Partially Thick Targets 48

2.2.6 Model of Lithium Metal Oxidation in Air 55

3 Feasibility of Near–Threshold BNCT **59**

3.1 What is necessary for a useful BNCT treatment beam? 59

3.2 Light Water versus Heavy Water 61

3.3 Demonstration of Feasibility 63

4 Near–Threshold BNCT Dosimetry **65**

4.1 BNCT Treatment Parameters 65

4.2 MCNP Design 69

4.3 Photons Produced in the Lithium Target 72

4.4 Dose Calculations 78

4.4.1 Moderator Considerations 79

4.4.2 Target Backing Considerations 86

4.4.3 Thermal Neutron Attenuation 92

4.4.4 Photon Attenuation 94

4.5 Choice of Beam 98

5 Near–Threshold BNCT Target Heat Removal **101**

5.1 Multi–Fin Target Heat Removal 102

5.1.1 Single Fin Theory 103

5.1.2 Extension to Multiple Fins 105

5.1.3 Low Power Heat Removal Experiments 112

5.1.4 High Power Heat Removal Experiments 117

5.1.5 Critical Heat Flux (CHF) Concerns 122

5.2 Heat Deposition Profiles of Proton Beams 123

5.2.1 Steady State Temperature Drops 124

5.2.2 Transient Temperature Behavior (Beam Pulsing) 133

6 Final Target Design **137**

7 Summary and Future Work **149**

7.1 Summary 149

7.2 Suggestions for Future Work 151

A Thick Target Neutron Yield Program (`li.f`) **155**

B Tabulated (p,n) Cross Section Coefficients (`sigmafile`) **177**

C Tabulated Spline Coefficients (`sigmaspline`) **179**

D Example MCNP Input **181**

E Multi–Fin Specific Temperature Rise Calculation (`flow.f`) **193**

F Heat Deposition Computational Method **199**

G Design of a Head Phantom for BNCT Beam Verification **203**

H Publications and Presentations **207**

List of Figures

1-1 Total (p,n) Cross Section for ^{7}Li. From [1]. The lower dashed curve is the cross section for the reaction leading to the ground state of ^{7}Be, while the solid curve is the cross section for reactions leading to both the ground and first excited states of ^{7}Be. 25

2-1 Proton Energy Contours for Thick Lithium Targets. 31

2-2 Differential Neutron Yield for 1.95 MeV Protons Incident on Natural Lithium Metal. 38

2-3 A Comparison of 0° Thick Target Neutron Yields. 39

2-4 Near–Threshold Thick Target Neutron Energy Spectra for Natural Lithium Metal. 41

2-5 Near–Threshold Thick Target Neutron Angular Distributions for Natural Lithium Metal. 42

2-6 Near–Threshold Thick Target Neutron Angular Yields for Natural Lithium Metal. These yields, with units of neutrons/degree mC, are obtained by multiplication of the angular distributions of Figure 2-5 by the solid angle differential element. 43

2-7 Calculated and Experimental Total Neutron Yields for Thick Lithium Metal Targets 45

2-8 Schematic of Long Counter Used to Measure Total Neutron Yields for Lithium Compounds [2] 47

2-9 Calculated and Experimental Total Neutron Yields for Thick LiF Targets 49

2-10 Calculated and Experimental Total Neutron Yields for Thick Li_2O Targets 50

2-11 Contours Defining Neutron Production in a Partially Thick Target. Neutrons are only produced with energy and angle combinations between the upper and lower contours. 52

2-12 Calculated Total Neutron Yields for Partially Thick LiF Targets . . . 53

2-13 Calculated and Experimental Total Neutron Yields for a 1 μm Target 54

2-14 Calculated and Experimental Total Neutron yields for a Thick Lithium Target Exposed to Air. A 1.5 μm LiOH target thickness is assumed. . 57

3-1 Neutron Energy Spectra as a Function of H_2O Moderator Thickness for 1.91 MeV Protons 62

4-1 BNCT Treatment Parameter Definition 67

4-2 MCNP geometry 69

4-3 Total cross section for (p,γ) reaction in ^{7}Li 73

4-4 Experimental 478 keV Gamma Yield for Inelastic Proton Scattering in Lithium. Experimental points are taken from Ref. [3]. The least squares quadratic fit to the data is given in Eq. 4.3 74

4-5 Effect of ^{7}Li$(p,p'\gamma)^7$Li Photons on BNCT Treatment Parameters . . . 76

4-6 Variation of RBE-AD with Moderator Thickness for Near–Threshold Beams 79

4-7 Variation of RBE-ADDR with Moderator Thickness for Near–Threshold Beams 80

4-8 Percentages of Healthy Tissue RBE Dose Components on Front Phantom Face for 1.95 MeV Proton Beams. 82

4-9 Comparison of RBE Advantage Depth and RBE Advantage Ratio for 1.95 MeV Proton Beams 83

4-10 Variation of RBE-AD and RBE-ADDR as a Function of Proton Beam Energy and Moderator Thickness. The vertical dotted line indicates the minimum acceptable RBE-AD of 5 cm. The upper and lower horizontal dotted lines correspond to total healthy tissue RBE doses of 2000 cGy and 1250 cGy, respectively. Points in the upper quadrant satisfy the requirements for a BNCT neutron beam. 85

4-11 Effect of Target Backing Materials on RBE Advantage Depth for 1.95 MeV Protons 87

4-12 Experimental 0° Photon Yields from Cu, Al, and Stainless Steel (Type 304) Backing Materials for 1.95 MeV Protons. Photons were detected using a $5'' \times 5''$ NaI crystal. 90

4-13 Effect of Gammas from Inelastic Proton Scattering in Aluminum on RBE Advantage Depth for 1.95 MeV Protons 91

4-14 Effects of Cd and ^{6}Li thermal neutron shields on RBE-AD for 1.95 MeV Protons 93

4-15 Variation of RBE-AD and RBE-ADDR with Moderator Thickness for 1.95 MeV Protons with and without Thermal Neutron Absorber Materials. The vertical dotted line indicates the minimum acceptable RBE-AD of 5 cm. The upper and lower horizontal dotted lines correspond to total healthy tissue RBE doses of 2000 cGy and 1250 cGy, respectively. Points in the upper quadrant satisfy the requirements for a BNCT neutron beam. 95

4-16 Effect of Lead Shielding on the Maximum RBE Advantage Depth for 1.95 MeV Protons 96

4-17 Variation of RBE-ADDR on Pb Thickness for 1.95 MeV Protons . . . 97

4-18 Effect of ^{6}Li and Pb on BNCT Treatment Parameters for 1.95 MeV Protons. The vertical dotted line indicates the minimum acceptable RBE-AD of 5 cm. The upper and lower horizontal dotted lines correspond to total healthy tissue RBE doses of 2000 cGy and 1250 cGy, respectively. Points in the upper quadrant satisfy the requirements for a BNCT neutron beam. 99

5-1 Definition of Fin Parameters. From [4]. 104

5-2 Multi–Fin Target Design 106

5-3 Calculated Temperature Drop per Unit Heat Input Across Fins for a Multi–Fin Target Design 111

5-4 Schematic of Low Power Heat Removal Experimental Setup for a Multi–Fin Target Design 113

5-5 Experimental Variation of Heat Input versus Thermistor Temperature Difference for a Multi–Fin Target Design. The coolant flow rate is 8 gallons per minute. 115

5-6 Comparison of Experimental and Calculated Multi–Fin Temperature Drops Across Low Power Experimental Setup 118

5-7 Target Regions and Associated Temperature Drops 125

5-8 Temperature Profile for 1.95 MeV Protons Stopping in Lithium and Copper. The lithium thickness is 9.43 μm, just enough to pass the (p,n) threshold at the lithium–copper boundary. The dotted line shows the incorrect temperature variation based on the assumption of all heat incident from the left. 128

5-9 Temperature Drop Across Stopping Region as a Function of Incident Proton Beam Energy. In all cases, the proton energy at the lithium/copper boundary was the (p,n) reaction threshold of 1.88 MeV. 129

5-10 Temperature Drop Across Stopping Region as a Function of Lithium Target Thickness 130

5-11 Maximum Deviation of Target Temperature from Average vs. Duty Factor for Several Repetition Rates. From [5]. 134

6-1 Moderator Design for Final CTU Design. Stainless steel surrounding the moderator unit is not shown, and the figure is not to scale. 138

6-2 Final CTU Design 141

6-3 RBE-AD and RBE-AR for Final Near–Threshold BNCT Neutron Source Design for Various Moderator Thicknesses. The proton energy is 1.95 MeV. 142

6-4 RBE-AD vs. RBE-ADDR for Final Near–Threshold BNCT Neutron Source Design for Various Moderator Thicknesses. The proton energy is 1.95 MeV. The vertical dotted line indicates the minimum acceptable RBE-AD of 5 cm. The upper and lower horizontal dotted lines correspond to total healthy tissue RBE doses of 2000 cGy and 1250 cGy, respectively. Points in the upper quadrant satisfy the requirements for a BNCT neutron beam. 143

6-5 Dose Depth Profiles along Phantom Centerline for 3 cm H_2O Moderator. The proton energy is 1.95 MeV. 144

6-6 Radial Variation of the Epithermal Neutron Flux Exiting the Moderator. The proton energy is 1.95 MeV. 145

6-7 Radial Variation of Advantage Region for a 3 cm Light Water Moderator. Each point indicates the depth at a given radial distance from the centerline where the tumor dose rate equals the maximum healthy tissue dose rate. The proton energy is 1.95 MeV. 147

G-1 Acrylic Head Phantom Design 206

List of Tables

2.1 Near–Threshold Thick Target Neutron Yields for Natural Lithium Metal 44

2.2 Near–Threshold Thick Target Neutron Yields for Lithium Compounds. Yields are in units of neutrons/mC. 51

3.1 Existing Epithermal Neutron Beams for BNCT Clinical Trials in the U.S. and Europe 60

3.2 Calculated Neutron Beam Parameters as a Function of Moderator Thickness for 1.91 and 1.95 MeV Protons 63

4.1 RBE Values for BNCT Calculations 68

4.2 Brain Material Specification for the MCNP Phantom 71

4.3 Comparison of Neutron and Photon Yields for Thick Lithium Targets 75

4.4 Q–Values for (p,n) Reactions in Target Backing Material Candidates 88

4.5 Total Gamma Yields from Inelastic Proton Scattering in Aluminum for 1.88 MeV Protons 90

4.6 Physical Properties of Target Backing Material Candidates 92

5.1 Geometrical Factors for Multi–Fin Target Flow Rate Calculations . . 108

5.2 Experimental Temperature Drops between Coolant and Copper Rod Thermistors 116

5.3 High Power Experimental Temperature Rises between Coolant and Copper Rod Surface 121

5.4 Comparison of Low and High Power Experimental Temperature Rises Across Fins 122

5.5 Temperature Drops for Near–Threshold and Higher Proton Energies . 132

6.1 Free Beam Parameters for Final Design of Near–Threshold BNCT Neutron Source 142

G.1 Physical Properties of Body Parts and Phantom 204

Chapter 1

Introduction

1.1 An Overview of BNCT

Extensive research has been undertaken in the past 50 years in the United States, Europe, and Japan in the area of boron neutron capture therapy (BNCT), a novel method for treating certain malignant brain cancers, such as glioblastoma multiforme (GBM). The GBM mass in the brain generally has a large central mass (the primary tumor mass) plus extensive, root-like fingerlets that invade the surrounding healthy tissue. GBM cells tend to be quite resistant to traditional (photon) radiation treatment, and the tumor fingerlets make surgical debulking ineffective since some of the fingerlets almost always remain. These tumors are also not generally diagnosed until they are quite large and able to affect normal brain function, and by this time, the expected patient survival time is short (often less than six months). In the United States alone, more than 11,000 people were diagnosed with GBMs in 1995, so there is a need and a market for an effective treatment of this tumor [6].

The BNCT treatment is a binary modality that consists of preferentially loading a compound containing ^{10}B into the tumor location, followed by the irradiation of the patient with a beam of neutrons. Damage to cancer cells comes from the

densely ionizing, high linear energy transfer (LET) heavy charged particles from the $^{10}B(n,\alpha)^{7}Li$ reaction, whose cross section follows a $1/v$ law and hence is dominant for thermal neutrons. Since the range of the reaction products is on the order of cell dimensions, the heaviest tissue damage is restricted to the tumor cells, provided the boron compound has a substantially higher concentration in tumor compared with the surrounding healthy tissue. The BNCT treatment modality is considered binary because two events must occur for high dose rates to tissue: introduction of ^{10}B and irradiation by thermal neutrons.

While BNCT in Japan has historically removed the skull cap during the treatment so that a thermal neutron beam can be used [7], the more common methodology in current practice and theory removes the skull cap during a surgical debulking of the primary tumor mass but replaces the cap during the irradiation [6]. Surgical debulking is generally necessary because by the time the tumor is diagnosed, the primary mass is large and has developed its own vasculature. Irradiation of this primary mass can destroy this system of blood vessels, causing internal bleeding in the brain. The replacement of the skull cap reduces chances for infection and allows somewhat less strenuous requirements on treatment room sterility. Since thermal neutrons do not have sufficient penetrability to reach deep seated tumors, an epithermal beam of neutrons is necessary in order for the skull cap to remain intact during patient treatment. (High energy neutrons are less desirable for reasons described in Section 1.2 below.) The epithermal neutrons slow down within the patient, reaching thermal energies in the tumor region.

Excellent summaries of many different aspects of BNCT are found in the May 1997 issue of *Journal of Neuro-Oncology*, including reviews of the rationale of BNCT [6], history [7], neutron beam requirements [8], boron compounds [9], and microdosimetry [10]. The 1996 review in *Cancer Investigation* is also excellent [11]. Finally, the bi–annually proceedings of the International Symposium on Neutron Cancer Therapy for

Cancer provide a centralized source for the latest developments in all areas of neutron capture therapy research.

1.2 Neutron Beam Requirements for BNCT

1.2.1 Neutron Energy Requirements

The neutron source requirements peculiar to the BNCT methodology are complex and difficult to achieve in practice. It is worth discussing each major requirement in detail, since these beam parameters will be crucial to the development of the neutron beams in this research.

As mentioned previously, BNCT beams utilize epithermal neutrons for patient treatment. The first question that comes to mind is: what energy range is considered epithermal for this application? Many authors have tackled this question, and the general consensus at the time of writing is from several electron-volts (eV) to several tens of keV [8, 12]. The criteria for determining this range basically rest on balancing the need for high penetrability and low dose to healthy tissue. High penetrability through the skull and outer brain allows the treatment of tumors located deep in the patient's head, obviously necessary for any practical radiation treatment modality. Low dose to healthy tissue is one of the biggest selling points of BNCT: there is the potential for selective damage to tumor relative to healthy tissue, so any components of the treatment beam that reduce this therapeutic advantage are undesirable.

1.2.2 Beam Contamination Components

Radiation dose to the patient in BNCT consists of three main components: neutron dose, which is often subdivided into fast, epithermal, and thermal doses; gamma dose; and dose due to the high LET heavy charged particles from the fission of ^{10}B, generally called the ^{10}B dose. Some amount of dose due to neutrons is inevitable, but fast and

thermal components of the beam striking the patient are undesirable for different reasons. Fast neutrons deposit dose primarily near the skin surface and skull, since these neutrons quickly slow down into the epithermal region. The primary drawback of the fast neutron component is the steady increase of KERMA values with neutron energy in the fast region—the principle neutron interaction for fast neutrons in tissue is proton recoils produced by elastic scattering with hydrogen, and increasing neutron energy leads to larger proton kinetic energies, and hence larger tissue doses—which deposits large, shallow doses that do nothing to aid the treatment of the deep-seated tumors in question.

Thermal neutrons deposit energy in tissue primarily from the $^{14}N(n,p)^{14}C$ reaction, which produces a 580 keV proton and a 40 keV recoiling ^{14}C nucleus [13]. In addition, thermal neutrons are unable to penetrate the skull, so they too are unable to aid in the BNCT process. Note, however, that while fast neutrons produce large doses at shallow depths, they can still slow down in tissue to thermal energies and be captured by ^{10}B in the tumor, so it is an oversimplification to consider them useless.

The dose from gamma contamination of the beam is indiscriminate: it affects both tumor and healthy tissue to the same degree, reducing the effectiveness of the treatment. Gamma contamination will always be present in a neutron beam, but careful beam design can reduce this component to acceptable levels (see Chapter 4). Gamma contamination is primarily produced from the radiative capture of thermal neutrons by hydrogen in the patient via the $^{1}H(n,\gamma)^{2}H$ reaction, which may be viewed as an irreducible gamma background that must be included in all patient treatment planning. Gamma contamination can also be produced from interactions in an accelerator target; target backing material; or moderator, filter, and reflector materials.

The final dose component, the ^{10}B dose, should be very high in the tumor and very low in healthy tissue. The only real control over this component is in the pharmacological aspects of the compound used to transport the boron to the tumor site.

A high tumor–to–healthy tissue uptake ratio, as well as high tumor uptake levels, are necessary for the success of a BNCT treatment. Sufficiently high uptake ratios and tumor uptake levels can swamp the relative contribution of the contamination doses, reduce treatment times, and improve the experience for the patient by reducing side effects like erythema and epilation. Since the control over this component lies in the hands of chemists and pharmacologists, it is effectively constant for this research, although the degree of beam thermalization will correlate with the ^{10}B dose. The specific tumor–to–healthy tissue uptake ratio and ^{10}B concentration in tumor used in this research are given in Section 3.1.

1.2.3 RBE Effects

Whenever radiation dose is applied to a biological organism, the concept of relative biological effectiveness (RBE) must be applied to dose calculations. The RBE concept is necessary since equal physical doses (energy absorption per unit mass) for different types of ionizing radiation do not produce identical biological effects. In general, higher LET radiations such as neutrons and heavy charged particles are more effective in producing damage in an organism, i.e. have higher RBE values, than lower LET particles such as electrons, positrons, and photons [14]. The definition of RBE for a particle i is generally taken to be the ratio D_X/D_i, where D_X and D_i are the doses of 250 kVp X rays and particle i, respectively, needed to produce a given biological endpoint [15]. It is important to note that RBE depends on many factors, including the biological endpoint of interest, the energies of the radiations considered, and in the case of ^{10}B dose, the microscopic distribution of ^{10}B in tumor and healthy tissue cells [16, 17, 18]. The exact RBE values for the dose components in BNCT are unknown, but reasonable estimates are necessary for adequate dosimetry and neutron beam design so that the relative contribution of good and bad components is accurately gauged. The exact RBE values used in this research will be discussed in Chapter 4.

1.3 Accelerator–Based BNCT

While only certain nuclear research reactors are currently performing clinical BNCT trials in the United States and Europe [19, 20], widespread future applicability of this treatment modality will likely require the use of charged particle accelerators that can be used in a clinical environment. The application of particle accelerators for this problem is not a trivial task. In order to allow for reasonable patient treatment times, accelerator currents will need to be on the order of milliamps [21, 22, 23, 24]. These high currents are not only difficult to obtain for heavy charged particles such as protons and deuterons; such high currents will also deposit kilowatts of heat as the charged particles lose energy in the target, making target cooling difficult. Finally, the particular requirements on the neutron beam for BNCT (discussed in the previous section), as well as the need for large neutron production rates, will dictate the choice(s) for the charged particle- induced reactions to be used. The specific aspects of the ^{7}Li(p,n)^{7}Be reaction that is considered in this research meet these criteria.

The ^{7}Li(p,n)^{7}Be reaction cross section is shown in Figure 1-1. The total cross sections for the reaction leading to the ground state of ^{7}Be, as well as the combination of ground and first excited ^{7}Be states, are given. The cross section is seen to rise rapidly from a threshold at 1.88 MeV to a plateau of about 269 mb from 1.93 MeV to 2.00 MeV. This plateau is followed by a large resonance centered at 2.25 MeV with a peak cross section of nearly 590 mb. This large cross section, combined with a low threshold energy, makes the ^{7}Li(p,n)^{7}Be reaction an excellent source of relatively low energy neutrons.

One may ask, why not use any nuclear reaction with high neutron yields for accelerator BNCT? For example, the D-D and D-T reactions are well studied and produce about 10^{9} and 10^{11} neutrons/sec/mA, respectively, at easily obtained deuteron energies of 100-300 keV [25]. Deuterated materials are easier to handle than pure lithium metal, which has a low melting point (181°C) and readily oxidizes in air and water

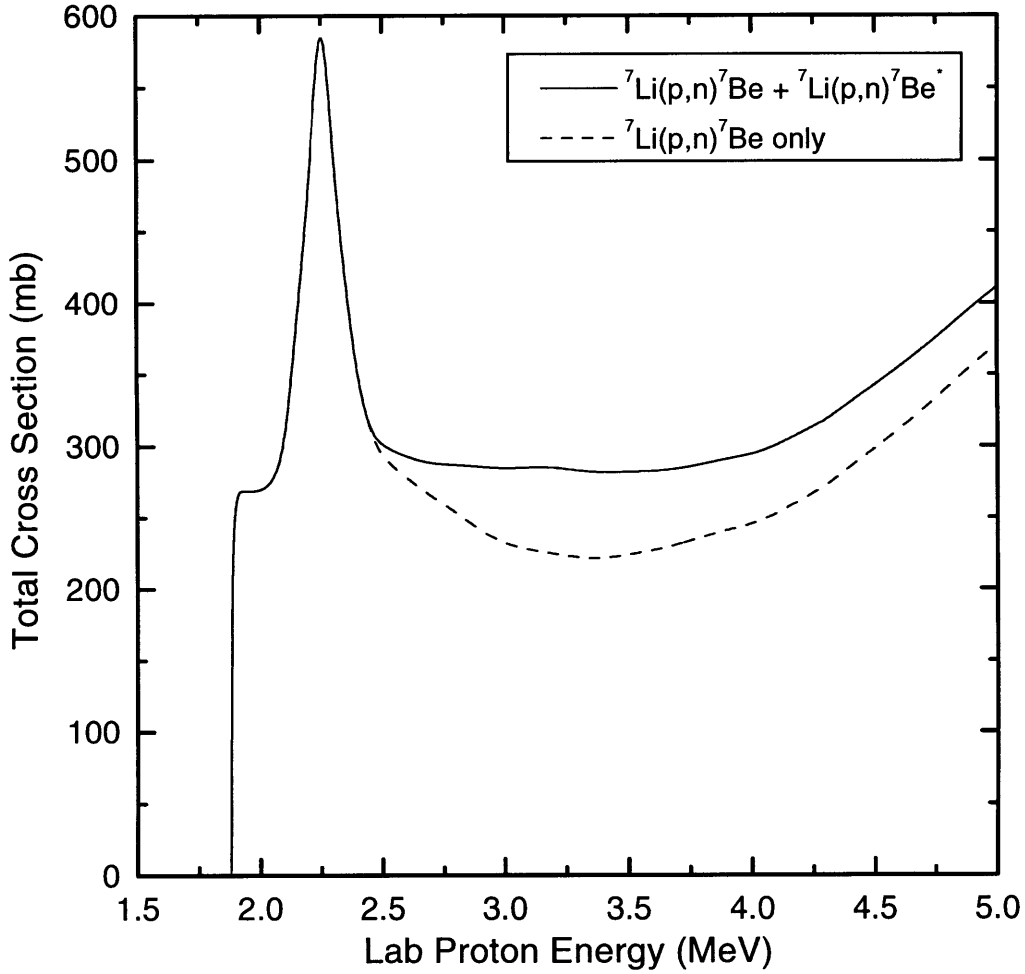

Figure 1-1: Total (p,n) Cross Section for ^{7}Li. From [1]. The lower dashed curve is the cross section for the reaction leading to the ground state of ^{7}Be, while the solid curve is the cross section for reactions leading to both the ground and first excited states of ^{7}Be.

[26]. So why use a (p,n) reaction, especially $^{7}Li(p,n)^{7}Be$?

The answer lies in the requirements for BNCT that were spelled out in Section 1.2, namely that useful neutron energies for BNCT are in the range of about 1 eV to 10 keV. The D-D and D-T reactions produce neutrons with energies of almost 3 MeV and 14 MeV, respectively, due to the positive Q–values of the reactions. These neutron energies are much too high for patient treatment [27], and hence need extensive (greater than 20 cm of D_2O) moderation to bring the average energy down to the useful range for BNCT. The concomitant attenuation of the neutron flux makes the current requirement very high if patient treatment times are to be reasonable, and even so, the fast neutron component of these sources can be reasonably high, especially when the high RBE values for fast neutrons are considered. By comparison, the maximum energy of neutrons from the bombardment of 2.5 MeV protons on a thick lithium target is 787 keV, the average neutron energy is 326 keV, and the neutron yield is 8.9×10^{11} neutrons/sec/mA.

One of the most striking features of Figure 1-1 is the extremely rapid rise of the cross section immediately after threshold. Specifically, the cross section reaches the plateau value of 269 mb within 50 keV of the reaction threshold. This fact, combined with the neutron beam requirements described in Section1.2, has led us to consider near–threshold reactions in lithium targets [28, 29, 30, 31, 32, 33, 34, 35]. Near–threshold BNCT uses an accelerator proton beam energy several tens of keV above the $^{7}Li(p,n)^{7}Be$ reaction threshold to produce neutrons for BNCT treatments. Working close to threshold reduces the thick target yield compared to higher beam energies such as 2.5 MeV, but the maximum and mean neutron energies are much lower, requiring less moderation and hence less attenuation of the raw neutron yield from the target. For comparison with the neutron yield and energies for 2.5 MeV protons described above, the maximum energy of neutrons from the bombardment of 1.91 MeV protons is 105.3 keV and the average neutron energy is only 42.4 keV,

while the neutron yield is 2.4×10^{10} neutrons/sec/mA, a substantial yield considering the lowered moderation requirements for this neutron source.

1.4 Research Goals and Thesis Summary

A study of the viability of near–threshold neutron beams as a neutron source for BNCT brain treatments requires a multidisciplinary analysis of the total engineering of the neutron beam source. Primary requirements include the development of a method for calculating near–threshold neutron yields, Monte Carlo simulation of head phantom dosimetry, and accelerator target heat removal.

First, a method was designed and implemented to accurately calculate thick target neutron yields for near–threshold proton beams that can be applied in a self–consistent manner to higher energy proton beams, in lithium metal as well as lithium compounds. After these yields were experimentally verified, they were used as sources for Monte Carlo (MCNP) simulations of neutron and photon transport in head phantoms in order to determine the effect of proton beam energy, moderator thickness, gamma production in the target, backing materials, and thermal neutron and gamma shielding on beam parameters such as penetration depth and treatment time. The engineering design of the neutron source involved theoretical and experimental determination of heat removal capabilities for a multi–fin target backing design, as well as numerical calculation of the heat deposition profiles for protons stopping in lithium and backing materials. The results of these studies were combined into a unified neutron source design, including the design of an acrylic head phantom for measuring the primary dose components of the final beam.

Chapter 2

Thick Target Neutron Yields

In the investigation of near–threshold BNCT, it is necessary to have an accurate method for computing thick target neutron yields. In particular, both the energy spectrum and angular distribution of the neutrons produced by protons of a certain bombarding energy are required. It has been determined that the existing data for computing thick target yields is insufficient for accurate yield calculation over the range of incident proton energies of interest in this research. In particular, tabulated cross sections provide excellent data for energies above about 1.95 MeV, but mathematical peculiarities close to the reaction threshold lead to erroneous results in this region. Analytical forms of the differential cross section work well close to threshold, but are incorrect for higher energies. A self–consistent method was developed for producing differential thick target neutron yields for all proton energies below 2.50 MeV. This method has also been modified to determine neutron yields from compounds that contain lithium, as well as extending the method to partially thick targets. Partially thick targets are of sufficient thickness to result in significant proton energy loss, but are not sufficiently thick to slow the proton energy below the reaction threshold. Finally, a model of the effect of the oxidation layer formed when lithium metal is exposed to air is presented.

This chapter describes the method developed to generate the thick target differential neutron yields from near–threshold protons, focusing on the mathematical difficulties that arise for calculations within several keV of the reaction threshold and the techniques for overcoming these complexities. The results of calculations using this method are presented, including differential and total yields for thick targets, partially thick targets, and targets exposed to air. Comparisons of calculated results with experimental measurements are included.

2.1 Theory

2.1.1 Near-Threshold Kinematics

For illustrative purposes, consider a monoenergetic incident proton beam energy, E_{p_0}, of 1.95 MeV striking a thick lithium target. A thick target is defined to be of sufficient thickness to slow protons down to energies below the reaction threshold. Figure 2-1 provides kinematic relations between θ, the polar angle of emission of the neutron in the laboratory (LAB) frame of reference; E_n, the LAB neutron energy; and E_p, the LAB proton energy that produced the neutron, for the ^{7}Li(p,n)^{7}Be reaction. Lines of constant E_p are plotted from E_{p_0} to $E_p = E_{th}$, the threshold energy of 1.88 MeV. When the proton beam impinges on a thick lithium target, the initial neutron yield will follow the energy and angle behavior shown on the uppermost contour. As the protons lose energy in the target, the energy and angular dependence of the neutron yield will be determined from contours of continuously decreasing proton energy, until neutrons are only produced in the forward direction at an energy of 29.7 keV at E_{th}. The neutron energy at threshold is determined from $E_n(E_{th}) = m_p m_n E_{th}/(m_{Be} + m_n)^2$, where m_p, m_n, and m_{Be} are the proton, neutron, and ^{7}Be nuclear masses, respectively. A thick lithium target will only produce neutrons with energies and angles corresponding to proton energies below E_{p_0}, i.e. neutrons will

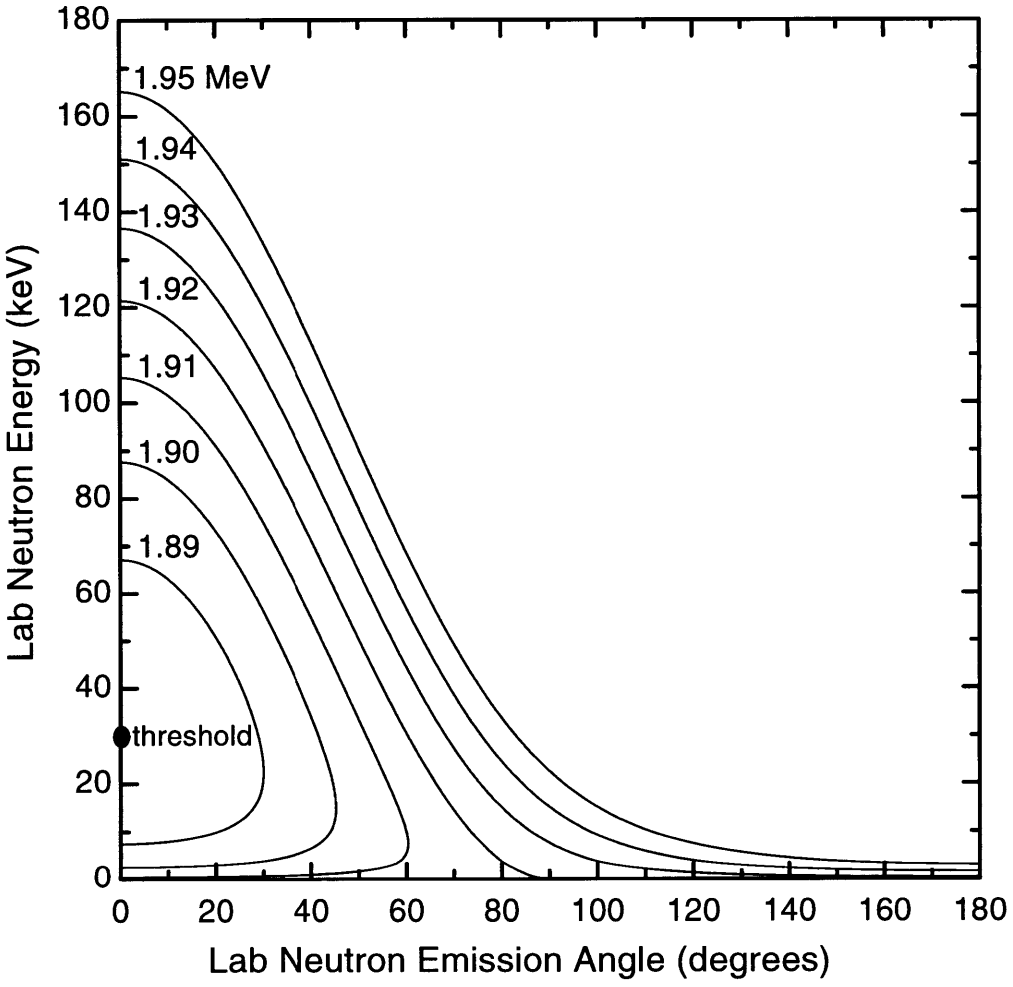

Figure 2-1: Proton Energy Contours for Thick Lithium Targets.

not be produced with energies and angles above the uppermost contour of Figure 2-1. Note that for proton energies below

$$E_p^* = \frac{m_{Be}(m_{Be} + m_n - m_p)}{m_{Be}(m_{Be} + m_n - m_p) - m_p m_n} E_{th} = 1.92 \text{ MeV}, \tag{2.1}$$

neutron production is double-valued, giving two neutron energies for each LAB angle of emission. In addition, neutrons are only produced in the forward direction ($\theta < 90°$).

It is clear from Figure 2-1 that any combination of θ and E_n uniquely specifies E_p, and the differential neutron yield is therefore a pointwise function of these variables. This observation means that it is not necessary to discretize the proton energy as the beam slows down in the target. The differential neutron yield at each proton energy is given by

$$\frac{d^2Y}{d\Omega\, dE_n}(\theta, E_n) = N_{Li-7} \frac{\frac{d\sigma_{pn}}{d\Omega'} \frac{d\Omega'}{d\Omega} \frac{dE_p}{dE_n}}{\frac{-dE_p}{dx}}, \tag{2.2}$$

where $d^2Y/d\Omega\, dE_n$ is the differential neutron yield in units of neutrons per keV per steradian per millicoulomb, N_{Li-7} is the ^{7}Li (target) atomic density, $d\sigma_{pn}/d\Omega'$ is the center-of-mass (CM) differential (p,n) cross section, $d\Omega$ and $d\Omega'$ are differential solid angles in the LAB and CM, respectively, and $-dE_p/dx$ is the proton stopping power in the target.

In order to have more compact notation in the equations that follow, it is useful to introduce two kinematic parameters, γ and ξ [36]. γ is defined as the ratio of the post–reaction speed of the CM to the speed of the neutron in the CM. The following expression for γ can be obtained from the nonrelativistic conservation of linear momentum and energy equations:

$$\gamma = \sqrt{\frac{m_p m_n}{m_{Be}(m_{Be} + m_n - m_p)} \left(\frac{E_p}{E_p - E_{th}}\right)}. \tag{2.3}$$

Note that as E_p approaches threshold, $\gamma \to \infty$, and for $E_p < E_p^*$, $\gamma > 1$. In addition, the parameter ξ is defined by

$$\xi^2 = 1/\gamma^2 - \sin^2\theta. \tag{2.4}$$

The first step in the determination of the thick target differential neutron yield is choosing a set of (θ,E_n) grid points at which $d^2Y/d\Omega\, dE_n$ is calculated. This research used 1°, 1-keV intervals ranging from 0° to 180° and 0 to 250 keV. It is important to note that a different grid spacing will lead to a different number of calculated yields, but the yield computed at a particular location is independent of mesh size and hence will not change. For each grid point, the proton energy E_p is calculated in a manner similar to that used to produce the contours of Figure 2-1. Once E_p has been determined, γ, ξ, and the mass stopping power are immediately calculated since these quantities are functions of E_p alone. The mass stopping power is determined from analytic formulas fit to experimental data [37].

Since the differential cross section $d\sigma_{pn}/d\Omega'$ is a function of the CM angle of emission, θ', the next step in the calculation is to determine the correct value of θ' corresponding to (θ,E_n). For $E_p > E_p^*$, neutron production is single-valued and

$$\theta' = \theta + \sin^{-1}(\gamma \sin\theta), \tag{2.5}$$

while for $E_p < E_p^*$, neutron production is double-valued and there are two possibilities for θ'. These CM angles, θ_1' and θ_2', are related to θ by

$$\theta_1' = \theta + \sin^{-1}(\gamma \sin\theta) \tag{2.6}$$

$$\theta_2' = \pi + \theta - \sin^{-1}(\gamma \sin\theta). \tag{2.7}$$

Note that θ_1' is the more forward-directed of these two angles and corresponds to

higher neutron energies, while θ_2' is directed in the backward direction and corresponds to lower neutron energies. Now define a neutron energy E_{equal}:

$$E_{equal} = (1+\gamma^2)E_n', \tag{2.8}$$

where E_n' is the CM neutron energy, given by

$$E_n' = \frac{m_{Be}(m_{Be}+m_n-m_p)}{(m_{Be}+m_n)^2}(E_p - E_{th}). \tag{2.9}$$

It is straightforward to demonstrate that for a given proton energy E_p, E_{equal} corresponds to the point where $\theta_1' = \theta_2' = \theta + 90°$. From the statements above, if $E_n \geq E_{equal}$ for the grid point in question, we will need θ_1' and Eq. (2.6) must be calculated; if $E_n < E_{equal}$, θ_2' is the correct CM angle and Eq. (2.7) must be used. Note from Eq. (2.6) that the maximum angle of emission for proton energies below E_p^* is given by $\theta_{max} = \sin^{-1}(1/\gamma)$.

It now remains to determine the CM differential cross section and the Jacobian transformations given in Eq. (2.2). These transformations are given by

$$\frac{d\Omega'}{d\Omega} = \pm\frac{\gamma}{\xi}(\cos\theta \pm \xi)^2 \tag{2.10}$$

$$\frac{dE_p}{dE_n} = \frac{1}{\cos\theta \pm \xi}\left[\frac{(m_{Be}+m_n)^2 E_p \xi}{m_p m_n E_p \xi(\cos\theta \pm \xi) \pm m_{Be}(m_{Be}+m_n-m_p)E_{th}}\right]. \tag{2.11}$$

In Eqs. (2.10) and (2.11), the + sign is used when $\theta' = \theta_1'$ and the − sign is used when $\theta' = \theta_2'$. Care must be taken in employing these expressions in various regions of (θ, E_n) space. For example, in the neighborhood of θ_{max}, $d\Omega'/d\Omega \to \infty$ and $dE_p/dE_n \to 0$. This means that Eq. (2.2) is indeterminate at points where $\theta = \theta_{max}$, and this will create a computational problem for (θ, E_n) values at or close to these points. However, this problem can be easily remedied by considering the product of $d\Omega'/d\Omega$

and dE_p/dE_n, given by

$$\frac{d\Omega'}{d\Omega}\frac{dE_p}{dE_n} = \frac{\pm(m_{Be}+m_n)^2(\cos\theta \pm \xi)\gamma E_p}{m_p m_n E_p \xi(\cos\theta \pm \xi) \pm m_{Be}(m_{Be}+m_n-m_p)E_{th}}. \tag{2.12}$$

Now the limit for this product of Jacobians is given by

$$\lim_{\theta\to\theta_{max}} \frac{d\Omega'}{d\Omega}\frac{dE_p}{dE_n} = \frac{(m_{Be}+m_n)^2 E_p}{m_{Be}(m_{Be}+m_n-m_p)E_{th}}\sqrt{\gamma^2-1}. \tag{2.13}$$

Using the product of the Jacobian transformations therefore circumvents the computational problems that arise when calculating each transformation separately. For this reason, and since the expression for the Jacobian product has the simple closed form given in Eq. (2.12), this expression is used in all differential yield calculations.

All calculational difficulties are not removed by the substitution given in Eq. (2.12). The greatest difficulty in near-threshold neutron yield calculations comes from the behavior of γ as $E_p \to E_{th}$: as pointed out earlier, γ becomes unbounded, and $d\Omega'/d\Omega\, dE_p/dE_n \to \infty$. We know that the CM differential cross section must go to zero at the reaction threshold, so Eq. (2.2) is still indeterminate $(0\cdot\infty)$ at $E_p = E_{th}$. To understand how this problem is overcome, the particular aspects of the ^{7}Li(p,n)^{7}Be cross section near threshold must be considered.

2.1.2 Near–Threshold (p,n) Cross Sections

In 1975, Liskien and Paulsen compiled extensive experimental cross section measurements from the existing literature and generated best fits to the data over the proton energy range from 1.95 MeV to 7 MeV for both the reaction leading to the ground state of ^{7}Be and the first excited state, which has a threshold at 2.37 MeV [1]. These

CM cross sections are given as Legendre polynomial expansions:

$$\frac{d\sigma_{pn}}{d\Omega'}(\theta') = \frac{d\sigma_{pn}}{d\Omega'}(0°) \sum_{i=0}^{3} A_i(E_p)\, P_i(\cos\theta'). \tag{2.14}$$

The proton energy-dependent parameters A_0, A_1, A_2, A_3, and $d\sigma_{pn}/d\Omega'(0°)$ are tabulated, making it extremely simple to use their fits for calculating reaction cross sections. In order to replicate the smooth variation of the cross section parameters with proton energy, cubic splines were fit through the data points given in Liskien and Paulsen's paper.

The Liskien and Paulsen tabulated cross section data are good for energies above 1.95 MeV, but they don't help to resolve the problem of indeterminacy near the reaction threshold. It is necessary to use an analytical form for the CM differential cross section to determine the actual near-threshold limits of the terms in Eq. (2.2). It has been pointed out by Newson *et al.*, as well as other sources [38, 39, 36, 40, 41, 42], that the reaction cross section has the form expected from a broad s–wave resonance centered at about 1.93 MeV. The resulting form of the theoretical cross section is

$$\frac{d\sigma_{pn}}{d\Omega'} = A \frac{x}{E_p\,(1+x)^2} \tag{2.15}$$

where $x = \Gamma_n/\Gamma_p$, the ratio of the neutron to proton channel widths, which has a functional form on the narrow energy range near threshold of $x = C_0\sqrt{1 - E_{th}/E_p}$, and C_0 and A are constants to be determined. A value of $C_0 = 6$ is consistent with the cross section data of Newson *et al.*. A proton energy of 1.925 MeV was chosen as the boundary between tabulated and theoretical cross section values. This energy is roughly the upper limit of applicability of Eq. (2.15) (~50 keV above threshold), and the theoretical expression for $d\sigma_{pn}/d\Omega'$ has zero slope at this energy, making a smooth transition to the interpolated values a simple matter. Theoretical and interpolated cross section values agree at this energy if $A = 164.913$ mbarn MeV/sr.

Now using the definition of γ in Eq. (2.3), it is possible to combine Eqs. (2.12) and (2.15) to give the cumbersome but useful formula

$$\frac{d\sigma_{pn}}{d\Omega'}\frac{d\Omega'}{d\Omega}\frac{dE_p}{dE_n} = \frac{\pm AC_0(m_{Be}+m_n)^2(\cos\theta\pm\xi)\sqrt{m_p m_n/m_{Be}(m_{Be}+m_n-m_p)}}{(1+x)^2[m_p m_n E_p\xi(\cos\theta\pm\xi)\pm m_{Be}(m_{Be}+m_n-m_p)E_{th}]} \tag{2.16}$$

for proton energies near threshold. Note that the threshold limit of Eq. (2.16) is a finite, non-zero value:

$$\lim_{E_p\to E_{th}}\frac{d\sigma_{pn}}{d\Omega'}\frac{d\Omega'}{d\Omega}\frac{dE_p}{dE_n} = \frac{AC_0(m_{Be}+m_n)^2\sqrt{m_p m_n/m_{Be}(m_{Be}+m_n-m_p)}}{m_{Be}(m_{Be}+m_n-m_p)E_{th}}. \tag{2.17}$$

For proton energies above the 1.925 MeV cutoff, the CM differential cross section is determined by interpolating the cross section parameters between their tabulated values using the cubic spline fits, and this is multiplied by the product of Jacobians given in Eq. (2.12). For proton energies below this cutoff, the expression given in Eq. (2.16) is used to determine the differential neutron yields. Finally, using expressions for the ^{7}Li density in natural lithium metal, the thick target differential neutron yield is given by

$$\frac{d^2Y}{d\Omega\, dE_n}(\theta,E_n) = \frac{f_{Li-7}N_0}{eA_{eff}}\frac{\frac{d\sigma_{pn}}{d\Omega'}\frac{d\Omega'}{d\Omega}\frac{dE_p}{dE_n}}{-\frac{1}{\rho}\frac{dE_p}{dx}}, \tag{2.18}$$

where f_{Li-7} is the ^{7}Li atomic fraction in natural lithium metal (92.5%), N_0 is Avogadro's number, e is the electronic charge, and A_{eff} is the atomic weight of natural lithium metal.

A complete listing of the Fortran 77 program, `li.f`, that was written to calculate thick target neutron yields using the techniques described above is given in Appendix A. The `li.f` program reads cross section data from `sigmafile` and `sigmaspline`, which contain tabulated CM differential cross section parameters and natural cubic spline parameters, respectively; these files are included in Appendices B

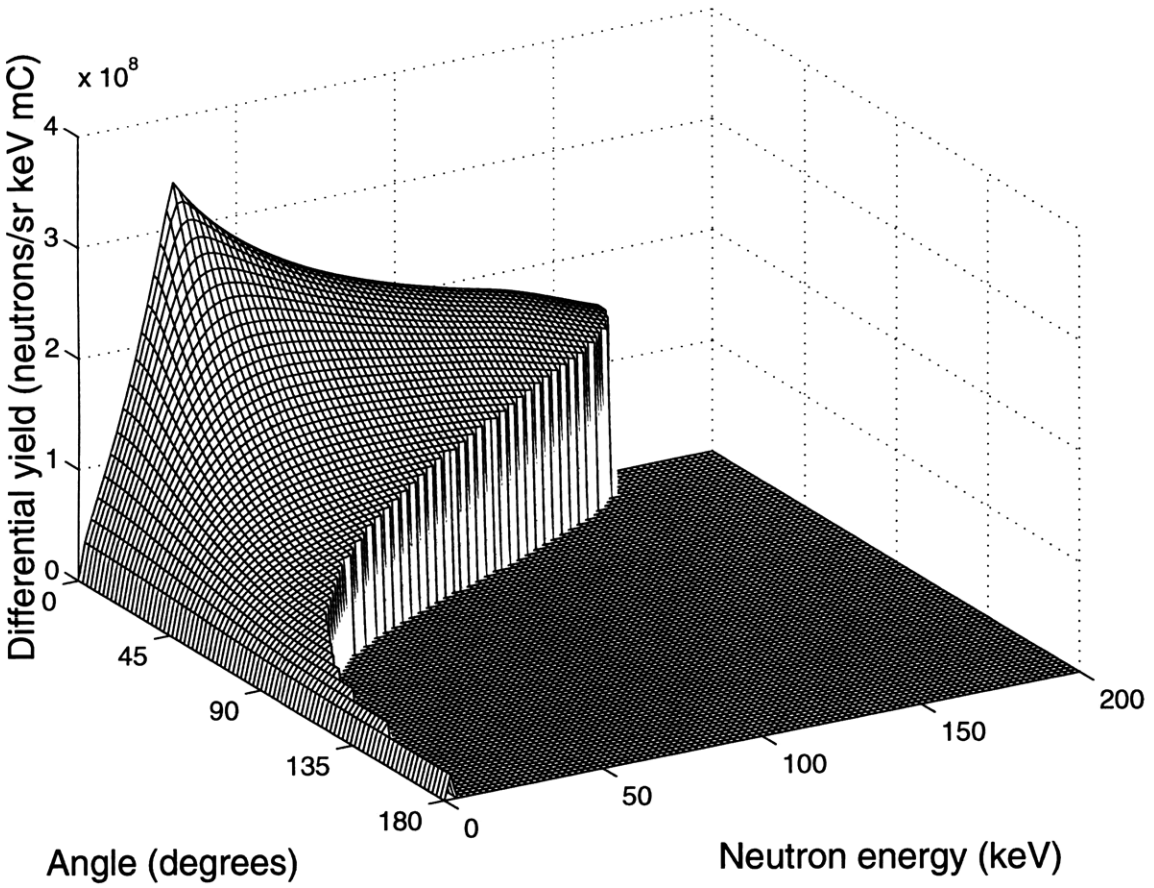

Figure 2-2: Differential Neutron Yield for 1.95 MeV Protons Incident on Natural Lithium Metal.

and C. Note that `li.f` can calculate thick target yields for natural lithium metal as well as certain lithium compounds; modifications of yield calculations for compounds is discussed in Section 2.2.4 below.

2.2 Calculated and Experimental Results

2.2.1 Thick Target Neutron Yield Surface

Figure 2-2 shows an example of a thick target differential neutron yield surface for 1.95 MeV incident proton energy. Note that the techniques described in the previous section have resulted in a smooth behavior of the yield surface in all regions of the calculation. An irregular, jagged boundary edge between zero and non-zero yields is

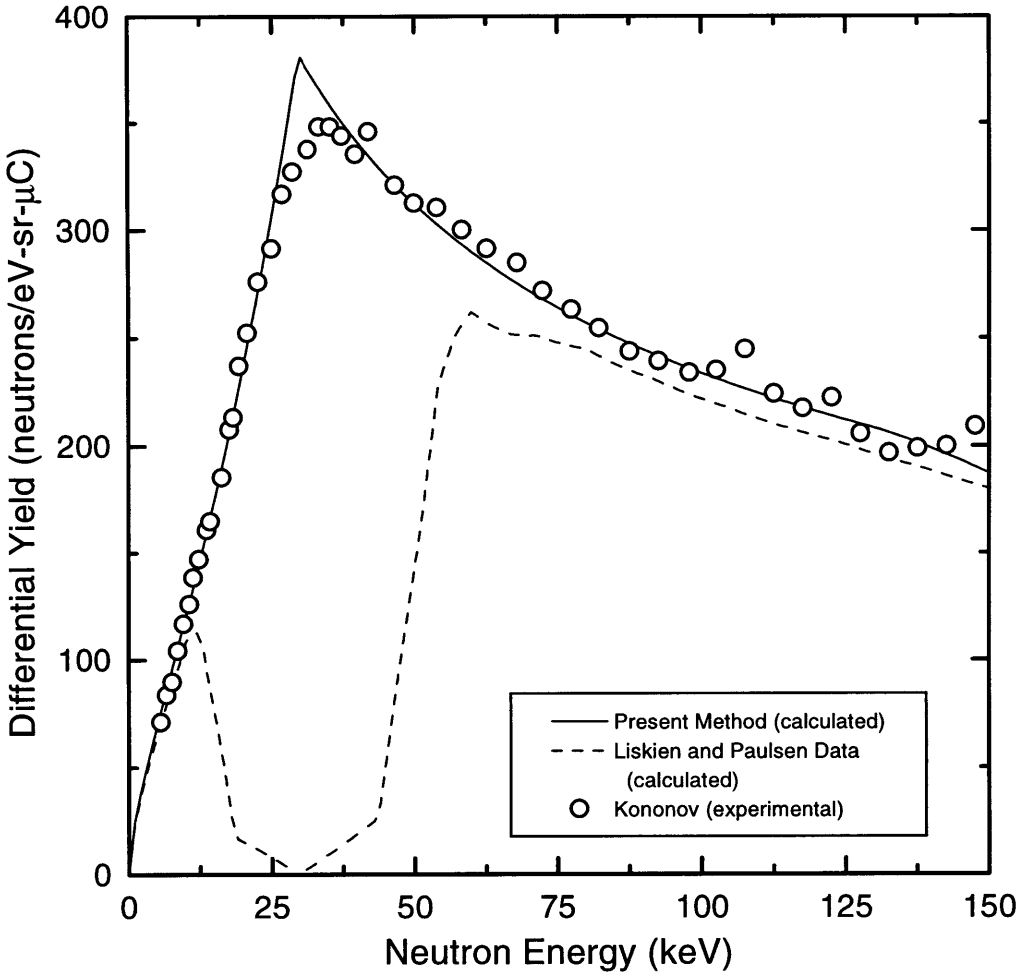

Figure 2-3: A Comparison of 0° Thick Target Neutron Yields.

apparent in Figure 2-2, which occurs because the yields are evaluated on a square array of grid points. There is actually a smooth line between the zero and non-zero values at the edge of the yield surface, which is the yield due to protons with an energy of precisely E_{p0}, but because this line does not intersect the grid points where computed yield values are displayed, it is not visible as a smooth edge. The computer program is designed to calculate the location of this edge and the corresponding differential neutron yields, so that energy spectra and angular distributions are integrated smoothly.

Figure 2-3 is a plot of the 0° thick target differential neutron yield for neutron en-

ergies between 0 and 150 keV, corresponding to an initial proton energy of 1.94 MeV. The calculations described previously have been modified in this plot to predict neutron yields for ^{7}Li metal, rather than natural lithium. The 0° differential yield shows good agreement with experimental data given by Kononov [43]. Error bars for these data were not given in the original reference. The rounding of the yield curve at threshold can be explained by the proton beam energy spread. For comparison, the same quantity is plotted using the tabulated data of Liskien and Paulsen for energies below 1.95 MeV in order to demonstrate the mathematical pathologies that occur near threshold.

2.2.2 Thick Target Energy Spectra and Angular Distributions

It is straightforward to calculate thick target neutron energy spectra and angular distributions by integrating Eq. (2.2) over solid angle and energy, respectively:

$$\frac{dY}{dE_n}(E_n) = 2\pi \int_0^{\theta_{max}(E_{p_0})} \frac{d^2Y}{d\Omega\, dE_n}(\theta, E_n) \sin\theta\, d\theta \tag{2.19}$$

$$\frac{dY}{d\Omega}(\theta) = \int_{E_{n,min}}^{E_{n,max}(E_{p_0})} \frac{d^2Y}{d\Omega\, dE_n}(\theta, E_n)\, dE_n \tag{2.20}$$

Thick target neutron energy spectra produced for near-threshold energies using Eq. (2.19) are shown in Figure 2-4, which gives the energy spectra for incident proton energies in steps of 10 keV between 1.89 MeV and 2.00 MeV. Note that there is no unusual behavior around 30 keV (E_n at the reaction threshold), where other yield computation techniques can produce erroneous spikes due to the infinity in the Jacobian product. The accuracy of these energy spectra should only be limited by the accuracy of the experimental cross section data, the nuclear masses, the mass stopping power, numerical roundoff error, and errors incurred by integrating using

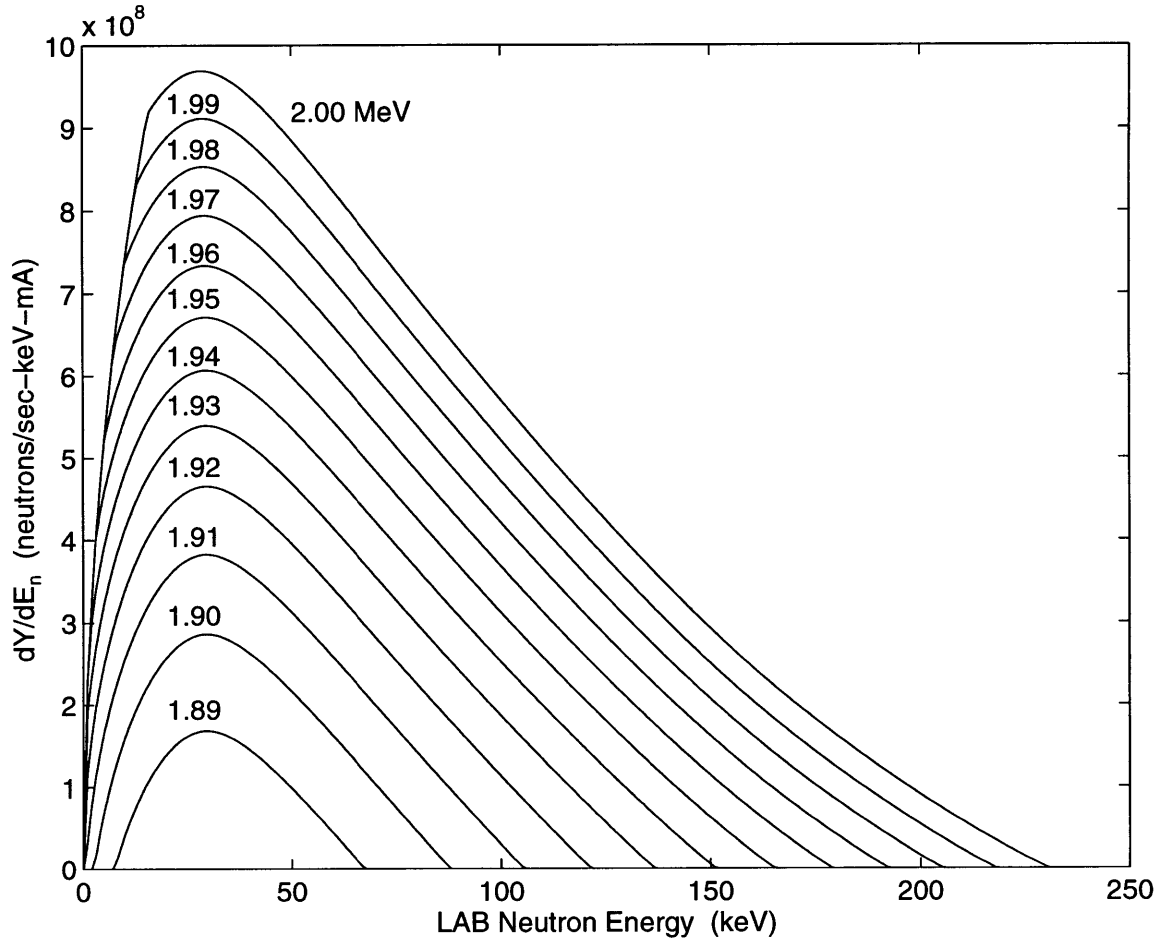

Figure 2-4: Near–Threshold Thick Target Neutron Energy Spectra for Natural Lithium Metal.

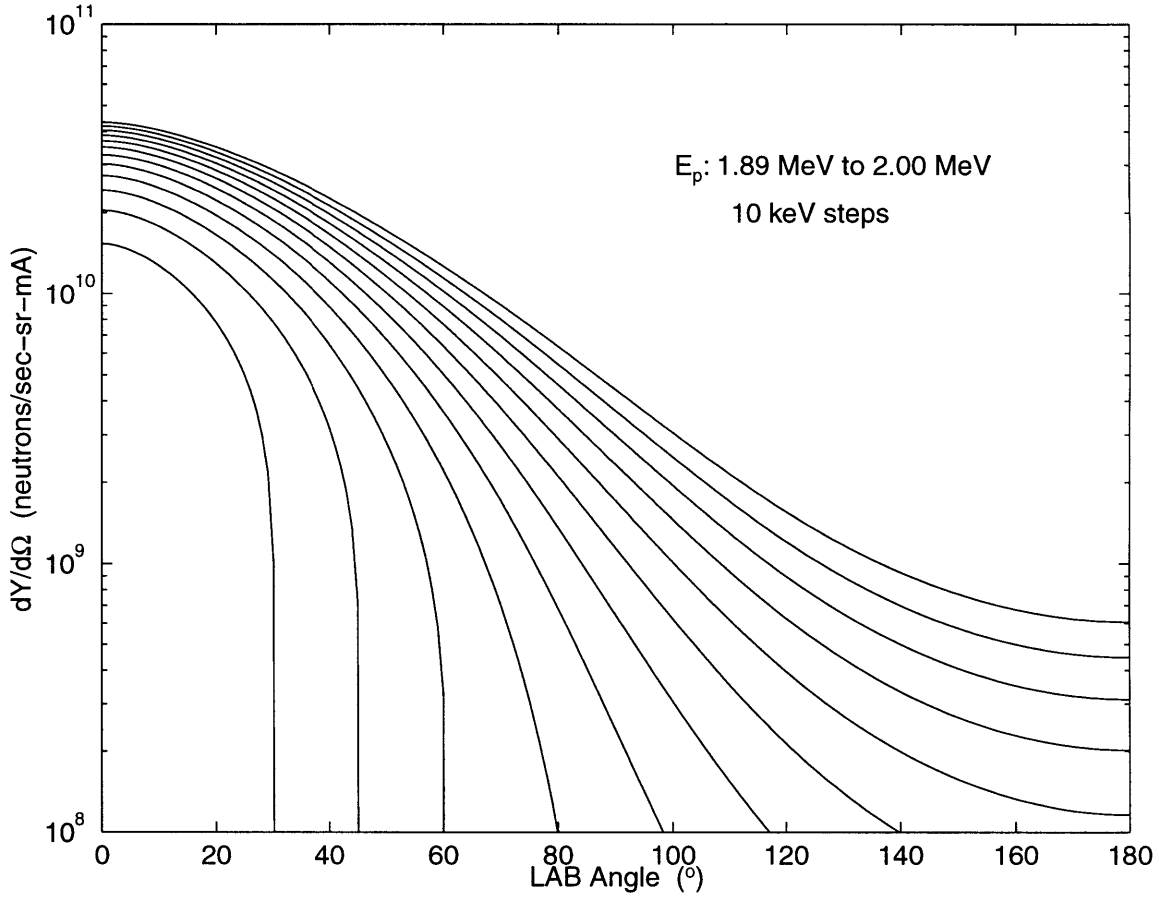

Figure 2-5: Near–Threshold Thick Target Neutron Angular Distributions for Natural Lithium Metal.

the trapezoidal method, all of which are expected to be small.

Figure 2-5 gives the thick target neutron angular distributions for incident proton energies between 1.89 MeV and 2.00 MeV. These distributions were determined as shown in Eq. (2.20). A logarithmic scale has been used for the angular distributions in order to show the extremely low yields in backward emission directions. For incident proton energies below E_p^*, no neutrons are produced for angles greater than $\theta_{max}(E_{p_0})$, as expected.

It is important to note that while the differential neutron angular yield, $dY/d\Omega(\theta)$, with units of neutrons/sr mC, in Figure 2-5 is peaked in the 0° direction, the peak in the actual neutron emission spectrum in the LAB will not be in the forward direction.

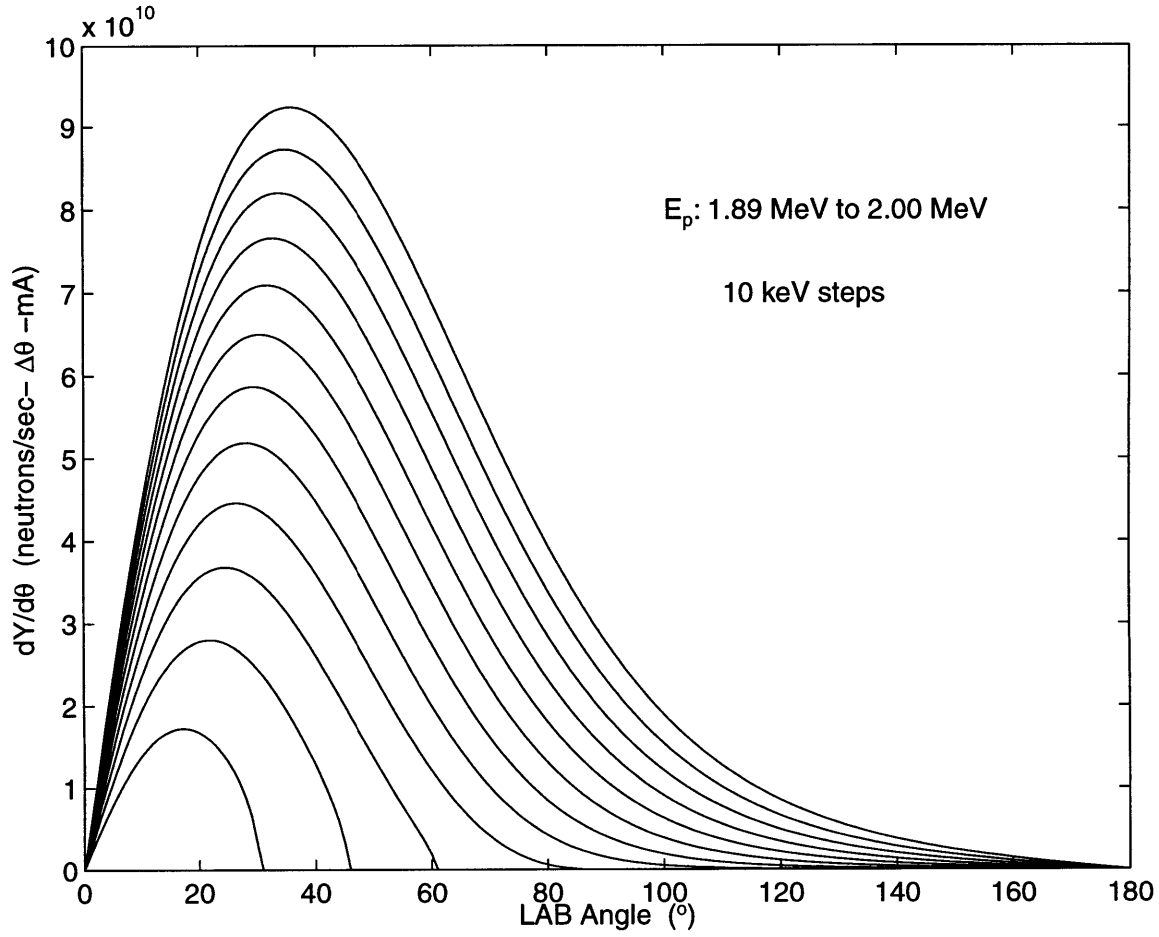

Figure 2-6: Near–Threshold Thick Target Neutron Angular Yields for Natural Lithium Metal. These yields, with units of neutrons/degree mC, are obtained by multiplication of the angular distributions of Figure 2-5 by the solid angle differential element.

In fact, there will be NO neutrons emitted in the 0° direction. This may be seen in Figure 2-6, where the angular distributions of Figure 2-5 are multiplied by the $2\pi \sin\theta$ term from the solid angle differential element. The differential neutron yield in Figure 2-6 is therefore given in units of neutrons/degree mC, and the neutron yield between two angles θ_1 and θ_2 is simply given by the integral of this new yield function over θ. The $\sin\theta$ term from the solid angle element forces the yield to go to zero in the forward direction, and the maximum yields in the near-threshold region are seen to be in the 20° to 40° range.

Table 2.1: Near–Threshold Thick Target Neutron Yields for Natural Lithium Metal

Incident Proton Energy (MeV)	Total Neutron Yield (n/sec/mA)	Maximum Neutron Energy (keV)	Mean Neutron Energy (keV)	Maximum Neutron Angle (degrees)	Mean Neutron Angle (degrees)
1.89	6.34×10^{9}	67.1	34.0	30.0	16.5
1.90	1.49×10^{10}	87.6	38.3	45.2	23.0
1.91	2.41×10^{10}	105.3	42.4	60.3	27.8
1.92	3.35×10^{10}	121.4	46.5	180	31.9
1.93	4.30×10^{10}	136.6	50.6	180	35.3
1.94	5.25×10^{10}	151.1	54.4	180	38.3
1.95	6.21×10^{10}	165.1	58.1	180	41.0
1.96	7.16×10^{10}	178.8	61.6	180	43.5
1.97	8.12×10^{10}	192.1	65.0	180	45.6
1.98	9.08×10^{10}	205.1	68.4	180	47.6
1.99	1.00×10^{11}	218.0	71.7	180	49.4
2.00	1.10×10^{11}	230.6	75.1	180	51.1
2.10	2.13×10^{11}	350.4	108.4	180	63.0
2.20	3.62×10^{11}	463.4	158.9	180	68.7
2.30	5.78×10^{11}	573.1	233.1	180	66.3
2.40	7.48×10^{11}	680.6	286.5	180	63.8
2.50	8.83×10^{11}	786.7	326.4	180	62.9

2.2.3 Thick Target Total Neutron Yields

Integrating the thick target differential neutron yields over both neutron energy and solid angle gives the total neutron yields for the various incident proton energies. Table 2.1 gives total thick target neutron yields, maximum and mean neutron energies over all angles, and maximum and mean emission angles over all energies.

Experimental verification of the total (4π) neutron yields for natural lithium metal are shown in Figure 2-7. A major concern in these measurements was the formation of a corrosion product layer on the lithium surface which could seriously impact the yield measurement (see Section 2.2.6). In order to remove this effect, the lithium target was formed inside the accelerator beam tube under vacuum. A piece of lithium was placed in a small wire cage at the base of a stainless steel (type 304) backing inside

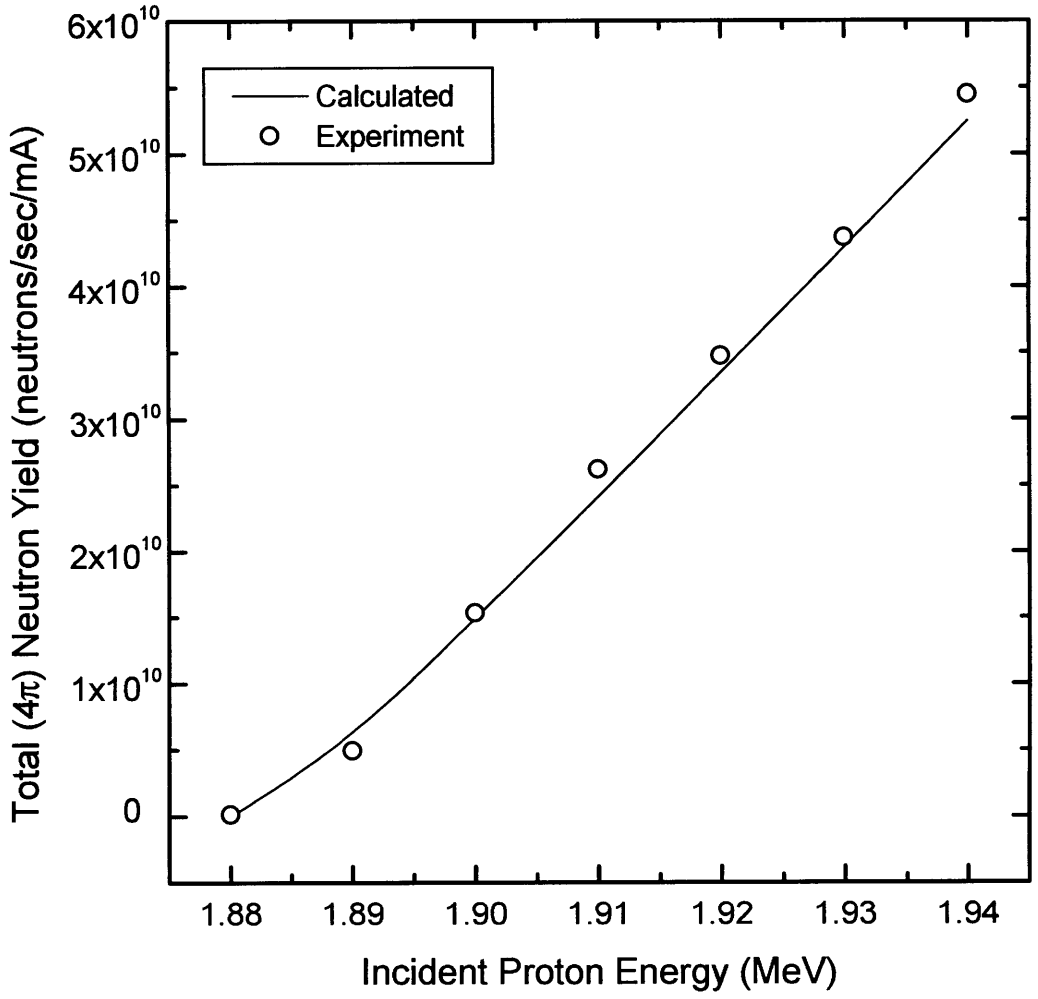

Figure 2-7: Calculated and Experimental Total Neutron Yields for Thick Lithium Metal Targets

a Van de Graaff beam tube. The cage was placed below the proton beam area so as to not interfere with the beam once irradiation began. The wire leads were attached outside the tube to a Variac voltage controller. Once a vacuum was established in the beam line, the Variac voltage was increased, vaporizing the lithium in the cage and depositing it on the stainless steel backing. Deposition times were increased until yield measurements no longer indicated that partially thick targets were being formed for the initial proton energy range of interest (see Section 2.2.5 below). This criterion was satisfied when the Variac voltage remained on for 10-15 minutes.

The total neutron yield was measured using a 4π detector [25] employing 12 18-inch long ^{3}He thermal neutron detectors. The counter, shown in Figure 2-8, was designed to have a flat neutron detection efficiency for neutron energies up to 100 keV [2]. The end flange of the beam line was placed at the midpoint of the central hole of the counter, and a paraffin plug was placed in the other end. The counter was calibrated before each measurement using a standard AmBe source. The relative error of each data point in Figure 2-7 is about 5%, primarily due to fluctuations in the energy of the proton beam.

2.2.4 Application to Lithium Compounds

It is a relatively simple matter to modify Eq. (2.18) to predict neutron yields in lithium compounds. We need to change the A_{eff} term to correspond to the molecular weight of the lithium compound, and in addition it is necessary to multiply by n, the number of lithium atoms per unit cell of the compound. For example, in the case of lithium oxide, Li_2O, there are two lithium atoms per molecular unit, so $n = 2$ in this case, and the molecular weight of Li_2O is now used for A_{eff}. Unless the ^{7}Li enrichment is changed, f_{Li-7} will not change. The only other change in calculating yields for lithium compounds is in the mass stopping power, which in the absence of experimental data must be estimated from the addivity rule for stopping powers. Our

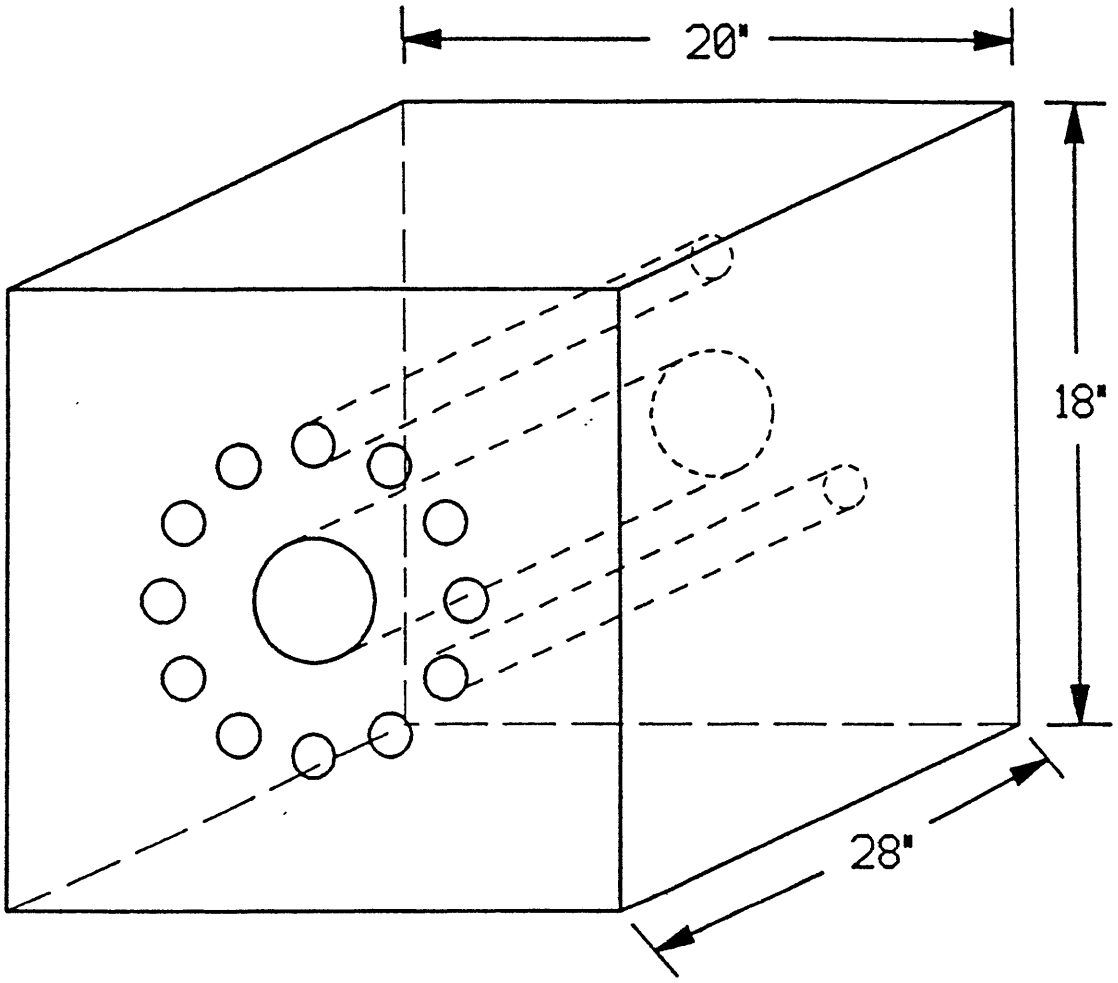

Figure 2-8: Schematic of Long Counter Used to Measure Total Neutron Yields for Lithium Compounds [2]

proton energy range of interest falls in the region of greatest applicability of the Bethe–Bloch formula [44], so that the Bragg–Kleeman rule is generally applicable [45, 46, 47]. Unlike lithium metal, lithium compound stopping powers are tabulated at particular proton energies, and linear interpolation is used to determine the stopping power at energies between these tabulated values. Tabulated elemental stopping powers used to construct compound stopping powers were taken from Janni [44].

Thick target yields have been calculated for Li_3N, Li_2O, LiF, LiOH, and LiH. These compounds were chosen because they have high lithium atom densities and low molecular weights. Although the lithium atom density is actually higher for all compounds listed above except LiOH, the neutron yields are lower than for lithium metal targets. This is due to the larger stopping powers that appear in the denominator of Eq. 2.18. The angular distributions and energy spectra of lithium compound neutrons are similar to those of lithium metal because the stopping powers of all elements have the same general energy variation in the proton energy range of interest. The greatest errors in compound stopping powers are expected to be for LiH, for which the Bragg–Kleeman rule has the least applicability. A comparison of thick target neutron yields for several compounds is given in Table 2.2. In addition, experimental and calculated total neutron yields are given for LiF in Figure 2-9 and for Li_2O in Figure 2-10. As with the experimental data for lithium metal given in Figure 2-7, the relative errors for all experimental points is about 5%. The good agreement between calculation and experiment verifies not only the capabilities of the calculational technique, but also the validity of the additivity rule for stopping powers for these compounds.

2.2.5 Partially Thick Targets

This technique is also well suited to the prediction of neutron yields from targets that are not sufficiently thick to slow the proton beam past the reaction threshold.

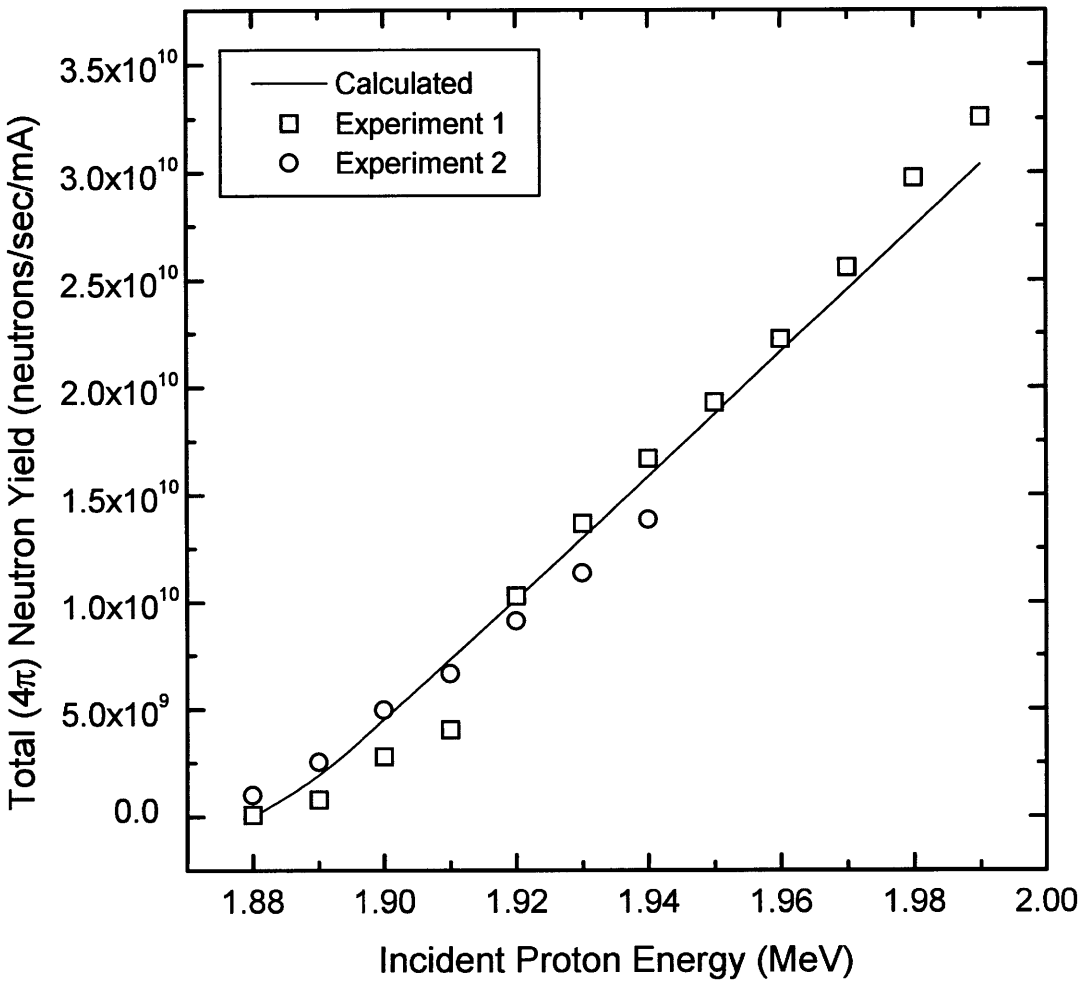

Figure 2-9: Calculated and Experimental Total Neutron Yields for Thick LiF Targets

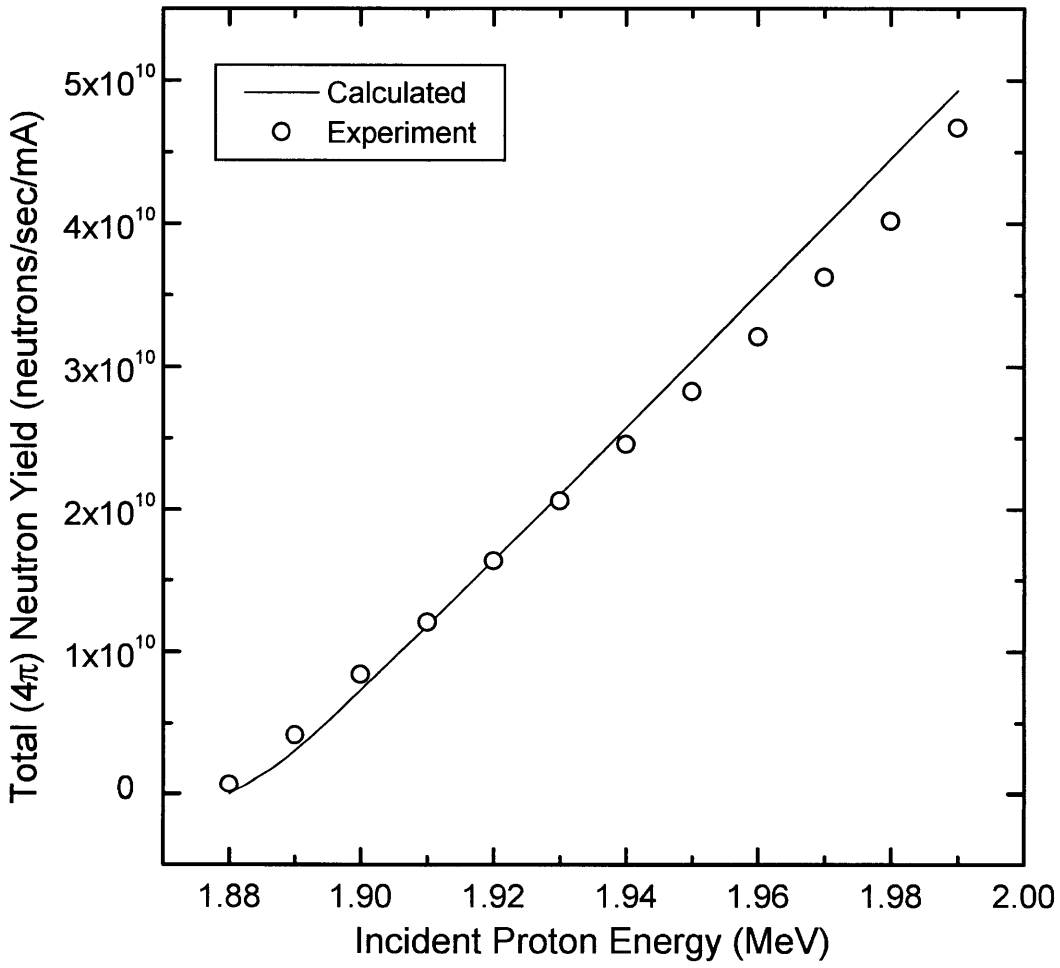

Figure 2-10: Calculated and Experimental Total Neutron Yields for Thick Li_2O Targets

Table 2.2: Near–Threshold Thick Target Neutron Yields for Lithium Compounds. Yields are in units of neutrons/mC.

Incident Proton Energy (MeV)	Li	LiF	Li_2O
1.89	6.34×10^9	1.92×10^9	3.11×10^9
1.90	1.49×10^{10}	4.52×10^9	7.33×10^9
1.91	2.41×10^{10}	7.29×10^9	1.18×10^{10}
1.92	3.35×10^{10}	1.01×10^{10}	1.64×10^{10}
1.93	4.30×10^{10}	1.30×10^{10}	2.11×10^{10}
1.94	5.25×10^{10}	1.57×10^{10}	2.57×10^{10}
1.95	6.21×10^{10}	1.88×10^{10}	3.04×10^{10}
1.96	7.16×10^{10}	2.17×10^{10}	3.51×10^{10}
1.97	8.12×10^{10}	2.45×10^{10}	3.98×10^{10}
1.98	9.08×10^{10}	2.75×10^{10}	4.45×10^{10}
1.99	1.00×10^{11}	3.04×10^{10}	4.93×10^{10}
2.00	1.10×10^{11}	3.33×10^{10}	5.40×10^{10}

Consider a proton beam passing through a partially thick target of thickness Δx. As the beam passes through the target, the mean beam energy decreases as before until it exits the lithium metal or compound with a mean beam energy of $E_{p,exit} > E_{th}$. Figure 2-11 is similar in composition to Figure 2-1, except that only contours for E_{p0} and $E_{p,exit}$ are shown. Since the proton beam leaves the target before reaching energies below $E_{p,exit}$, the differential neutron yield for proton energies below this is zero. Neutrons will only be produced in the region bounded by these contours, but in all other ways, this calculation is identical to the one described before. It only remains to determine $E_{p,exit}$.

Consider a function $\mathcal{R}_i(E_p)$, defined as the range of protons of energy E_p in material i. After passing through a partially thick target, the range is reduced and we may invert this function to determine the exit energy:

$$E_{p,exit} = \mathcal{R}_i^{-1}[\mathcal{R}_i(E_{p0}) - \Delta x], \tag{2.21}$$

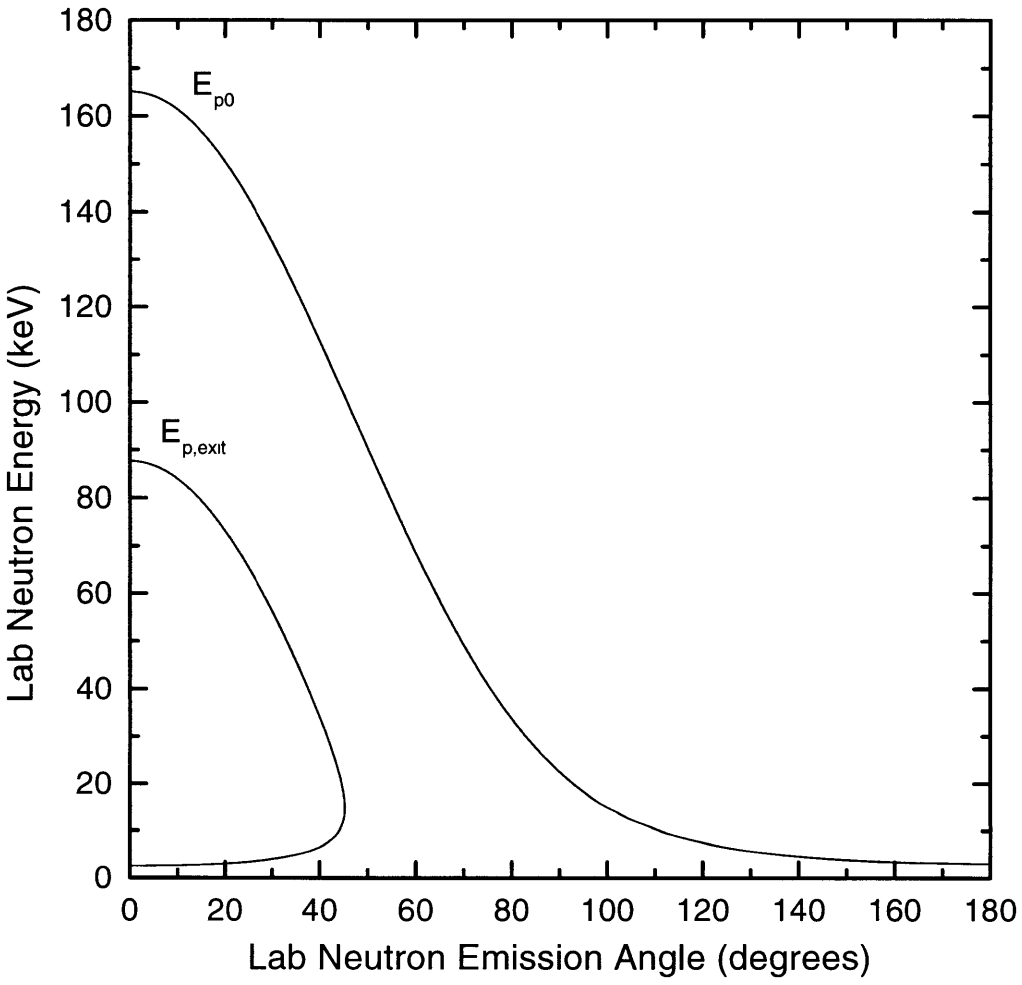

Figure 2-11: Contours Defining Neutron Production in a Partially Thick Target. Neutrons are only produced with energy and angle combinations between the upper and lower contours.

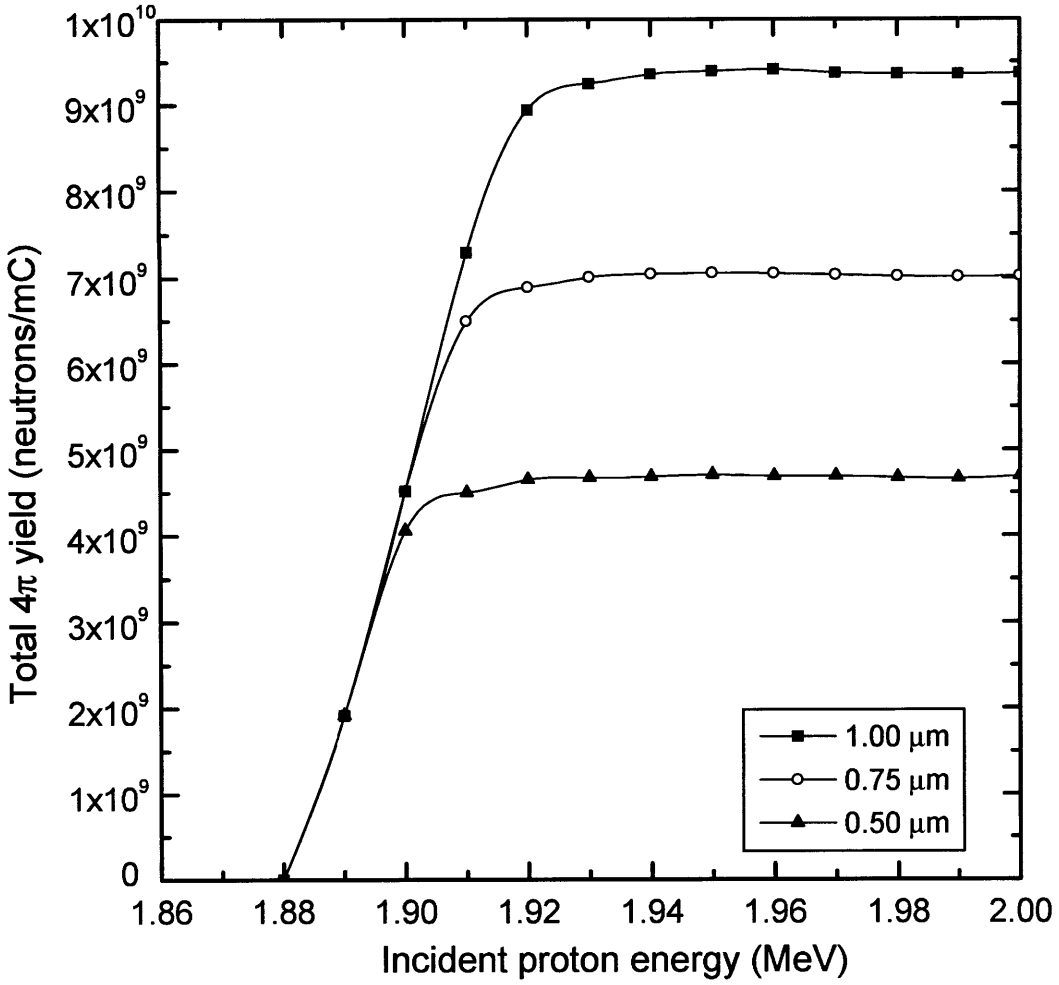

Figure 2-12: Calculated Total Neutron Yields for Partially Thick LiF Targets

where $\mathcal{R}_i^{-1}(x)$ is the proton energy whose range in material i is x. This method is applicable for small target thicknesses such that range and pathlength straggling are not appreciable. In this research, the range is well fit to a least squares quadratic, which is easily inverted by finding the roots of the quadratic.

Figure 2-12 shows calculated total neutron yields as a function of proton beam energy for several partially thick targets of LiF. Note that there is an abrupt bend in the yield at a proton energy that is characteristic of the target thickness. The total yield levels out, decreasing slightly for higher proton energies. It is important to note that while the total neutron yield is essentially constant for proton energies above the

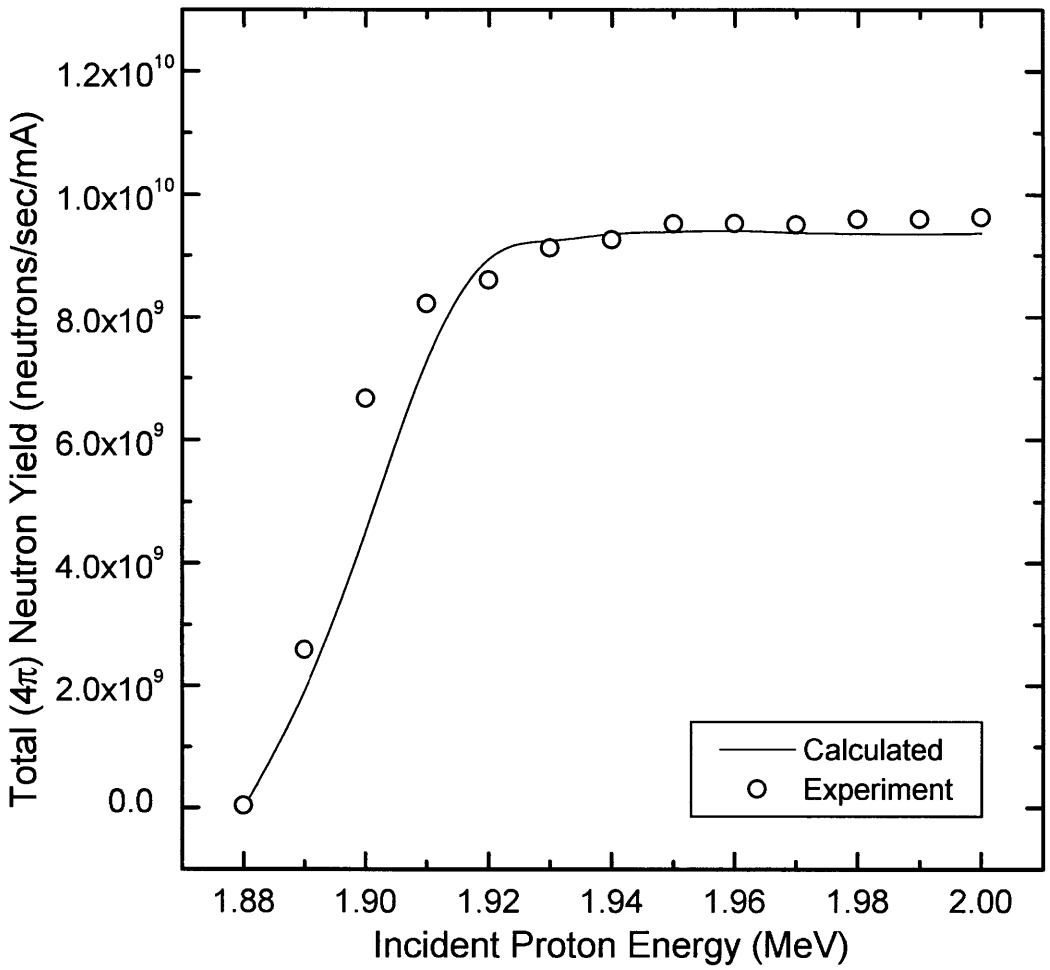

Figure 2-13: Calculated and Experimental Total Neutron Yields for a 1 μm Target

location of this knee, the energy spectra and angular distributions of these yields are not equivalent (see Figure 2-11).

Figure 2-13 gives a comparison of experimental and calculated total neutron yields as a function of incident proton energy for a partially thick 1 μm LiF target. 99.5% pure LiF powder was vapor evaporated in vacuum onto a copper disk, and the target thickness was measured using a Maxtek[1] thickness monitor. Total yields were then calculated based on this target thickness and compared with yields measured with

[1]The Maxtek thickness monitor uses variations in the resonant frequency of a crystal to determine both thickness and deposition rate.

the long counter of Section 2.2.3. As with all long counter measurements described here, the relative error in these yields was on the order of 5%.

2.2.6 Model of Lithium Metal Oxidation in Air

The rapid corrosion of lithium metal when exposed to air presents difficulties in measurements of thick target lithium yields. The black film that forms on the target surface will consist of a mixture of lithium compounds, and while neutrons will still be produced in this film, the yield will be lower than the metal yield, as discussed in Section 2.2.4 above. If the film thickness is less than the distance to slow down past threshold, however, the beam will produce some neutrons in pure metal after passing through the film, so that the degree of yield reduction will depend on the incident proton energy E_{p_0}.

The oxidation of lithium metal is modeled as a film of thickness Δx_{film} covering the surface of a thick lithium metal target. The film is produced while the target is attached to the accelerator beam tube and prior to the establishment of a vacuum in the tube. Once the vacuum is established, the corrosion film is assumed to remain constant in thickness and composition.

There is some question as to the exact composition of the black corrosion film, but it is agreed to be a combination of anhydrous and singly hydrated LiOH, Li_2O, Li_3N, and Li_2CO_3 [48, 49, 50]. The fraction of each component in the film depends on many variables, including exposure time to atmosphere, temperature, and humidity. There is evidence that the initial product is primarily anhydrous LiOH, with small amounts of Li_2O and Li_3N, although water in the air is incorporated within minutes to form primarily hydrated hydroxide [51]. Given sufficient exposure times, the film will become almost entirely Li_2CO_3, a white, flaky powder [52]. Since the lithium metal target is attached to the beam tube in the span of a few minutes of its initial exposure to air, the corrosion film has been modeled as LiOH.

To predict the neutron yields from these exposed targets, Eq. (2.21) must be modified to determine the mean proton beam energy at the point where the LiOH layer ends and the lithium metal begins:

$$E_{p,transition} = \mathcal{R}^{-1}_{\mathrm{LiOH}}[\mathcal{R}_{\mathrm{LiOH}}(E_{p_0}) - \Delta x_{film}]. \tag{2.22}$$

For proton energies between E_{p_0} and $E_{p,transition}$, the differential neutron yield is calculated for LiOH, while for energies between $E_{p,transition}$ and E_{th}, the yield is for lithium metal.

An example of the total neutron yield of a thick lithium metal target exposed to air is given in Figure 2-14. These yields were measured with the 4π detector described in Section 2.2.3, with relative errors again on the order of 5%. Also shown is the total neutron yield calculated for a 1.5 μm LiOH layer using the technique described above. This thickness was chosen by adjusting the hydroxide layer thickness to the value that minimized the squared error between calculated and experimental values. A distinct knee is observed in the total yield, whose location is strongly dependent on the assumed film thickness. Note that since the slope of the curve below the knee depends on the corrosion layer material (a layer that consists primarily of another corrosion compound, such as Li_2O, will have a greater slope than that in Figure 2-14), the agreement in the slopes of the calculated and experimental results below the knee indicates that the corrosion layer is primarily LiOH, as assumed.

This method has been demonstrated to correctly account for the change in the variation of the thick target neutron yield with incident proton energy, using a single adjustable parameter ($E_{p,transition}$). While this model is unable to predict thick target neutron yields from corroded lithium targets in general, the agreement with experiment indicates that the basic assumptions of the model are valid, e.g. the corrosion layer is primarily anhydrous lithium hydroxide.

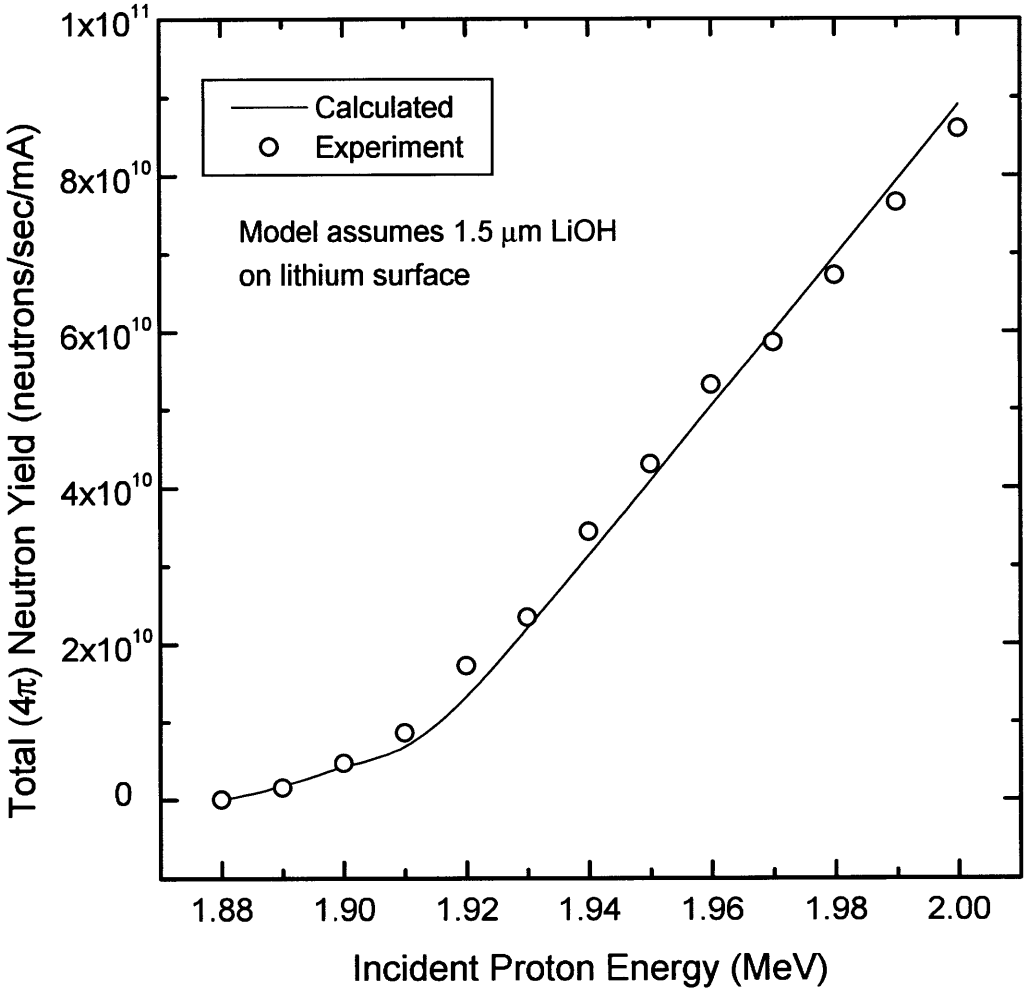

Figure 2-14: Calculated and Experimental Total Neutron yields for a Thick Lithium Target Exposed to Air. A 1.5 μm LiOH target thickness is assumed.

Chapter 3

Feasibility of Near–Threshold BNCT

This chapter consists of basic demonstrations of the feasibility of near–threshold BNCT, using the thick target neutron yield results of Chapter 2. The main purpose here is to demonstrate that the epithermal neutron flux is sufficiently intense for reasonable accelerator proton beam currents to allow for realistic patient treatment times. It is also necessary to consider the magnitudes of the fast and gamma fluxes in order to see if they will be low enough to make the near–threshold BNCT concept viable.

3.1 What is necessary for a useful BNCT treatment beam?

The general requirements on neutron beams for BNCT were outlined in Chapter 1, but quantitative descriptions of beam parameters is necessary for detailed beam design. Moss *et al.* list the following as basic requirements for a useful BNCT treatment beam [8]:

- epithermal neutron flux, ϕ_{epi}: 10^9 neutrons/cm^2-sec
- neutron energy, E_n: 1 eV to 10 keV
- gamma dose rate, D_γ: ≤ 1.0 Gy/hour (2.8×10^{-11} cGy-cm^2/neutron)
- fast neutron dose rate, D_n: ≤ 0.5 Gy/hour (1.4×10^{-11} cGy-cm^2/neutron)
- current-to-flux ratio, J/ϕ: ≥ 0.8

There is some question, however, whether these requirements are unnecessarily stringent for BNCT neutron source design. For comparison with the values given above, consider the beam parameters for existing BNCT treatment beams shown in Table 3.1 [11]. The beams considered are the Brookhaven Medical Research Reactor (BMRR) at Brookhaven National Laboratory (BNL), the Massachusetts Institute of Technology (MIT) Reactor (MITR-II), and the High Flux Reactor (HFR) at Petten in the Netherlands. The epithermal neutron flux is defined to be between 1 eV and 10 keV, and all doses are physical, not RBE, doses. It seems reasonable that if this simple feasibility assessment can predict near–threshold beams that are comparable to the beams in Table 3.1, there should be ample motivation for further analysis of these beams.

Table 3.1: Existing Epithermal Neutron Beams for BNCT Clinical Trials in the U.S. and Europe

Parameter	Units	BMRR	MITR-II	HFR
ϕ_{epi}	(n/cm^2-sec)	1.8×10^9	0.21×10^9	0.33×10^9
D_n/ϕ_{epi}	(cGy-cm^2/n)	4.3×10^{-11}	9.3×10^{-11}	8.6×10^{-11}
D_γ/ϕ_{epi}	(cGy-cm^2/n)	1.4×10^{-11}	14.1×10^{-11}	10×10^{-11}
D_n	(Gy/hour)	2.79	0.70	1.02
D_γ	(Gy/hour)	0.91	1.07	1.19
J/ϕ	—	0.67	0.55	> 0.8

3.2 Light Water versus Heavy Water

It is clear from Figure 2-4 that even the lowest near–threshold beams will require moderation of the neutrons to get them into the ~1 eV to 10 keV range. For most accelerator–based neutron beams for BNCT, light water (H_2O) is not used because the large moderation requirements of those high energy neutrons produce high thermal neutron fluxes in the moderator, the hydrogen capture gammas from the source reduce the effectiveness of the beam, and the hydrogen capture itself reduces the overall efficiency of the moderator assembly. Other moderators, such as heavy water (D_2O) and AlF_3, have therefore been considered to alleviate this gamma source problem and to improve the overall filter efficiency. For near–threshold beams, however, the lower neutron energies produced in the target (which are only tens of keV above the epithermal region) require less moderation, so there will be a much lower thermal neutron flux and hence gamma flux. Light water has, in fact, been found to be the ideal moderator for near–threshold beams [34].

Figure 3-1 shows how the neutron energy spectrum changes with light water moderator thickness for a near–threshold proton energy of 1.91 MeV. This energy is based on the optimum beam energy determined by Kudchadker [34]. The vertical lines on the figure are lines of demarcation for the epithermal energy range, 1 eV to 10 keV. These spectra were calculated by the Monte Carlo neutron and photon transport program MCNP [53], using a source spectrum calculated from the `li.f` program described in Chapter 2. As expected, the fast neutron flux decreases steadily with increasing moderator thickness. Figure 3-1 indicates that a moderator thickness between 3 and 6 cm is necessary to reduce the fast neutron flux without substantially reducing the epithermal flux.

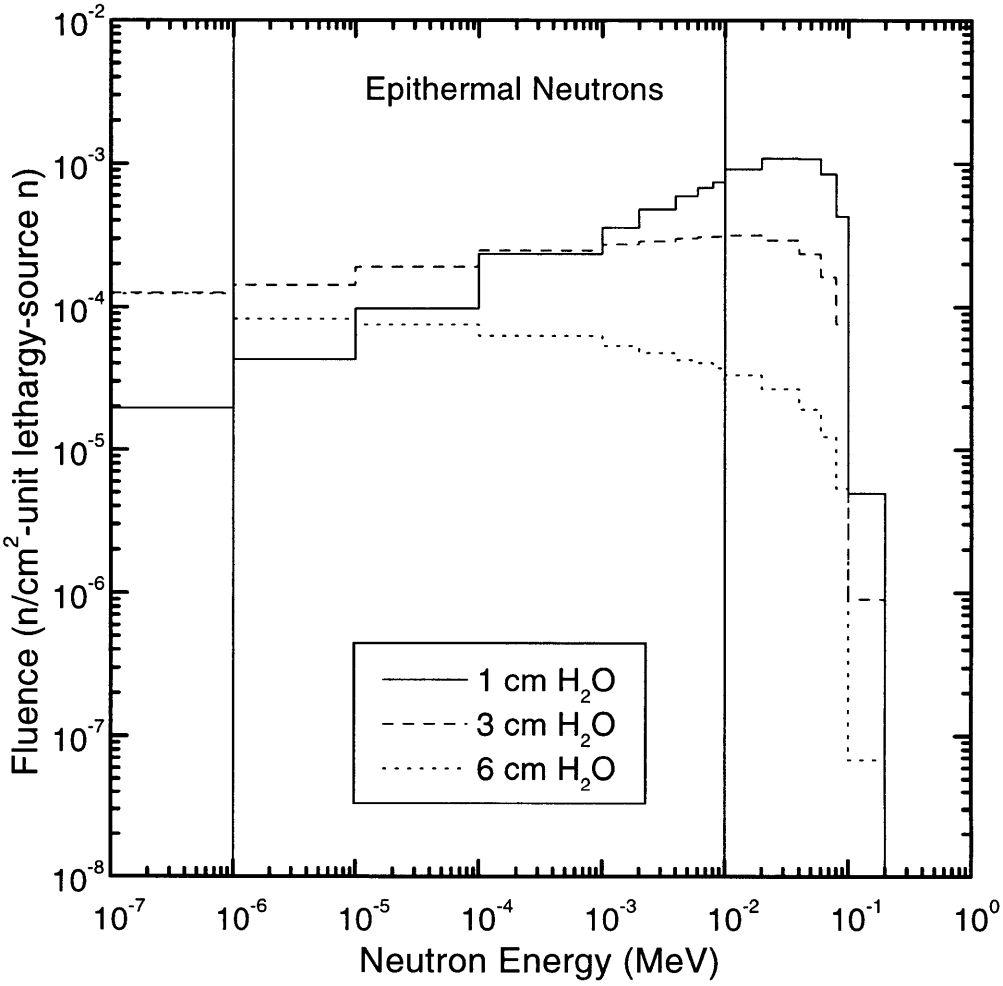

Figure 3-1: Neutron Energy Spectra as a Function of H_2O Moderator Thickness for 1.91 MeV Protons

Table 3.2: Calculated Neutron Beam Parameters as a Function of Moderator Thickness for 1.91 and 1.95 MeV Protons

Incident Proton Energy (MeV)	Moderator Thickness (cm)	Epithermal Neutron Flux (n/cm^2-sec/mA)	Fast Neutron Dose (cGy-cm^2/n)	Gamma Dose (cGy-cm^2/n)
1.91	1	3.7×10^7	31×10^{-11}	1.1×10^{-11}
	3	3.0×10^7	8.3×10^{-11}	16×10^{-11}
	6	0.68×10^7	5.3×10^{-11}	140×10^{-11}
1.95	1	9.0×10^7	42×10^{-11}	1.3×10^{-11}
	3	6.9×10^7	12×10^{-11}	16×10^{-11}
	6	1.7×10^7	6.7×10^{-11}	140×10^{-11}

3.3 Demonstration of Feasibility

Results of MCNP calculations using 1.91 and 1.95 MeV proton beams are shown in Table 3.2. Comparing these values with those of Table 3.1, we see that comparable fast neutron doses per epithermal neutron flux are achievable with 3-6 cm of water, and the proton beam currents necessary to be comparable with the MITR-II are 7 and 3 mA for 3 cm of water with 1.91 and 1.95 MeV protons, respectively. These currents are reasonable for a hospital–based BNCT accelerator. The only point of concern is the gamma dose, which is higher than one would like. However, this simple geometry does not include any kind of beam filter or photon attenuator, such as lead or bismuth. The gamma flux can be easily reduced by placing a thin sheet of one of these materials on the outside of the moderator, with a small reduction in the epithermal neutron flux. These numbers are sufficient to support further analysis of near–threshold beams.

Chapter 4

Near–Threshold BNCT Dosimetry

Now that the feasibility of near–threshold BNCT has been established, it is necessary to determine, in a more quantitative way, how effective these near–threshold beams are for BNCT treatments. To do this, a descriptive set of treatment parameters must be defined to allow for comparison of neutron beams from different proton beam energies. These parameters will be used to compare the therapeutic effectiveness for different components of the neutronic design of the target, target backing, moderator, and reflector.

4.1 BNCT Treatment Parameters

In addition to the three physical beam parameters given in Chapter 3, there are three descriptors of neutron beams that give information about therapeutic efficacy: depth of treatment, relative dose to tumor compared to surrounding healthy tissue, and treatment time. These beam descriptors may be quantitatively defined using the treatment parameters advantage depth (AD), advantage ratio (AR), and advantage depth dose rate (ADDR), respectively. These parameters were initially defined by Zamenhof [54].

The advantage depth is defined as that distance along the centerline of the phan-

tom at which the tumor dose rate is equal to the maximum healthy tissue dose rate. For distances in the phantom less than the AD, the tumor will receive a larger dose than the maximum allowed healthy tissue dose. Any tumor located outside the "advantage zone" defined by the AD will receive less dose than certain parts of the healthy brain, thus reducing any treatment "advantage" for that neutron beam. For the treatment of deeply seated brain tumors, it is desirable to have as large an AD as possible. For other BNCT treatment applications, the AD may not be as important a factor.

The advantage ratio is defined as the ratio of the areas under the dose rate curves for tumor and healthy tissue along the phantom centerline from the surface to the advantage depth; in other words,

$$\mathrm{AR} = \frac{\int_0^{\mathrm{AD}} D_{tumor}(z)\,dz}{\int_0^{\mathrm{AD}} D_{tissue}(z)\,dz}, \tag{4.1}$$

where $D_{tumor}(z)$ and $D_{tissue}(z)$ are the doses to tumor and healthy tissue, respectively, along the centerline (z-axis) of the phantom. The AR indicates the dose that any tumor located within the "advantage zone" will receive relative to the surrounding healthy brain tissue. A beam with a high AR is potentially more effective than a beam with a lower AR, so that high AR values are desirable. Note that the AR is always greater than one, by definition.

Finally, the advantage depth dose rate is defined as the tumor dose rate at the advantage depth, which is necessarily equal to the maximum healthy tissue dose rate according to the definition of AD. Since the total dose to healthy tissue is usually a limiting factor of treatment designs, the maximum healthy tissue dose rate determines the treatment time for the patient (treatment time = allowed healthy tissue dose / maximum healthy tissue dose rate). Again, the ADDR should be as large as possible to reduce the treatment time.

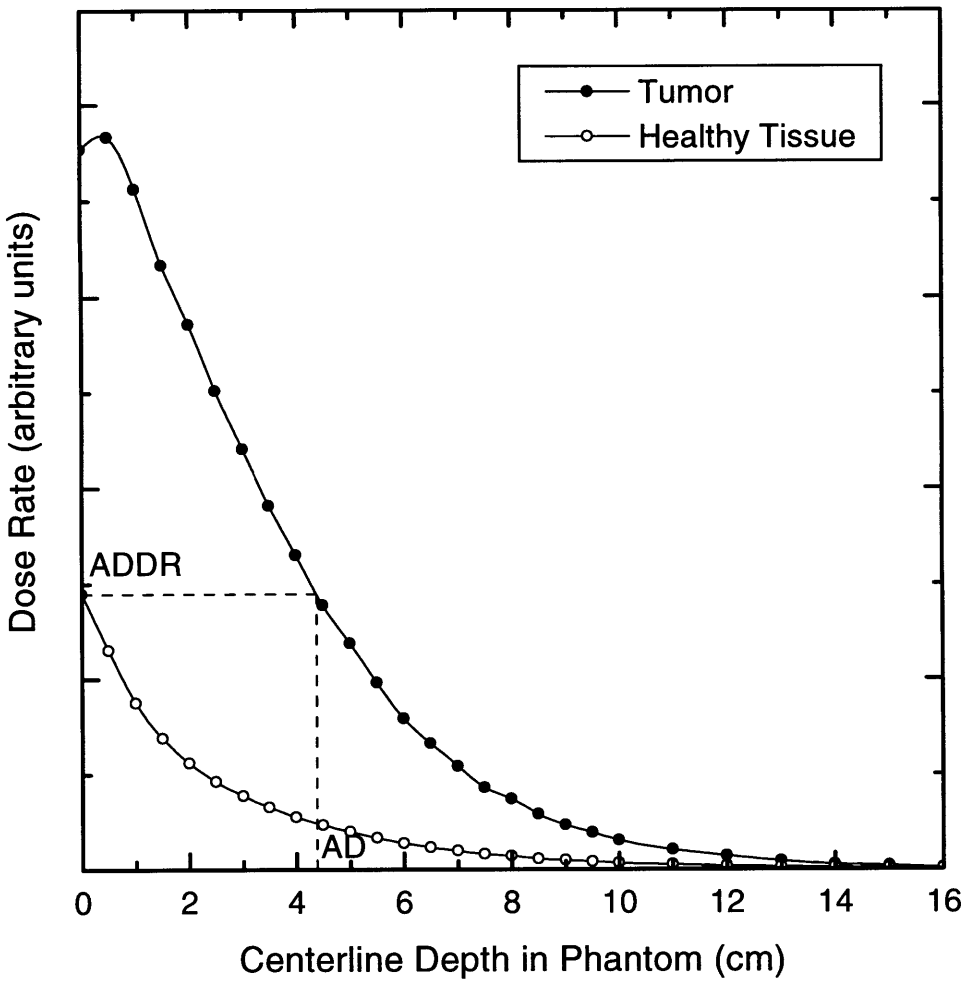

Figure 4-1: BNCT Treatment Parameter Definition

Figure 4-1 demonstrates the definitions of these three parameters for a hypothetical BNCT treatment beam. Plotted are centerline doses for both tumor and healthy tissue along the full length of the phantom. The AD is determined by drawing a horizontal line from the maximum healthy tissue dose rate to the point of intersection with the tumor dose curve. The AR is calculated by integrating under each curve and taking the ratio, as described in Eq. 4.1. The ADDR is self–explanatory. For an accelerator–based neutron beam, the parameters AD and ADDR have units of centimeters and centigrays per minute per mA of proton beam current, and the AR is dimensionless. If RBE values are used in the determination of these parameters

Table 4.1: RBE Values for BNCT Calculations

Dose Component	RBE Value
Fast neutron	3.2
Thermal neutron	3.2
^{10}B (tissue)	1.35
^{10}B (tumor)	3.8
Photon	1.0

(see Section 1.2.3), they are called RBE-AD, RBE-AR, and RBE-ADDR.

The RBE values used for different dose components are given in Table 4.1. Values listed are those currently used in clinical BNCT trials at MIT and BNL [17], and they are considered the best choice in current practice. Any adjustment of these RBE values will change all three BNCT treatment parameters defined above, and intercomparisons of the results presented here with published results for other neutron beams will not be completely equivalent for this reason. In addition, it is conceivable that RBE values for near–threshold beams will differ from reactor beams, but since RBE values have not been determined for the former, the values in Table 4.1 are considered a "best guess". The effect of RBE values is further discussed in Section 4.4.1. In addition, the tumor–to–healthy tissue uptake ratio of ^{10}B is taken to be 3.5, and the tumor uptake concentration is 40 μg ^{10}B/g tissue, or 40 ppm. These are realistic values for the pharmaceutical boronophenylalanine (BPA), which is used in the current clinical trials at BNL and MIT [20, 17].

It is important to recognize that, in most cases, an adjustment to a neutron beam that improves one of these treatment parameters will reduce at least one of the other parameters. Since it is desirable to have high values for all three parameters, a compromise will be necessary in determining what target/moderator/reflector combination (hereafter called the combined target unit, or CTU) to use for a prototypical near–threshold BNCT neutron beam. This also means that it is unlikely that

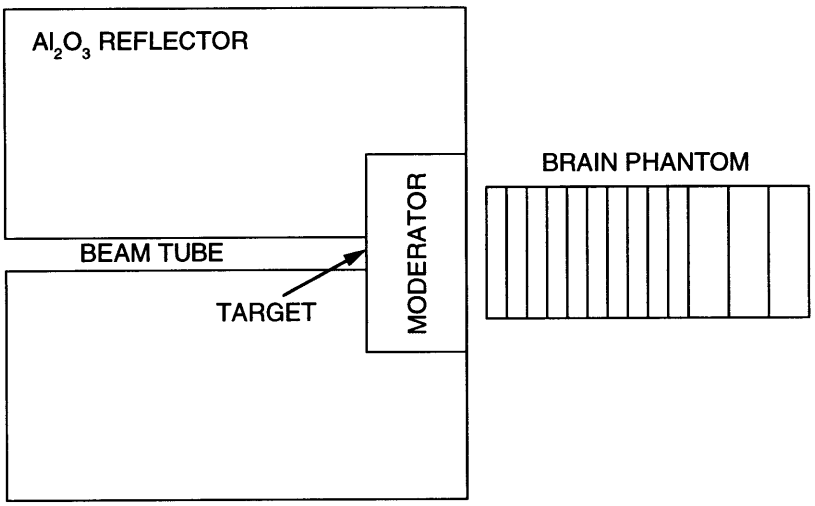

Figure 4-2: MCNP geometry

any particular neutron beam will be clearly "optimum". Rather, the requirements described in Section 3.1 will dictate minimally acceptable values for the advantage depth and advantage depth dose rate.

4.2 MCNP Design

The radiation transport necessary to calculate the BNCT treatment parameters described in Section 4.1 was performed using MCNP[1]. The MCNP input consisted of four main sections: geometry specification, source definition, materials specification, and tally description. Explanations of each of these sections is given below.

The basic MCNP geometry is given in Figure 4-2. Note that there is cylindrical symmetry for all objects shown. In the simplest MCNP runs, only the beam tube, moderator, reflector, and phantom were modeled. The target was not included in the

[1]Monte Carlo N–Particle radiation transport computer program.

model since it has dimensions on the order of microns to tens of microns (see Section 4.3 below), so a negligible number of reactions occur in the target and including it in the model needlessly slows down the computation. The moderator thickness was variable, and the outer edge of the reflector was always even with the outer surface of the moderator, but all other dimensions were invariant. The front of the phantom was always located 1 cm from the outer surface of the moderator, so that the location of the phantom relative to the target changed with increases or decreases in moderator thickness or the addition of material layers on the outside of the moderator. The 16 cm long phantom was divided into twelve disks so that fluxes and doses could be tallied as a function of depth into the phantom. Concentric cylinders were also defined to allow the radial variation of the fluxes and doses to be computed.

The source definition for the MCNP input deck was defined within a circular region of the surface at the end of the beam tube where the target is placed. The neutron source was uniform within this disk. The neutron energy input was defined as a histogram distribution determined by integrating the energy spectra of Section 2.2.2 over 10-keV intervals and normalizing with the total neutron yield. The full angular and energy dependence was implemented by defining the angular variable of the source as a function of the energy variable. In other words, there is a certain probability that a neutron is produced with an energy in a given energy interval. For this interval, there is an angular distribution of the neutrons, which is different for every energy interval. The angular distributions for each energy interval were represented by 10°-wide angle histograms. These histograms were determined by first binning the differential neutron yield surfaces calculated in Chapter 2 in 1-keV, 1° bins. These bins were then combined into 10-keV, 10° bins for MCNP, and the normalized bin values for each energy interval were used as the angular distribution definition.

The beam tube was taken to be a vacuum, while the moderator and reflector were light water (H_2O) and aluminum oxide (Al_2O_3), respectively. The phantom was made

Table 4.2: Brain Material Specification for the MCNP Phantom

Element	Weight Percentage (%)
H	10.57
C	13.97
N	1.84
O	72.59
Na	0.14
P	0.39
Cl	0.14
K	0.39

of brain-equivalent material consisting of a 50/50 combination of white and grey brain matter by weight [55]. The density was taken to be 1.047 g/cm^3, and the specific material composition is given in Table 4.2. Note that the MT material cards, which provide accurate thermal neutron transport in certain materials in MCNP, were used for light water.

The neutron flux was tallied both within cells defined by the thirteen planes and nine cylinders making up the phantom, as well as on the planes themselves. The neutron flux was modified in certain tallies by dose functions, which are essentially KERMA values for neutron and ^{10}B doses. The neutron KERMA values were taken from tabulated values from Caswell [56], while the ^{10}B KERMA values are those determined by Zamenhof [54]. The photon dose was calculated in a similar manner. These tallies, while producing very large output files, allow very detailed mapping of the principal dose components that were described in Section 1.2.2. One million source particles were used in all calculations to produce doses with relative errors less than 5% for all depths below 10 cm.

A sample MCNP input file is given in Appendix D. This input file calculates neutron and photon doses, as well as ^{10}B doses for a 1 μg/g concentration, for a 1.95 MeV proton beam with 5 cm of H_2O moderator.

4.3 Photons Produced in the Lithium Target

While neutrons are the most important BNCT source component from a lithium target, photons can also be produced from different reactions, the most significant of which are radiative capture (p,γ) and inelastic proton scattering ($p,p'\gamma$). The (p,γ) reaction is important because it produces very hard gammas in the energy range from 14 to 18 MeV due to the extremely low binding energy of the residual nucleus, ^{8}Be [57]. The shielding of these gammas would be very difficult, and the resulting effect on the treatment efficacy could be important. Inelastic proton scattering produces 478 keV gammas [58], which are not as energetic as the radiative capture gammas but could present a greater problem if the reaction cross section is larger. The first step in designing MCNP simulations of lithium targets requires an evaluation of the contribution of each of these components.

The yield of photons from the (p,γ) reaction may be estimated from the cross section and the formula

$$Y_{p-\gamma} = N_{Li-7} \int_0^{E_{p0}} \frac{\sigma_{p-\gamma}(E_p)}{-\frac{dE_p}{dx}} dE_p, \tag{4.2}$$

where $Y_{p-\gamma}$ is the total photon yield due to the (p,γ) reaction in lithium, $\sigma_{p-\gamma}(E_p)$ is the total cross section as a function of proton energy E_p, and the other variables are defined as in Section 2.1.1. Eq. 4.2 is seen to be an integration of Eq. 2.2 over solid angle for the (p,γ) reaction. The (p,γ) cross section is shown in Figure 4-3 [59, 60]. It is important to recognize that the scale of the cross section is on the order of microbarns, as compared to that of the (p,n) reaction, whose cross section is on the order of millibarns. There is, however, a relatively large, narrow resonance located at 441 keV, with a width of only 12 keV [61]. The 441 keV energy corresponds to the 17.63 MeV excited energy level in the compound nucleus ^{8}Be [62]. Using this cross section and tabulated proton stopping powers in lithium from Janni [44], the thick

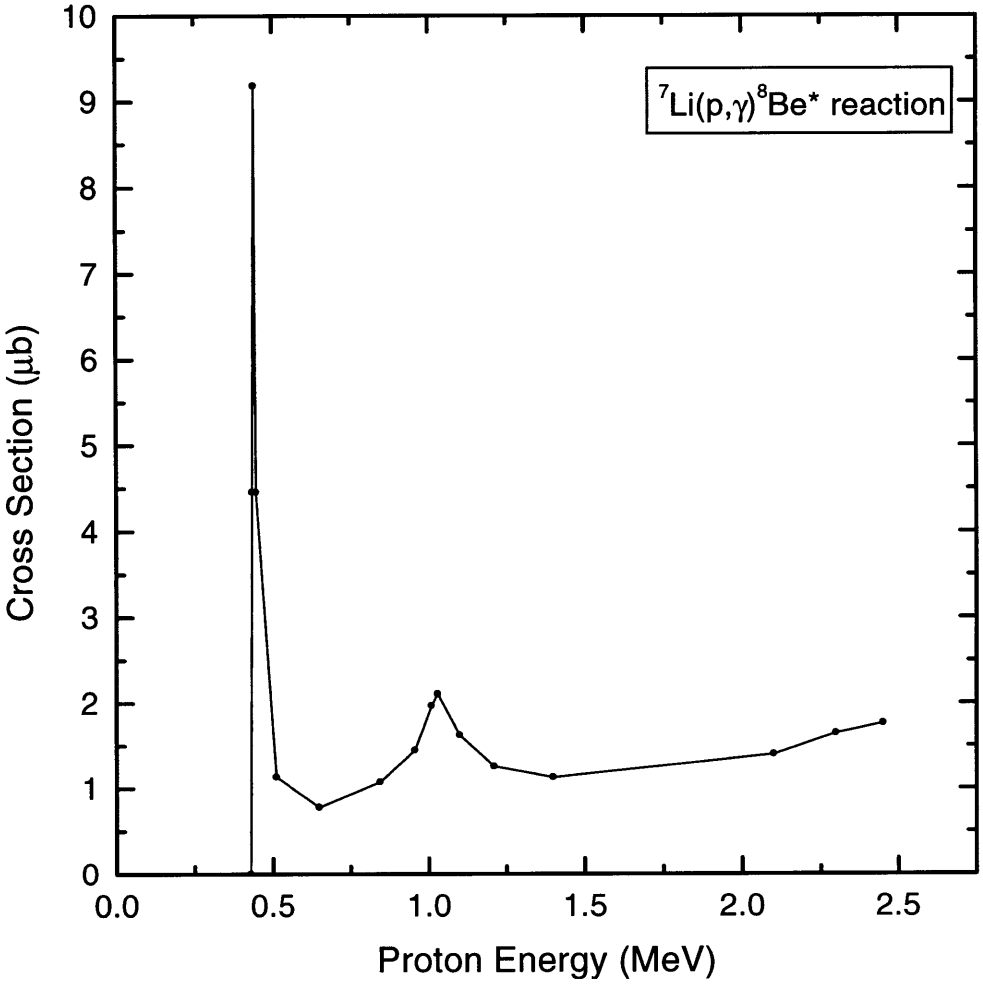

Figure 4-3: Total cross section for (p,γ) reaction in ^{7}Li

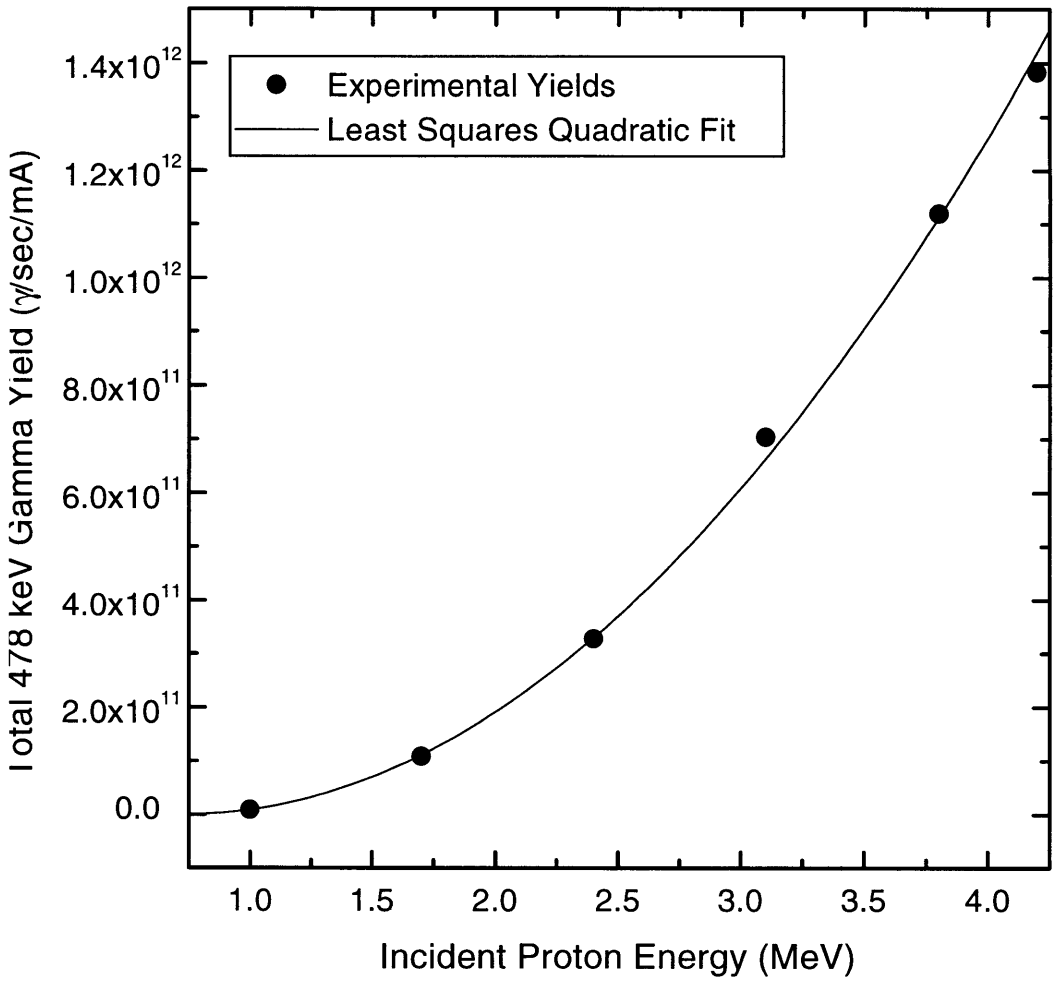

Figure 4-4: Experimental 478 keV Gamma Yield for Inelastic Proton Scattering in Lithium. Experimental points are taken from Ref. [3]. The least squares quadratic fit to the data is given in Eq. 4.3

target (p,γ) gamma yield is calculated to be 5.62×10^6 gammas/sec/mA. Comparison of this yield with the thick target neutron yields in Table 2.1 shows that the effect due to these gammas will be low. They will be neglected in future calculations for this reason.

For the inelastic proton scattering in the target, Eq. 4.2 will not be necessary, since tabulated thick target gamma yields for this reaction are available [3]. These tabulated yields are shown in Figure 4-4, along with a quadratic least squares fit to the data. The least squares fit is given by the equation

Table 4.3: Comparison of Neutron and Photon Yields for Thick Lithium Targets

Incident Proton Energy (MeV)	Neutron Yield (n/sec/mA)	478 keV Gamma Yield (γ/sec/mA)	Gamma Yield Relative to Neutron Yield (%)
1.89	6.34×10^{9}	1.59×10^{11}	2510
1.90	1.49×10^{10}	1.62×10^{11}	1090
1.91	2.41×10^{10}	1.65×10^{11}	684
1.92	3.35×10^{10}	1.68×10^{11}	500
1.93	4.30×10^{10}	1.70×10^{11}	396
1.94	5.25×10^{10}	1.73×10^{11}	330
1.95	6.21×10^{10}	1.76×10^{11}	284
1.96	7.16×10^{10}	1.79×10^{11}	250
1.97	8.12×10^{10}	1.82×10^{11}	224
1.98	9.08×10^{10}	1.85×10^{11}	204
1.99	1.00×10^{11}	1.88×10^{11}	188
2.00	1.10×10^{11}	1.91×10^{11}	174
2.10	2.13×10^{11}	2.22×10^{11}	104
2.20	3.62×10^{11}	2.56×10^{11}	70.6
2.30	5.78×10^{11}	2.91×10^{11}	50.4
2.40	7.78×10^{11}	3.30×10^{11}	42.4
2.50	8.83×10^{11}	3.70×10^{11}	41.9

$$\sqrt{Y_{p-p'\gamma}} = 343227.2E_p - 249579.0, \tag{4.3}$$

where $Y_{p-p'\gamma}$ is the 478 keV gamma yield in gammas/sec/mA and E_p is the incident proton energy in MeV. Table 4.3 gives a comparison of neutron and photon yields for thick lithium targets. It is clear that for all proton beam energies discussed up to this point, and especially for near–threshold energies, the gamma yield from inelastic proton scattering in the target completely dominates the neutron yield. The effect of these photons on the BNCT treatment parameters for a 1.93 MeV proton beam is shown in Figure 4-5. The MCNP geometry for this example only consists of 3 cm of water moderator and an Al_2O_3 reflector. The two curves with open symbols correspond to results in which the 478 keV gammas are ignored. The neutron beam appears to have an RBE-AD of 4.38 cm, an RBE-AR of 4.34, and an RBE-ADDR

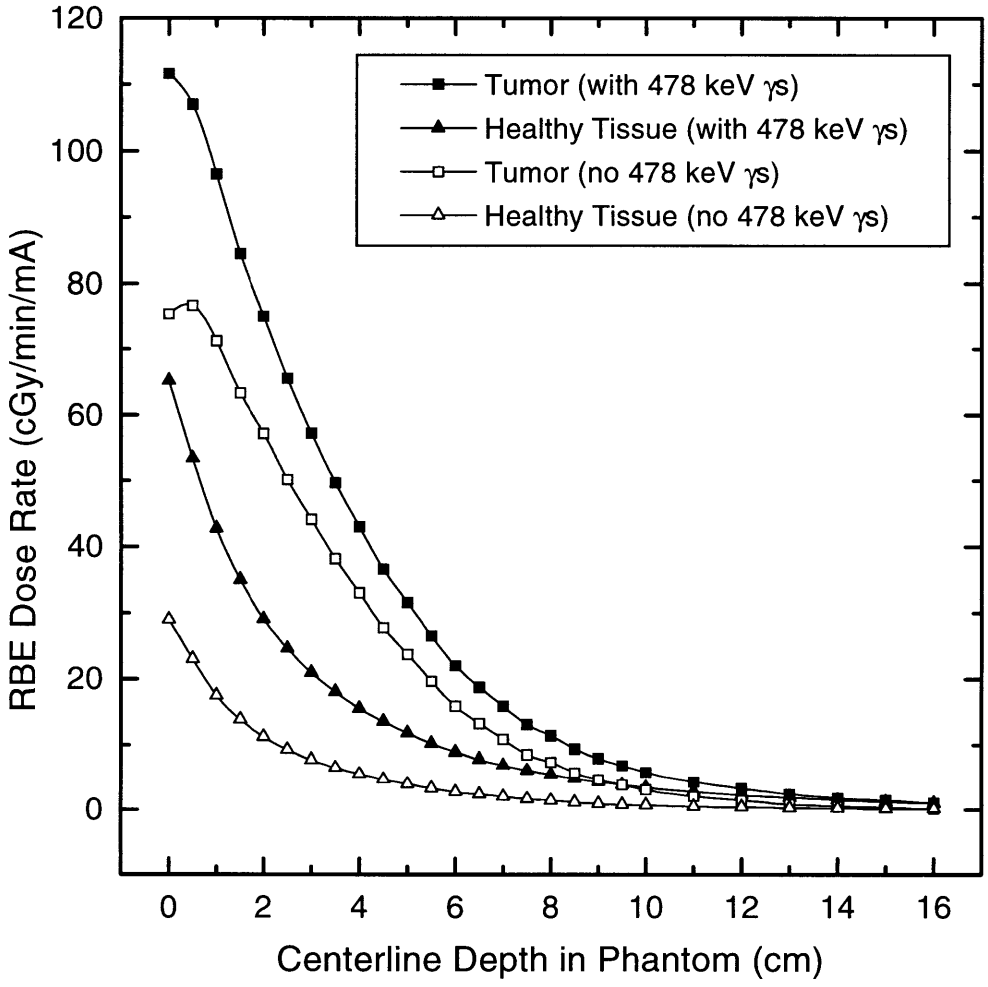

Figure 4-5: Effect of $^{7}\mathrm{Li}(p,p'\gamma)^{7}\mathrm{Li}$ Photons on BNCT Treatment Parameters

of 28.97 cGy/min/mA. The two curves with solid symbols include the effects of the inelastic proton scattering gammas. These doses are calculated in a separate MCNP run that only tracks photons and uses an isotropic, 478 keV photon source having a total yield given by Eq. 4.3. The total photon dose in the phantom is just the sum of the doses from photons produced in the combined neutron–photon run with the (p,n) neutron source and from photons from the 478 keV photon source in the photon–only run. The RBE-ADDR is seen to increase dramatically, but the RBE-AD drops to only 2.52 cm, with a similar drop of the RBE-AR to 2.20. The neutron beam has very little penetrability due to the gammas from inelastic proton scattering.

Based on this scenario, one would conclude that this approach is not feasible. However, the answer to this dilemma lies in the fact that neutrons are only produced in lithium for proton energies above 1.88 MeV, while 478 keV gammas are produced for proton energies down to 550 keV. If the lithium target is only made thick enough for the proton beam to slow down past the (p,n) threshold, there will be no loss of neutron yield, but the gamma yield from inelastic proton scattering will be reduced significantly. Note that this target concept is completely different from the partially thick lithium targets described in Section 2.2.5, which were too thin for the proton beam to slow down past the (p,n) threshold. These reduced thickness targets may be constructed by vapor deposition of lithium or a lithium compound directly onto the backing material. The remaining proton slowing down therefore will occur in the target backing, which itself may produce significant gammas from similar reactions (see Section 4.4.2). The reduced gamma yield for incident proton energy E_p, denoted $Y^*_{p-p'\gamma}(E_p)$, is given by the difference $Y^*_{p-p'\gamma}(E_p) = Y_{p-p'\gamma}(E_p) - Y_{p-p'\gamma}(E_{th})$. This concept reduces the gamma yield to levels that allow near–threshold treatment beams to again be feasible, although the 478 keV gamma source is still a significant effect and must always be taken into account. All subsequent MCNP calculations include the dose due to these gammas from inelastic proton scattering in the reduced thickness

lithium target. It should be noted that reduced thickness targets have additional advantages for target heat removal (see Section 5.2), but there are questions regarding target stability and lifetime that will need to be addressed (see Chapter 7).

4.4 Dose Calculations

Once the gammas produced in the lithium target were included in the MCNP calculations, the effects of various beam parameters on the BNCT treatment parameters were studied. The following beam parameters were studied:

- Proton Beam Energy (1.89 MeV to 1.99 MeV)
- Light Water (H_2O) Moderator Thickness
- Target Backing Material (Cu, Al, Stainless Steel)
- Thermal Neutron Shields (Cd, ^{6}Li)
- Photon Shields (Pb).

There are many other beam parameters that can be varied, but it was felt that the parameters listed above most strongly effect the behavior of BNCT neutron beams and also are least understood in terms of their effects for near–threshold beams. Other parameters that were not varied, i.e. remained constant for all computations, included proton beam spot size (1 cm radius); reflector material (Al_2O_3) and inner and outer radii (12 cm and 30 cm, respectively); moderator radius (12 cm); distance from moderator face to phantom face (1 cm); and phantom shape (cylindrical) and size (8 cm radius, 16 cm length). Previous studies have established the effect of these parameters on BNCT treatment [63, 13, 64, 65].

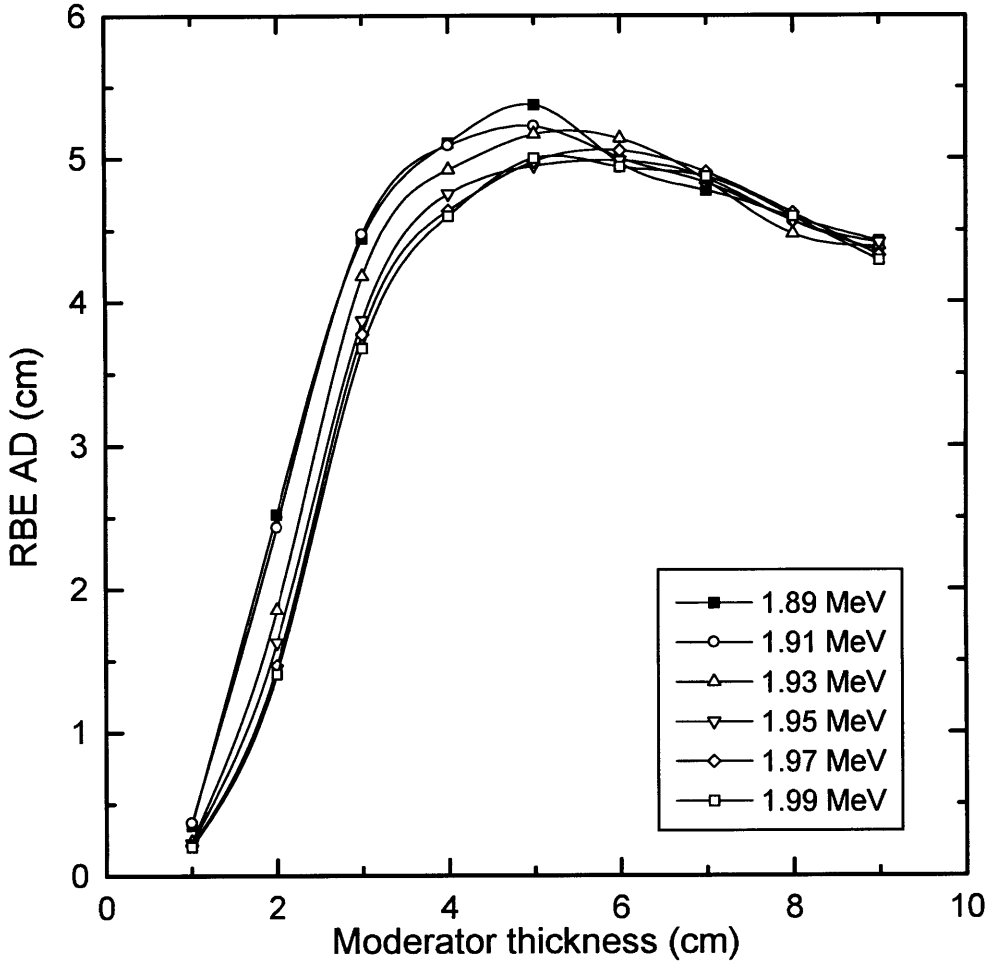

Figure 4-6: Variation of RBE-AD with Moderator Thickness for Near–Threshold Beams

4.4.1 Moderator Considerations

The primary parameters that influence the treatment parameters—proton beam energy and moderator thickness—were the first to be characterized using the basic CTU configuration of beam tube, moderator, reflector, and phantom. The variation of RBE-AD with moderator thickness is shown in Figure 4-6, while Figure 4-7 provides the RBE-ADDR variation. For all data points in Figure 4-6, the absolute errors in the RBE-AD are less than 0.20 cm, and relative errors in the RBE-ADDR are under 5%. For all near–threshold energies, the RBE-AD increases rapidly for small

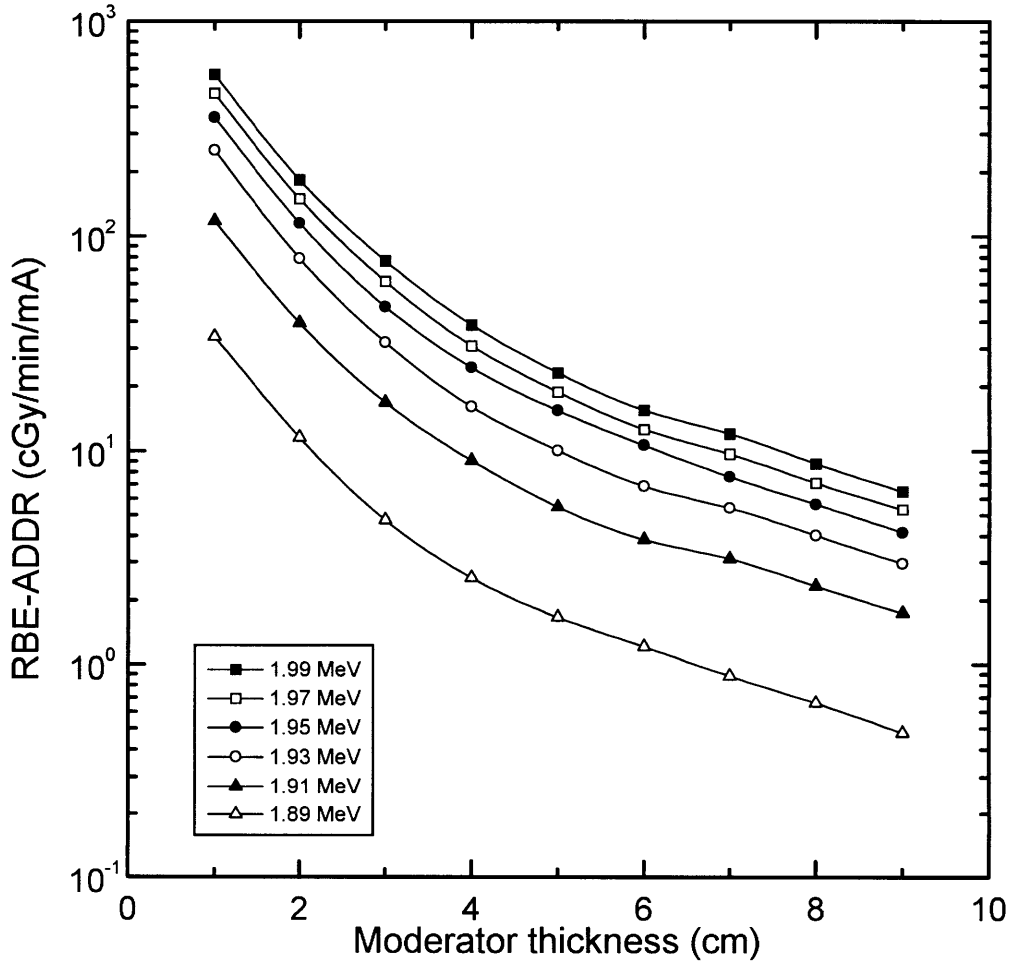

Figure 4-7: Variation of RBE-ADDR with Moderator Thickness for Near–Threshold Beams

moderator thicknesses, then reaches a peak around 5-6 cm and slowly decreases. It is also clear from the data that there is little or no difference in near–threshold beams for moderator thicknesses above ~5 cm. The RBE-ADDR in Figure 4-7 is seen to be highest for the highest proton beam energies, as expected, and decreases continuously with moderator thickness.

Ideally, a beam of epithermal neutrons with no fast neutron, thermal neutron, or gamma components incident on the front face of the phantom is desired. It is therefore important to study the percentage contribution to healthy tissue dose at the center of the phantom's front face from each component. Using the 1.95 MeV proton beam as a representative example, a plot of the variation of the percentage doses of these components, as well as the healthy tissue ^{10}B dose, with moderator thickness is given in Figure 4-8. The fast neutron dose is seen to completely dominate the dose for low moderator thicknesses; this is to be expected, since there is not enough moderator to substantially reduce the fast neutron component. The fast neutron dose affects both tumor and healthy tissue equally and hence reduces the advantage depth. As the moderator thickness increases, the fast component is quickly reduced (and the RBE-AD quickly improves), while the other components slowly increase. Since a larger thermal neutron flux will produce more hydrogen capture gammas in the moderator, the gamma dose will continuously increase with moderator thickness. As with fast neutron contamination, the gamma dose equally affects tumor and healthy tissue, so a point is reached where this dose begins to erode all the gains made in the RBE-AD by reducing the fast neutron component. This effect on the RBE-AD is not as dramatic as it is at shallow moderator thicknesses because the fast neutron RBE is 3.2, while the gamma RBE is only 1.0.

Still using 1.95 MeV as a representative example, Figure 4-9 presents the variation of both RBE-AD and RBE-AR with moderator thickness. The shapes are seen to be substantially similar, although the advantage depth drops to almost 0 cm for shallow

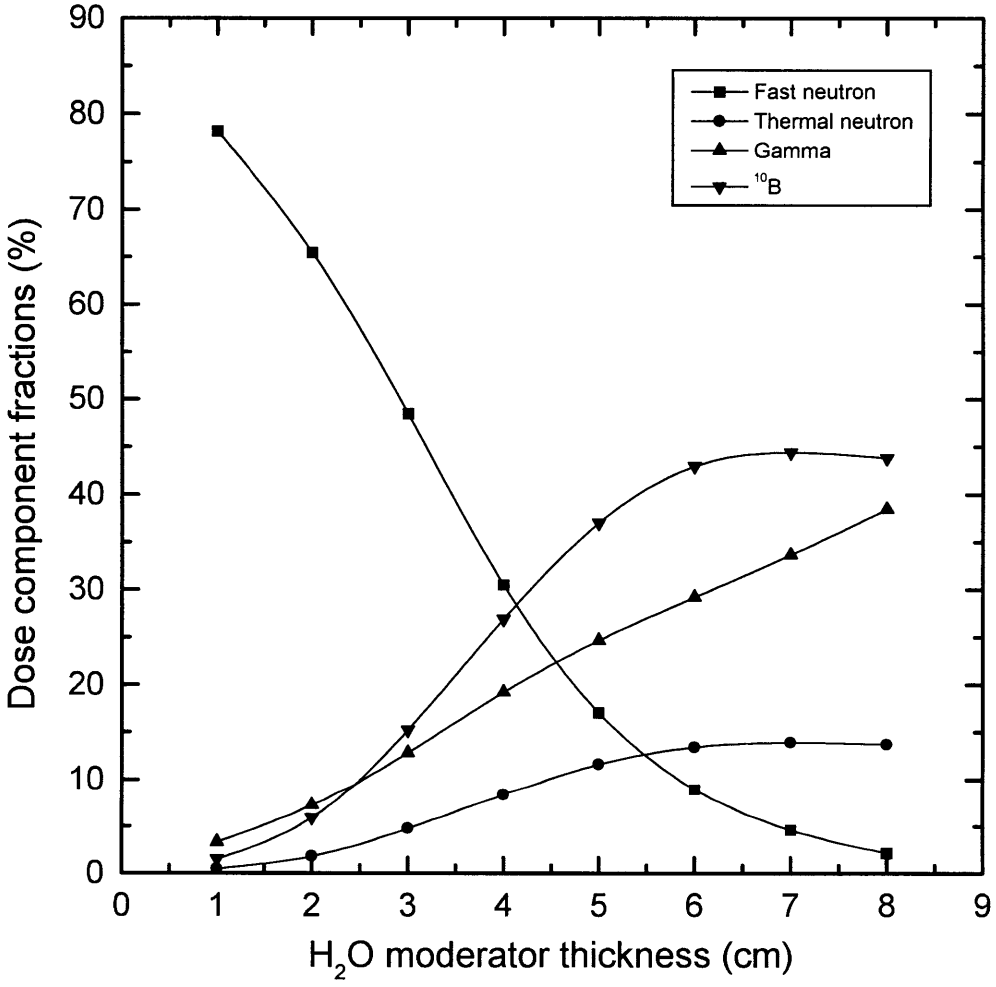

Figure 4-8: Percentages of Healthy Tissue RBE Dose Components on Front Phantom Face for 1.95 MeV Proton Beams.

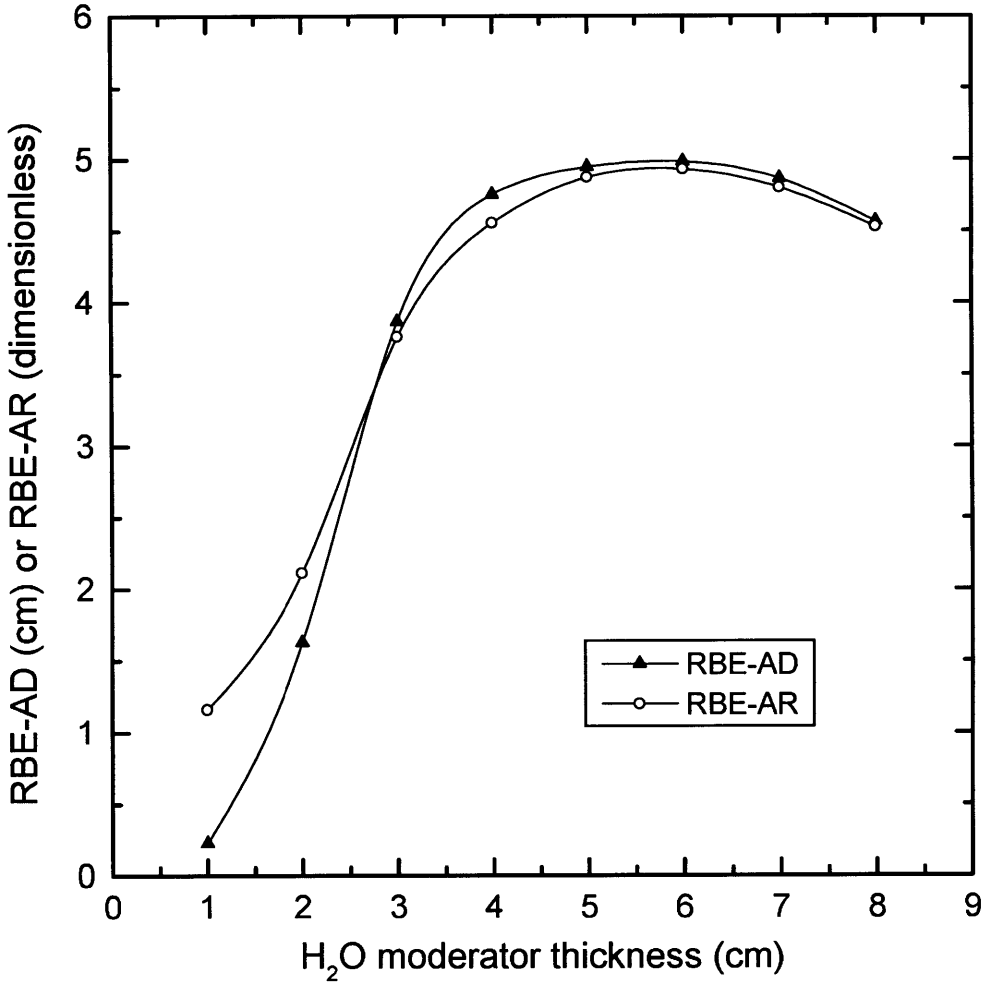

Figure 4-9: Comparison of RBE Advantage Depth and RBE Advantage Ratio for 1.95 MeV Proton Beams

moderator thickness, while the advantage ratio can never drop below a value of 1. The RBE-AR will not be presented in future sections, because changes in RBE-AD almost always reflect the changes in the RBE-AR. If important differences in the RBE-AD and RBE-AR are observed for certain CTU configurations, they will be noted in the text.

Figures 4-6 and 4-7 are useful for seeing how the BNCT treatment parameters vary with moderator thickness, but it is difficult to see how they vary in unison for different CTU configurations. The plot in Figure 4-10 facilitates this comparison by plotting the RBE-AD versus RBE-ADDR for each proton beam energy / moderator thickness combination. As the moderator thickness increases, the RBE-AD (horizontal axis) increases and the RBE-ADDR (vertical axis) decreases until the maximum RBE-AD is reached at about 5 cm moderator thickness. The RBE-AD will then begin to decrease (and hence bend back to the left) while the RBE-ADDR continues to decrease. All BNCT near–threshold beams follow this behavior.

As expected, there is no clear–cut optimum near–threshold proton beam energy, although 5 cm of water seems to be a likely contender for ideal moderator thickness. Instead of seeking an optimum proton energy, we consider a set of minimally acceptable values for the RBE-AD and RBE-ADDR, and any beam that meets both requirements is considered a useful BNCT treatment beam. It is reasonable to take 5 cm as a minimum advantage depth; this will permit irradiation with "advantage" to virtually all parts of the brain. As for the advantage depth dose rate, we take a value of 2000 RBE-cGy for the maximum healthy tissue dose, given in [66, 67], a treatment time of 60 minutes, and an accelerator current 5 mA to be reasonably achievable. This gives a minimum RBE-ADDR of 6.67 cGy/min/mA. The minimum RBE-AD and RBE-ADDR are plotted as dotted lines in Figure 4-10. Any points located in the upper quadrant above and to the right of these lines will meet our minimum requirements. It is seen that 1.93 MeV through 1.97 MeV proton energies

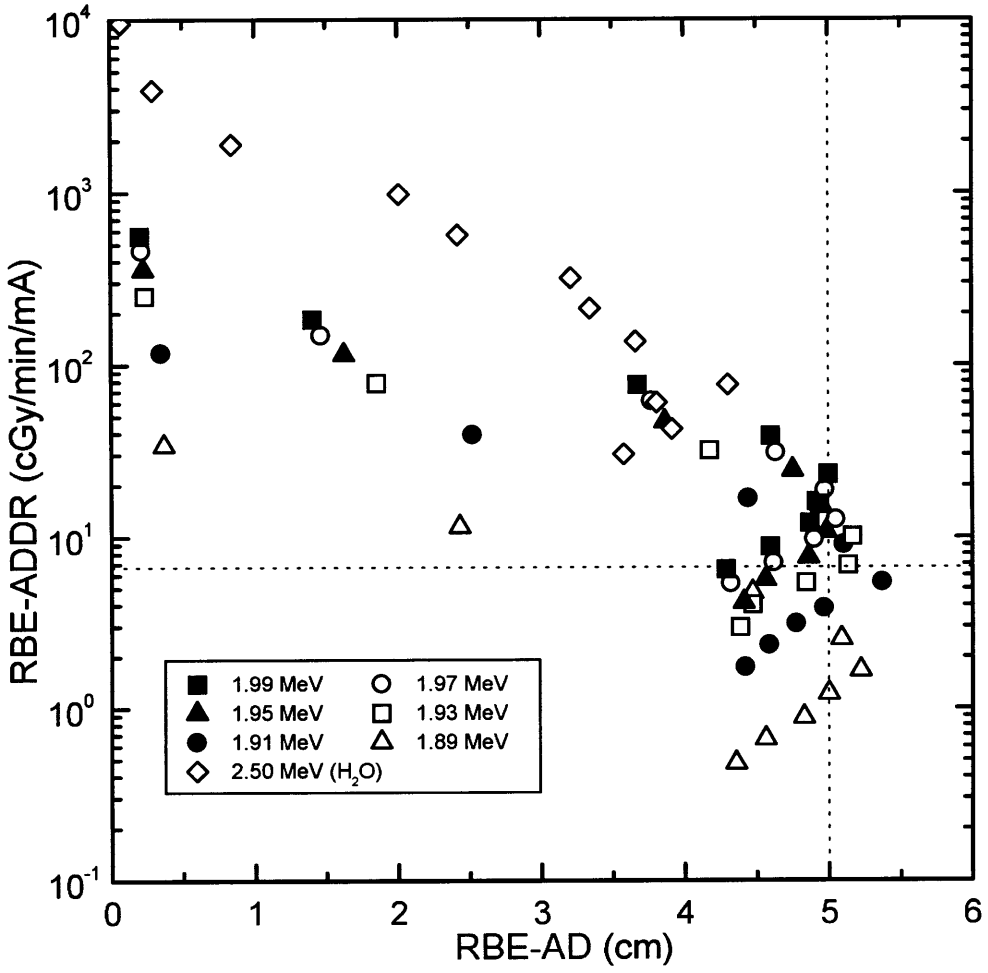

Figure 4-10: Variation of RBE-AD and RBE-ADDR as a Function of Proton Beam Energy and Moderator Thickness. The vertical dotted line indicates the minimum acceptable RBE-AD of 5 cm. The upper and lower horizontal dotted lines correspond to total healthy tissue RBE doses of 2000 cGy and 1250 cGy, respectively. Points in the upper quadrant satisfy the requirements for a BNCT neutron beam.

contain points that meet these requirements. For comparison, a maximum healthy tissue dose of 1250 RBE-cGy is currently used in the BNL clinical trial protocol, which for the treatment times and beam currents established above corresponds to an RBE-ADDR of 4.17 cGy/min/mA. This RBE-ADDR is also plotted in Figure 4-10. Incident proton energies from 1.91 to 1.97 MeV satisfy the less stringent beam requirements based on this reduced dose.

4.4.2 Target Backing Considerations

It is also important to consider what target backing material will be used. Using a vapor deposited lithium target means that most of the slowing down of the proton beam will occur in the target backing, so the effect of different candidate materials on BNCT treatment parameters must be assessed. Three candidate materials were considered: copper, aluminum, and stainless steel (type 304). These materials were chosen based primarily on familiarity and low cost.

As a first step, let us compare the BNCT treatment parameters with no backing material (calculated in Section 4.4.1) with the same parameters after the addition of 0.25 cm of these materials for 1.95 MeV protons. The RBE-AD is shown for each case in Figure 4-11. There is a small increase in the RBE-AD, as well as the RBE-AR, and of course a small decrease in the RBE-ADDR, due almost entirely to the $1/r^2$ effect. The small increase in the RBE-AD is due to the large number of resonances in the epithermal and fast regions of the neutron cross sections for the backing materials considered. These resonances lead to a small reduction in the fast neutron component of the beam, so that the advantage depth increases slightly. This small increase in the RBE-AD will produce a small increase in the RBE-AR as well, since the range of integration in Eq. 4.1 will increase. The most important thing to note in Figure 4-11 is that there is essentially no difference in the three backing materials from a neutronics point of view.

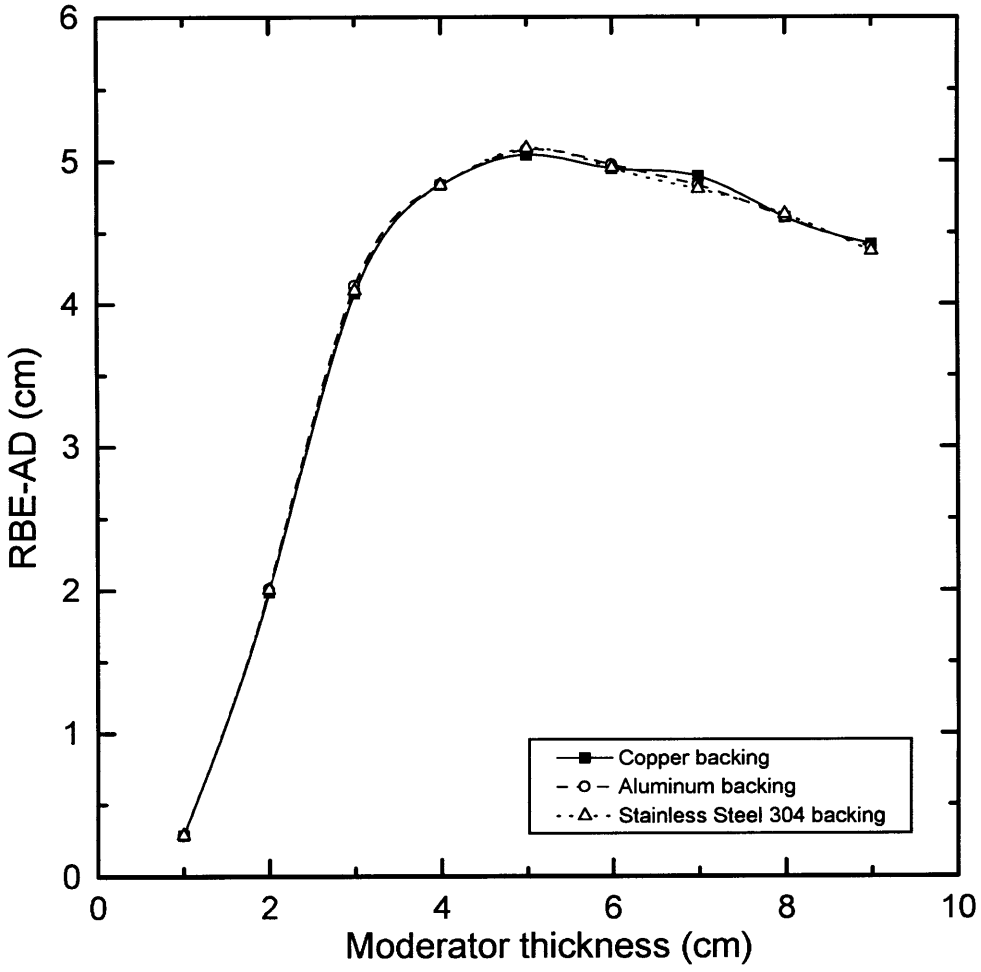

Figure 4-11: Effect of Target Backing Materials on RBE Advantage Depth for 1.95 MeV Protons

Table 4.4: Q–Values for (p,n) Reactions in Target Backing Material Candidates

Nuclide	Concentration (%)	Q–value (MeV)
Aluminum		
^{27}Al	100	-5.594
Copper		
^{63}Cu	69.2	-4.150
^{65}Cu	30.8	-2.133
Stainless Steel 304		
^{50}Cr	0.827	-8.415
^{52}Cr	15.920	-5.494
^{53}Cr	**1.805**	**-1.379**
^{54}Cr	0.448	-2.160
^{55}Mn	**0.020**	**-1.014**
^{54}Fe	4.031	-9.024
^{56}Fe	63.801	-5.349
^{57}Fe	**1.494**	**-1.619**
^{58}Fe	0.202	-3.091
^{58}Ni	6.489	-9.345
^{60}Ni	2.480	-6.910
^{61}Ni	0.107	-3.021
^{62}Ni	0.341	-4.732
^{64}Ni	0.086	-2.457

Now the effect of proton reactions in the backing materials must be gauged. The possible reactions that can occur in the target backing are: (p,n), (p,γ), and $(p,p'\gamma)$. Table 4.4 gives the concentrations of the primary constituents of the backing materials under consideration, as well as the Q–value for the (p,n) reaction in each nuclide. Atomic masses to determine these Q–values are taken from Krane [68] and the Table of Isotopes [58]. Since the backing material should only see proton energies below the threshold of the ^{7}Li$(p,n)^{7}$Be reaction, it is only necessary to consider nuclides with (p,n) Q–values greater than -1.644 MeV, the Q–value for ^{7}Li: ^{53}Cr, ^{55}Mn, and ^{57}Fe, shown in boldface, meet this criterion. However, the thick target neutron yields from (p,n) reactions in these three nuclides are less than 0.5% of the thick target yield in

the lithium target according to Tanaka et al. [69], Lee and Mooring [70], Chapman and Slattery [71], and Piertrzyk et al. [72]. Additional neutron production in the backing materials under consideration may thus be neglected.

Thick target photon yields from (p,γ) reactions in the nuclides listed in Table 4.4 may be obtained from the scientific literature [73, 74, 75, 76, 77, 78]. In all cases, the photon yield is negligible compared with the 478 keV gamma yield from inelastic proton scattering in the lithium target. Only the contribution of inelastic proton scattering is left to consider.

The relative contributions from inelastic proton scattering in each backing material under consideration were experimentally measured with a $5'' \times 5''$ NaI detector. The resulting photon spectrum is shown in Figure 4-12. Note that the photon yields from the aluminum target are greater than for either the copper of stainless steel target. This indicates that if the effect on the BNCT treatment parameters due to inelastic proton scattering in the backing material is negligible for aluminum, it will also be negligible for the other two candidate materials.

It is necessary to quantify the photon yields in the thick aluminum disk. The same reference that provided thick target gamma yields for inelastic proton scattering in lithium (see Section 4.3) has thick target gamma yields for aluminum as well [3]. These thick target gamma yields are given in Table 4.5 for an incident proton energy of 1.88 MeV.

MCNP calculations were performed using a photon source consisting of the five largest contributions to the inelastic proton scattering gamma yield. All source gammas were assumed isotropic. The contribution to the gamma dose in the phantom was added to that from the calculations shown in Figure 4-11, and new BNCT treatment parameters were calculated for various moderator thicknesses for 1.95 MeV protons. The variation of RBE-AD with moderator thickness for the cases of no target backing, Al backing including inelastic proton scattering gammas from lithium, and Al back-

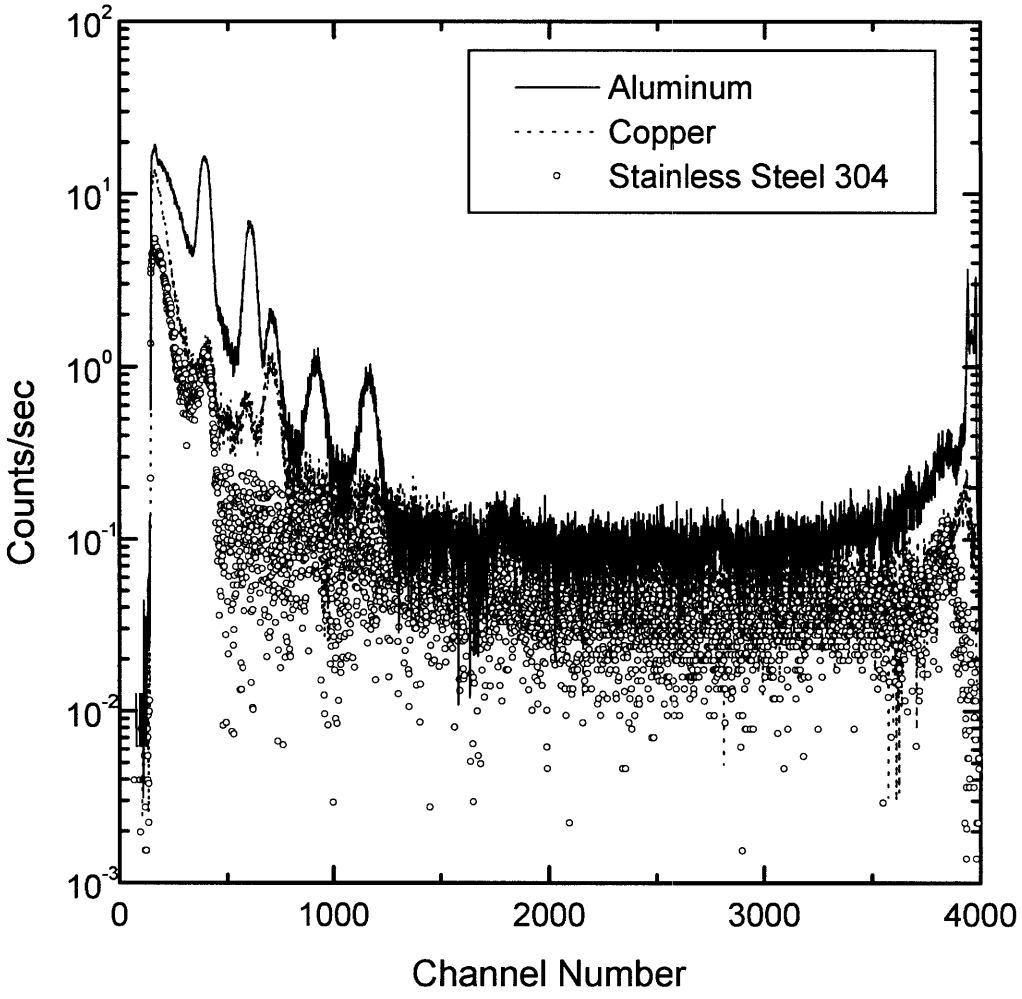

Figure 4-12: Experimental 0° Photon Yields from Cu, Al, and Stainless Steel (Type 304) Backing Materials for 1.95 MeV Protons. Photons were detected using a $5'' \times 5''$ NaI crystal.

Table 4.5: Total Gamma Yields from Inelastic Proton Scattering in Aluminum for 1.88 MeV Protons

Gamma Energy (keV)	Total Yield (%)
844	30.36
1014	58.05
1369	7.10
1779	4.09
2839	0.40

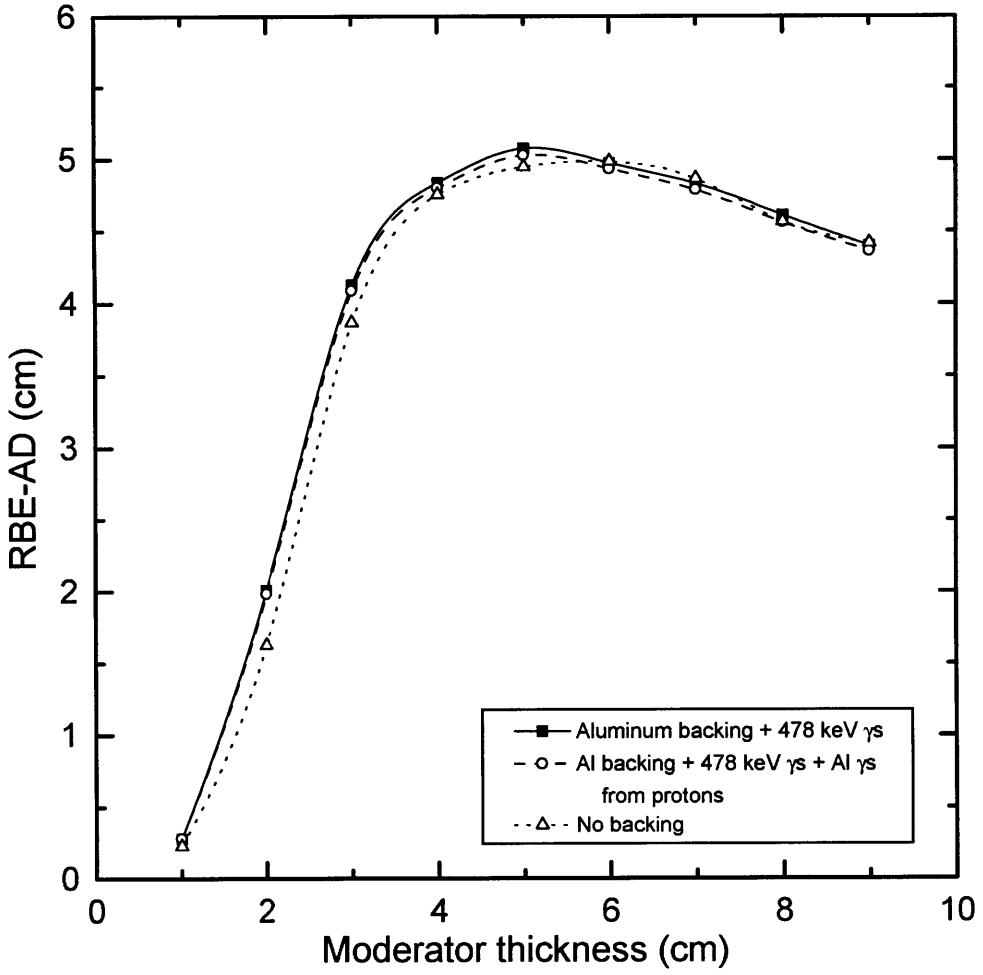

Figure 4-13: Effect of Gammas from Inelastic Proton Scattering in Aluminum on RBE Advantage Depth for 1.95 MeV Protons

ing including inelastic proton scattering gammas from both lithium and aluminum is shown in Figure 4-13. While a small increase in the RBE-AD is evident in going from no backing material to the addition of aluminum (for reasons discussed above), there is no apparent effect on the RBE-AD by including the inelastic proton scattering gammas in the calculations. We may therefore neglect all proton reactions in aluminum, as well as the other backing material candidates, in further calculations of BNCT treatment parameters. The backing material itself, however, must be included in the geometry of the MCNP input.

Table 4.6: Physical Properties of Target Backing Material Candidates

Material	Thermal Conductivity (300 K) (W/m-°C)	Melting Point (°C)	Linear Expansion Coefficient (10^{-6}/°C)
Copper	401	1083	16.5
Aluminum	237	660	23.1
Stainless Steel 304	15	1425	17.3
Lithium	**85**	**181**	**46**

Because there is no strong neutronic advantage to any of the backing materials considered, other properties must determine the best choice. Table 4.6 shows several relevant physical properties of the materials under consideration. All properties were taken from the CRC Handbook [26]. Although there is not a big difference in the linear expansion coefficients, copper is clearly superior in terms of thermal conductivity. For this reason, copper is chosen as the backing material in all subsequent calculations.

4.4.3 Thermal Neutron Attenuation

In an effort to reduce the thermal neutron component and thus improve the RBE-AD and RBE-AR of the beams under consideration, thin sheets of natural cadmium and ^{6}Li were placed behind the moderator. The 0.25 cm copper backing from Section 4.4.2 was included in the calculations. Figure 4-14 shows the effects on the RBE-AD for each thermal neutron absorber for a 1.95 MeV proton beam. The absorber thickness is 0.01 cm in both cases.

The penetrability of the beam is sharply reduced with the addition of cadmium, while it increases for ^{6}Li. The RBE-AD decrease with cadmium is due to the very large number of neutron capture gammas that are produced. These gammas overwhelm any advantage that is gained by the reduction of the thermal neutron flux. In the case of ^{6}Li, however, there is not a gamma production problem, so there is a noticeable increase in the RBE-AD. Of course, there is also a complementary decrease

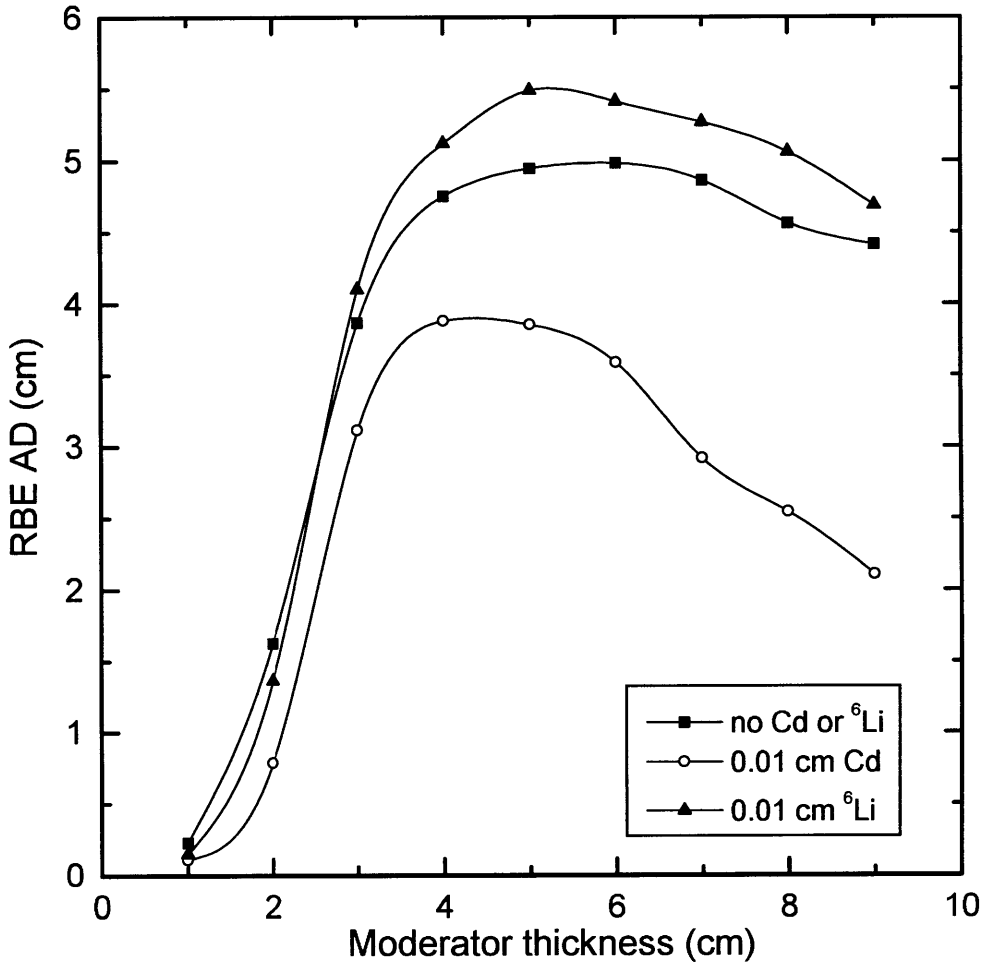

Figure 4-14: Effects of Cd and ^{6}Li thermal neutron shields on RBE-AD for 1.95 MeV Protons

in the RBE-ADDR. The combined change in RBE-AD and RBE-ADDR for 1.95 MeV protons is shown in Figure 4-15. While the RBE-ADDR is decreased with the addition of ^{6}Li relative to no thermal neutron absorber, the decrease is not great, and the increase in the RBE-AD pushes the neutron beam firmly into the useful region in the upper right quadrant of the figure.

4.4.4 Photon Attenuation

An alternative way to improve the RBE-AD and RBE-AR of these beams is to reduce the gamma flux from the moderator. There will always be an irreducible gamma flux in the head due to the hydrogen capture gammas, but any additional photons from the target will degrade the effectiveness of the beam. Lead sheets are considered here to attenuate the gamma flux from the target, since its high Z value leads to high cross sections and it is relatively inexpensive. It is important to note that there are two primary gamma energies that the lead shield is expected to attenuate: 478 keV gammas from the inelastic proton scattering in lithium and 2.22 MeV gammas from the thermal neutron capture reaction in hydrogen, ^{1}H(n,γ)^{2}H. The attenuation coefficient μ varies as a function of energy and is greater for the lower energy 478 keV gammas, meaning that for a given thickness of lead, there will be much more attenuation of the inelastic proton scattering gammas than the hydrogen capture gammas.

Several thicknesses of lead were placed behind the moderator to gauge the effect of gamma attenuation on the BNCT treatment parameters. As with the thermal neutron shields described in Section 4.4.3 above, the 0.25 cm copper backing is included in all MCNP calculations. For each thickness of lead, the BNCT treatment parameters were calculated for the entire range of moderator thickness from 1 to 9 cm of H_2O in order to determine the water moderator thickness that gives the maximum RBE-AD for a given lead thickness. This moderator thickness was found to always be in the range from 5 to 6 cm. The maximum RBE-AD for 1.95 MeV protons with lead

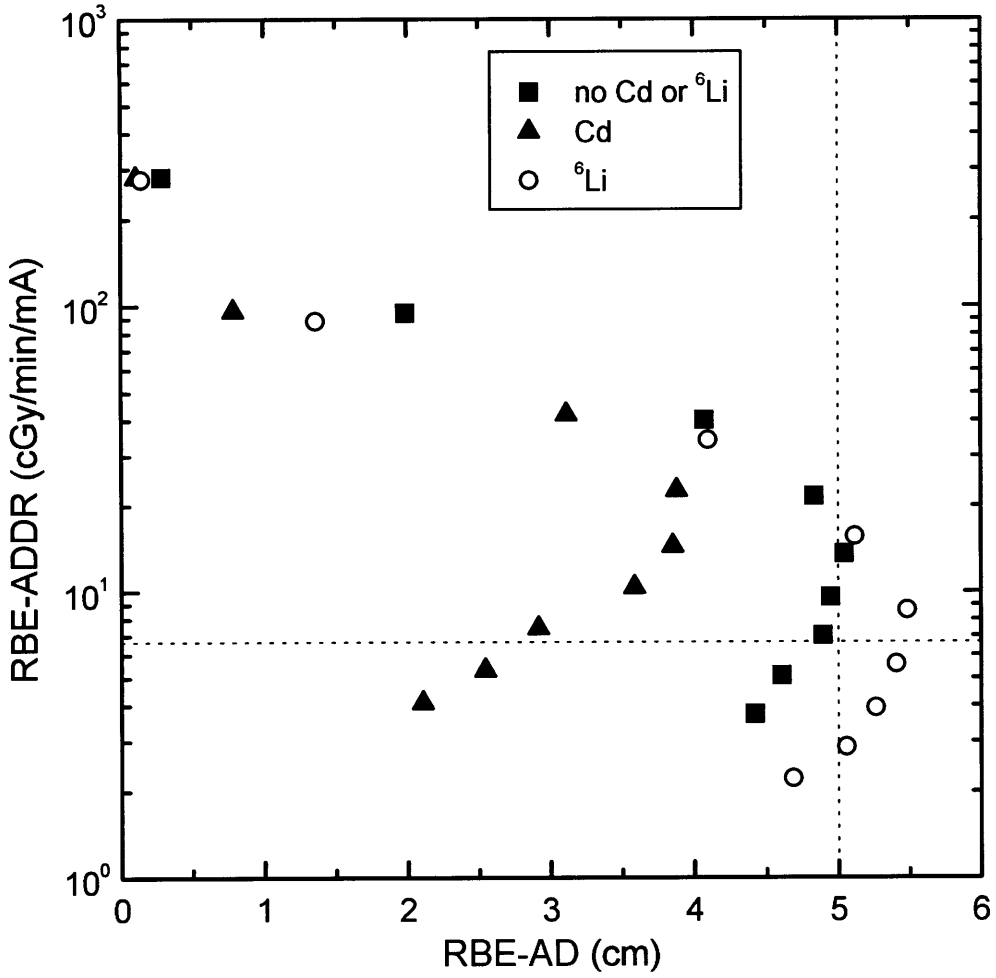

Figure 4-15: Variation of RBE-AD and RBE-ADDR with Moderator Thickness for 1.95 MeV Protons with and without Thermal Neutron Absorber Materials. The vertical dotted line indicates the minimum acceptable RBE-AD of 5 cm. The upper and lower horizontal dotted lines correspond to total healthy tissue RBE doses of 2000 cGy and 1250 cGy, respectively. Points in the upper quadrant satisfy the requirements for a BNCT neutron beam.

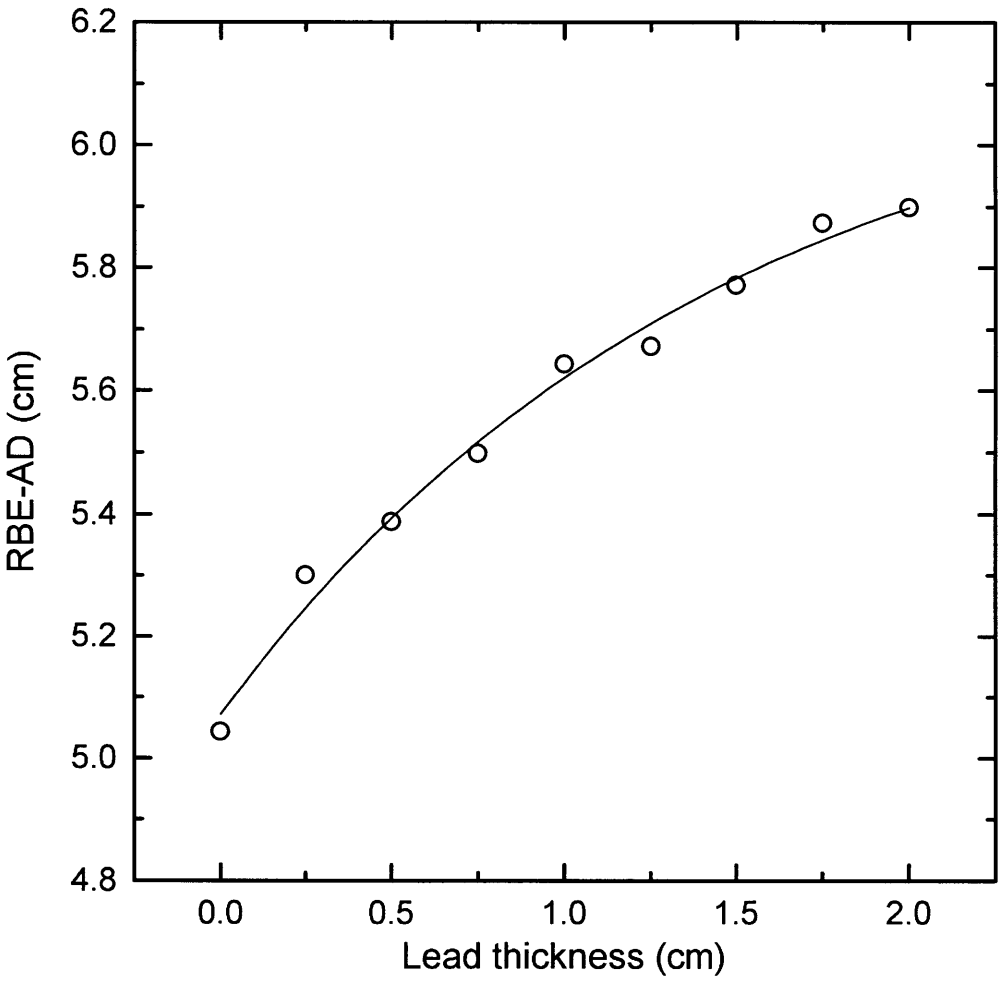

Figure 4-16: Effect of Lead Shielding on the Maximum RBE Advantage Depth for 1.95 MeV Protons

shielding can be fit very well, over the range of lead thicknesses from 0 to 2 cm, by the function

$$\text{RBE} - \text{AD(cm)} = 5.07204 + 1.10664(1 - e^{-t/1.45784}) \tag{4.4}$$

with a chi–square value of $\chi^2 = 0.00113$. This variation is shown in Figure 4-16. As in previous calculations of RBE advantage depth, the errors are on the order of ± 0.15cm. Further thicknesses of lead are not shown since the RBE-ADDR is already much lower for 2 cm than our cutoff of 6.67 cGy/min/mA. This is shown in Figure 4-17.

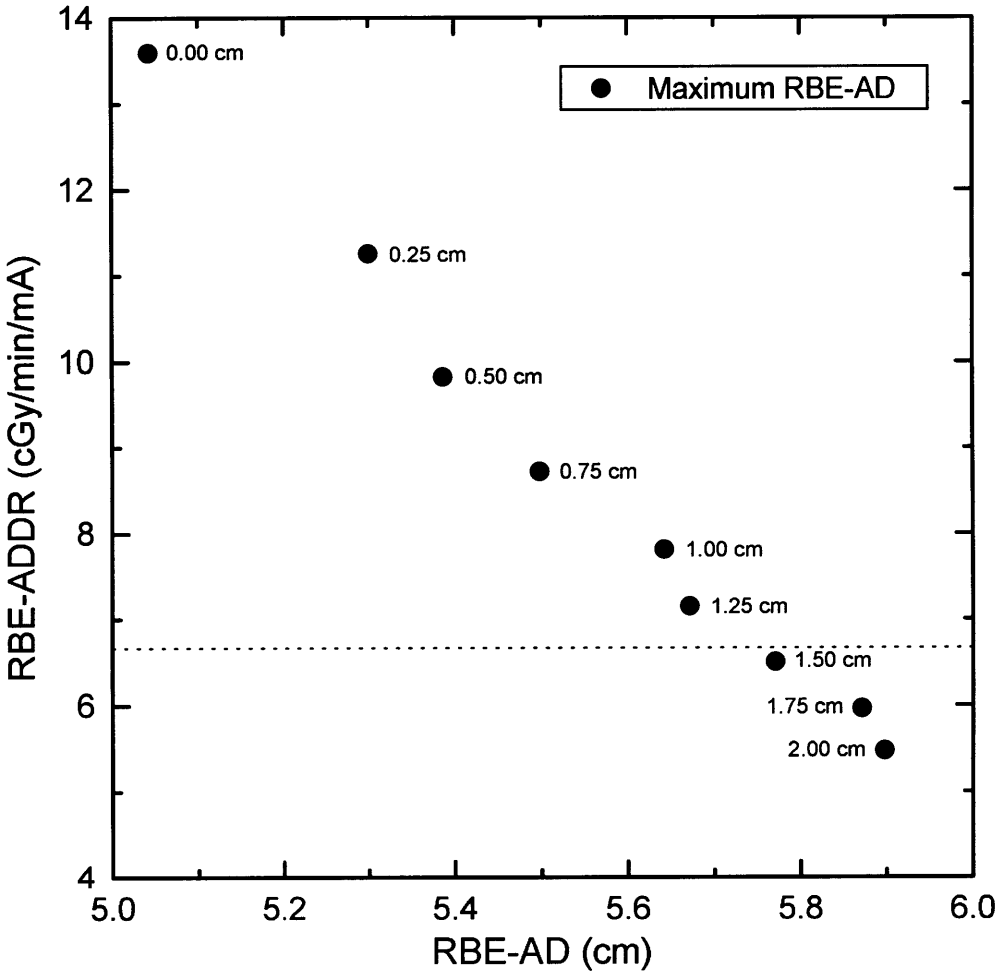

Figure 4-17: Variation of RBE-ADDR on Pb Thickness for 1.95 MeV Protons

It is worth comparing the gains in our BNCT treatment parameters due to a thermal neutron shield, using ^{6}Li, and a photon shield, using Pb. These gains are shown in Figure 4-18, for which the RBE-AD and RBE-ADDR are plotted for 1.95 MeV protons with no shielding, 0.01 cm of ^{6}Li shielding, and 0.25 cm of Pb shielding. The ^{6}Li thermal neutron shield (open circles) is seen to give larger advantage depths, but the Pb shield (solid triangles) gives higher advantage depth dose rates within the acceptability region. The combination of thermal neutron and photon shielding (open diamonds) is, as expected, better still, with a maximum RBE-AD of nearly 6 cm.

4.5 Choice of Beam

Using all the neutronic results from this chapter, it is clear that a good BNCT treatment beam using near–threshold reactions will require moderator, reflector, ^{6}Li, and Pb shielding. In all cases studied, the maximum RBE-AD for a given proton beam energy corresponds to a water moderator thickness of 5 cm, so this will be adopted as the ideal moderator thickness for the CTU. Based on Figure 4-18, a 0.01 cm sheet of ^{6}Li and and a 0.25 cm sheet of Pb will be added, in that order, to the back of the moderator. A 0.25 cm copper backing will be used with a vapor deposited lithium metal target with a reduced thickness sufficient to slow the proton beam just past the (p,n) reaction threshold energy of 1.88 MeV. As for proton beam energy, the range of near–threshold proton energies that produce beams with RBE-AD $\geq$ 5 cm and BRE-ADDR $\geq$ 6.67 cGy/min/mA extends from 1.95 MeV to 1.99 MeV.

A final CTU design will require detailed modeling of a target cooling configuration, but all the parameters described here should be about the same with the more detailed model. Once the cooling design is included, MCNP dosimetry calculations will be performed to determine a final set of BNCT treatment parameters for this prototypical beam.

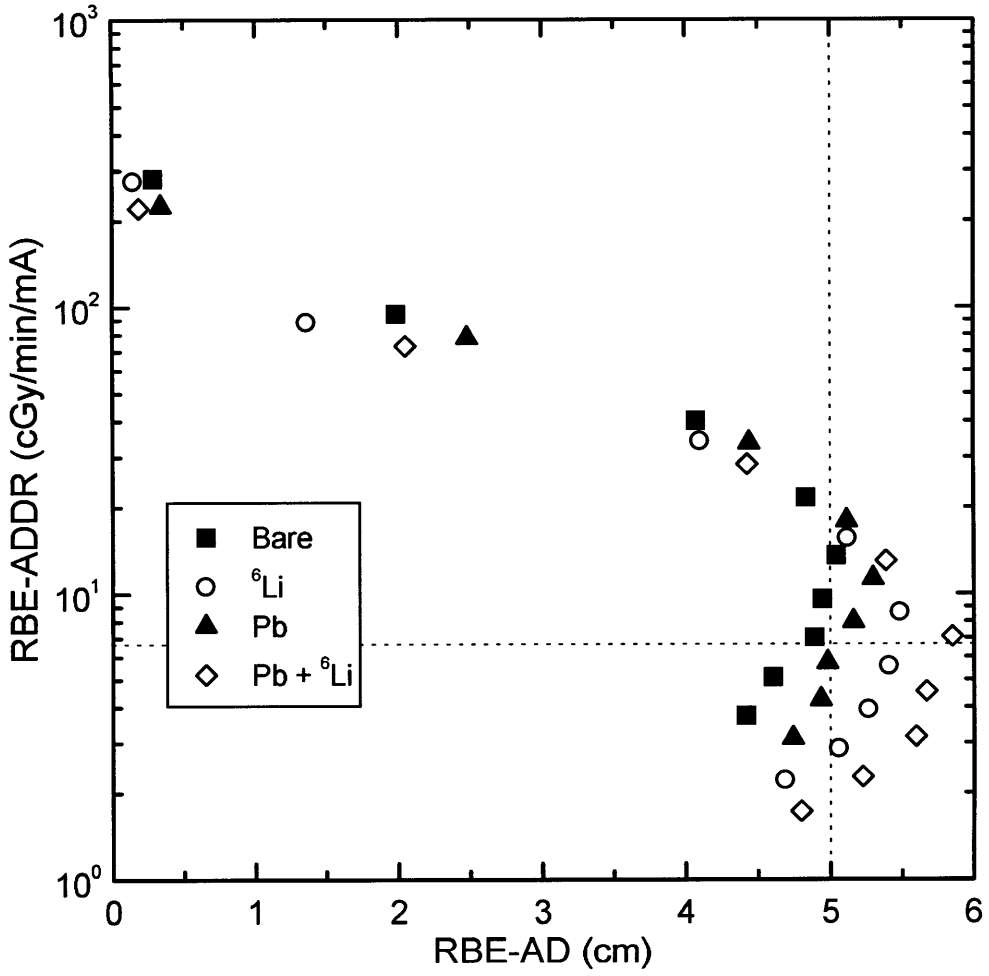

Figure 4-18: Effect of ^{6}Li and Pb on BNCT Treatment Parameters for 1.95 MeV Protons. The vertical dotted line indicates the minimum acceptable RBE-AD of 5 cm. The upper and lower horizontal dotted lines correspond to total healthy tissue RBE doses of 2000 cGy and 1250 cGy, respectively. Points in the upper quadrant satisfy the requirements for a BNCT neutron beam.

Chapter 5

Near–Threshold BNCT Target Heat Removal

Having decided on a proton beam energy based on the MCNP simulations, the engineering design of the CTU is possible. The single most important, as well as challenging, aspect of the engineering design of this neutron source is heat removal from the lithium target. This is due, as mentioned in Chapter 1, to the very low melting point of lithium metal (181°C) [26]. A quick calculation shows that for a proton beam with energy of 2 MeV and current of 1 mA, the total power deposition in the target will be 2 kilowatts. In addition, this power deposition will occur over the range of protons in the target, tens to hundreds of microns.

The heat removal studies are divided into two sections: determination of the heat removal capabilities of a specific cooling design based on both heat transfer theory and experiment, and calculation of temperature profiles based on proton stopping powers in lithium targets and copper backing. The results of these two studies are combined to give a estimate of the heat removal capabilities of this target cooling design.

5.1 Multi–Fin Target Heat Removal

Consider a simple target and backing geometry in which forced convection with a light water coolant is used to remove the heat from the target. The target backing is a vertically oriented disk with lithium on one side (the beam side) and coolant flowing on the other side. A uniform heat source of area A and intensity Q impinges on the face of the lithium target. The total temperature drop between the maximum target temperature $(T_{Li})_{max}$ and the bulk coolant temperature $T_{coolant}$ is given by a series of temperature drops:

$$(\Delta T)_{total} = (\Delta T)_{\mathrm{Li}} + (\Delta T)_{\mathrm{Cu}} + (\Delta T)_{convection} \tag{5.1}$$

where $(\Delta T)_{\mathrm{Li}}$ is the temperature drop across the lithium target, $(\Delta T)_{\mathrm{Cu}}$ is the temperature drop across the copper target backing, and $(\Delta T)_{convection}$ is the temperature drop between the back of the copper and the bulk coolant temperature. Fourier's Law of Conduction ($Q = -kA\Delta T/\Delta x$) and Newton's Law of Cooling ($Q = hA\Delta T$) may be used in Eq. 5.1 to determine the heat transfer coefficient h necessary to keep $(T_{Li})_{max}$ below the lithium melting temperature:

$$h = \frac{1}{\left[\dfrac{A(\Delta T)_{total}}{Q} - \dfrac{\Delta x_{\mathrm{Li}}}{k_{\mathrm{Li}}} - \dfrac{\Delta x_{\mathrm{Cu}}}{k_{\mathrm{Cu}}}\right]} \tag{5.2}$$

Now if $T_{coolant}$ is taken to be 20°C, the beam area A is taken to be a circular region of radius 1.27 cm, Δx_{Li} is taken to be about 10 μm (see Section 4.3), Δx_{Cu} is taken to be 0.25 cm, and k_{Li} and k_{Li} are taken from Table 4.6, then for the lithium surface temperature to remain below T_{melt} for even a low heat input of 2 kW, the effective heat transfer coefficient h must be about 52,800 W/m^2-°C.

The Dittus–Boelter correlation for turbulent forced convective heat transfer may be used to estimate the relation between h and the coolant flow rate [79]. The Dittus–

Boelter correlation is

$$\mathrm{Nu} = 0.023\,\mathrm{Re}^{0.8}\,\mathrm{Pr}^{0.4}, \tag{5.3}$$

where Nu, Re, and Pr are the Nussult, Reynolds and Prandtl numbers for the coolant. Using property values for a water temperature of 20°C [4], the relation $\mathrm{Nu} = hD/k_{\mathrm{H_2O}}$ implies a Reynolds number of 225,000. For a reasonable hydraulic diameter of 1 cm, this translates to a flow rate of about 130 gallons per minute! This simple calculation demonstrates that a more effective method of heat removal is needed for BNCT targets.

5.1.1 Single Fin Theory

Extended surfaces such as fins are an effective way to increase heat transfer from a solid surface. The improved heat removal is due to the increase in surface area from which the heat is removed, either by natural or forced convection or radiation [80]. Consider the fin shown in Figure 5-1. It may be shown [4] that provided the dimensions of the fin satisfy the relation $hA/kP \ll 1$, where P is the fin perimeter along the flow direction, k is the fin thermal conductivity, and A is the cross sectional area of the fin, heat flow within the fin may be modeled as 1-D conduction. For the fin dimensions considered in the target design below, a representative value of hA/kP is 0.088, satisfying our criterion. It is also well known that if heat loss from the end of the fin may be neglected, the differential equation governing the heat conduction in the fin is [81]

$$\frac{d^2\left[T_{fin}(x) - T_{coolant}\right]}{dx^2} = m^2\left[T_{fin}(x) - T_{coolant}\right] \tag{5.4}$$

where $m = \sqrt{hP/kA}$. The solution of Eq. 5.4 leads to the well–known fin equations, which include equations for $T_{fin}(x)$, the temperature distribution across the fin, and $(\Delta T/Q)_{fin}$, the temperature drop between the base of the fin and the bulk coolant,

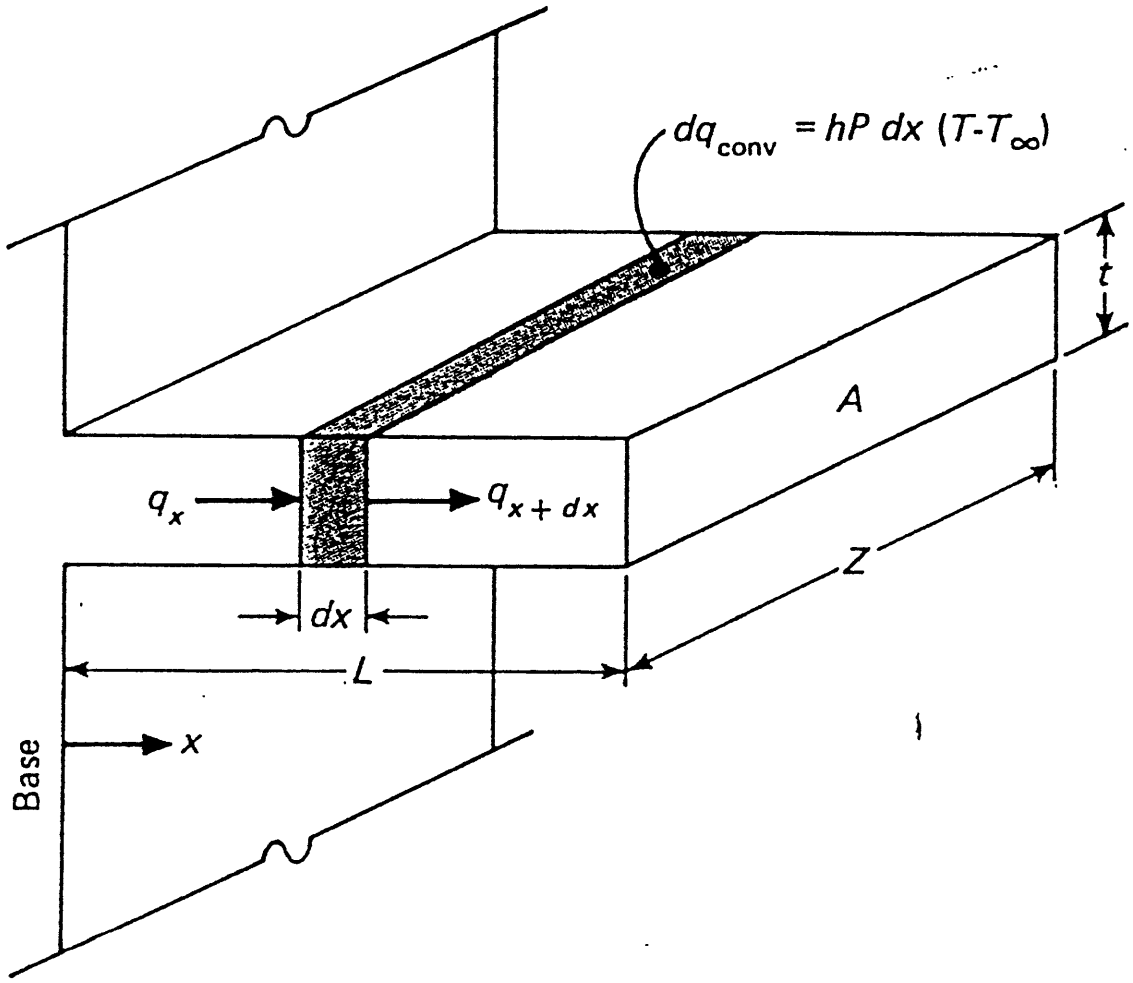

Figure 5-1: Definition of Fin Parameters. From [4].

per unit heat input [80]:

$$T_{fin}(x) = T_{coolant} + (T_0 - T_{coolant})\frac{\cosh\left[m(L-x)\right]}{\cosh mL} \tag{5.5}$$

$$\left(\frac{\Delta T}{Q}\right)_{fin} = \frac{T_0 - T_{coolant}}{Q} = \frac{1}{\sqrt{hkAP}\tanh(mL)} \tag{5.6}$$

where T_0 is the temperature at the base of the fin ($x = 0$).

5.1.2 Extension to Multiple Fins

Instead of a single fin to remove the heat from the target backing, a series of rectangular fins was added to the backing to form channels for coolant flow. The multiple fins produce turbulence in the water stream, increasing the convective heat transfer coefficient. This configuration also spreads the fin effect over the entire beam area, making the heat transfer more uniform than with a single fin.

A complication of this geometry, hereafter called a "multi–fin" target geometry and shown in Figure 5-2, is the creation of a strong non–uniformity of flow speeds in each channel. It should be clear from a quick look at the geometry that there will be higher flow rates in the central channels because there are fewer entrance and exit losses than for outer channels. Since the flow speed is directly incorporated into the Reynolds number and hence heat transfer coefficient for each channel, the fin parameters such as mL also change with each channel: $mL \rightarrow m_i L_i$. Each fin will also experience a different heat transfer coefficient on each side, so the equations from the previous section will need to be modified to account for this difference.

An algorithm was developed to model the steady state behavior of this particular heat removal design by incorporating the important aspects described above. There was a desire, however, to keep the model as simple as possible while still accurately predicting the variation of the temperature drop with coolant flow rate. The first step is suitably modifying the fin equations from Section 5.1.1 above.

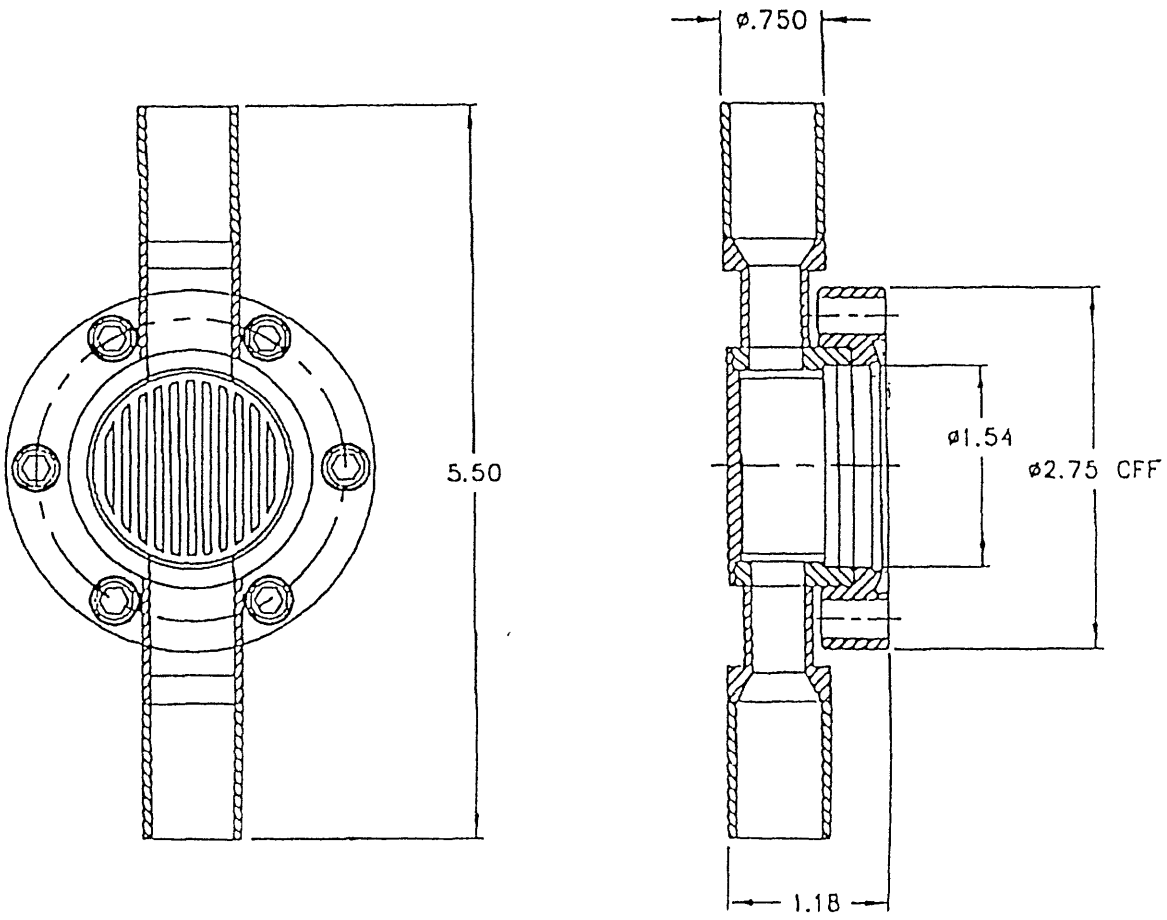

Figure 5-2: Multi-Fin Target Design

A heat balance on a differential element of a rectangular fin with heat transfer coefficients of h_1 on one side and h_2 on the other leads to the following differential equation for the temperature variation in the fin:

$$\frac{d^2\left[T(x) - T_{coolant}\right]}{dx^2} = \frac{(h_1 + h_2)\,P}{2kA}\left[T(x) - T_{coolant}\right] \tag{5.7}$$

Comparison with Eq. 5.4 indicates that the single fin relations (Eqs. 5.5 and 5.6) may be used for calculations of the response of each fin in the multi–fin target by using an effective heat transfer coefficient $\bar{h}$, defined as the arithmetic mean of the two individual coefficients: $\bar{h} \equiv \frac{1}{2}(h_1 + h_2)$.

The next step is determining the flow rate in each channel. The key to this analysis is to recognize that the head losses in all channels must be equal, since they all start and end at the same location. The head loss in each channel is a combination of primarily frictional and geometrical loss mechanisms. These losses may be written as [82]

$$\mathcal{H}_i = \left[f_i\left(\frac{L}{D}\right)_i + \sum_j K_{ij}\right]\frac{W_i^2}{2gA_i^2} \tag{5.8}$$

where f_i is the Moody friction factor in channel i, $(L/D)_i$ is the length–to–hydraulic diameter ratio for channel i, W_i is the volumetric flow rate in channel i, A_i is the cross sectional area of channel i, and K_{ij} is the jth type of geometrical head loss in channel i. Types of geometrical head loss include abrupt entrances and exits, as well as entrances into side channels (called "T-branch" losses) and flow past side entrances (called "T-line" losses). The head loss is denoted $\mathcal{H}$ to distinguish it from the heat transfer coefficient h.

Geometrical head losses present some difficulty. Because of the curved flow passages around the fins, the entrance angles for the outer channels vary and are not equal to 45° or 90°, for which standard values are tabulated [82]. These losses will also depend on the size of the channel into which the coolant is flowing; since these

Table 5.1: Geometrical Factors for Multi–Fin Target Flow Rate Calculations

Channel	(L/D)	A (m^2)	K coefficients
A	12.2823	2.3165×10^{-5}	$K_{entrance} = 0.5$ $K_{exit} = 1.0$
B	12.0834	2.3165×10^{-5}	$K_{entrance} = 0.5$ $K_{exit} = 1.0$
C	11.4675	2.3165×10^{-5}	$K_{T-branch} = 3.0$
D	12.0104	2.3165×10^{-5}	$K_{T-branch} = 3.0$ $K_{T-line} = 0.9$
E	12.1488	2.3165×10^{-5}	$K_{T-branch} = 3.0$ $K_{T-line} = 0.9$
F	14.5611	3.6548×10^{-5}	$K_{T-line} = 0.9$

channels are very small, an extrapolation of tabulated values for larger flow areas is necessary. Making educated guesses about each of these factors, the following equations are adopted to describe the head losses in channels $A - F$ (symmetry only requiring specification of half the channels):

$$\mathcal{H}_A = \left[f_A \left(\frac{L}{D} \right)_A + K_{entrance} + K_{exit} \right] \frac{W_A^2}{2gA_A^2} \tag{5.9}$$

$$\mathcal{H}_B = \left[f_B \left(\frac{L}{D} \right)_B + K_{entrance} + K_{exit} \right] \frac{W_B^2}{2gA_B^2} \tag{5.10}$$

$$\mathcal{H}_C = \left[f_C \left(\frac{L}{D} \right)_C + 2K_{T-branch} \right] \frac{W_C^2}{2gA_C^2} \tag{5.11}$$

$$\mathcal{H}_D = \left[f_D \left(\frac{L}{D} \right)_D + 2K_{T-branch} + 2K_{T-line} \right] \frac{W_D^2}{2gA_D^2} \tag{5.12}$$

$$\mathcal{H}_E = \left[f_E \left(\frac{L}{D} \right)_E + 2K_{T-branch} + 4K_{T-line} \right] \frac{W_E^2}{2gA_E^2} \tag{5.13}$$

$$\mathcal{H}_F = \left[f_F \left(\frac{L}{D} \right)_F + 6K_{T-line} \right] \frac{W_F^2}{2gA_F^2} \tag{5.14}$$

The values for the geometrical factors in Eqs. 5.9 through 5.14 are given in Table 5.1. These parameters do not change during the course of a calculation; the parameters f

and W, however, do change as described below.

The algorithm to calculate the overall temperature drop across the multi–fin target consists of 5 steps:

1. Assume the volumetric flow rate is equal in all channels. Then for channel A, $W_A^{(0)} = W_{total}/12$. The (j) superscript indicates the iteration number.

2. For $(n) \geq 0$, calculate $\mathcal{H}_A^{(n)}$, the head loss in channel A. To determine the friction factor $f_i^{(n)}$, the following semi-empirical equation for turbulent flows in smooth pipes may be iteratively solved [26]:

$$\sqrt{f_i} = \frac{1}{2\log_{10}(\mathrm{Re}_i\sqrt{f_i}) - 0.8} \tag{5.15}$$

3. For channels $B - F$,

   (a) Rearrange Eqs. 5.10 through 5.14 to solve for $W_B^{(n)}$ to $W_F^{(n)}$, assuming the same head loss determined in Step 2. Solving these equations will require an initial assumption about the friction factor f; namely, the initial guess in each iteration for the friction factor for each channel will be based on the volumetric flow rate assumed for that channel in the previous iteration.

   (b) Iteratively solve for $W_B^{(n)}$ to $W_F^{(n)}$. This step is iterative in the sense that once an initial friction factor $f_i^{(n)}$ is guessed in Step 3(a) above, an initial new value for $W_i^{(n)}$ is calculated. This new flow rate, however, will lead to a new value for $f_i^{(n)}$. Alternating between calculations of $f_i^{(n)}$ and $W_i^{(n)}$ will eventually converge to a single value of each parameter.

4. Summing the new volumetric flow rates gives an adjusted total flow rate, $W_{adjusted}^{(n)}$. This new total flow rate will not, in general, be equal to the true total flow rate, W_{total}, which is known.

5. Adjust all channel flow rates from the previous iteration so that the total flow rate is equal to the true total flow rate:

$$W_i^{(n+1)} = W_i^{(n)} \frac{W_{total}}{W_{adjusted}^{(n)}} \tag{5.16}$$

6. Increase the iteration number by one and repeat Steps 2 - 5 until all W_i do not change between iteration (n) and $(n+1)$, within a tolerance of $\epsilon < 10^{-4}$.

The converged flow rates are used with the Dittus–Boelter equation (Eq. 5.3) to determine the effective heat transfer coefficients $\bar{h}$ for each fin. The modified fin equations presented above are then used for the geometry shown in Figure 5-2 to determine the mean temperature drop between the back of the copper backing and the coolant temperature. This algorithm is implemented using the Fortran 77 program `flow.f`; a listing of this program is given in Appendix E.

The results of calculations using `flow.f` are shown in Figure 5-3. The beam area is taken to be a uniform, 1.27 cm radius disk, and the coolant temperature is taken to be 20°C. The temperature drop per unit heat input decreases drastically for low flow rates, but then changes slowly for flow rates above 4 to 5 gallons per minute, indicating diminishing returns for higher flow rates. In fact, doubling the coolant flow rate from ten to twenty gallons per minute only decreases the temperature drop per unit heat input by 24.7%. Any substantial improvement in the heat removal properties will require changes in the CTU geometry or material properties, i.e. different backing material or coolant. The temperature drop per unit heat input may be converted to temperature drop per unit beam current by multiplication with the incident proton energy E_{p_0}. This will be useful when combining these results with the results of later sections, but keeping everything in terms of unit heat input is more convenient at this stage.

The calculated temperature drop across the fins is less than 10°C/kW for flow

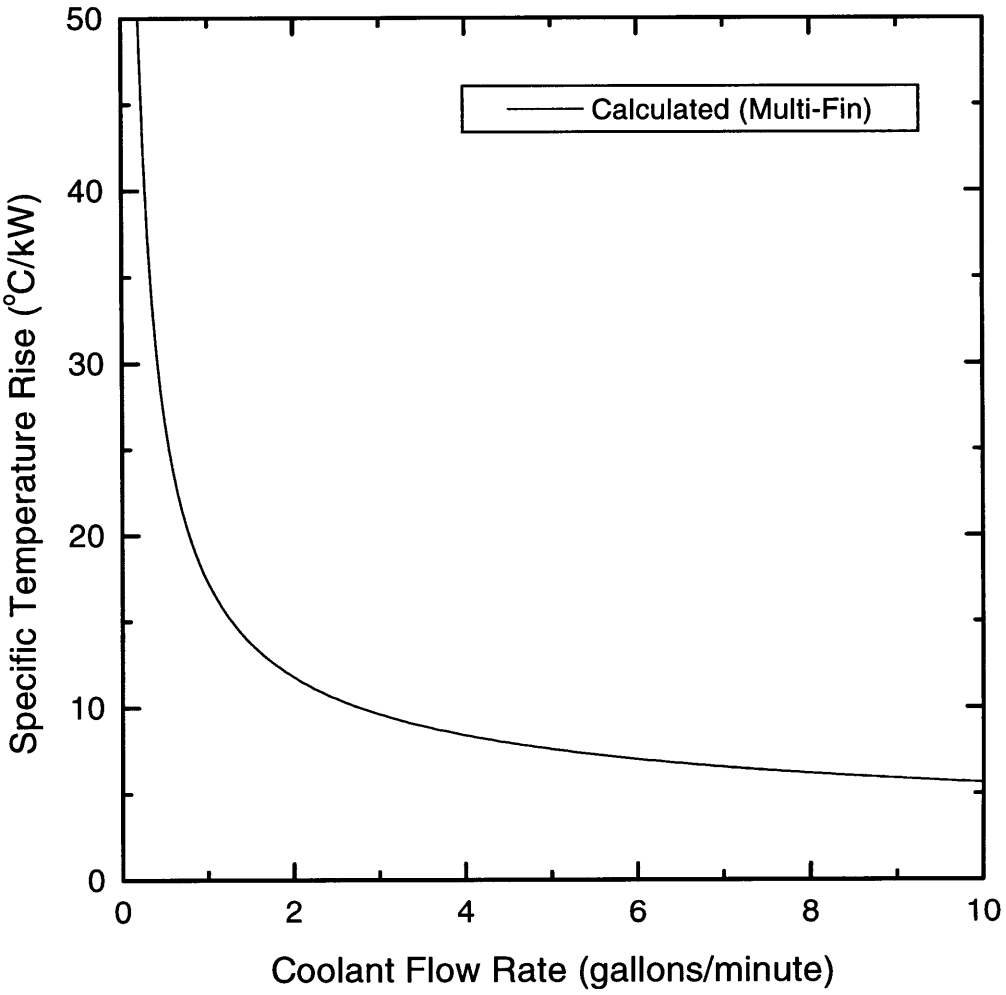

Figure 5-3: Calculated Temperature Drop per Unit Heat Input Across Fins for a Multi–Fin Target Design

rates greater than 4 gallons per minute. The validity of this result will be evaluated in the next two sections.

5.1.3 Low Power Heat Removal Experiments

The heat removal properties of the multi–fin target were tested using the experimental setup shown in Figure 5-4. A hole was bored into a 1 inch diameter, 6 inch long copper rod to a depth of 4.5 inches. An electric resistive heater was placed into this hole, and a low melting point bismuth compound (Cerrobend) was heated and used to fill the gaps between the heater and the rod in order to have good thermal contact. The bottom of the heater was silver–soldered to the top of the multi–fin copper backing. Two thermistors were placed inside small holes bored into the copper rod below the bottom of the heater, and Cerrobend was again used to provide good thermal contact. The copper rod and heater were surrounded by an aluminum foil sheath to minimize radiant heat losses. The entire apparatus was placed inside a sealed chamber attached to a diffusion pump capable of maintaining a vacuum of better than 10^{-5} torr. The vacuum system was used to eliminate natural convective losses that would occur if the experiment were conducted in air. The electrical leads to the heater were attached to a Variac voltage controller, and a digital voltmeter was placed in parallel to measure the voltage drop across the heater. The current to the heater was measured with an Ampere clampmeter. Thermistors were also placed at the entrance and exit of the coolant line. All thermistor resistances were measured with digital ohmmeters.

Using this experimental setup, the mean temperature drop between the copper backing surface and the coolant was determined. For each coolant flow rate between 1 and 10 gallons per minute, the Variac setting was varied in 10 V steps between 0 and 140 V, the heater current was recorded, the system was allowed to come to equilibrium, and the resistance readings of the thermistors were recorded. The thermistor resistances were converted to temperatures using double–exponential fits to

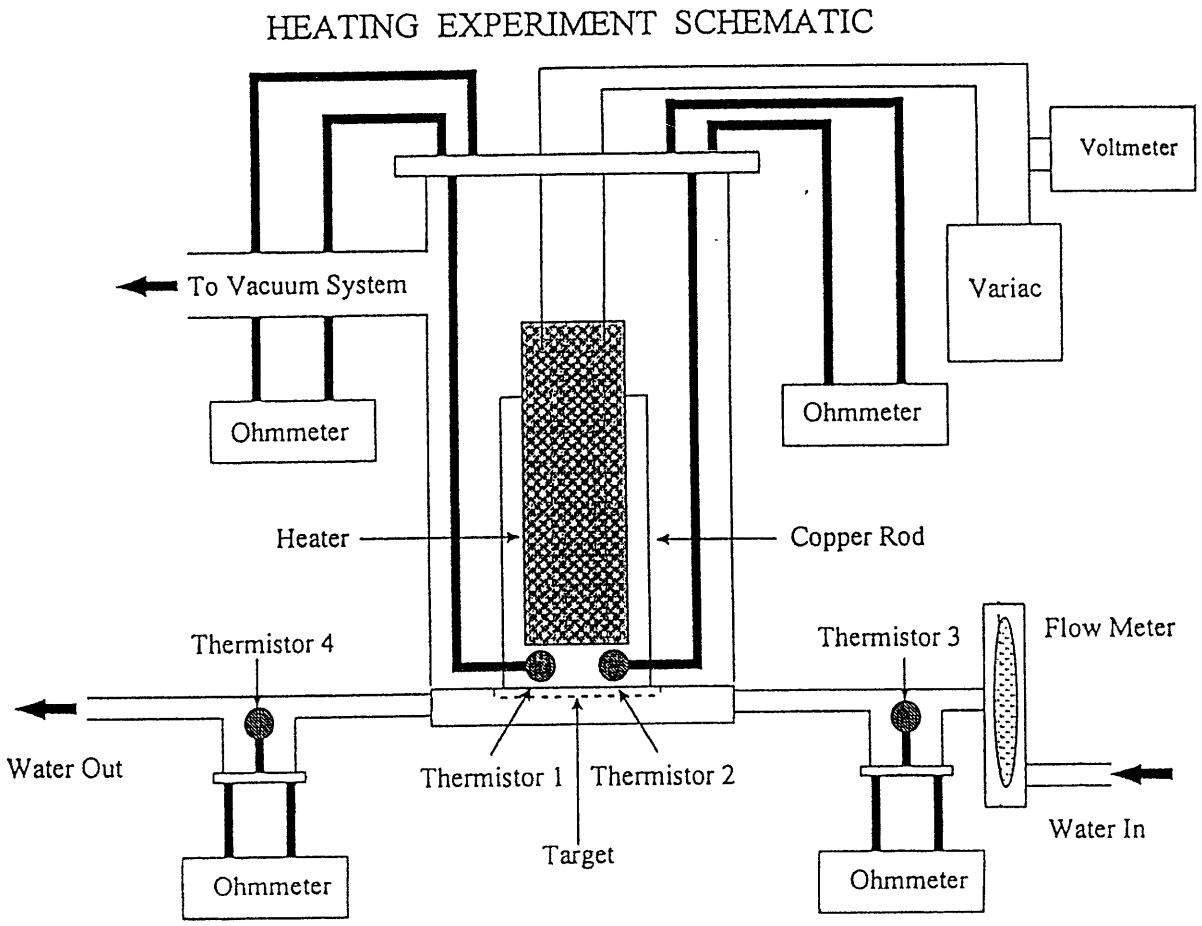

Figure 5-4: Schematic of Low Power Heat Removal Experimental Setup for a Multi-Fin Target Design

data from separate experiments. In these experiments, a beaker of water or oil was heated with a heating plate and stirred with a magnetic stirrer, and the thermistors placed in the bath were attached to digital ohmmeters. Due to the rapid change in the resistance for low temperatures, a separate experiment incorporating ice and water was performed for these temperatures. The following fits to the data were used to convert thermistor readings to temperatures:

- High Temperature Copper Rod ($> 25°$):

$$R\,(\mathrm{k}\Omega) = 0.55113 + 27.57 \exp\left[-\frac{T(°\mathrm{C}) - 24.723}{25.60}\right] + 0.3568 \exp\left[-\frac{T(°\mathrm{C}) - 24.723}{0.6298}\right] \tag{5.17}$$

- Low Temperature Copper Rod ($< 25°$):

$$R\,(\mathrm{k}\Omega) = -9.715 + 25.23 \exp\left[-\frac{T(°\mathrm{C}) - 8.660}{36.86}\right] + 58.97 \exp\left[-\frac{T(°\mathrm{C}) - 8.660}{19.59}\right] \tag{5.18}$$

- Coolant:

$$R\,(\mathrm{k}\Omega) = 2.747 \exp\left[-\frac{T(°\mathrm{C}) - 4.943}{32.26}\right] + 4.105 \exp\left[-\frac{T(°\mathrm{C}) - 4.943}{14.46}\right] \tag{5.19}$$

A typical plot of heat input Q versus total temperature rise ΔT is shown in Figure 5-5 for a coolant flow rate of 8 gallons per minute. The line is a modified least–squares fit to the data in which the y–intercept is forced to be zero, since this is the behavior that one expects physically. Solution of the least–squares equations for this case with gives a slope m for the line of

$$m = \frac{\sum_i Q_i \Delta T_i}{\sum_i Q_i^2} \tag{5.20}$$

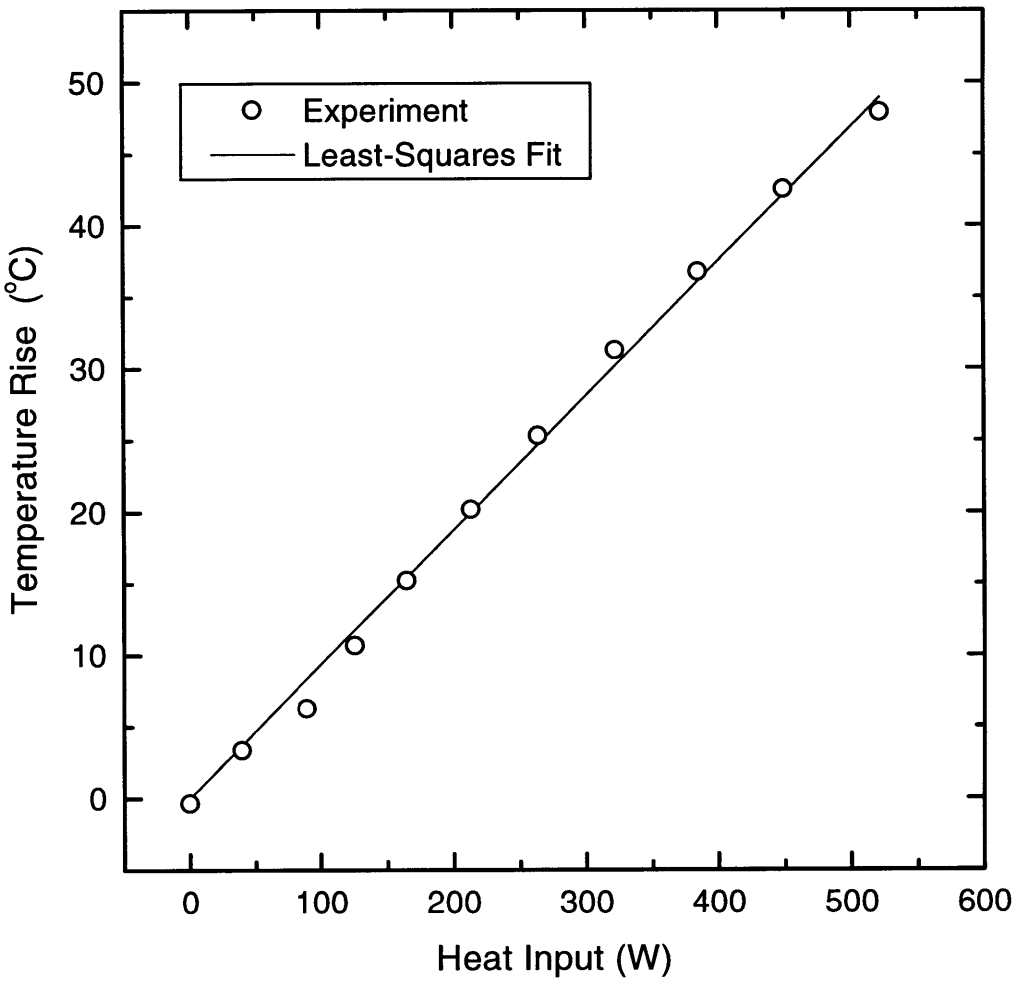

Figure 5-5: Experimental Variation of Heat Input versus Thermistor Temperature Difference for a Multi–Fin Target Design. The coolant flow rate is 8 gallons per minute.

Table 5.2: Experimental Temperature Drops between Coolant and Copper Rod Thermistors

Coolant Flow Rate (gal/min)	$(T_{rod} - T_{coolant})/Q$ (°C/kW)
1.0	112.2094
2.0	104.5342
3.0	100.5317
4.0	97.7911
5.0	97.5140
6.0	97.5324
7.0	95.1640
8.0	93.7311
9.0	92.1825
10.0	95.9660

Table 5.2 gives the least–squares fits for the temperature rise between thermistors for the flow rates considered. In all cases, the correlation coefficient r is greater than 0.99. It is very important to realize that this is not the temperature drop between the coolant and the back of the copper that we want; there are additional temperature gradients across the copper disk, the solder connection, and the copper rod that must be accounted for. All these temperature drops will uniformly shift the curve of Figure 5-3 up by a certain amount. Provided the variation of the experimental temperature drop with coolant flow rate agrees with the predicted temperature drop curve plus a constant determined from the experimental geometry and material properties, these low power experiments should provide evidence that the multi–fin model predictions are correct.

The temperature drop across the copper disk is easily calculated; it is equal to $\Delta x_{\mathrm{Cu}}/k_{\mathrm{Cu}}A$. For a 0.25 cm thick copper backing and 1 inch diameter heat source, this gives a temperature rise of 12.304°C/kW. The thermistors in the copper rod, which were placed 1.0 cm above the surface of the copper backing, also add a 49.215°C/kW temperature drop. The difficult part of the calculation is the solder, since the exact

composition and thickness of the connection is unknown. However, silver solders have thermal conductivities in the range 50-60 W/m °C [83]. Using a reasonable solder thickness of $\Delta x_{solder} = 0.5 \pm 0.25$ mm and $k_{solder} = 55 \pm 5$ W/m-°C gives a temperature drop across the solder connection of 17.941 ± 8.971°C/kW and a total temperature drop across the copper and solder of 79.46 ± 10.76°C/kW. This value is in good agreement with the least squares fit between calculation and experiment, 78.125°C/kW. The calculated temperature drops, corrected for the additional temperature drops in the experimental setup, are plotted with the experimental temperature drops in Figure 5-6. The greatest contribution to the experimental error bars is the variability of the Variac voltage readings, while the primary errors in the adjusted calculation are the solder thickness and thermal conductivity.

5.1.4 High Power Heat Removal Experiments

Since the heat inputs for a near–threshold BNCT neutron source will be on the order of kilowatts, it was decided that higher power heat tests were needed to confirm the results of the low power tests of Section 5.1.3. Specifically, heat inputs of several kilowatts were desired, which for a 1.27 cm radius beam area corresponds to power densities greater than 3.95 MW/m^2; power sources with heat densities of this magnitude are difficult to obtain. We had the additional restriction of an existing target design around which the heat source had to be fashioned. These restrictions led us to consider acetylene welding torches.

Acetylene torches are capable of high heat outputs and extremely high flame temperatures, but there are limitations and complications associated with them for this application. For example, quantification of the heat input to the copper backing is of fundamental importance, but the torch can at best only indicate the relative amounts of acetylene and oxygen gases being used. The heat source should be uniform for comparison with the low power experiments, but most torches have a narrow,

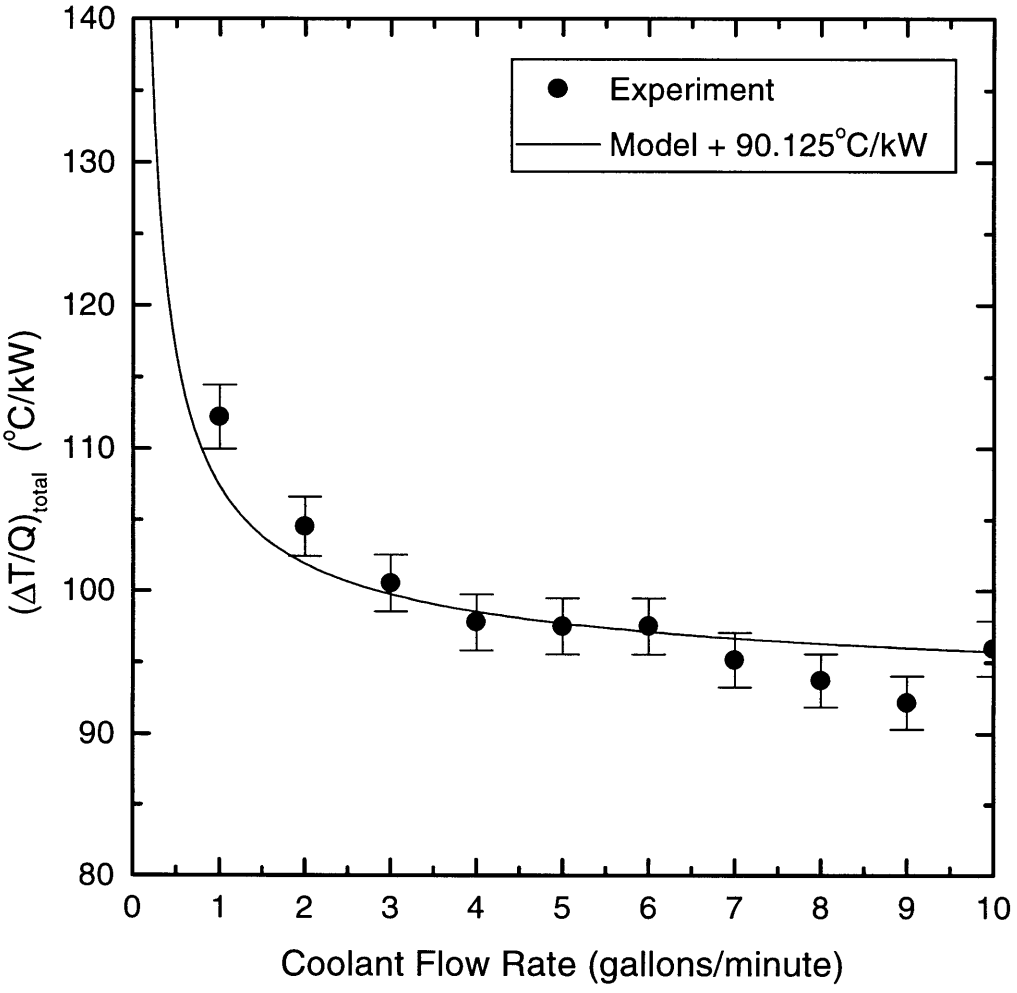

Figure 5-6: Comparison of Experimental and Calculated Multi–Fin Temperature Drops Across Low Power Experimental Setup

high temperature wick surrounded by lower temperature combustion products. The heat flux area should be the same size as the copper rod used in the lower power experiment, but a torch flame will generally spread out over an ill-defined area and swamp the entire target face. Finally, the surface temperature of the copper must be measured in order to calculate a temperature drop across the fins, but exposure of a thermocouple or similar temperature measuring device to such high flame temperatures and heat fluxes can destroy the device. These challenges to the high power temperature measurements are addressed below.

The quantification of the heat input is based on a simple thermal balance for the target. At steady state, the total heat input to the coolant comes from the heat input to the copper from the torch, provided there is not significant heat transfer through the stainless steel housing. Heat may be radiated from this housing or lost through natural convection to the surrounding air, or heat may enter the housing by conduction of the heat from the flange that is in contact with the copper backing (see Figure 5-2). These mechanisms are not appreciable, since the housing temperatures remained below room temperature (27°C) for all heat inputs considered, based on temperature measurements from a copper/constantan thermocouple attached to the back of the target unit. Now we have the simple heat balance

$$Q = \dot{m} c_p \Delta T \tag{5.21}$$

where $\dot{m}$ is the coolant mass flow rate, c_p is the coolant specific heat, and ΔT is the temperature rise between the coolant entrance to and exit from the target unit. By reducing the coolant flow rate to less than 1 gallon per minute, the heat inputs supplied with our torch led to distinct, quantifiable temperature rises measured with the same cooling line thermistors used in the low power experiments of Section 5.1.3. Heat inputs up to 2.2 kW were achievable with the rosebud torch used in this experiment

(see below).

The second concern, heat flux uniformity, was overcome by using a special torch attachment called a "rosebud". A rosebud torch head is small and circular, with eight gas outlets uniformly arranged around the outer edge. This configuration produces a flame with highly uniform heat flux and temperature [84]. It also produces a flame spot of approximately the same dimensions as the copper rod used in the low power experiments.

Due to the intense flame temperatures, the thermocouple to measure the surface temperature of the copper cannot be placed in the center of the flame, and it must be shielded from the flame. This was accomplished using a small copper tube bent into a hook shape and placed between the thermocouple and flame. A small water flow (less than 1 gallon per minute) through the copper hook provided cooling of the thermocouple wires. The copper tube was not in direct contact with the surface of the copper backing, but the thermocouple leads were wrapped around the tube to cool them and preserve the thermocouple reading. The copper/constantan thermocouple was soldered to the copper surface at the edge of the rosebud flame, so the copper tubing led to very little distortion of the heat transfer area. A digital meter was used to read the thermocouple temperature.

The thermocouple temperature measured at this point can be related to the average surface temperature that was measured in the low power experiments using formulas for steady state conduction [85]. The temperature distribution for the cylindrical geometry of the copper backing was used to estimate the relationship between the average temperature over the heat input area, $\bar{T}$, and the temperature at the thermocouple location, $T(R_T)$. If a temperature drop between the coolant and the thermocouple of $\Delta T_{thermocouple}$ is measured at radial value R_T, the adjusted temper-

Table 5.3: High Power Experimental Temperature Rises between Coolant and Copper Rod Surface

Coolant Flow Rate	ΔT (°C)		
(gal/min)	1.4 kW	1.9 kW	2.2 kW
2.0	62.54	76.47	91.98
4.0	51.70	72.30	75.97
5.5	48.82	67.68	74.42

ature drop for comparison with the other experiment is

$$\Delta T_{average} = \left(\frac{\bar{T}}{T(R_T)}\right) \Delta T_{thermocouple} \tag{5.22}$$

For the high power heat removal experiment, the ratio $(\bar{T}/T(R_T)$ was calculated to be 1.07.

The results of measurements with heat inputs of 1.4, 1.9, and 2.2 kW and coolant flow rates of 2.0, 4.0, and 5.5 gallons per minute are given in Table 5.3. Again, the measured temperature drop is not equal to $(\Delta T)_{fins}$; there is an additional temperature drop across the copper backing. In order to compare the low power results of Section 5.1.3 with these high power measurements, the total experimental temperature drops must be reduced to temperature drops across the fins only by subtracting the additional contributions of the copper rod and solder connection (in the case of low power measurements) and the copper backing (in both cases). Using the estimated temperature drops across these regions that were given at the end of the previous section, and averaging the three heat inputs given in Table 5.3, the temperature drops across the fins are given in Table 5.4. The experimental temperature drops across the fins per unit heat input, $(\Delta T/Q)_{fins}$, agree fairly well with each other, as well as with the calculated estimates. Considering the many sources of experimental error and the different geometries in the low and high power measurements, the agreement

Table 5.4: Comparison of Low and High Power Experimental Temperature Rises Across Fins

Coolant Flow Rate	$(\Delta T/Q)_{fins}$ (°C/kW)		
(gal/min)	Low Power	High Power	Calculation
2.0	25.1 ± 2.6	29.9 ± 10	23.8
4.0	18.3 ± 2.0	24.2 ± 10	20.4
5.5	18.1 ± 1.9	22.5 ± 10	19.3

of experiment and calculation appears satisfactory.

5.1.5 Critical Heat Flux (CHF) Concerns

the primary mechanism of target failure for this cooling design is envisioned to be the onset of subcooled nucleate boiling, leading to the formation of a vapor film if the bubble detachment diameter is greater than the coolant channel width and hence can wet the edges of the channel. This film would cause a nearly instantaneous jump in the target temperature. The heat flux that leads to this target failure is the critical heat flux (CHF) for this design. A detailed study of CHF for the multi–fin CTU is beyond the intended scope of this thesis, but a few basic calculations will be performed to give an order of magnitude estimate of the CHF concerns for this design.

In the scenario outlined above, target failure should not occur if subcooled nucleate boiling is never reached. A heat balance indicates that for circular tubes with uniform heating, the onset of subcooled nucleate boiling cannot occur for heat fluxes less than ϕ_{min}, given by [79]

$$\phi_{min} = \frac{(\Delta T_{SUB})_{inlet}}{\left[\frac{4z}{Gc_{pf}D} + \frac{1}{h_{fo}}\right]} \tag{5.23}$$

In Eq. 5.23, $(\Delta T_{SUB})_{inlet}$ is the degree of subcooling below the saturation temperature at the inlet of the channel, z is the height of the heated region of the channel, G is the mass velocity (kg/m^2-sec), c_{pf} is the specific heat of the liquid phase, D is the

diameter, and h_{fo} is the heat transfer coefficient for total flow assumed liquid. Using an equivalent hydraulic diameter for the central channel of the multi–fin CTU in place of D and $\bar{h}$ calculated in Section 5.1.2 for h_{fo}, ϕ_{min} for a 10 gallon per minute total coolant flow rate with 20°C inlet coolant temperature at atmospheric pressure is roughly 13.5 MW/m^2. This is less than the 19.2 MW/m^2 heat flux of a 1.27 cm radius, 5 mA, 1.95 MeV beam, so subcooled nucleate boiling is a concern. If we adjust ϕ_{min} by the ratio of the total channel heating area to the beam area, we obtain the more realistic value of 63.9 MW/m^2. However, the system will have to be pressurized to overcome losses, which will increase the degree of subcooling and hence ϕ_{min}. It is important to point out that exceeding ϕ_{min} does not guarantee that boiling will occur; this is just a lower bound on the possible CHF.

Collier gives the following equation, which estimates the bubble diameter D_d at the point of detachment from the wall [79]:

$$D_d = 0.0208 \left[\frac{\sigma}{g(\rho_f - \rho_g)} \right]^{1/2} \tag{5.24}$$

For 20°C light water at atmospheric pressure, Eq. 5.24 gives an estimate of 1.8 mm for D_d. This exceeds the 1.52 mm channel width, so once nucleate boiling begins, dryout can occur very rapidly if the bubble wets the walls of the channel. These results indicate that CHF is not an obvious problem for this geometry, but it is certainly an issue that needs to be addressed further.

5.2 Heat Deposition Profiles of Proton Beams

In addition to the temperature drop between the back of the copper and the coolant, there are also temperature gradients across the copper and lithium. In order to have a complete description of the temperature behavior of the CTU, these gradients need to be considered. This is not trivial, however; the heat deposition in the target and

backing is due to the slowing down of the proton beam in these materials, so that the temperature variation will be determined by the spatial variation of the proton stopping power. To complicate matters, the decision to make the lithium target only thick enough for the proton energy to pass the (p,n) threshold requires most of the energy loss to occur in the copper, which has very different material and stopping properties compared to lithium.

5.2.1 Steady State Temperature Drops

Steady state calculations of temperature drops across the lithium target and copper backing were performed. Because their stopping powers differ by an order of magnitude, the total range of monoenergetic protons has a strong, nonlinear dependence on the lithium thickness. This thickness will also determine the proton energy E_{edge} at the lithium/copper interface. It is important to note that pathlength and energy straggling will be neglected in these calculations. Based on the energy range of interest, the only significant straggling will occur in about the last 100 keV of energy loss, which corresponds to only 2.7% of the total range. The heat deposition will be modeled as one dimensional. The success of the 1-D multi–fin model in the previous sections supports this approximation. Also, since the target dimensions are on the order of millimeters or microns in the axial direction and centimeters in the radial direction, the radial flux is expected to be small compared to the axial flux. The beam area A is taken to be a disk of radius 1.27 cm.

Figure 5-7 shows a schematic of the different parts of the target geometry and examples of the associated temperature drops in each region. It is important to note that lengths are not to scale. The total temperature rise between the coolant and maximum target temperature per unit proton beam current, $(\Delta T/I)_{total}$, is the sum

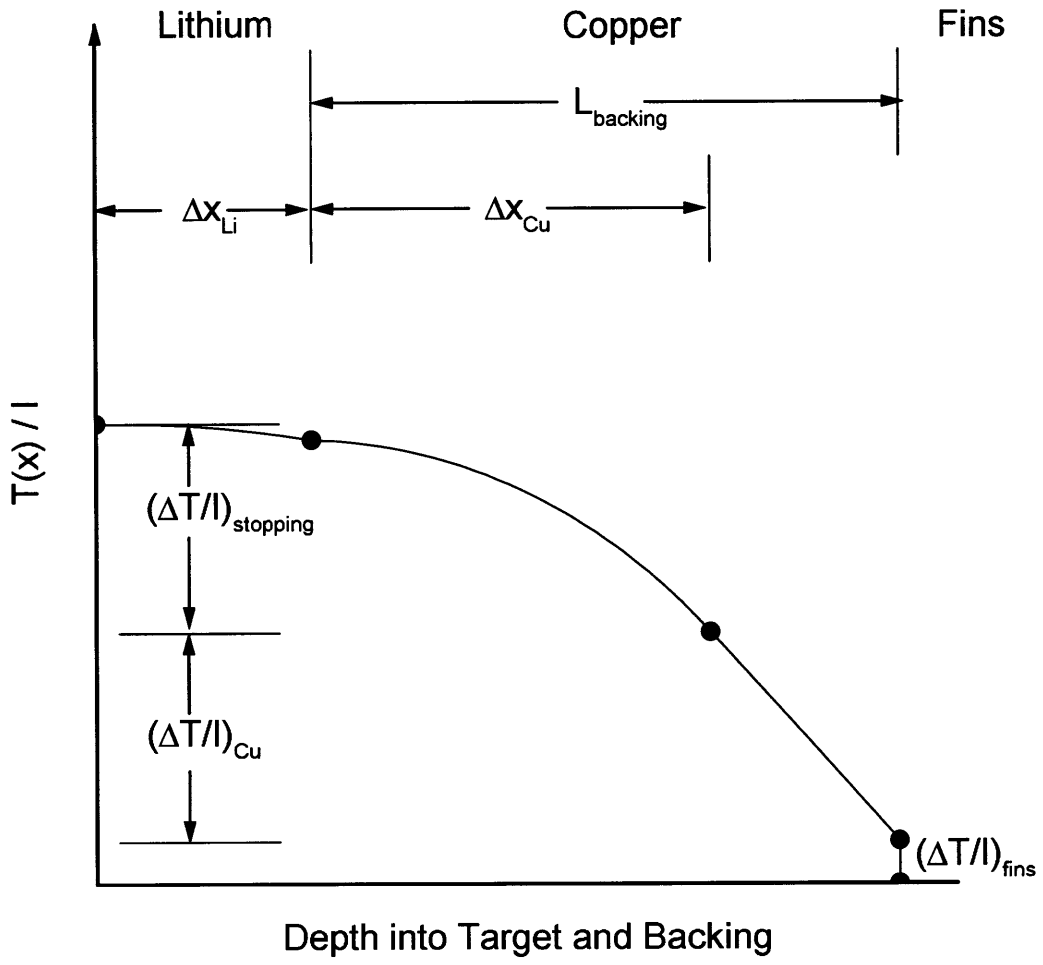

Figure 5-7: Target Regions and Associated Temperature Drops

of these temperature drops in series:

$$\left(\frac{\Delta T}{I}\right)_{total} = \left(\frac{\Delta T}{I}\right)_{fins} + \left(\frac{\Delta T}{I}\right)_{\mathrm{Cu}} + \left(\frac{\Delta T}{I}\right)_{stopping} \tag{5.25}$$

The terms in Eq. 5.25 represent the temperature drops between the coolant and back of the copper (*fins*); between the back of the copper and the endpoint of the proton range (Cu); and in the region where the proton beam is slowing down and depositing heat (*stopping*). The temperature rise across the fins has already been considered in Sections 5.1.1 through 5.1.4. The temperature rise across the region of the copper backing where proton stopping is not taking place is straightforward in a 1-D geometry — the temperature will vary linearly with a slope of $1/I(dT/dx)_{\mathrm{Cu}} = -E_{p_0}/k_{\mathrm{Cu}}A$ and an associated temperature drop of

$$\left(\frac{\Delta T}{I}\right)_{\mathrm{Cu}} = \frac{E_{p_0}(L_{backing} - \Delta x_{\mathrm{Cu}})}{k_{\mathrm{Cu}}A}. \tag{5.26}$$

The temperature variation in the stopping region is determined with the 1-D steady state heat conduction equations with a volumetric heat source due to the spatial variation of the proton stopping power. This leads to a Poisson equation:

$$\nabla^2 T = -\frac{Q'''}{k} \tag{5.27}$$

where Q''' is the volumetric heat source in kW/m^3 and k is the thermal conductivity. For heat deposition due to heavy charged particle stopping, $Q''' = -(I/A)dE_p/dx$, so that for a 1-D calculation,

$$\frac{d^2T}{dx^2}(x) = -\frac{I}{kA}\frac{dE_p}{dx}(x) \tag{5.28}$$

Appendix F gives a summary of the computational method used to numerically

solve Eq. 5.28. This includes setting up the computational spatial mesh, which is not uniform and varies with incident proton energy and lithium thickness, and incorporating physically meaningful boundary conditions into the solution method. As a sample result of this technique, the spatial variation of the temperature for 1.95 MeV protons is shown in Figure 5-8 for a lithium target thickness of 9.43 μm, just thick enough to pass the (p,n) threshold. For comparison, the temperature drop assuming a total heat input of IE_{p_0} kW from the left is shown. Is is clear that assuming all heat input from the left severely overestimates the temperature drop over the proton stopping range. The temperature drop across the proton stopping range is seen to be only 0.079 °C/mA for this case.

Figure 5-9 shows the effect of incident proton energy E_{p_0} on temperature drop across the stopping region. In all cases, the lithium target is only thick enough to slow past the (p,n) reaction threshold, so that $E_{edge} = E_{th} = 1.88$MeV. This is considered the minimum target thickness for effective BNCT. The temperature drop across the stopping region is seen to increase with increasing incident proton energy, as expected, but the increase is strongly nonlinear, which is not so obvious. The nonlinearity is due to the increased stopping distance for higher E_{p_0} resulting from greater energy loss in lithium, which has much lower stopping powers than copper. Also worth noting are the surprisingly low temperature drops over these regions. Even for 2.50 MeV incident protons, $(\Delta T/I)_{stopping}$ is only 0.75°C/mA. This implies much lower temperature rises than are usually assumed for BNCT targets. Does this indicate a flaw or error in our calculations?

Consider Figure 5-10, which shows the effect of lithium target thickness on temperature drop across the stopping region. The uppermost value corresponds to a proton beam completely stopping in the lithium target and entering the copper backing right at the end of the stopping range. This is still a somewhat thin slice of lithium; for 1.95 and 2.50 MeV protons, the lithium thicknesses are 160.6 μm and

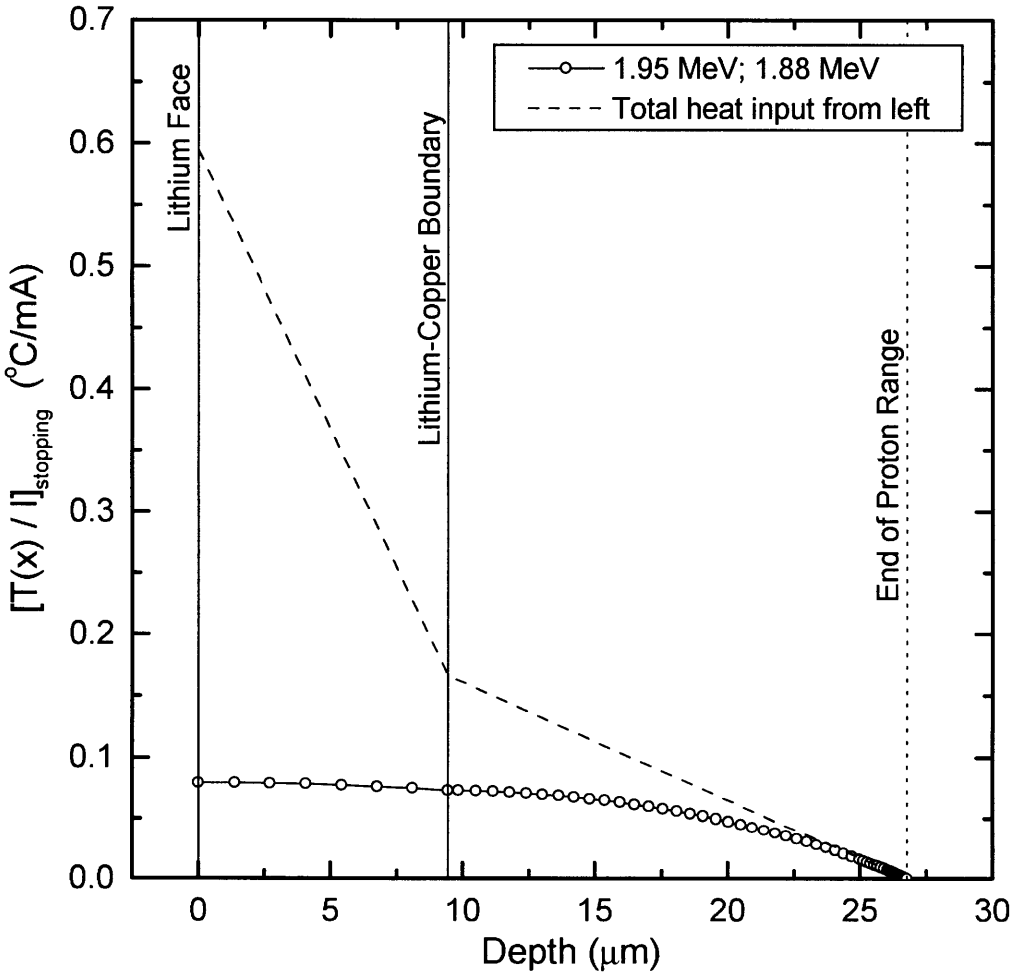

Figure 5-8: Temperature Profile for 1.95 MeV Protons Stopping in Lithium and Copper. The lithium thickness is 9.43 μm, just enough to pass the (p,n) threshold at the lithium–copper boundary. The dotted line shows the incorrect temperature variation based on the assumption of all heat incident from the left.

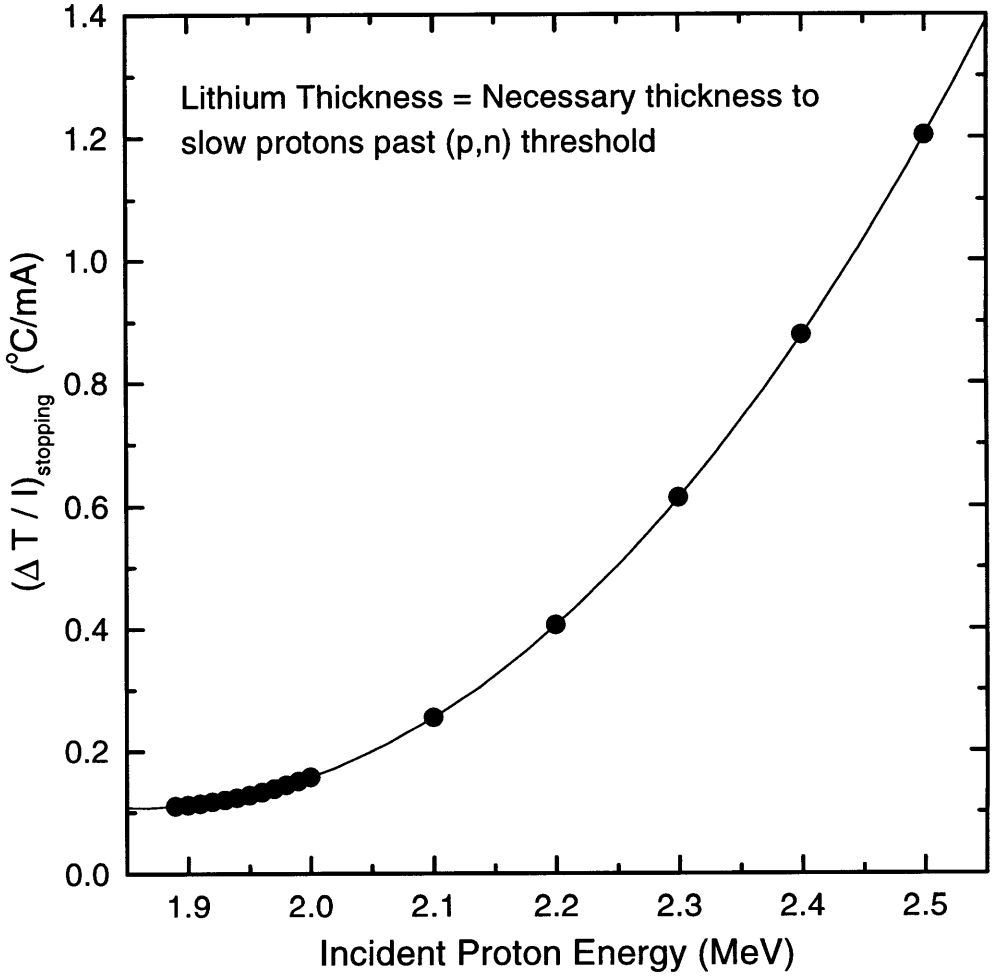

Figure 5-9: Temperature Drop Across Stopping Region as a Function of Incident Proton Beam Energy. In all cases, the proton energy at the lithium/copper boundary was the (p,n) reaction threshold of 1.88 MeV.

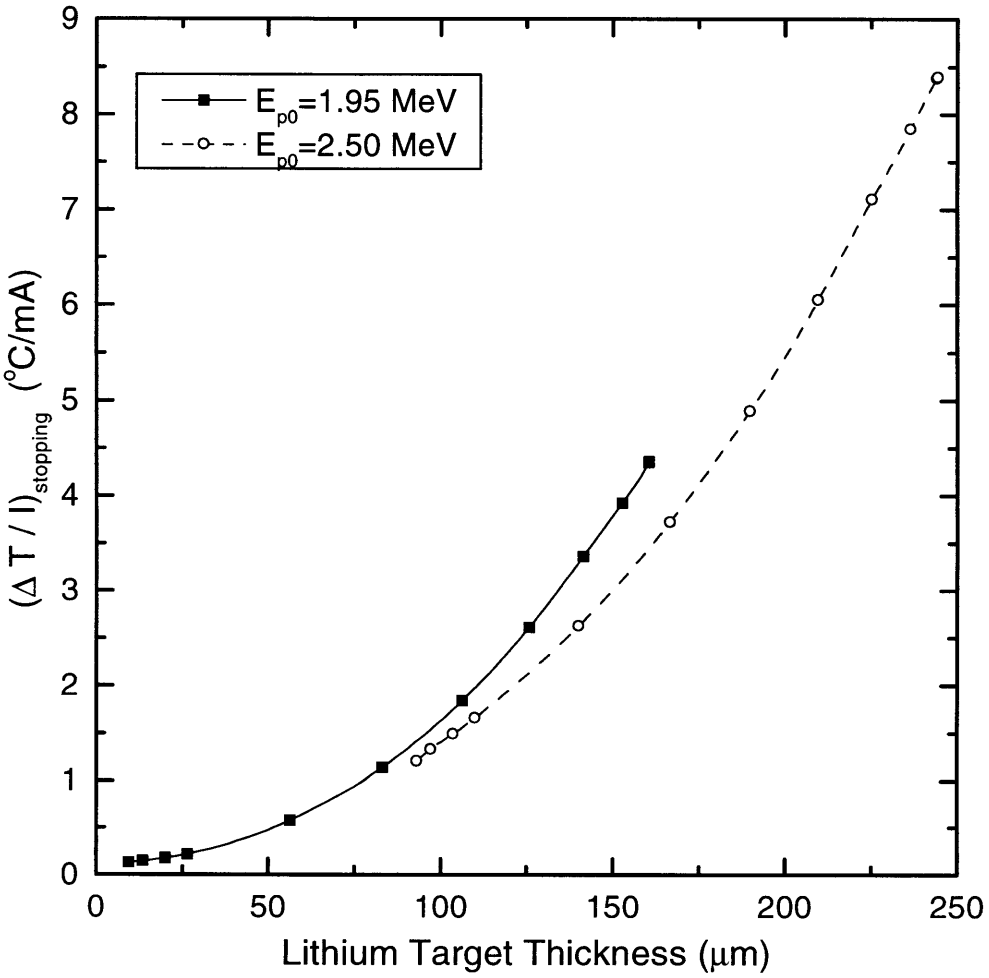

Figure 5-10: Temperature Drop Across Stopping Region as a Function of Lithium Target Thickness

244.2 μm, respectively. However, the temperature drops increase significantly from the values in Figure 5-9 to 2.70°C/mA and 5.20°C/mA. Note that if the lithium target is any thicker than the proton range, an additional temperature drop must be added to Eq. 5.25 that accounts for the linear temperature variation in the extra portion of lithium.

As an example, consider a copper backing thickness of 0.25 cm and incident proton energy of 2.50 MeV. If the lithium target is made only 93.1 μm thick, so that the proton energy at the lithium/copper boundary is 1.88 MeV, then the protons continue to stop for a distance of 17.3 μm in the backing. From Figure 5-9, the temperature drop across the stopping range is 0.746°C/mA, and the temperature drop across the remaining copper is calculated using Eq. 5.26, giving 30.5°C/mA for a total temperature drop across the target and backing of 31.1°C/mA. Now if the lithium is made 1 mm thick, the total temperature drop is the sum of the drops across the copper (30.5°C/mA), over the stopping range of the protons (5.20°C/mA), and across the remaining lithium (43.96°C/mA), or 79.71°C/mA. If, in addition, the entire heat deposition is assumed to be a heat flux incident from the left, then the total temperature drop is calculated (incorrectly) as 88.94°C/mA. Besides dramatically reducing the 478 keV gamma yield from the target (see Section 4.3), another advantage of reducing the lithium thickness to only pass the (p,n) reaction threshold has been found. The results of these temperature drop calculations are therefore consistent with the much higher temperature drops normally encountered in the BNCT literature, but the enormous impact of reducing the lithium thickness to only pass the (p,n) reaction threshold is clear.

Table 5.5 gives the individual temperature drops listed in Eq. 5.25, as well as total temperature drop, for proton energies between 1.89 MeV and 2.50 MeV. The coolant flow rate in all cases is 10 gallons per minute. One of the largest components of the total temperature drop is seen to be across the copper backing after the protons have

Table 5.5: Temperature Drops for Near–Threshold and Higher Proton Energies

Incident Proton Energy	Temperature Drops (°C/mA)			
(MeV)	$(\Delta T/I)_{stopping}$	$(\Delta T/I)_{\mathrm{Cu}}$	$(\Delta T/I)_{fins}$	$(\Delta T/I)_{total}$
1.89	0.0680	23.0928	33.3319	56.4927
1.90	0.0691	23.2150	33.5083	56.7924
1.91	0.0705	23.3372	33.6846	57.0923
1.92	0.0722	23.4593	33.8610	57.3925
1.93	0.0742	23.5815	34.0374	57.6931
1.94	0.0766	23.7037	34.2137	57.9940
1.95	0.0792	23.8258	34.3901	58.2951
1.96	0.0822	23.9480	34.5664	58.5966
1.97	0.0855	24.0702	34.7428	58.8985
1.98	0.0891	24.1924	34.9192	59.2007
1.99	0.0930	24.3146	35.0955	59.5031
2.00	0.0973	24.4368	35.2719	59.8060
2.10	0.1576	25.6586	37.0355	62.8517
2.20	0.2515	26.8805	38.7991	65.9311
2.30	0.3801	28.1023	40.5627	69.0451
2.40	0.5445	29.3241	42.3263	72.1949
2.50	0.7462	30.5460	44.0899	75.3821

completely stopped. This drop is very easy to reduce; a reduction of the backing thickness $L_{backing}$ results in a nearly proportional decrease in this component. The largest temperature drop, across the fins, may be reduced by changing the coolant temperature, fin material, or fin geometry.

5.2.2 Transient Temperature Behavior (Beam Pulsing)

In the thermal analysis of Sections 5.1.1 through 5.2.1, all models assumed a steady state heat source. This amounts to an assumption of a continuous wave (CW) accelerator. However, it is likely that the proton accelerator used for near–threshold BNCT will be a pulsed machine. This will lead to a transient or oscillatory behavior of the temperature, and the peak lithium temperature will exceed the predictions of Section 5.2.1, possibly to the point of target failure. The reason this needs to be considered is obvious — if a machine is running at an average current I_{ave} with a duty factor of $d\%$, then the peak beam current will actually be $100I_{ave}/d$. This problem has been addressed by Dobelbower and Blue, but with lithium targets of 1 mm and average beam currents of 30 mA [5]. While a detailed analysis of the time–dependent behavior of this system needs to be studied to verify that it can successfully remove heat from milliamp level currents, it is not appropriate to go into such detail here. However, the problem should be at least partially addressed.

The time–dependent behavior of the temperature drop across the CTU should be a function of duty factor (%) and repetition rate (Hz). A typical design may consist of a 10% duty factor with a 200 Hz repetition rate [86]. We can estimate how much the maximum temperature drop exceeds the steady state temperature drop using a plot from Dobelbower and Blue's paper, given in Figure 5-11, which for the duty factor and repetition rate stated above is 32.38°C. The calculation was based on a number of assumptions, however, which must be at least partially corrected for the target geometry presented here. First, all heat is assumed to be incident from the

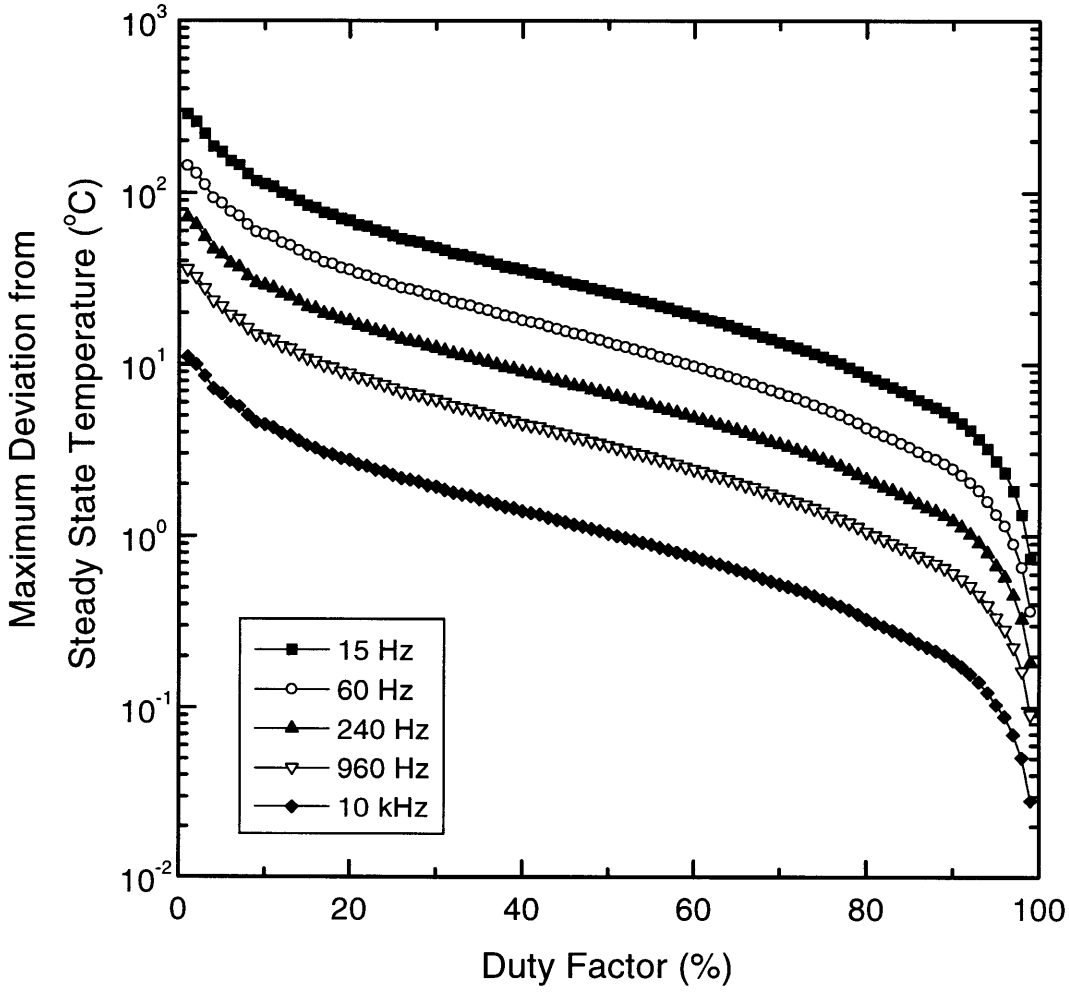

Figure 5-11: Maximum Deviation of Target Temperature from Average vs. Duty Factor for Several Repetition Rates. From [5].

left, a non-physical boundary condition. Since the resulting steady state temperature drops across the lithium and copper are linear, the fraction of the total temperature drop across each component may be estimated. For Dobelbower and Blue's geometry and property values, 18.2% of the temperature drop is in the copper and 81.8% is in the lithium. We can now estimate the total temperature deviation due to pulsing at 10%, 200 Hz for a lithium/copper target with our thicknesses ($\sim$10 μm and 0.25 cm, respectively) as 7.2°C. However, to get an answer in terms of temperature drop per unit current, we must divide this result by Dobelbower's assumed current, which was 30 mA. This gives us an estimated temperature deviation due to beam pulsing of 0.24°C/mA. Finally, the power density is higher for our design than the 1.53 MW/m^2 in Blue's paper; adjusting the temperature deviation by the ratio of power densities increases the estimate for near–threshold temperature deviation due to beam pulsing to 3.02°C/mA. While this additional temperature drop places a greater constraint on the beam, currents of several milliamps are still possible, quite sufficient for a prototype neutron source. In addition, note that this result was based on a simple adjustment of results obtained with a different geometry and very different boundary conditions; detailed analysis is necessary to establish a firm constraint on allowable beam current.

To put all the information presented in this chapter into perspective, the predicted total temperature drop across this multi–fin target with a 0.25 cm backing, operating at 1.95 MeV with a 1.27 cm radius proton beam, operating at a 10% duty factor and 200 Hz repetition rate, is 61.32°C/mA. For a coolant temperature of 20°C, a safety margin of 15°C below the lithium melting temperature may be maintained with an average accelerator current of 2.4 mA.

Chapter 6

Final Target Design

The results of calculations and experiments from previous chapters are now combined into a final design for a near–threshold CTU neutron source prototype.

The basic geometry of the design is similar to that given in Figure 4-2, but with several small modifications. The Al_2O_3 reflector is still a 30 cm radius cylinder with a length necessary to place the end of the reflector even with the moderator face. The inner walls of the reflector are flush with the beam line, target, and moderator to provide maximum benefit. The reflector density is reduced to 2.5 g/cm^3 to mimic the measured density of certain Al_2O_3 bricks available at Idaho State University; the density reduction is due to porosity of the bricks. Holes are bored in the top and bottom of the reflector to allow placement of the coolant lines.

The moderator is modified to permit ease of handling, as well as adjust for the multi–fin geometry of the target. A diagram of the modified moderator geometry is given in Figure 6-1. The base moderator is still a disk of radius 12 cm and depth to be determined, but two additional hemispherical wedges are placed on either side of the inner face of the moderator. These wedges fit tightly around either side of the multi–fin target and increase moderation without increasing distance to the patient. A thin (0.1 mm) sheet of thermal neutron absorber (^{6}Li) is placed behind the moderator, and

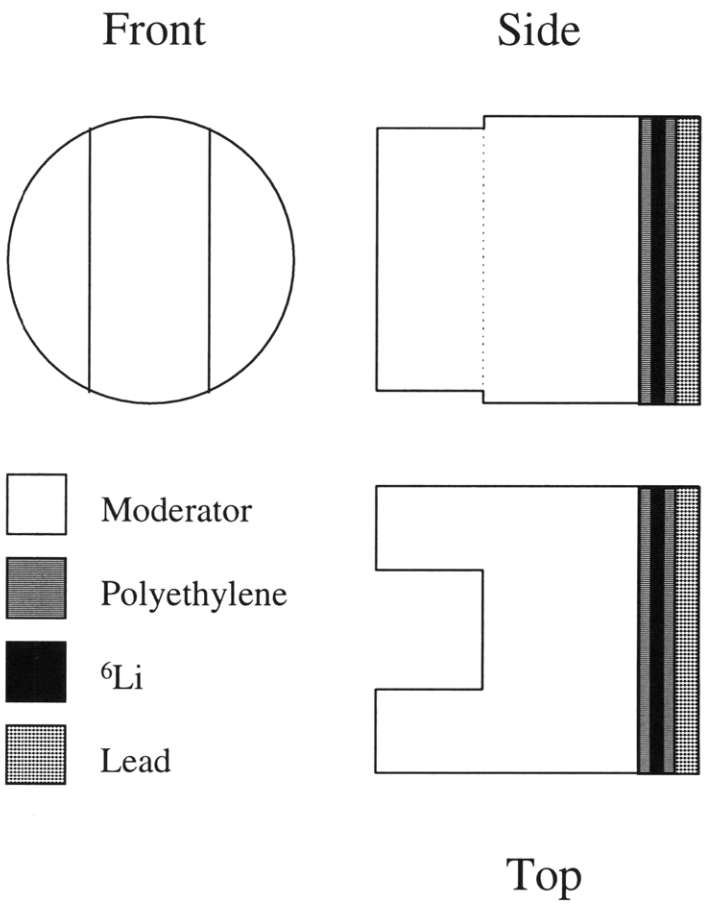

Figure 6-1: Moderator Design for Final CTU Design. Stainless steel surrounding the moderator unit is not shown, and the figure is not to scale.

a 0.25 cm sheet of lead is placed behind that for gamma attenuation (see Sections 4.4.3 and photonattenuation). The ^{6}Li sheet is surrounded by 0.5 mm of polyethylene to inhibit reactions with other materials. The entire moderator/^{6}Li/lead unit is encased in 1 mm of type 304 stainless steel so that it is all contained as a single unit.

The proton source is a 1.95 MeV, 2.54 cm diameter beam. The multi–fin target geometry in Figure 5-2 is used, but the copper backing thickness is reduced from 2.5 mm to 1.5 mm. This thickness will still have sufficient strength to allow a coolant flow rate of 10 gallons per minute, due to the structural support of the fins, but it will greatly reduce the temperature drop across the CTU (see below).

The envisioned procedure for preparing this near–threshold BNCT neutron source is as follows:

1. The multi–fin target, under an argon atmosphere or vacuum, is attached to the accelerator beam line using a vacuum lock system. This will prevent exposure to air which will reduce the neutron yield (see Section 2.2.6). The coolant inlet and outlet are oriented vertically.

2. The coolant lines are attached to the inlet and outlet of the multi–fin target.

3. The beam line and target are enclosed in the reflector. The reflector is symmetric about the vertical centerline, so it may be constructed as two separate sections that are simply pushed together to enclose the system. The reflector should be placed on a mechanical horizontal sliding system so that the operator only needs to push a button or pull a lever to accomplish this step. The requirements of this system are not extreme, since the estimated total reflector mass is only 271 kg. The relatively light weight of the reflector also makes it feasible to mount on an isocentric gantry to allow irradiations from multiple directions. This setup has the added advantage of easy access to the beam line, if needed.

4. The moderator/^{6}Li/lead unit is placed into the cavity behind the multi–fin

target. The estimated moderator thicknesses given below will permit these units to weigh around 4-5 kg, sufficiently light that operators can lift them into place and clamp them down. This is a major advantage over many other BNCT concepts that have moderators and reflectors weighing hundreds or even thousands of kilograms.

Figure 6-2 shows a schematic of the moderator, multi–fin target, and coolant lines.

Since the target and moderator geometry is different from the cases modeled in Chapter 4, new MCNP simulations were performed using the detailed geometry of the multi–fin target and modified moderator shape described above. The results for light water moderator thicknesses of 1 to 5 cm are given in Figures 6-3 and 6-4. Note that the coolant channels in the multi–fin geometry provide some additional moderation. This design allows the minimum RBE-ADDR of 6.67 cGy/min/mA to be achieved with just under 3 cm of moderator, with an RBE-AD of 5.69 cm and an RBE-AR of 4.32. The dose depth distribution along the phantom centerline with a 3 cm light water moderator is given in Figure 6-5. Alternatively, the minimum RBE-AD of 5 cm may be achieved with an RBE-ADDR of 11.5 cGy/min/mA (corresponding to treatment times of 35 minutes with a 5 mA beam or 70 minutes with a 2.5 mA beam), but with a reduced RBE-AR of 3.81. For comparison, an RBE-AD of 5 cm may be achieved with a 22 minute treatment time using a 5 mA beam or a 44 minute treatment time using a 2.5 mA beam if a maximum healthy tissue dose of 1250 RBE-cGy, which corresponds to the current BNL clinical trial protocol, is desired.

This near–threshold neutron source may also be described using the in–air parameters defined in Chapter 3. These parameters are given in Table 6.1. Comparison with Table 3.1 suggests that a current of 3.7 to 5.9 mA will produce an epithermal neutron flux ϕ_{epi} and neutron dose to epithermal neutron flux ratio D_n/ϕ_{epi} comparable to MIT and Petten. The ratio of gamma dose to epithermal neutron flux D_γ/ϕ_{epi} is an order of magnitude larger than for any of the existing reactor beams. However,

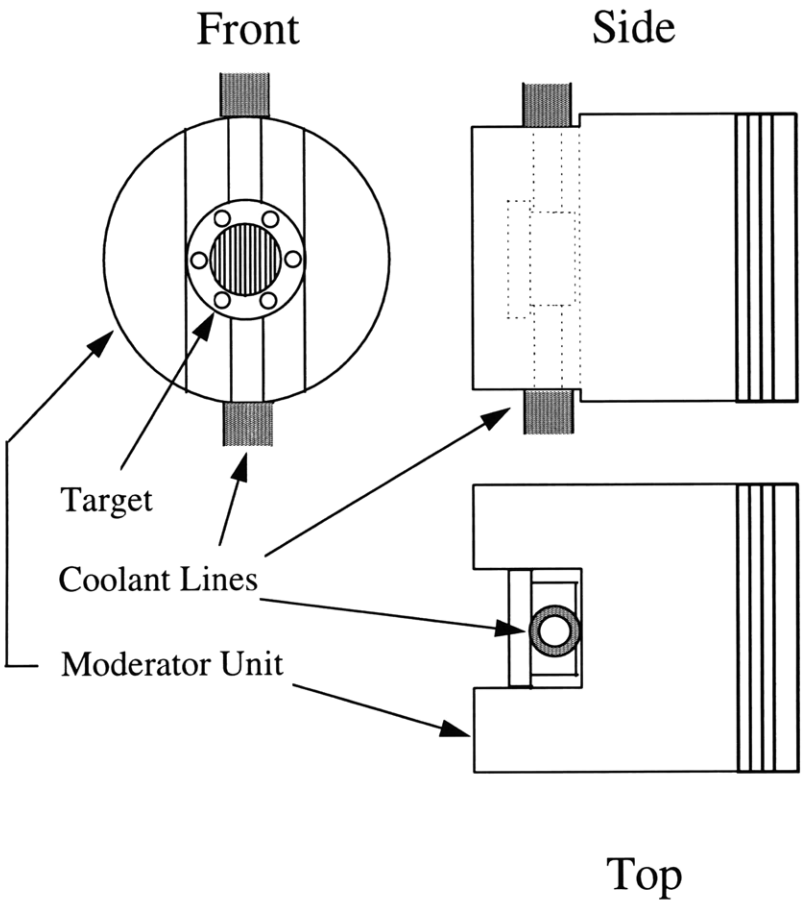

Figure 6-2: Final CTU Design

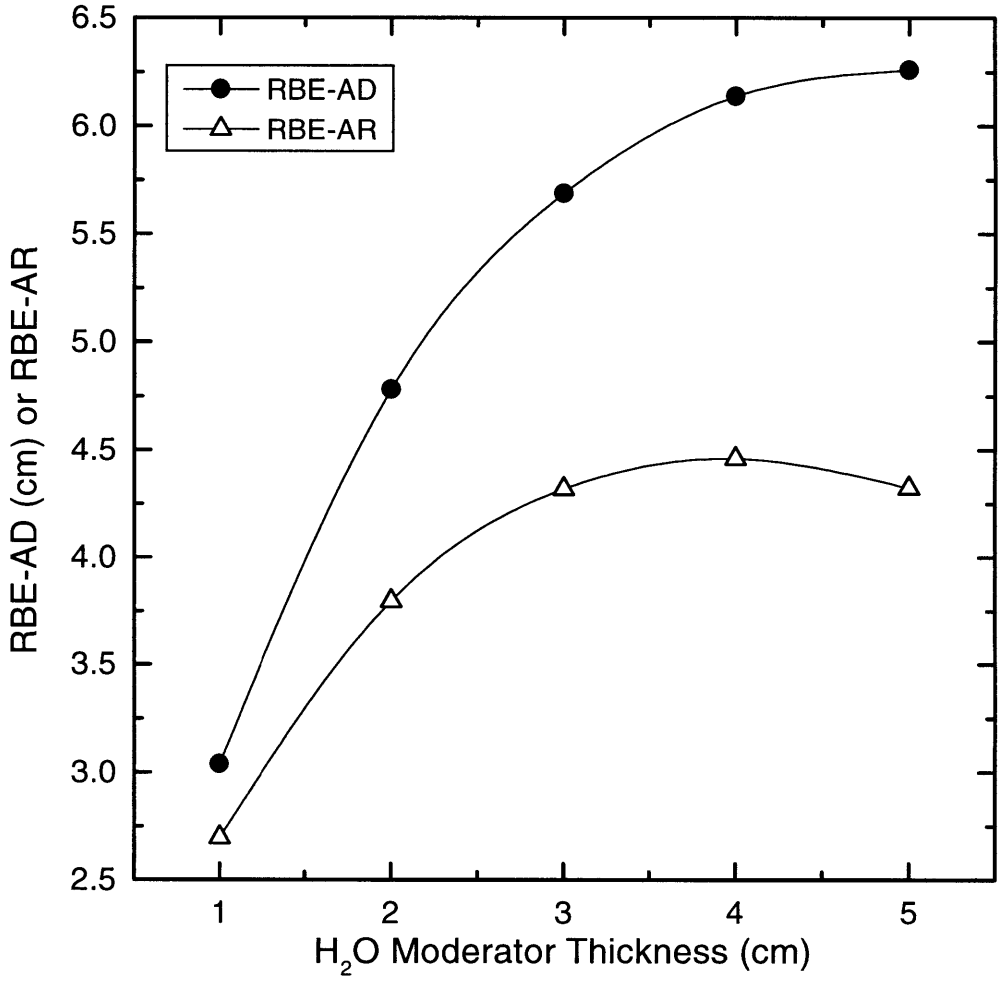

Figure 6-3: RBE-AD and RBE-AR for Final Near–Threshold BNCT Neutron Source Design for Various Moderator Thicknesses. The proton energy is 1.95 MeV.

Table 6.1: Free Beam Parameters for Final Design of Near–Threshold BNCT Neutron Source

Parameter	Units	Centerline ($\leq$ 1 cm)	Head Phantom Size ($\leq$ 8 cm)	Beam Port Size ($\leq$ 12 cm)
ϕ_{epi}	(n/cm^2-sec/mA)	2.2×10^{8}	6.6×10^{7}	3.9×10^{7}
D_n/ϕ_{epi}	(cGy-cm^2/n)	10.0×10^{-11}	6.9×10^{-11}	5.0×10^{-11}
D_n	(Gy/hour)$_{5mA}$	4.0	0.82	0.35
D_γ/ϕ_{epi}	(cGy-cm^2/n)	6.7×10^{-11}	9.1×10^{-11}	18.0×10^{-11}
D_γ	(Gy/hour)$_{5mA}$	2.7	1.1	1.3
J/ϕ	—	0.66	0.59	0.56

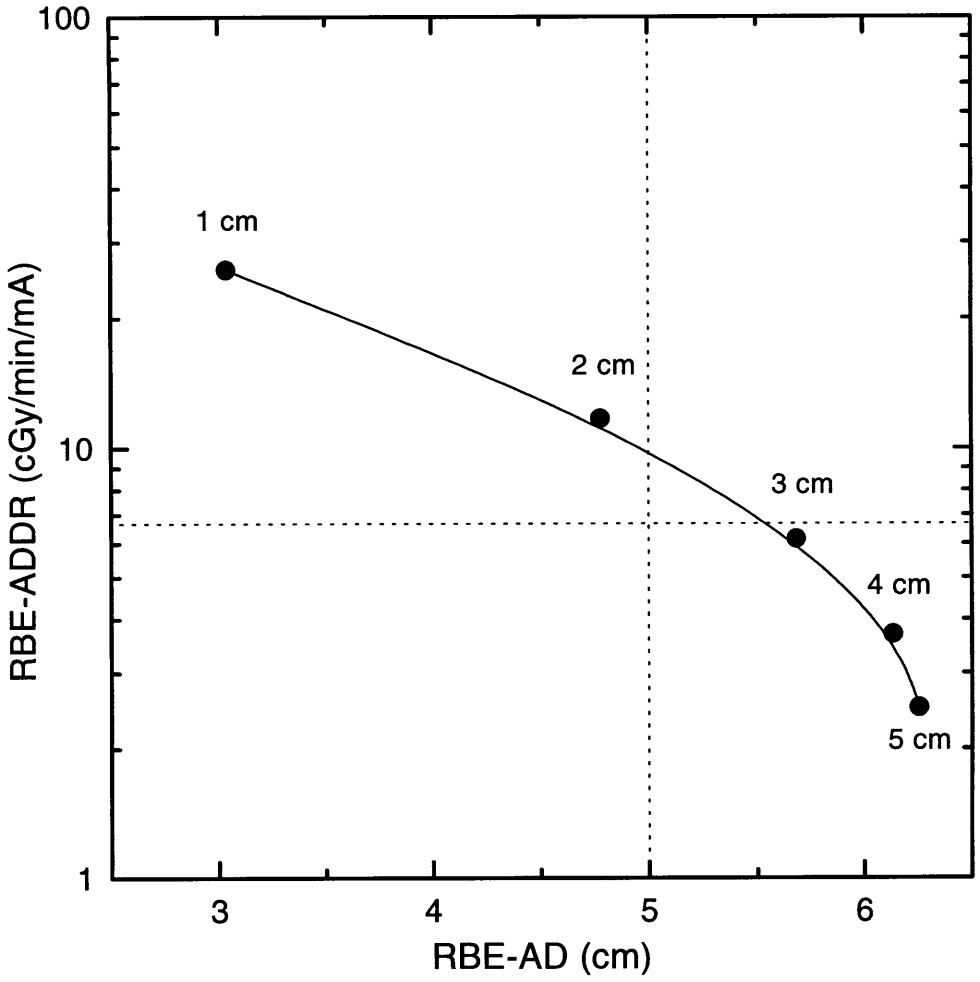

Figure 6-4: RBE-AD vs. RBE-ADDR for Final Near–Threshold BNCT Neutron Source Design for Various Moderator Thicknesses. The proton energy is 1.95 MeV. The vertical dotted line indicates the minimum acceptable RBE-AD of 5 cm. The upper and lower horizontal dotted lines correspond to total healthy tissue RBE doses of 2000 cGy and 1250 cGy, respectively. Points in the upper quadrant satisfy the requirements for a BNCT neutron beam.

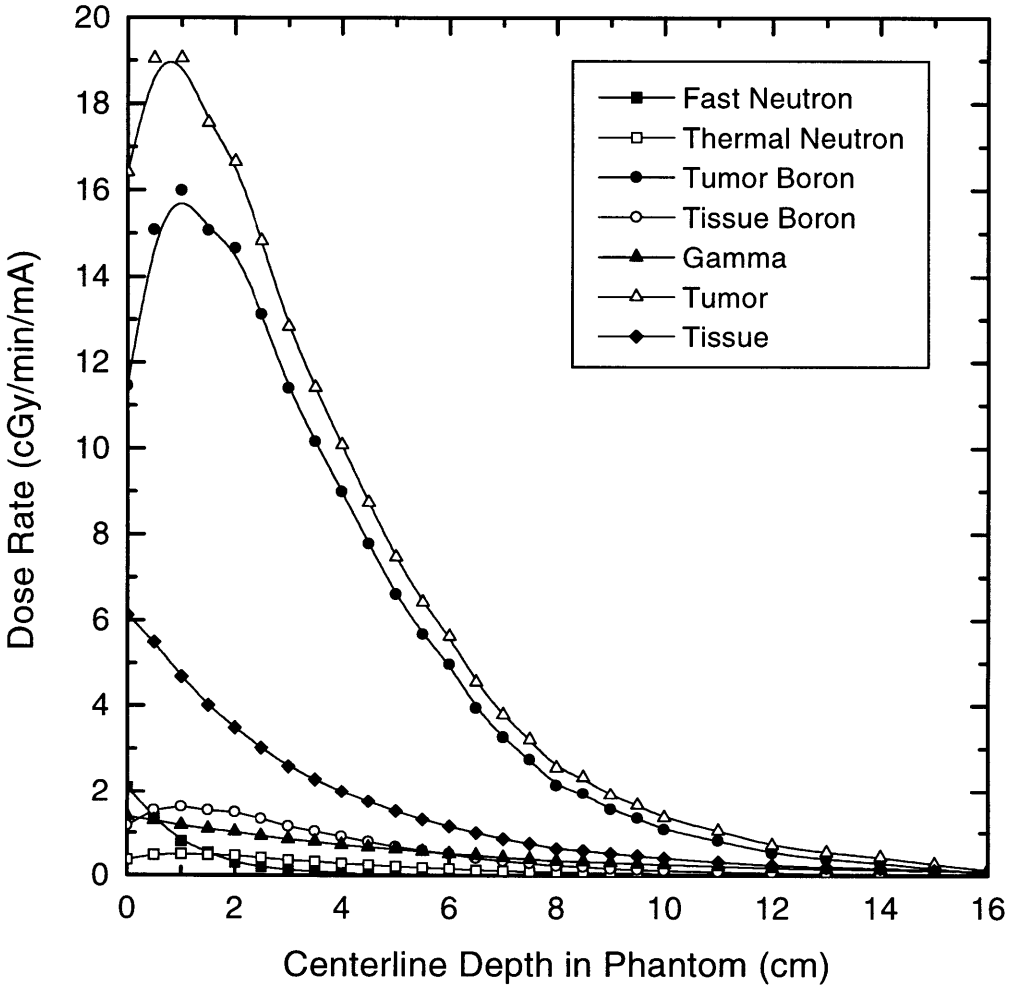

Figure 6-5: Dose Depth Profiles along Phantom Centerline for 3 cm H_2O Moderator. The proton energy is 1.95 MeV.

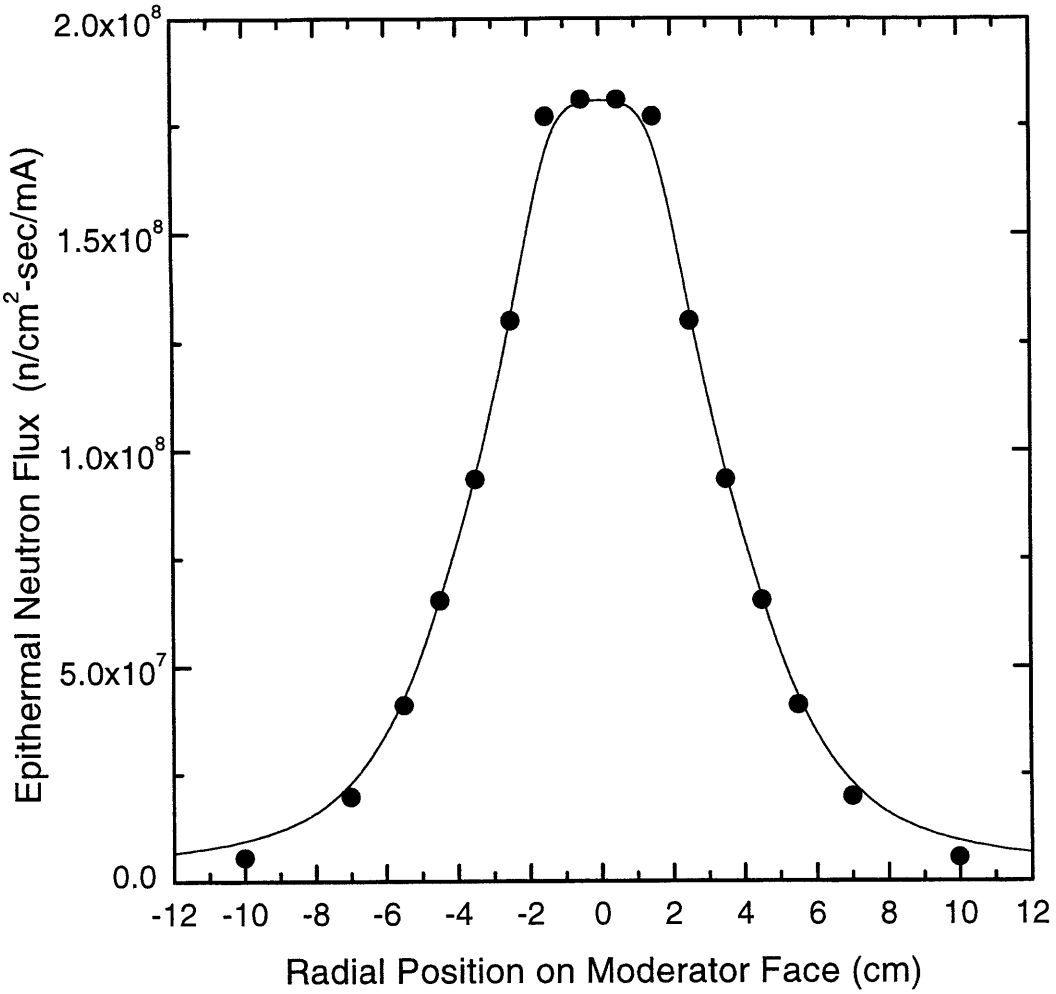

Figure 6-6: Radial Variation of the Epithermal Neutron Flux Exiting the Moderator. The proton energy is 1.95 MeV.

the dose profiles shown in Figure 6-5 indicate that this is not problematic, due to the lower RBE value of photons compared with other dose components. The current–to–flux ratio J/ϕ is comparable to the BNL and MIT beams. The mean energy of the neutron beam is 5.2 keV. This near–threshold beam is seen to be comparable to existing reactor BNCT beams.

The epithermal neutron flux given in Table 6.1 does not give a complete picture of the neutron flux exiting the moderator. This is clear from Figure 6-6, which shows the radial variation of the epithermal neutron flux on the outer face of the moderator

assembly. The flux is relatively flat within 2 cm of the centerline, but drops off rapidly as the radial distance increases. This strong radial flux variation leads to the radial variation of the advantage depth envelope shown in Figure 6-7. Any tumor located within this region will have a therapeutic advantage as described in Chapter 4. Ideally, the advantage envelope should be flat so that any tumor fingerlets will experience high doses. The advantage envelope for this design can be made more uniform with a larger beam spot size and/or increased moderator thickness, but this will also increase the proton current requirement. Note that a smaller advantage region may be preferable for certain BNCT applications other than the treatment of brain tumors, since the total dose to healthy tissue will be reduced.

Note that the light weight of the components of this design allows moderators to be easily changed. A series of moderators of varying thickness may be constructed for different applications, and the operator may simply exchange one moderator unit for another depending on what treatment parameter is considered most important.

Bombarding a target that is only microns thick with a milliamp–level proton beam is expected to erode the surface, primarily through sputtering [87]. An estimate of the erosion rate, based on typical sputtering yields for MeV–level protons on light elements [88], predicts a loss of 1.3×10^{-4} μm/sec/mA. At this rate, the target will be completely eroded away in 3.9 hours, certainly a problem for hospital treatments. However, if the target thickness is increased to 28.6 μm, then it will not drop below the 9.43 μm necessary to maintain the full thick target neutron yield with operation at 5 mA for up to 8 hours. Since it is easy to change targets in this design, a series of CTUs may be prepared on a continuous basis so that when one target is used up after one day, another CTU may be attached. The old CTU can have the corroded lithium washed away, cleaned, and a new layer of lithium can be vapor deposited onto the copper backing. This increased lithium thickness will not appreciably increase the 478 keV gamma yield or the temperature drop across the target.

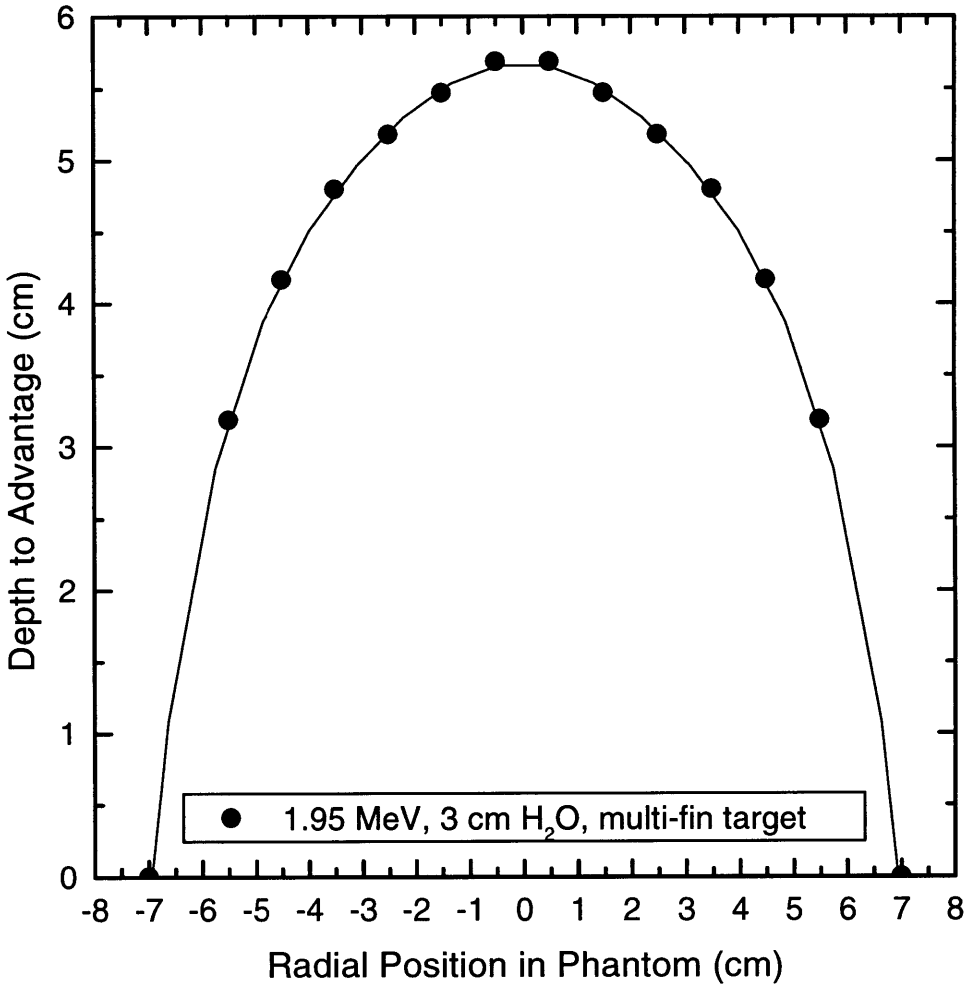

Figure 6-7: Radial Variation of Advantage Region for a 3 cm Light Water Moderator. Each point indicates the depth at a given radial distance from the centerline where the tumor dose rate equals the maximum healthy tissue dose rate. The proton energy is 1.95 MeV.

The new copper backing thickness requires a new estimate for the total temperature drop across the CTU. Referring to Table 5.5, the temperature drops across the proton stopping range and fins will not change from their tabulated values of 0.0792°C/mA and 34.3901°C/mA. The reduced copper thickness will lead to a value of 14.2294°C/mA for $(\Delta T/I)_{\mathrm{Cu}}$, a reduction of 40% from the tabulated value. Finally, the adjusted deviation of the maximum target temperature from its average value due to beam pulsing is estimated to be 1.832°C/mA, giving a maximum total temperature drop across the CTU of 50.53°C/mA. For cooling water at 20°C and maximum permissible target temperature of 166°C (to give a 15°C safety margin below T_{melt}), the maximum allowable average beam current is 2.89 mA.

One way to increase the allowed current would be to chill the coolant; a coolant temperature of 5°C will lead to a maximum average beam current of 3.14 mA, based on adjustments to the coolant property values in `flow.f`. Increasing the coolant flow rate to a higher value of 20 gallons per minute would lead to a maximum average beam current of 3.33 mA, again based on `flow.f` calculations. Additional increases are possible by increasing the duty factor and repetition rate, changing the fin material to a material with a higher thermal conductivity, i.e. high purity silver, or changing the fin geometry.

A head phantom may be used to test the predictions of the dosimetric calculations performed for this near–threshold neutron source. A cylindrical acrylic head and neck phantom was designed and constructed for this purpose. A description of the design is given in Appendix G. This design allows almost unlimited spatial resolution in measurements of neutron and gamma doses and thermal neutron fluxes.

Chapter 7

Summary and Future Work

7.1 Summary

An intense, prototypical neutron source for accelerator–based BNCT has been designed using near–threshold reactions. The source is capable of producing 3.11×10^{11} neutrons per second with a 1.95 MeV, 5 mA proton beam incident on a 9.5 μm thick lithium target on a copper backing. This neutron source has been estimated to provide a BNCT treatment beam capable of producing an RBE advantage depth of more than 6 cm, an RBE advantage ratio of 3.8-4.3, and an RBE advantage depth dose rate of better than 6.5 cGy/min/mA, allowing healthy tissue RBE doses of 20 Gy in about 1 hour. In the process of designing this beam, several sub–issues have been addressed.

A self–consistent method for accurate calculation of near–threshold, as well as higher energy, thick target yields for the ^{7}Li(p,n)^{7}Be reaction have been developed. These methods use a carefully determined combination of analytical and tabulated experimental cross section and stopping power data to calculate the neutron yields. The method was also expanded to include yield calculations for certain low weight lithium compounds, as well as partially thick targets. A model was also developed to

predict changes in neutron yield due to corrosion of lithium metal targets in air. Neutron yield predictions were experimentally confirmed for several target thicknesses, proton energies, and compounds.

The dosimetric behavior of near–threshold beams in cylindrical head phantoms was evaluated using MCNP simulations. Advantage depths were seen to reach a maximum with around 5 cm of light water moderator for all near–threshold energies. The greatest improvement in near–threshold dosimetry comes from reducing the target thickness to tens of microns to reduce the 478 keV photon yield from inelastic proton scattering in the target. The effect of several backing materials was evaluated, with negligible differences in treatment parameters for the materials considered here. A ^{6}Li thermal neutron absorber only 0.1 mm thick is shown to strongly improve beam properties, but a cadmium absorber creates a worse beam due to the large number of neutron capture gammas that are produced. Lead also improves the advantage depth and ratio of the beams, but the reduction of the advantage depth dose rate is unacceptably high for shields greater than 0.25 cm thick.

A multi–fin target has been shown to provide superior heat removal capabilities for accelerator beams up to about 5 mA. A theoretical model of temperature drops across these fins, based on fluid and heat transport models, is shown to agree well with experimental temperature drops over a wide range of coolant flow rates. High power tests with heat inputs up to 2.2 kW also demonstrate the effectiveness of this design for removing heat from the target. Temperature profiles across target and backing were calculated based on the energy loss of the proton beam in these regions. Reduced target thicknesses to only allow proton slowing down past the (p,n) reaction threshold lead to temperature drops across the proton stopping range of less than 0.1°C/mA for near–threshold beams. The greatest temperature drops in the combined target unit are across the copper backing plate. Estimates of temperature deviations due to accelerator beam pulsing, as well as critical heat flux concerns, are discussed. Finally,

a head phantom was designed to allow very detailed spatial resolution of neutron and gamma doses, as well as thermal flux mapping for boron and nitrogen doses.

This research has demonstrated the feasibility of near–threshold reactions for providing intense neutron beams acceptable for NCT applications. The final design of the source, while described as prototypical, actually provides a neutron beam of about the same intensity as existing source designs and reactor beams used in current clinical trials.

7.2 Suggestions for Future Work

While this project has established the clinical and engineering feasibility of near–threshold BNCT, many questions remain unanswered in this area. Indeed, certain questions have arisen from this research that were not obvious prior to its completion.

While the differential (p,n) cross sections for ^{7}Li are well established, the differential yields of 478 keV gammas from inelastic proton scattering in lithium are not well known. This research assumed an isotropic distribution, but any significant anisotropy will have a great effect on the BNCT treatment parameters calculated here. Further evaluation of this photon source distribution is necessary for more accurate dose models for near–threshold BNCT.

All BNCT treatment parameters determined in this research are based on specific RBE values taken from BNCT reactor studies, as described in Chapter 4. While the gamma, boron, and nitrogen doses are not expected to differ greatly between reactor–based and accelerator–based BNCT, the neutron RBE factor, which is strongly dependent on neutron energy, can be expected to be very different in accelerator sources. For near–threshold beams, in which neutrons with energies greater than 200 keV are kinematically forbidden, this difference should be even more pronounced. The need for experimentally determined neutron RBE values for near–threshold neutron

sources cannot be overemphasized.

While many parameters of the combined target unit were studied in this work, many others have not been addressed. For example, Kudchadker's research indicates that for near–threshold beams above about 1.95 MeV, light water ceases to be the most effective moderator [34]. In addition, other materials such as high density polyethylene have a higher hydrogen atom density than light water, so less moderator is needed and the $1/r^2$ losses are reduced.

The largest number of unanswered questions are related to the multi–fin target. While the average, steady state heat removal of the system is excellent, the geometry of the coolant channels makes non–uniformity of the target temperature in the transverse direction a concern. More detailed, three dimensional modeling of the target is needed to answer these questions. One possibility for a more uniform cooling distribution is the use of spines instead of fins. Spines are round pegs that stick out of the target backing, like fins, but they can be arranged in a honeycomb pattern that creates turbulence and removes about the same level of heat as fins, but with a more homogeneous temperature distribution. More detailed experimental verification of the heat removal is also needed, preferably using large diameter charged particle beams to more accurately mimic the expected clinical demands of the target. Effects of energy and range straggling in the proton stopping process are also necessary for more accurate estimates of temperature profiles in the target and backing. Much greater detail is also needed in evaluations of beam pulsing effects on temperatures and critical heat flux concerns.

In the process of doing this research, it became clear that lithium targets with thicknesses on the order of microns are necessary to make near–threshold BNCT viable, and the heat removal benefits of these thicknesses can even be extended to higher proton energies. However, the best technique for creating these micron–thick targets on copper backings has yet to be determined, and the stability of these targets

under the demands of milliamp level beam currents and hours of operation must be gauged. The answers to these questions are of prime importance to the final design and construction of any near–threshold neutron source.

Finally, the results of near–threshold BNCT may be applicable to other areas of neutron capture research other than the treatment of glioblastomas. In particular, boron neutron capture synovectomy (BNCS) uses the same method as BNCT to ablate the synovial tissue in the joints of rheumatoid arthritis patients [87]. The reduced treatment depth, smaller treatment region, and higher optimum neutron energies are all suited to a near–threshold source. The simplicity and low cost of the design is also a great advantage to this technique, which must compete with existing surgical techniques. Another possible application is the prevention of restenosis, or hardening of the artery wall following balloon dilation angioplasty [88]. Studies of the suitability of near–threshold BNCT to these and other applications should be performed to increase the attractiveness of this neutron production technique.

Appendix A

Thick Target Neutron Yield Program (li.f)

```
       program li
*
************************************************************
*
*     This program calculates the neutron energy-angle
*     yield for an incident proton beam per unit current,
*     i.e. 1/Ip d2Y(theta,En)/d(theta)dEn = the number
*     of neutrons per second emitted in solid angle d(Omega)
*     about angle theta in the energy interval En to
*     En + dEn per unit proton current.
*     (neutrons/sec-steradian-keV-mA)
*
************************************************************
*
       integer enint,thetaint,mult,nmax,nmin,compound
       real ep0,eth,theta(721),en(251),ep,en0,xi,s,na,aeff,s0,
     +      yield(721,251),cm2mb,hk,ix,li7fraction,eptable(51),sig(51),
     +      dsigma0(51),a0(51),a1(51),a2(51),a3(51),q,mp,mh,mn,mbe,
     +      mli,anglewidth,elec,gamma,gamma0,enprime,enprime0,epmax,
     +      epmin,dsigma0max,dsigma0min,sigmax,sigmin,a1max,a1min,
     +      a2max,a2min,a3max,a3min,dsigma0smax,dsigma0smin,enequal,
     +      sigsmax,sigsmin,a1smax,a1smin,a2smax,a2smin,a3smax,sigep,
     +      a3smin,dsigma0s(51),sigs(51),a1s(51),a2s(51),a3s(51),
     +      dsigma0ep,a0ep,a1ep,a2ep,a3ep,sign,product2,product3,
     +      theta0,thetaprime0,enequal0,yield0,dyden(251),dydom(721),
     +      enmax0,enmin0,thetaprimemin0,yieldmin0,deltaen,thetamax
*
       print*, '     1 = Li metal'
       print*, '     2 = LiH'
       print*, '     3 = Li2O'
       print*, '     4 = LiOH'
```

```
      print*, '     5 = Li3N'
      print*, '     6 = LiF'
      print*, 'What lithium compound do you want (type number 1-6)?'
      read*, compound
*
      anglewidth=1.0     ! LAB angle interval width in degrees
*
*     Aeff for natural lithium = 7.016003 u * 92.5% + 6.015121 u * 7.5%
*
      if (compound.eq.1) then
         mult=1          ! Multiplicity of Li atoms per material
                         !  unit, e.g. mult=2 for Li2O
         aeff=6.940934   ! Atomic weight of Li metal (g/mole)
      elseif (compound.eq.2) then
         mult=1
         aeff=7.948913
      elseif (compound.eq.3) then
         mult=2
         aeff=29.88158
      elseif (compound.eq.4) then
         mult=1
         aeff=23.948623
      elseif (compound.eq.5) then
         mult=3
         aeff=34.828974
      elseif (compound.eq.6) then
         mult=1
         aeff=25.939340
      else
         print*, 'Invalid response.  Start over.'
         go to 9900
      endif
      li7fraction=0.925  ! Fraction of Li atoms that are Li-7
      pi=4.0*atan(1.0)
      na=6.022045e23     ! Avogadro's constant
      elec=1.602189e-16  ! Charge on the proton (in millicoulombs)
      mp=938.2800        ! Proton mass in MeV
      mh=938.7910        ! Hydrogen atom mass in MeV
      mn=939.5735        ! Neutron mass in MeV
      mbe=6536.2825      ! Beryllium-7 atomic mass in MeV
      mli=6535.4208      ! Lithium-7 atomic mass in MeV
      q=mh+mli-mn-mbe    ! Reaction Q-value in MeV
*
      print*, 'What is the incident proton energy (MeV)?'
      read*, ep0
*
      cm2mb=1e-27           ! 1e-27 cm**2/millibarn
*
      mbe=6534.2385                  ! Remaining calcs need nuclear mass
      eth=-q*(mbe+mn)/(mbe+mn-mp)    ! Li(p,n)Be threshold energy
      if (ep0.le.eth) then
         print*, 'Incident energy too low'
         go to 9900
      endif
```

```
*
*************************************************************
*
* Calculate the maximum neutron energy generated, and
* compute the interval endpoints for the enint neutron
* energy intervals.
*
*************************************************************
*
        gamma0=sqrt(mp*mn*ep0/mbe/(mbe+mn-mp)/(ep0-eth))
        enprime0=mbe*(mbe+mn-mp)*(ep0-eth)/(mbe+mn)**2
        en0=enprime0*(1.0+gamma0)**2
        if (en0.le.0.250) then
           deltaen=0.001
        elseif (en0.gt.0.250.and.en0.le.0.500) then
           deltaen=0.002
        elseif (en0.gt.0.500.and.en0.le.1.0) then
           deltaen=0.004
        else
           deltaen=0.010
        endif
        enint=250
        do 20 k=1,enint+1
           en(k)=real(k-1)*deltaen
20 continue
*
*************************************************************
*
* Compute the interval endpoints for the thetaint neutron
* emission angle intervals.
*
*************************************************************
*
        thetaint=nint(180.0/anglewidth)  ! Number of angle intervals
        anglewidth=180.0/real(thetaint)  ! Readjust angle width in degrees
        theta(1)=0
        theta(thetaint+1)=pi
        do 30 i=2,thetaint
           theta(i)=pi*real(i-1)*anglewidth/180.0
 30 continue
*
*************************************************************
*
* Read in cross section parameters:
*   eptable(jj) is the jjth energy listed in the table (MeV)
*   disgma0(jj) is the 0-degree diff. cross section at energy
*                     eptable(jj), in mb/steradian
*   a0(jj)-a3(jj) are the Legendre coefficients for the
*               corresponding Legendre polynomials P0-P3
*
*************************************************************
*
        jj=1
        open (unit=13,file='sigmafile',status='unknown')
```

```
 35     read (13,*,end=40) eptable(jj),dsigma0(jj),a0(jj),
     +                     a1(jj),a2(jj),a3(jj)
        sig(jj)=4.0*pi*dsigma0(jj)*a0(jj)
        jj=jj+1
        go to 35
 40 n=jj-1
        close (unit=13)
*
*****************************************************************
*
* This section reads the parameters s(k) which
* define the natural cubic spline fits through the cross
* section data points.  These s(k) values were calculated
* using the spline.f program.
*
*****************************************************************
*
        open (unit=13,file='sigmaspline',status='unknown')
        do 60 j=1,n-1
           read (13,*) eptable(j),sigs(j),dsigma0s(j),a1s(j),
     +                 a2s(j),a3s(j)
60 continue
        close (unit=13)
        dsigma0s(n+1)=0.0
        sigs(n+1)=0.0
        a1s(n+1)=0.0
        a2s(n+1)=0.0
        a3s(n+1)=0.0
*
        do 2000 i=1,enint+1
           do 1000 j=1,thetaint+1
              ep=(sqrt(mp*mn*en(i))*cos(theta(j))-sqrt(mp*mn*en(i)*
     +           (cos(theta(j)))**2+(mbe-mp)*((mbe+mn)*en(i)-
     +            mbe*q)))**2/(mbe-mp)**2
              if (ep.lt.eth.or.ep.gt.ep0) then
                 yield(j,i)=0.0
                 go to 1000
              elseif (en(i).eq.0.0) then
                 yield(j,i)=0.0
                 go to 1000
              else
                 gamma=sqrt(mp*mn*ep/mbe/(mbe+mn-mp)/(ep-eth))
                 xi=(1.0/gamma**2-(sin(theta(j)))**2)
                 if (xi.lt.0.0) then
                    xi=0.0
                 else
                    xi=sqrt(xi)
                 endif
                 enprime=mbe*(mbe+mn-mp)*(ep-eth)/(mbe+mn)**2
                 if (gamma.lt.1.0) then
                    thetaprime=theta(j)+asin(gamma*sin(theta(j)))
                    sign=1.0
                 elseif (gamma.eq.1.0) then
                    thetaprime=2.0*theta(j)
```

```
                  sign=1.0
               elseif (gamma.gt.1.0) then
                  enequal=enprime*(gamma**2-1.0)
                  if (en(i).ge.enequal) then
                     thetaprime=gamma*sin(theta(j))
                     if (thetaprime.gt.1.0) then
                        thetaprime=theta(j)+pi/2.0
                     else
                        thetaprime=theta(j)+asin(thetaprime)
                     endif
                     sign=1.0
                  elseif (en(i).lt.enequal) then
                     thetaprime=gamma*sin(theta(j))
                     if (thetaprime.gt.1.0) then
                        thetaprime=theta(j)+pi/2.0
                     else
                        thetaprime=pi+theta(j)-asin(thetaprime)
                     endif
                     sign=-1.0
                  endif
               endif
               if (compound.eq.1) then
                  call stoppingpower(ep,s)
               elseif (compound.eq.2) then
                  call stoppingpowerlih(ep,s)
               elseif (compound.eq.3) then
                  call stoppingpowerli2o(ep,s)
               elseif (compound.eq.4) then
                  call stoppingpowerlioh(ep,s)
               elseif (compound.eq.5) then
                  call stoppingpowerli3n(ep,s)
               elseif (compound.eq.6) then
                  call stoppingpowerlif(ep,s)
               endif
*
               if (ep.le.eptable(1)) then
                  x=6.0*sqrt(1.0-eth/ep)
*
*     product3 = dsigma/domega * dompdom * depden
*
                  product3=164.9127*sqrt(mp*mn/mbe/(mbe+mn-mp))*6.0/ep/
     +                 (1.0+x)**2*(xi+sign*cos(theta(j)))*(mbe+mn)**2*
     +                  ep/(mp*mn*ep*xi*(cos(theta(j))+sign*xi)+
     +                  sign*mbe*(mbe+mn-mp)*eth)
                  yield(j,i)=product3
               else
*
*     product2 = dompdom * depden
*
                  product2=(mbe+mn)**2*(xi+sign*cos(theta(j)))*
     +                  gamma*ep/(mp*mn*ep*xi*(cos(theta(j))+
     +                  sign*xi)+sign*mbe*(mbe+mn-mp)*eth)
*
*******************************************************
```

```
*
* This section calculates the differential cross
* section parameters for energies ep(j) using
* natural cubic spline fits to the data.  The first
* loop determines the energy interval in which ep(j)
* falls for each j; the cross section parameters at
* the lower end of the interval are labeled with -min
* and those at the upper end are labeled with -max.
*
*******************************************************
*
                  do 90 jj=2,n+1
                     if (ep.lt.eptable(jj).and.ep.ge.eptable(jj-1)) then
                        epmax=eptable(jj)
                        epmin=eptable(jj-1)
                        dsigma0max=dsigma0(jj)
                        dsigma0min=dsigma0(jj-1)
                        sigmax=sig(jj)
                        sigmin=sig(jj-1)
                        a1max=a1(jj)
                        a1min=a1(jj-1)
                        a2max=a2(jj)
                        a2min=a2(jj-1)
                        a3max=a3(jj)
                        a3min=a3(jj-1)
                        dsigma0smax=dsigma0s(jj)
                        dsigma0smin=dsigma0s(jj-1)
                        sigsmax=sigs(jj)
                        sigsmin=sigs(jj-1)
                        a1smax=a1s(jj)
                        a1smin=a1s(jj-1)
                        a2smax=a2s(jj)
                        a2smin=a2s(jj-1)
                        a3smax=a3s(jj)
                        a3smin=a3s(jj-1)
                     endif
 90               continue
*
*********************************************************
*
* This section determines the energy interval width (hk)
* and distance above the lower energy bound (ix).  The
* cross section parameters are then computed using the
* interpolate subroutine.
*
*********************************************************
*
                  hk=epmax-epmin
                  ix=ep-epmin
                  call interpolate(hk,ix,dsigma0min,dsigma0max,
     +                        dsigma0smin,dsigma0smax,dsigma0ep)
                  call interpolate(hk,ix,sigmin,sigmax,sigsmin,
     +                        sigsmax,sigep)
                  call interpolate(hk,ix,a1min,a1max,a1smin,
```

```
     +                        a1smax,a1ep)
                   call interpolate(hk,ix,a2min,a2max,a2smin,
     +                        a2smax,a2ep)
                   call interpolate(hk,ix,a3min,a3max,a3smin,
     +                        a3smax,a3ep)
                   a0ep=0.5*((sigep/4.0/pi/dsigma0ep)+
     +                       (1.0-a1ep-a2ep-a3ep))
                   dsigma=dsigma0ep*(a0ep+a1ep*cos(thetaprime)+
     +                      a2ep*0.5*(3.0*(cos(thetaprime))**2-1.0)+
     +                      a3ep*0.5*(5.0*(cos(thetaprime))**3-3.0*
     +                      cos(thetaprime)))
                   yield(j,i)=product2*dsigma
                endif
                yield(j,i)=yield(j,i)*real(mult)*li7fraction*
     +                       cm2mb*na/aeff/elec/1000.0/s
             endif
             if (yield(j,i).eq.0) then
                print*, 'WARNING! Yield=0'
                print*, j, i, 'Ep=', ep
                print*
             endif
1000    continue
2000 continue
*
************************************************************
*
* NEUTRON ENERGY SPECTRUM
*
************************************************************
*
* This section determines the neutron energy spectrum
* dY/dEn (neutrons/sec-keV-mA).  It is the integral
* over theta of 2*pi*theta*yield.  The upper boundary
* of integration is either 180 degrees or is determined
* by ep0.
*
************************************************************
*
        if (compound.eq.1) then
           call stoppingpower(ep0,s0)
        elseif (compound.eq.2) then
           call stoppingpowerlih(ep0,s0)
        elseif (compound.eq.3) then
           call stoppingpowerli2o(ep0,s0)
        elseif (compound.eq.4) then
           call stoppingpowerlioh(ep0,s0)
        elseif (compound.eq.5) then
           call stoppingpowerli3n(ep0,s0)
        elseif (compound.eq.6) then
           call stoppingpowerlif(ep0,s0)
        endif
*
************************************************************
*
```

```
* This section calculates the differential cross
* section parameters for energy ep0 using
* natural cubic spline fits to the data.  The first
* loop determines the energy interval in which ep0
* falls for each j; the cross section parameters at
* the lower end of the interval are labeled with -min
* and those at the upper end are labeled with -max.
*
*********************************************************
*
        do 2090 jj=2,n+1
           if (ep0.le.eptable(jj).and.ep0.gt.eptable(jj-1)) then
              epmax=eptable(jj)
              epmin=eptable(jj-1)
              dsigma0max=dsigma0(jj)
              dsigma0min=dsigma0(jj-1)
              sigmax=sig(jj)
              sigmin=sig(jj-1)
              a1max=a1(jj)
              a1min=a1(jj-1)
              a2max=a2(jj)
              a2min=a2(jj-1)
              a3max=a3(jj)
              a3min=a3(jj-1)
              dsigma0smax=dsigma0s(jj)
              dsigma0smin=dsigma0s(jj-1)
              sigsmax=sigs(jj)
              sigsmin=sigs(jj-1)
              a1smax=a1s(jj)
              a1smin=a1s(jj-1)
              a2smax=a2s(jj)
              a2smin=a2s(jj-1)
              a3smax=a3s(jj)
              a3smin=a3s(jj-1)
           endif
2090 continue
*
*********************************************************
*
* This section determines the energy interval width (hk)
* and distance above the lower energy bound (ix).  The
* cross section parameters are then computed using the
* interpolate subroutine.
*
*********************************************************
*
        hk=epmax-epmin
        ix=ep0-epmin
        call interpolate(hk,ix,dsigma0min,dsigma0max,
     +                   dsigma0smin,dsigma0smax,dsigma0ep)
        call interpolate(hk,ix,sigmin,sigmax,sigsmin,sigsmax,sigep)
        call interpolate(hk,ix,a1min,a1max,a1smin,a1smax,a1ep)
        call interpolate(hk,ix,a2min,a2max,a2smin,a2smax,a2ep)
        call interpolate(hk,ix,a3min,a3max,a3smin,a3smax,a3ep)
```

```
        a0ep=0.5*((sigep/4.0/pi/dsigma0ep)+(1.0-a1ep-a2ep-a3ep))
*
        do 3000 i=1,enint+1
           dyden(i)=0.0
           if (i.eq.1) then
              dyden(i)=0.0              !  dY/dEn=0 when En=0
              go to 3000
           elseif (en(i).gt.en0) then
              dyden(i)=0.0              !  dY/dEn=0 when En>En0,max
              go to 3000
           else
              if (yield(thetaint+1,i).ne.0.0) then
*
* If yield(thetaint+1,i)=yield(180 degrees,i) is not zero,
* then the angular integration will automatically be performed
* over the entire angular range (0-180 degrees).  For trapezoidal
* integration,
*
* dyden(i)=0.5*anglewidth*(2*pi)*[sin(theta(1))*yield(1,i) +
*          sin(theta(thetaint+1)*yield(thetaint+1,i) +
*          2 * sum_j=2 ^j=thetaint{sin(theta(j)*yield(j,i)}]
*
* However, sin(theta(1))=sin(theta(thetaint+1))=0, so only the
* sum remains and
*
* dyden(i)=pi*anglewidth*[2 * sum_j=2 ^j=thetaint
*                         {sin(theta(j)*yield(j,i)}]
*
                 do 2100 j=2,thetaint
                    dyden(i)=dyden(i)+2.0*sin(theta(j))*yield(j,i)
2100             continue
                 dyden(i)=dyden(i)*pi*(pi*anglewidth/180.0)
              else
                 theta0=((mbe+mn)*en(i)-mbe*q-(mbe-mp)*ep0)/
     +                       2.0/sqrt(mp*mn*en(i)*ep0)
                 if (theta0.ge.1.0) then
                    dyden(i)=0.0
                    go to 3000
                 else
                    theta0=acos(theta0)
                 endif
                 xi=(1.0/gamma0**2-(sin(theta0))**2)
                 if (xi.lt.0.0) then
                    xi=0.0
                 else
                    xi=sqrt(xi)
                 endif
                 if (gamma0.lt.1.0) then
                    thetaprime0=theta0+asin(gamma0*sin(theta0))
                    sign=1.0
                 elseif (gamma0.eq.1.0) then
                    thetaprime0=2.0*theta0
                    sign=1.0
                 elseif (gamma0.gt.1.0) then
```

```
                  enequal0=enprime0*(gamma0**2-1.0)
                  if (en(i).ge.enequal0) then
                     thetaprime0=gamma0*sin(theta0)
                     if (thetaprime0.gt.1.0) then
                        thetaprime0=theta0+pi/2.0
                     else
                        thetaprime0=theta0+asin(thetaprime0)
                     endif
                     sign=1.0
                  elseif (en(i).lt.enequal0) then
                     thetaprime0=gamma0*sin(theta0)
                     if (thetaprime0.gt.1.0) then
                        thetaprime0=theta0+pi/2.0
                     else
                        thetaprime0=pi+theta0-asin(thetaprime0)
                     endif
                     sign=-1.0
                  endif
               endif
               dsigma=dsigma0ep*(a0ep+a1ep*cos(thetaprime0)+
     +                 a2ep*0.5*(3.0*(cos(thetaprime0))**2-1.0)+
     +                 a3ep*0.5*(5.0*(cos(thetaprime0))**3-3.0*
     +                 cos(thetaprime0)))
*
*     product2 = dompdom * depden
*
               product2=(mbe+mn)**2*(xi+sign*cos(theta0))*gamma0*
     +                  ep0/(mp*mn*ep0*xi*(cos(theta0)+sign*xi)+
     +                  sign*mbe*(mbe+mn-mp)*eth)
               x=6.0*sqrt(1.0-eth/ep0)
*
*     product3 = dtheta(theoretical) * dompdom * depden
*
               product3=164.9127*sqrt(mp*mn/mbe/(mbe+mn-mp))*6.0/ep0/
     +                 (1.0+x)**2*(xi+sign*cos(theta0))*(mbe+mn)**2*
     +                  ep0/(mp*mn*ep0*xi*(cos(theta0)+sign*xi)+
     +                  sign*mbe*(mbe+mn-mp)*eth)
*
               if (ep0.lt.eptable(1)) then
                  yield0=product3
               else
                  yield0=product2*dsigma
               endif
               yield0=yield0*real(mult)*li7fraction*cm2mb*
     +                   na/aeff/elec/1000.0/s0
               do 2200 j=1,thetaint
                  if (yield(j,i).ne.0.0.and.yield(j+1,i).eq.0.0) then
                     nmax=j
                  endif
2200              continue
*
* Angular integration will be performed over the range
* (0-theta(nmax) degrees).  For trapezoidal integration,
*
```

```
* dyden(i)=0.5*anglewidth*(2*pi)*[sin(theta(1))*yield(1,i) +
*          sin(theta(nmax)*yield(nmax,i) +
*          2 * sum_j=2 ^j=nmax-1{sin(theta(j)*yield(j,i)}]
*
* However, sin(theta(1))=0, so only the last term and
* sum remain and
*
* dyden(i)=pi*anglewidth*[2 * sum_j=2 ^j=nmax-1
*          {sin(theta(j)*yield(j,i)} +
*          sin(theta(nmax)*yield(nmax,i)]
*
* Note that nmax changes for each En(i).
*
                do 2300 j=2,nmax-1
                   dyden(i)=dyden(i)+2.0*sin(theta(j))*yield(j,i)
2300            continue
                dyden(i)=dyden(i)+sin(theta(nmax))*yield(nmax,i)
                dyden(i)=dyden(i)*pi*(pi*anglewidth/180.0)
                dyden(i)=dyden(i)+pi*(theta0-theta(nmax))*
     +                   (sin(theta0)*yield0+sin(theta(nmax))*
     +                   yield(nmax,i))
             endif
          endif
3000    continue
*
************************************************************
*
* NEUTRON ANGULAR DISTRIBUTION
*
************************************************************
*
* This section determines the neutron angular distribution
* dY/dOmega (neutrons/sec-sr-mA).  It is the integral
* of yield over En.  The lower boundary of integration
* is either En=0 or is determined by ep0; the upper
* boundary of integration is always determined by ep0.
* This section uses the same s0, dsigma0ep, a0ep, a1ep,
* a2ep, and a3ep values based on ep0 that were calculated
* in the previous section.
*
************************************************************
*
        do 4000 i=1,thetaint+1
           dydom(i)=0.0
           if (gamma0.lt.1.0) then
              enmax0=(sqrt(mp*mn*ep0)*cos(theta(i))+sqrt(mp*mn*ep0*
     +               (cos(theta(i)))**2+(mbe+mn)*((mbe-mp)*ep0+
     +               mbe*q)))**2/(mbe+mn)**2
              xi=(1.0/gamma0**2-(sin(theta(i)))**2)
              if (xi.lt.0.0) then
                 xi=0.0
              else
                 xi=sqrt(xi)
              endif
```

```
              thetaprime0=theta(i)+asin(gamma0*sin(theta(i)))
              sign=1.0
              dsigma=dsigma0ep*(a0ep+a1ep*cos(thetaprime0)+
     +               a2ep*0.5*(3.0*(cos(thetaprime0))**2-1.0)+
     +               a3ep*0.5*(5.0*(cos(thetaprime0))**3-3.0*
     +               cos(thetaprime0)))
*
*     product2 = dompdom * depden
*
              product2=(mbe+mn)**2*(xi+sign*cos(theta(i)))*gamma0*
     +                 ep0/(mp*mn*ep0*xi*(cos(theta(i))+sign*xi)+
     +                 sign*mbe*(mbe+mn-mp)*eth)
              x=6.0*sqrt(1.0-eth/ep0)
*
*     product3 = dtheta(theoretical) * dompdom * depden
*
              product3=164.9127*sqrt(mp*mn/mbe/(mbe+mn-mp))*6.0/ep0/
     +                 (1.0+x)**2*(xi+sign*cos(theta(i)))*
     +                 (mbe+mn)**2*ep0/(mp*mn*ep0*xi*(cos(theta(i))+
     +                 sign*xi)+sign*mbe*(mbe+mn-mp)*eth)
*
              if (ep0.lt.eptable(1)) then
                 yield0=product3
              else
                 yield0=product2*dsigma
              endif
                 yield0=yield0*real(mult)*li7fraction*cm2mb*
     +                  na/aeff/elec/1000.0/s0
              do 3200 j=1,enint
                 if (yield(i,j).ne.0.0.and.yield(i,j+1).eq.0.0) then
                    nmax=j
                 endif
3200          continue
*
* Energy integration will be performed over the range
* (0-En(nmax) keV).  For trapezoidal integration,
*
* dydom(i)=0.5*deltaen*[yield(i,1) + yield(i,nmax) +
*          2 * sum_j=2 ^j=nmax-1 {yield(i,j)}]
*
* However, yield(i,1)=0, so only the last term and
* sum remain.  Adding the contribution from En(nmax) to Enmax0
* gives
*
* dydom(i)=0.5*deltaen*[2 * sum_j=2 ^j=nmax-1 {yield(i,j)} +
*          yield(i,nmax)] + 0.5*(enmax0-en(nmax))*[yield0 +
*          yield(i,nmax)]
*
* Note that nmax changes for each theta(i).
*
              do 3300 j=2,nmax-1
                 dydom(i)=dydom(i)+2.0*yield(i,j)
3300          continue
              dydom(i)=dydom(i)+yield(i,nmax)
```

```
               dydom(i)=dydom(i)*0.5*deltaen
               dydom(i)=dydom(i)+0.5*(enmax0-en(nmax))*
     +                   (yield0+yield(i,nmax))
               dydom(i)=1000.0*dydom(i)
*
            elseif (gamma0.ge.1.0) then
               thetamax=asin(1.0/gamma0)
               if (theta(i).ge.thetamax) then
                  dydom(i)=0.0
               else
                  enmax0=(sqrt(mp*mn*ep0)*cos(theta(i))+sqrt(mp*mn*ep0*
     +                  (cos(theta(i)))**2+(mbe+mn)*((mbe-mp)*ep0+
     +                  mbe*q)))**2/(mbe+mn)**2
                  enmin0=(sqrt(mp*mn*ep0)*cos(theta(i))-sqrt(mp*mn*ep0*
     +                  (cos(theta(i)))**2+(mbe+mn)*((mbe-mp)*ep0+
     +                  mbe*q)))**2/(mbe+mn)**2
                  xi=(1.0/gamma0**2-(sin(theta(i)))**2)
                  if (xi.lt.0.0) then
                     xi=0.0
                  else
                     xi=sqrt(xi)
                  endif
                  thetaprime0=theta(i)+asin(gamma0*sin(theta(i)))
                  thetaprimemin0=pi+theta(i)-asin(gamma0*sin(theta(i)))
*
* thetaprime0 --> sign=1.0 --> calculate yield0
*
                  dsigma=dsigma0ep*(a0ep+a1ep*cos(thetaprime0)+
     +                  a2ep*0.5*(3.0*(cos(thetaprime0))**2-1.0)+
     +                  a3ep*0.5*(5.0*(cos(thetaprime0))**3-3.0*
     +                  cos(thetaprime0)))
*
*     product2 = dompdom * depden
*
                  product2=(mbe+mn)**2*(xi+cos(theta(i)))*gamma0*
     +                    ep0/(mp*mn*ep0*xi*(cos(theta(i))+xi)+
     +                    mbe*(mbe+mn-mp)*eth)
                  x=6.0*sqrt(1.0-eth/ep0)
*
*     product3 = dtheta(theoretical) * dompdom * depden
*
                  product3=164.9127*sqrt(mp*mn/mbe/(mbe+mn-mp))*6.0/ep0/
     +                    (1.0+x)**2*(xi+cos(theta(i)))*
     +                    (mbe+mn)**2*ep0/(mp*mn*ep0*xi*(cos(theta(i))+
     +                    xi)+mbe*(mbe+mn-mp)*eth)
*
                  if (ep0.lt.eptable(1)) then
                     yield0=product3
                  else
                     yield0=product2*dsigma
                  endif
                  yield0=yield0*real(mult)*li7fraction*cm2mb*
     +                  na/aeff/elec/1000.0/s0
*
```

```
* thetaprimemin0 --> sign=-1.0 --> calculate yieldmin0
*
                  dsigma=dsigma0ep*(a0ep+a1ep*cos(thetaprimemin0)+
     +                   a2ep*0.5*(3.0*(cos(thetaprimemin0))**2-1.0)+
     +                   a3ep*0.5*(5.0*(cos(thetaprimemin0))**3-3.0*
     +                   cos(thetaprimemin0)))
*
*     product2 = dompdom * depden
*
                  product2=(mbe+mn)**2*(xi-cos(theta(i)))*gamma0*
     +                    ep0/(mp*mn*ep0*xi*(cos(theta(i))-xi)-
     +                    mbe*(mbe+mn-mp)*eth)
                  x=6.0*sqrt(1.0-eth/ep0)
*
*     product3 = dtheta(theoretical) * dompdom * depden
*
                  product3=164.9127*sqrt(mp*mn/mbe/(mbe+mn-mp))*6.0/ep0/
     +                    (1.0+x)**2*(xi-cos(theta(i)))*
     +                    (mbe+mn)**2*ep0/(mp*mn*ep0*xi*(cos(theta(i))-
     +                    xi)-mbe*(mbe+mn-mp)*eth)
*
                  if (ep0.lt.eptable(1)) then
                     yieldmin0=product3
                  else
                     yieldmin0=product2*dsigma
                  endif
                  yieldmin0=yieldmin0*real(mult)*li7fraction*cm2mb*
     +                   na/aeff/elec/1000.0/s0
                  do 3600 j=1,enint
                     if (yield(i,j).ne.0.0.and.yield(i,j+1).eq.0.0) then
                        nmax=j
                     endif
3600              continue
*
                  do 3700 j=2,enint+1
                     if (yield(i,j-1).eq.0.0.and.yield(i,j).ne.0.0) then
                        nmin=j
                     endif
3700              continue
*
* Energy integration will be performed over the range
* (En(nmin)-En(nmax) keV).  For trapezoidal integration,
*
* dydom(i)=0.5*deltaen*[yield(i,nmin) + yield(i,nmax) +
*          2 * sum_j=nmin+1 ^j=nmax-1 {yield(i,j)}]
*
* Adding the contribution from Enmin0 to En(nmin) and
* En(nmax) to Enmax0 gives
*
* dydom(i)=0.5*deltaen*[yield(i,nmin) + yield(i,nmax) +
*          2 * sum_j=nmin+1 ^j=nmax-1 {yield(i,j)}] +
*          0.5*(en(nmin)-enmin0)*[yieldmin0 + yield(i,nmin)] +
*          0.5*(enmax0-en(nmax))*[yield0 + yield(i,nmax)]
*
```

```
* Note that nmin and nmax change for each theta(i).
*
                do 3800 j=nmin+1,nmax-1
                   dydom(i)=dydom(i)+2.0*yield(i,j)
3800            continue
                dydom(i)=dydom(i)+yield(i,nmax)+yield(i,nmin)
                dydom(i)=dydom(i)*0.5*deltaen
                dydom(i)=dydom(i)+0.5*(enmax0-en(nmax))*
     +                   (yield0+yield(i,nmax))+0.5*(en(nmin)-enmin0)*
     +                   (yieldmin0+yield(i,nmin))
                dydom(i)=1000.0*dydom(i)
             endif
          endif
4000    continue
*
*******************************************************
*
* Write file containing the incident proton energy,
* 25 neutron energy bin boundaries, and yields
* in each coarse bin.  This output has the form
*       of an M-file that can be used in Matlab.
*
*******************************************************
*
        open (unit=13,file='liyield.m',status='unknown')
        do 4050 k=1,enint+1
           write (13,9000) k,en(k)
4050    continue
        do 4075 i=1,thetaint+1
           write (13,9100) i,theta(i)*180.0/pi
4075    continue
        do 5000 i=1,thetaint+1
           do 4095 k=1,enint+1
              write (13,9200) i,k,yield(i,k)
4095       continue
5000    continue
        do 6000 i=1,enint+1
           write (13,9300) i,dyden(i)
6000    continue
        do 7000 i=1,thetaint+1
           write (13,9400) i,dydom(i)
7000    continue
        write (13,*)
        close (unit=13)
9000    format(1x,'en(',i3,')=',f9.4,';')
9100    format(1x,'theta(',i3,')=',f6.2,';')
9200    format(1x,'yield(',i3,',',i3,')=',e13.5,';')
9300    format(1x,'dyden(',i3,')=',e13.5,';')
9400    format(1x,'dydom(',i3,')=',e13.5,';')
*
        print*
        print*, 'Program is finished.'
9900    end
```

```
        subroutine stoppingpower(ep,s)
*
*******************************************************
*
*     This subroutine calculates the stopping power in
*     Li metal for a given proton energy Ep
*
*******************************************************
*
        real a,b,a0,a1,a2,a3,a4,ep,beta,mp,epk,sum,s
*
        mp=938.2800         ! rest mass of proton (MeV)
        a=0.1328499         ! These are parameters used in
        b=2.147e4           !  calculating the stopping
        a0=-0.5831          !  power of protons in Li metal
        a1=0.562
        a2=-0.1183
        a3=0.009298
        a4=-0.0002498
*
        beta=sqrt(1.0-(1.0/(1.0+(ep/mp))**2))  ! beta=v/c
        epk=ep*1000               ! epk=proton kinetic energy in keV
        sum=a0+a1*log(epk)+a2*(log(epk))**2+
     +         a3*(log(epk))**3+a4*(log(epk))**4
        s=a*(log(b*beta**2/(1.0-beta**2))-beta**2-sum)/beta**2
        return
        end


        subroutine stoppingpowerlih(ep,s)
*
*******************************************************
*
*     This subroutine calculates the stopping power in
*     LiH for a given proton energy Ep; the tabulated
*     values for Li and H are taken from Janni,
*     At. Nuc. Data Tables, vol. 27, pp.147-339 (1982).
*
*******************************************************
*
        real ep,e0(10),s0(10),e0min,e0max,s0min,s0max,s
*
        e0(1)=1.75          ! These are the proton energy
        s0(1)=185.20        !  values and their corresponding
        e0(2)=2.00          !  stopping powers for LiH, in
        s0(2)=166.96        !  MeV-cm**2/g, calculated from
        e0(3)=2.25          !  tabulated Li and H data
        s0(3)=152.27
        e0(4)=2.50
        s0(4)=140.16
        e0(5)=2.75
        s0(5)=129.99
        e0(6)=3.00
```

```
      s0(6)=121.30
      e0(7)=3.50
      s0(7)=107.26
      e0(8)=4.00
      s0(8)=96.349
      e0(9)=4.50
      s0(9)=87.612
      e0(10)=5.00
      s0(10)=80.445
*
      do 50 j=1,9
         if (ep.gt.e0(j).and.ep.le.e0(j+1)) then
            e0min=e0(j)
            e0max=e0(j+1)
            s0min=s0(j)
            s0max=s0(j+1)
         endif
 50   continue
      s=(s0max-s0min)*(ep-e0min)/(e0max-e0min)+s0min
      return
      end


      subroutine stoppingpowerli2o(ep,s)
*
*****************************************************
*
*     This subroutine calculates the stopping power in
*     Li2O for a given proton energy Ep; the tabulated
*     values for Li and O are taken from Janni,
*     At. Nuc. Data Tables, vol. 27, pp.147-339 (1982).
*
*****************************************************
*
      real ep,e0(10),s0(10),e0min,e0max,s0min,s0max,s
*
      e0(1)=1.75          ! These are the proton energy
      s0(1)=143.85        !  values and their corresponding
      e0(2)=2.00          !  stopping powers for Li2O, in
      s0(2)=130.49        !  MeV-cm**2/g, calculated from
      e0(3)=2.25          !  tabulated Li and O data
      s0(3)=119.66
      e0(4)=2.50
      s0(4)=110.67
      e0(5)=2.75
      s0(5)=103.07
      e0(6)=3.00
      s0(6)=96.540
      e0(7)=3.50
      s0(7)=85.895
      e0(8)=4.00
      s0(8)=77.555
      e0(9)=4.50
      s0(9)=70.828
```

```
        e0(10)=5.00
        s0(10)=65.273
*
        do 50 j=1,9
           if (ep.gt.e0(j).and.ep.le.e0(j+1)) then
              e0min=e0(j)
              e0max=e0(j+1)
              s0min=s0(j)
              s0max=s0(j+1)
           endif
 50     continue
        s=(s0max-s0min)*(ep-e0min)/(e0max-e0min)+s0min
        return
        end


        subroutine stoppingpowerlioh(ep,s)
*
*******************************************************
*
*     This subroutine calculates the stopping power in
*     LiOH for a given proton energy Ep; the tabulated
*     values for Li, H, and O are taken from Janni,
*     At. Nuc. Data Tables, vol. 27, pp.147-339 (1982).
*
*******************************************************
*
        real ep,e0(10),s0(10),e0min,e0max,s0min,s0max,s
*
        e0(1)=1.75          ! These are the proton energy
        s0(1)=154.07        !  values and their corresponding
        e0(2)=2.00          !  stopping powers for LiOH, in
        s0(2)=139.78        !  MeV-cm**2/g, calculated from
        e0(3)=2.25          !  tabulated Li, H, and O data
        s0(3)=128.18
        e0(4)=2.50
        s0(4)=118.56
        e0(5)=2.75
        s0(5)=110.43
        e0(6)=3.00
        s0(6)=103.44
        e0(7)=3.50
        s0(7)=92.033
        e0(8)=4.00
        s0(8)=83.118
        e0(9)=4.50
        s0(9)=75.916
        e0(10)=5.00
        s0(10)=69.967
*
        do 50 j=1,9
           if (ep.gt.e0(j).and.ep.le.e0(j+1)) then
              e0min=e0(j)
              e0max=e0(j+1)
```

```
            s0min=s0(j)
            s0max=s0(j+1)
         endif
 50      continue
         s=(s0max-s0min)*(ep-e0min)/(e0max-e0min)+s0min
         return
         end


         subroutine stoppingpowerli3n(ep,s)
*
*********************************************************
*
*     This subroutine calculates the stopping power in
*     Li3N for a given proton energy Ep; the tabulated
*     values for Li and N are taken from Janni,
*     At. Nuc. Data Tables, vol. 27, pp.147-339 (1982).
*
*********************************************************
*
         real ep,e0(10),s0(10),e0min,e0max,s0min,s0max,s
*
         e0(1)=1.75          ! These are the proton energy
         s0(1)=148.05        !  values and their corresponding
         e0(2)=2.00          !  stopping powers for Li3N, in
         s0(2)=134.13        !  MeV-cm**2/g, calculated from
         e0(3)=2.25          !  tabulated Li and N data
         s0(3)=122.83
         e0(4)=2.50
         s0(4)=113.47
         e0(5)=2.75
         s0(5)=105.56
         e0(6)=3.00
         s0(6)=98.777
         e0(7)=3.50
         s0(7)=88.066
         e0(8)=4.00
         s0(8)=79.120
         e0(9)=4.50
         s0(9)=72.171
         e0(10)=5.00
         s0(10)=66.440
*
         do 50 j=1,9
            if (ep.gt.e0(j).and.ep.le.e0(j+1)) then
               e0min=e0(j)
               e0max=e0(j+1)
               s0min=s0(j)
               s0max=s0(j+1)
            endif
 50      continue
         s=(s0max-s0min)*(ep-e0min)/(e0max-e0min)+s0min
         return
         end
```

```
        subroutine stoppingpowerlif(ep,s)
*
*******************************************************
*
*     This subroutine calculates the stopping power in
*     LiF for a given proton energy Ep; the tabulated
*     values for Li and F are taken from Janni,
*     At. Nuc. Data Tables, vol. 27, pp.147-339 (1982).
*
*******************************************************
*
        real ep,e0(10),s0(10),e0min,e0max,s0min,s0max,s
*
        e0(1)=1.75          ! These are the proton energy
        s0(1)=134.19        !  values and their corresponding
        e0(2)=2.00          !  stopping powers for LiF, in
        s0(2)=122.02        !  MeV-cm**2/g, calculated from
        e0(3)=2.25          !  tabulated Li and F data
        s0(3)=112.05
        e0(4)=2.50
        s0(4)=103.76
        e0(5)=2.75
        s0(5)=96.743
        e0(6)=3.00
        s0(6)=90.722
        e0(7)=3.50
        s0(7)=80.880
        e0(8)=4.00
        s0(8)=73.149
        e0(9)=4.50
        s0(9)=66.896
        e0(10)=5.00
        s0(10)=61.723
*
        do 50 j=1,9
           if (ep.gt.e0(j).and.ep.le.e0(j+1)) then
              e0min=e0(j)
              e0max=e0(j+1)
              s0min=s0(j)
              s0max=s0(j+1)
           endif
 50     continue
        s=(s0max-s0min)*(ep-e0min)/(e0max-e0min)+s0min
        return
        end



        subroutine interpolate(hk,ix,fmin,fmax,fsmin,fsmax,f)
*
*****************************************************************
*                                                               *
```

```
*     This subroutine interpolates the value of f for the energy    *
*     value specified in ix on the interval hk, given the tabulated *
*     endpoint f values (fmin and fmax) and first derivatives of f  *
*     at the endpoints (fsmin and fsmax) using cubic splines values *
*     taken from newnewnewsigmaspline.dat.                          *
*                                                                   *
*********************************************************************
*
        real hk,ix,b0,b1,b2,b3,fmin,fmax,fsmin,fsmax,f
*
        b0=fmin
        b1=fsmin
        b2=3.0*(fmax-fmin)/hk**2-(2.0*fsmin+fsmax)/hk
        b3=2.0*(fmin-fmax)/hk**3+(fsmin+fsmax)/hk**2
        f=b0+b1*ix+b2*ix**2+b3*ix**3
        return
        end
```

Appendix B

Tabulated (p,n) Cross Section Coefficients (`sigmafile`)

This file is ordered as follows:

- Column 1: Proton LAB Energy (MeV)
- Column 2: (p,n) 0° CM Cross Section (mb)
- Column 3: CM Legendre Coefficient $A_0(E_p)$
- Column 4: CM Legendre Coefficient $A_1(E_p)$
- Column 5: CM Legendre Coefficient $A_2(E_p)$
- Column 6: CM Legendre Coefficient $A_3(E_p)$

These cross section parameters are used by `li.f` to calculate the CM differential (p,n) cross section using Eq. 2.14 in Chapter 2.

```
1.9245512 21.375 1.000  0.000 0.000  0.000
1.950     19.0   1.125 -0.125 0.000  0.000
2.000     15.0   1.425 -0.430 0.005  0.000
2.050     12.1   1.805 -0.825 0.020  0.000
2.100     13.1   1.810 -0.845 0.035  0.000
2.150     22.6   1.380 -0.435 0.055  0.000
2.200     46.7   0.815  0.110 0.075  0.000
```

2.250	79.2	0.585	0.330	0.085	0.000
2.300	83.4	0.475	0.430	0.095	0.000
2.350	71.4	0.460	0.440	0.100	0.000
2.400	61.2	0.445	0.445	0.110	0.000
2.450	53.0	0.465	0.420	0.115	0.000
2.500	47.4	0.490	0.400	0.110	0.000
2.600	40.5	0.545	0.350	0.105	0.000
2.700	36.0	0.585	0.320	0.095	0.000
2.800	34.2	0.590	0.330	0.080	0.000
2.900	33.0	0.580	0.350	0.070	0.000
3.000	32.0	0.575	0.365	0.060	0.000
3.100	31.2	0.580	0.360	0.060	0.000
3.200	30.5	0.585	0.355	0.060	0.000
3.300	29.9	0.590	0.345	0.065	0.000
3.400	29.3	0.600	0.330	0.070	0.000
3.500	28.7	0.620	0.305	0.075	0.000
3.600	28.2	0.640	0.295	0.080	-0.015
3.700	27.8	0.660	0.285	0.095	-0.040
3.800	27.4	0.685	0.275	0.105	-0.065
3.900	27.0	0.710	0.250	0.125	-0.085
4.000	26.7	0.730	0.225	0.145	-0.100
4.100	27.1	0.740	0.210	0.175	-0.125
4.200	28.2	0.740	0.200	0.210	-0.150
4.300	30.0	0.720	0.190	0.260	-0.170
4.400	32.2	0.705	0.180	0.295	-0.180
4.500	34.6	0.685	0.165	0.320	-0.170
4.600	37.5	0.660	0.155	0.340	-0.155
4.700	41.1	0.630	0.140	0.355	-0.125
4.800	44.8	0.605	0.130	0.360	-0.095
4.900	48.1	0.590	0.115	0.365	-0.070
5.000	50.0	0.590	0.090	0.365	-0.045

Appendix C

Tabulated Spline Coefficients (`sigmaspline`)

This file is used by `li.f` to interpolate between tabulated values of the (p,n) cross section parameters defined in Eq. 2.14 using natural cubic splines. This file is organized as follows:

- Column 1: Proton LAB Energy (MeV)
- Column 2: (p,n) 0° CM Cross Section (mb)
- Column 3: CM Legendre Coefficient $A_0(E_p)$
- Column 4: CM Legendre Coefficient $A_1(E_p)$
- Column 5: CM Legendre Coefficient $A_2(E_p)$
- Column 6: CM Legendre Coefficient $A_3(E_p)$

These parameters are used by the `interpolate` subroutine of the `li.f` program.

```
1.9245e+00  0.0000e+00  0.0000e+00  0.0000e+00  0.0000e+00  0.0000e+00
1.9500e+00 -1.0943e+01 -1.2239e+02 -6.7114e+00  1.3698e-02  2.4619e-14
2.0000e+00  6.4873e+01 -6.4365e+01 -7.4560e+00  2.1877e-01 -1.4597e-13
2.0500e+00  1.0242e+02 -3.4146e+01 -5.4642e+00  3.1119e-01  5.5929e-13
2.1000e+00  1.2867e+03  8.6951e+01  4.4129e+00  3.3643e-01 -2.0911e-12
```

2.1500e+00	1.7985e+03	3.1633e+02	1.1212e+01	4.4306e-01	7.8054e-12
2.2000e+00	2.3383e+03	6.6369e+02	8.0374e+00	2.9130e-01	-2.9130e-11
2.2500e+00	2.6627e+02	4.2488e+02	2.5376e+00	1.9170e-01	1.0871e-10
2.3000e+00	-2.2314e+03	-1.6124e+02	1.0119e+00	1.4189e-01	-4.0573e-10
2.3500e+00	-1.5103e+03	-2.4790e+02	1.4496e-02	1.4073e-01	1.5142e-09
2.4000e+00	-1.0623e+03	-1.7914e+02	-1.6995e-01	1.9515e-01	-5.6511e-09
2.4500e+00	-4.2222e+02	-1.3951e+02	-5.3468e-01	-2.1364e-02	2.1090e-08
2.5000e+00	-2.7071e+02	-9.0796e+01	-3.9131e-01	-1.0969e-01	-7.8711e-08
2.6000e+00	-1.0593e+02	-5.5192e+01	-4.8275e-01	-4.9077e-02	4.3008e-07
2.7000e+00	-1.2212e+02	-3.0433e+01	-7.7677e-02	-1.4399e-01	-1.6416e-06
2.8000e+00	-1.1978e+02	-1.2072e+01	1.9346e-01	-1.2495e-01	6.1364e-06
2.9000e+00	-1.2255e+02	-1.1276e+01	2.0383e-01	-1.0620e-01	-2.2904e-05
3.0000e+00	-6.0291e+01	-8.8212e+00	4.1197e-02	-5.0241e-02	8.5479e-05
3.1000e+00	-2.9859e+01	-7.4384e+00	-6.8626e-02	7.1666e-03	-3.1901e-04
3.2000e+00	-3.0442e+01	-6.4249e+00	-6.6692e-02	2.1574e-02	1.1905e-03
3.3000e+00	-1.9901e+01	-5.8618e+00	-1.1460e-01	5.6535e-02	-4.4433e-03
3.4000e+00	1.1086e+01	-6.1277e+00	-2.2489e-01	5.2283e-02	1.6582e-02
3.5000e+00	3.3233e+01	-5.6271e+00	-1.8582e-01	3.4329e-02	-6.1887e-02
3.6000e+00	3.2412e+01	-4.3634e+00	-8.1794e-02	1.1039e-01	-2.1903e-01
3.7000e+00	4.5969e+01	-3.9188e+00	-8.6994e-02	1.2407e-01	-2.6198e-01
3.8000e+00	5.5521e+01	-3.9609e+00	-1.7022e-01	1.4328e-01	-2.3304e-01
3.9000e+00	4.1831e+01	-4.2372e+00	-2.8210e-01	2.0278e-01	-1.5583e-01
4.0000e+00	4.9339e+01	-8.9991e-02	-2.0136e-01	2.4557e-01	-1.9360e-01
4.1000e+00	9.4071e+01	7.5972e+00	-1.1242e-01	3.1492e-01	-2.6975e-01
4.2000e+00	9.3490e+01	1.4701e+01	-9.8939e-02	4.4472e-01	-2.2736e-01
4.3000e+00	1.1479e+02	2.0598e+01	-9.1818e-02	4.5616e-01	-1.7076e-01
4.4000e+00	1.3836e+02	2.2905e+01	-1.3378e-01	2.8061e-01	1.0444e-02
4.5000e+00	1.2382e+02	2.5781e+01	-1.2303e-01	2.2136e-01	1.2899e-01
4.6000e+00	1.3881e+02	3.2970e+01	-1.2407e-01	1.8391e-01	2.2358e-01
4.7000e+00	1.4729e+02	3.7337e+01	-1.3065e-01	9.2971e-02	3.2666e-01
4.8000e+00	1.5943e+02	3.6678e+01	-1.0328e-01	4.4200e-02	2.6974e-01
4.9000e+00	1.5215e+02	2.5949e+01	-2.0620e-01	3.0228e-02	2.4435e-01

Appendix D

Example MCNP Input

```
Phantom dosimetry for BNCT (1.95 MeV protons) with 5 cm H2O
1    0              1   -2   -20       imp:n=1 imp:p=1
2    1    -3.965    1   -2    20  -18  imp:n=1 imp:p=1
3    1    -3.965    2   -3    19  -18  imp:n=1 imp:p=1
4    2    -1.000    2   -3   -19       imp:n=1 imp:p=1
5    0              3   -4   -18       imp:n=1 imp:p=1
6    3    -1.047    4   -5   -21       imp:n=1 imp:p=1
7    3    -1.047    5   -6   -21       imp:n=1 imp:p=1
8    3    -1.047    6   -7   -21       imp:n=1 imp:p=1
9    3    -1.047    7   -8   -21       imp:n=1 imp:p=1
10   3    -1.047    8   -9   -21       imp:n=1 imp:p=1
11   3    -1.047    9  -10   -21       imp:n=1 imp:p=1
12   3    -1.047   10  -11   -21       imp:n=1 imp:p=1
13   3    -1.047   11  -12   -21       imp:n=1 imp:p=1
14   3    -1.047   12  -13   -21       imp:n=1 imp:p=1
15   3    -1.047   13  -14   -21       imp:n=1 imp:p=1
16   3    -1.047   14  -15   -21       imp:n=1 imp:p=1
17   3    -1.047   15  -16   -21       imp:n=1 imp:p=1
18   3    -1.047   16  -17   -21       imp:n=1 imp:p=1
19   0             -1                 imp:n=0 imp:p=0
20   0              4  -17    21  -18  imp:n=1 imp:p=1
21   0             17                 imp:n=0 imp:p=0
22   0              1  -17    18       imp:n=0 imp:p=0

1    pz       0
2    pz      18
3    pz      23
4    pz      24
5    pz      25
6    pz      26
7    pz      27
8    pz      28
9    pz      29
10   pz      30
11   pz      31
```

```
12   pz      32
13   pz      33
14   pz      34
15   pz      36
16   pz      38
17   pz      40
18   cz      30
19   cz      12
20   cz       2
21   cz       8
23   cz       1
26   cz       3
27   cz       4
28   cz       5
29   cz       6
30   cz       7

m1   13027.50c     2       8016.50c    3
m2    1001.50c     2       8016.50c    1
mt2   lwtr.01t
m3    1001.50c    -.1057
      6000.50c    -.1397
      7014.50c    -.0184
      8016.50c    -.7259
     11023.50c    -.0014
     15031.50c    -.0039
     17000.50c    -.0014
     19000.50c    -.0039
mt3   lwtr.01t
c
c   Source multiplier for yield in n/sec/mA=0.62029E+11
sdef sur=2   pos=0 0 18
     erg=d2  vec=0 0 1    dir=ferg d3
si2  h   0.00000  0.01000  0.02000  0.03000  0.04000  0.05000  0.06000
         0.07000  0.08000  0.09000  0.10000  0.11000  0.12000  0.13000
         0.14000  0.15000  0.16000  0.17000
sp2  d   0.00000  0.06691  0.09731  0.10660  0.10682  0.10068  0.09212
         0.08284  0.07344  0.06403  0.05483  0.04590  0.03741  0.02886
         0.02102  0.01370  0.00669  0.00086
ds3  s   4 5 6 7 8 9 10 11 12 13 14 15 16 17 18 19 20
si4  h  -1.00000 -0.98481 -0.93969 -0.86603 -0.76604 -0.64279 -0.50000
        -0.34202 -0.17365  0.00000  0.17365  0.34202  0.50000  0.64279
         0.76604  0.86603  0.93969  0.98481  1.00000
sp4  d   0.00000E+00 0.10064E-03 0.29927E-03 0.49002E-03 0.91212E-03
         0.14681E-02 0.25070E-02 0.43766E-02 0.57148E-02 0.60600E-02
         0.63497E-02 0.65677E-02 0.66176E-02 0.64466E-02 0.60066E-02
         0.52495E-02 0.41384E-02 0.26728E-02 0.92737E-03
si5  h  -1.00000 -0.98481 -0.93969 -0.86603 -0.76604 -0.64279 -0.50000
        -0.34202 -0.17365  0.00000  0.17365  0.34202  0.50000  0.64279
         0.76604  0.86603  0.93969  0.98481  1.00000
sp5  d   0.00000E+00 0.00000E+00 0.00000E+00 0.00000E+00 0.00000E+00
         0.00000E+00 0.00000E+00 0.60457E-04 0.24962E-02 0.85225E-02
         0.10848E-01 0.11267E-01 0.11722E-01 0.11905E-01 0.11672E-01
         0.10847E-01 0.91910E-02 0.64145E-02 0.23625E-02
```

```
si6  h  -1.00000 -0.98481 -0.93969 -0.86603 -0.76604 -0.64279 -0.50000
        -0.34202 -0.17365  0.00000  0.17365  0.34202  0.50000  0.64279
         0.76604  0.86603  0.93969  0.98481  1.00000
sp6  d   0.00000E+00 0.00000E+00 0.00000E+00 0.00000E+00 0.00000E+00
         0.00000E+00 0.00000E+00 0.00000E+00 0.00000E+00 0.45773E-03
         0.95085E-02 0.13590E-01 0.14079E-01 0.14558E-01 0.14625E-01
         0.14055E-01 0.12503E-01 0.93951E-02 0.38258E-02
si7  h  -1.00000 -0.98481 -0.93969 -0.86603 -0.76604 -0.64279 -0.50000
        -0.34202 -0.17365  0.00000  0.17365  0.34202  0.50000  0.64279
         0.76604  0.86603  0.93969  0.98481  1.00000
sp7  d   0.00000E+00 0.00000E+00 0.00000E+00 0.00000E+00 0.00000E+00
         0.00000E+00 0.00000E+00 0.00000E+00 0.00000E+00 0.00000E+00
         0.91048E-03 0.13175E-01 0.15479E-01 0.15989E-01 0.16186E-01
         0.15704E-01 0.14136E-01 0.10780E-01 0.44548E-02
si8  h  -1.00000 -0.98481 -0.93969 -0.86603 -0.76604 -0.64279 -0.50000
        -0.34202 -0.17365  0.00000  0.17365  0.34202  0.50000  0.64279
         0.76604  0.86603  0.93969  0.98481  1.00000
sp8  d   0.00000E+00 0.00000E+00 0.00000E+00 0.00000E+00 0.00000E+00
         0.00000E+00 0.00000E+00 0.00000E+00 0.00000E+00 0.00000E+00
         0.00000E+00 0.42687E-02 0.16454E-01 0.16772E-01 0.16959E-01
         0.16409E-01 0.14645E-01 0.10904E-01 0.42684E-02
si9  h  -1.00000 -0.98481 -0.93969 -0.86603 -0.76604 -0.64279 -0.50000
        -0.34202 -0.17365  0.00000  0.17365  0.34202  0.50000  0.64279
         0.76604  0.86603  0.93969  0.98481  1.00000
sp9  d   0.00000E+00 0.00000E+00 0.00000E+00 0.00000E+00 0.00000E+00
         0.00000E+00 0.00000E+00 0.00000E+00 0.00000E+00 0.00000E+00
         0.00000E+00 0.00000E+00 0.11774E-01 0.17247E-01 0.17288E-01
         0.16606E-01 0.14611E-01 0.10593E-01 0.40046E-02
si10 h  -1.00000 -0.98481 -0.93969 -0.86603 -0.76604 -0.64279 -0.50000
        -0.34202 -0.17365  0.00000  0.17365  0.34202  0.50000  0.64279
         0.76604  0.86603  0.93969  0.98481  1.00000
sp10 d   0.00000E+00 0.00000E+00 0.00000E+00 0.00000E+00 0.00000E+00
         0.00000E+00 0.00000E+00 0.00000E+00 0.00000E+00 0.00000E+00
         0.00000E+00 0.00000E+00 0.32105E-02 0.17425E-01 0.17370E-01
         0.16539E-01 0.14348E-01 0.10183E-01 0.37689E-02
si11 h  -1.00000 -0.98481 -0.93969 -0.86603 -0.76604 -0.64279 -0.50000
        -0.34202 -0.17365  0.00000  0.17365  0.34202  0.50000  0.64279
         0.76604  0.86603  0.93969  0.98481  1.00000
sp11 d   0.00000E+00 0.00000E+00 0.00000E+00 0.00000E+00 0.00000E+00
         0.00000E+00 0.00000E+00 0.00000E+00 0.00000E+00 0.00000E+00
         0.00000E+00 0.00000E+00 0.00000E+00 0.12449E-01 0.17320E-01
         0.16337E-01 0.13997E-01 0.97728E-02 0.35667E-02
si12 h  -1.00000 -0.98481 -0.93969 -0.86603 -0.76604 -0.64279 -0.50000
        -0.34202 -0.17365  0.00000  0.17365  0.34202  0.50000  0.64279
         0.76604  0.86603  0.93969  0.98481  1.00000
sp12 d   0.00000E+00 0.00000E+00 0.00000E+00 0.00000E+00 0.00000E+00
         0.00000E+00 0.00000E+00 0.00000E+00 0.00000E+00 0.00000E+00
         0.00000E+00 0.00000E+00 0.00000E+00 0.43890E-02 0.17164E-01
         0.16067E-01 0.13621E-01 0.93896E-02 0.33930E-02
si13 h  -1.00000 -0.98481 -0.93969 -0.86603 -0.76604 -0.64279 -0.50000
        -0.34202 -0.17365  0.00000  0.17365  0.34202  0.50000  0.64279
         0.76604  0.86603  0.93969  0.98481  1.00000
sp13 d   0.00000E+00 0.00000E+00 0.00000E+00 0.00000E+00 0.00000E+00
         0.00000E+00 0.00000E+00 0.00000E+00 0.00000E+00 0.00000E+00
```

```
         0.00000E+00 0.00000E+00 0.00000E+00 0.43465E-04 0.13515E-01
         0.15739E-01 0.13247E-01 0.90395E-02 0.32425E-02
si14 h  -1.00000 -0.98481 -0.93969 -0.86603 -0.76604 -0.64279 -0.50000
        -0.34202 -0.17365  0.00000  0.17365  0.34202  0.50000  0.64279
         0.76604  0.86603  0.93969  0.98481  1.00000
sp14 d   0.00000E+00 0.00000E+00 0.00000E+00 0.00000E+00 0.00000E+00
         0.00000E+00 0.00000E+00 0.00000E+00 0.00000E+00 0.00000E+00
         0.00000E+00 0.00000E+00 0.00000E+00 0.00000E+00 0.58685E-02
         0.15317E-01 0.12880E-01 0.87214E-02 0.31105E-02
si15 h  -1.00000 -0.98481 -0.93969 -0.86603 -0.76604 -0.64279 -0.50000
        -0.34202 -0.17365  0.00000  0.17365  0.34202  0.50000  0.64279
         0.76604  0.86603  0.93969  0.98481  1.00000
sp15 d   0.00000E+00 0.00000E+00 0.00000E+00 0.00000E+00 0.00000E+00
         0.00000E+00 0.00000E+00 0.00000E+00 0.00000E+00 0.00000E+00
         0.00000E+00 0.00000E+00 0.00000E+00 0.00000E+00 0.35494E-03
         0.13161E-01 0.12468E-01 0.84320E-02 0.29937E-02
si16 h  -1.00000 -0.98481 -0.93969 -0.86603 -0.76604 -0.64279 -0.50000
        -0.34202 -0.17365  0.00000  0.17365  0.34202  0.50000  0.64279
         0.76604  0.86603  0.93969  0.98481  1.00000
sp16 d   0.00000E+00 0.00000E+00 0.00000E+00 0.00000E+00 0.00000E+00
         0.00000E+00 0.00000E+00 0.00000E+00 0.00000E+00 0.00000E+00
         0.00000E+00 0.00000E+00 0.00000E+00 0.00000E+00 0.00000E+00
         0.58821E-02 0.11955E-01 0.81375E-02 0.28889E-02
si17 h  -1.00000 -0.98481 -0.93969 -0.86603 -0.76604 -0.64279 -0.50000
        -0.34202 -0.17365  0.00000  0.17365  0.34202  0.50000  0.64279
         0.76604  0.86603  0.93969  0.98481  1.00000
sp17 d   0.00000E+00 0.00000E+00 0.00000E+00 0.00000E+00 0.00000E+00
         0.00000E+00 0.00000E+00 0.00000E+00 0.00000E+00 0.00000E+00
         0.00000E+00 0.00000E+00 0.00000E+00 0.00000E+00 0.00000E+00
         0.42357E-03 0.10059E-01 0.77651E-02 0.27738E-02
si18 h  -1.00000 -0.98481 -0.93969 -0.86603 -0.76604 -0.64279 -0.50000
        -0.34202 -0.17365  0.00000  0.17365  0.34202  0.50000  0.64279
         0.76604  0.86603  0.93969  0.98481  1.00000
sp18 d   0.00000E+00 0.00000E+00 0.00000E+00 0.00000E+00 0.00000E+00
         0.00000E+00 0.00000E+00 0.00000E+00 0.00000E+00 0.00000E+00
         0.00000E+00 0.00000E+00 0.00000E+00 0.00000E+00 0.00000E+00
         0.00000E+00 0.37367E-02 0.73334E-02 0.26253E-02
si19 h  -1.00000 -0.98481 -0.93969 -0.86603 -0.76604 -0.64279 -0.50000
        -0.34202 -0.17365  0.00000  0.17365  0.34202  0.50000  0.64279
         0.76604  0.86603  0.93969  0.98481  1.00000
sp19 d   0.00000E+00 0.00000E+00 0.00000E+00 0.00000E+00 0.00000E+00
         0.00000E+00 0.00000E+00 0.00000E+00 0.00000E+00 0.00000E+00
         0.00000E+00 0.00000E+00 0.00000E+00 0.00000E+00 0.00000E+00
         0.00000E+00 0.22569E-04 0.42020E-02 0.24621E-02
si20 h  -1.00000 -0.98481 -0.93969 -0.86603 -0.76604 -0.64279 -0.50000
        -0.34202 -0.17365  0.00000  0.17365  0.34202  0.50000  0.64279
         0.76604  0.86603  0.93969  0.98481  1.00000
sp20 d   0.00000E+00 0.00000E+00 0.00000E+00 0.00000E+00 0.00000E+00
         0.00000E+00 0.00000E+00 0.00000E+00 0.00000E+00 0.00000E+00
         0.00000E+00 0.00000E+00 0.00000E+00 0.00000E+00 0.00000E+00
         0.00000E+00 0.00000E+00 0.60527E-04 0.79793E-03
c
mode n p
c
```

```
f2:n     3
e2       4e-6  0.04  5
fs2    -19
c
*f12:n   3
e12      4e-6  0.04  5
fs12   -19
c
f22:n    3
e22      4e-6  0.04  5
fs22   -23 -20 -26 -27 -28 -29 -21 -19
c
*f32:n   3
e32      4e-6  0.04  5
fs32   -23 -20 -26 -27 -28 -29 -21 -19
c
f4:n     6 7 8 9 10 11 12 13 14 15 16 17 18
e4       4e-6  0.04  5
fs4    -23 -20 -26 -27 -28 -29 t
sd4   (3.141593E+00 9.424778E+00 1.570796E+01 2.199115E+01 2.827433E+01
       3.455752E+01 8.796459E+01 2.010619E+02)
      (3.141593E+00 9.424778E+00 1.570796E+01 2.199115E+01 2.827433E+01
       3.455752E+01 8.796459E+01 2.010619E+02)
      (3.141593E+00 9.424778E+00 1.570796E+01 2.199115E+01 2.827433E+01
       3.455752E+01 8.796459E+01 2.010619E+02)
      (3.141593E+00 9.424778E+00 1.570796E+01 2.199115E+01 2.827433E+01
       3.455752E+01 8.796459E+01 2.010619E+02)
      (3.141593E+00 9.424778E+00 1.570796E+01 2.199115E+01 2.827433E+01
       3.455752E+01 8.796459E+01 2.010619E+02)
      (3.141593E+00 9.424778E+00 1.570796E+01 2.199115E+01 2.827433E+01
       3.455752E+01 8.796459E+01 2.010619E+02)
      (3.141593E+00 9.424778E+00 1.570796E+01 2.199115E+01 2.827433E+01
       3.455752E+01 8.796459E+01 2.010619E+02)
      (3.141593E+00 9.424778E+00 1.570796E+01 2.199115E+01 2.827433E+01
       3.455752E+01 8.796459E+01 2.010619E+02)
      (3.141593E+00 9.424778E+00 1.570796E+01 2.199115E+01 2.827433E+01
       3.455752E+01 8.796459E+01 2.010619E+02)
      (6.283185E+00 1.884956E+01 3.141593E+01 4.398230E+01 5.654867E+01
       6.911504E+01 1.759292E+02 4.021239E+02)
      (6.283185E+00 1.884956E+01 3.141593E+01 4.398230E+01 5.654867E+01
       6.911504E+01 1.759292E+02 4.021239E+02)
      (6.283185E+00 1.884956E+01 3.141593E+01 4.398230E+01 5.654867E+01
       6.911504E+01 1.759292E+02 4.021239E+02)
de4    0.25300E-07 0.36000E-07 0.63000E-07 0.11000E-06 0.20000E-06
       0.36000E-06 0.63000E-06 0.11000E-05 0.20000E-05 0.36000E-05
       0.63000E-05 0.11000E-04 0.20000E-04 0.36000E-04 0.63000E-04
       0.11000E-03 0.20000E-03 0.36000E-03 0.63000E-03 0.11000E-02
       0.20000E-02 0.36000E-02 0.63000E-02 0.11000E-01 0.20000E-01
       0.36000E-01 0.63000E-01 0.82000E-01 0.86000E-01 0.90000E-01
       0.94000E-01 0.98000E-01 0.10500E+00 0.11500E+00 0.12500E+00
       0.13500E+00 0.14500E+00 0.15500E+00 0.16500E+00 0.17500E+00
       0.18500E+00 0.19500E+00 0.21000E+00 0.23000E+00 0.25000E+00
```

```
       0.27000E+00 0.29000E+00 0.31000E+00 0.33000E+00 0.35000E+00
       0.37000E+00 0.39000E+00 0.42000E+00 0.46000E+00 0.50000E+00
       0.54000E+00 0.58000E+00 0.62000E+00 0.66000E+00 0.70000E+00
       0.74000E+00 0.78000E+00 0.82000E+00 0.86000E+00 0.90000E+00
       0.94000E+00 0.98000E+00 0.10500E+01 0.11500E+01 0.12500E+01
       0.13500E+01 0.14500E+01 0.15500E+01 0.16500E+01 0.17500E+01
       0.18500E+01 0.19500E+01 0.21000E+01 0.23000E+01 0.25000E+01
       0.27000E+01 0.29000E+01 0.31000E+01 0.33000E+01 0.35000E+01
       0.37000E+01 0.39000E+01 0.42000E+01 0.46000E+01 0.50000E+01
       0.54000E+01 0.58000E+01 0.62000E+01 0.66000E+01 0.70000E+01
       0.74000E+01 0.78000E+01 0.82000E+01 0.86000E+01 0.90000E+01
       0.94000E+01 0.98000E+01 0.10500E+02 0.11500E+02 0.12500E+02
       0.13500E+02 0.14500E+02 0.15500E+02 0.16500E+02 0.17500E+02
       0.18500E+02 0.19500E+02 0.21000E+02 0.23000E+02 0.25000E+02
       0.27000E+02 0.29000E+02
df4    0.14906E-10 0.12626E-10 0.95326E-11 0.72163E-11 0.53570E-11
       0.39915E-11 0.30255E-11 0.22902E-11 0.17185E-11 0.13008E-11
       0.10200E-11 0.83822E-12 0.74959E-12 0.78283E-12 0.96992E-12
       0.13931E-11 0.22914E-11 0.39420E-11 0.67553E-11 0.11681E-10
       0.21001E-10 0.37503E-10 0.64423E-10 0.10871E-09 0.18933E-09
       0.31302E-09 0.48604E-09 0.57658E-09 0.60727E-09 0.62625E-09
       0.64523E-09 0.66321E-09 0.69460E-09 0.73741E-09 0.77801E-09
       0.81664E-09 0.85415E-09 0.88955E-09 0.92283E-09 0.95620E-09
       0.98633E-09 0.10165E-08 0.10608E-08 0.11171E-08 0.11662E-08
       0.12252E-08 0.12742E-08 0.13240E-08 0.13649E-08 0.14184E-08
       0.14663E-08 0.15349E-08 0.16689E-08 0.16906E-08 0.16548E-08
       0.17126E-08 0.17716E-08 0.18332E-08 0.18948E-08 0.19537E-08
       0.20022E-08 0.20624E-08 0.21142E-08 0.21695E-08 0.22364E-08
       0.23410E-08 0.25239E-08 0.25592E-08 0.25373E-08 0.26439E-08
       0.27315E-08 0.27787E-08 0.28538E-08 0.29648E-08 0.30038E-08
       0.31285E-08 0.31463E-08 0.32421E-08 0.32899E-08 0.34205E-08
       0.35717E-08 0.37110E-08 0.38390E-08 0.41820E-08 0.42670E-08
       0.43694E-08 0.43007E-08 0.44285E-08 0.44386E-08 0.46851E-08
       0.45749E-08 0.47860E-08 0.49020E-08 0.50300E-08 0.52379E-08
       0.55138E-08 0.54495E-08 0.54063E-08 0.55679E-08 0.56697E-08
       0.57173E-08 0.58403E-08 0.59787E-08 0.63920E-08 0.63770E-08
       0.66125E-08 0.68648E-08 0.70318E-08 0.70804E-08 0.72128E-08
       0.73173E-08 0.74422E-08 0.75855E-08 0.75641E-08 0.75124E-08
       0.75391E-08 0.74094E-08
c
f14:n  6 7 8 9 10 11 12 13 14 15 16 17 18
e14    4e-6  0.04  5
fs14  -23 -20 -26 -27 -28 -29 t
sd14  (3.141593E+00 9.424778E+00 1.570796E+01 2.199115E+01 2.827433E+01
       3.455752E+01 8.796459E+01 2.010619E+02)
      (3.141593E+00 9.424778E+00 1.570796E+01 2.199115E+01 2.827433E+01
       3.455752E+01 8.796459E+01 2.010619E+02)
      (3.141593E+00 9.424778E+00 1.570796E+01 2.199115E+01 2.827433E+01
       3.455752E+01 8.796459E+01 2.010619E+02)
      (3.141593E+00 9.424778E+00 1.570796E+01 2.199115E+01 2.827433E+01
       3.455752E+01 8.796459E+01 2.010619E+02)
      (3.141593E+00 9.424778E+00 1.570796E+01 2.199115E+01 2.827433E+01
       3.455752E+01 8.796459E+01 2.010619E+02)
      (3.141593E+00 9.424778E+00 1.570796E+01 2.199115E+01 2.827433E+01
```

```
       3.455752E+01 8.796459E+01 2.010619E+02)
      (3.141593E+00 9.424778E+00 1.570796E+01 2.199115E+01 2.827433E+01
       3.455752E+01 8.796459E+01 2.010619E+02)
      (3.141593E+00 9.424778E+00 1.570796E+01 2.199115E+01 2.827433E+01
       3.455752E+01 8.796459E+01 2.010619E+02)
      (3.141593E+00 9.424778E+00 1.570796E+01 2.199115E+01 2.827433E+01
       3.455752E+01 8.796459E+01 2.010619E+02)
      (3.141593E+00 9.424778E+00 1.570796E+01 2.199115E+01 2.827433E+01
       3.455752E+01 8.796459E+01 2.010619E+02)
      (6.283185E+00 1.884956E+01 3.141593E+01 4.398230E+01 5.654867E+01
       6.911504E+01 1.759292E+02 4.021239E+02)
      (6.283185E+00 1.884956E+01 3.141593E+01 4.398230E+01 5.654867E+01
       6.911504E+01 1.759292E+02 4.021239E+02)
      (6.283185E+00 1.884956E+01 3.141593E+01 4.398230E+01 5.654867E+01
       6.911504E+01 1.759292E+02 4.021239E+02)
c
f24:p  6 7 8 9 10 11 12 13 14 15 16 17 18
fs24  -23 -20 -26 -27 -28 -29 t
sd24  (3.141593E+00 9.424778E+00 1.570796E+01 2.199115E+01 2.827433E+01
       3.455752E+01 8.796459E+01 2.010619E+02)
      (3.141593E+00 9.424778E+00 1.570796E+01 2.199115E+01 2.827433E+01
       3.455752E+01 8.796459E+01 2.010619E+02)
      (3.141593E+00 9.424778E+00 1.570796E+01 2.199115E+01 2.827433E+01
       3.455752E+01 8.796459E+01 2.010619E+02)
      (3.141593E+00 9.424778E+00 1.570796E+01 2.199115E+01 2.827433E+01
       3.455752E+01 8.796459E+01 2.010619E+02)
      (3.141593E+00 9.424778E+00 1.570796E+01 2.199115E+01 2.827433E+01
       3.455752E+01 8.796459E+01 2.010619E+02)
      (3.141593E+00 9.424778E+00 1.570796E+01 2.199115E+01 2.827433E+01
       3.455752E+01 8.796459E+01 2.010619E+02)
      (3.141593E+00 9.424778E+00 1.570796E+01 2.199115E+01 2.827433E+01
       3.455752E+01 8.796459E+01 2.010619E+02)
      (3.141593E+00 9.424778E+00 1.570796E+01 2.199115E+01 2.827433E+01
       3.455752E+01 8.796459E+01 2.010619E+02)
      (3.141593E+00 9.424778E+00 1.570796E+01 2.199115E+01 2.827433E+01
       3.455752E+01 8.796459E+01 2.010619E+02)
      (6.283185E+00 1.884956E+01 3.141593E+01 4.398230E+01 5.654867E+01
       6.911504E+01 1.759292E+02 4.021239E+02)
      (6.283185E+00 1.884956E+01 3.141593E+01 4.398230E+01 5.654867E+01
       6.911504E+01 1.759292E+02 4.021239E+02)
      (6.283185E+00 1.884956E+01 3.141593E+01 4.398230E+01 5.654867E+01
       6.911504E+01 1.759292E+02 4.021239E+02)
de24   0.55E-01  0.30E+00  0.75E+00  0.15E+01  0.25E+01
       0.35E+01  0.45E+01  0.55E+01  0.65E+01
df24   7.42E-11  1.51E-10  3.82E-10  6.71E-10  9.63E-10
       1.21E-09  1.43E-09  1.64E-09  1.85E-09
c
f34:n  6 7 8 9 10 11 12 13 14 15 16 17 18
e34    4e-6  0.04  5
fs34  -23 -20 -26 -27 -28 -29 t
sd34  (3.141593E+00 9.424778E+00 1.570796E+01 2.199115E+01 2.827433E+01
       3.455752E+01 8.796459E+01 2.010619E+02)
```

```
      (3.141593E+00 9.424778E+00 1.570796E+01 2.199115E+01 2.827433E+01
       3.455752E+01 8.796459E+01 2.010619E+02)
      (3.141593E+00 9.424778E+00 1.570796E+01 2.199115E+01 2.827433E+01
       3.455752E+01 8.796459E+01 2.010619E+02)
      (3.141593E+00 9.424778E+00 1.570796E+01 2.199115E+01 2.827433E+01
       3.455752E+01 8.796459E+01 2.010619E+02)
      (3.141593E+00 9.424778E+00 1.570796E+01 2.199115E+01 2.827433E+01
       3.455752E+01 8.796459E+01 2.010619E+02)
      (3.141593E+00 9.424778E+00 1.570796E+01 2.199115E+01 2.827433E+01
       3.455752E+01 8.796459E+01 2.010619E+02)
      (3.141593E+00 9.424778E+00 1.570796E+01 2.199115E+01 2.827433E+01
       3.455752E+01 8.796459E+01 2.010619E+02)
      (3.141593E+00 9.424778E+00 1.570796E+01 2.199115E+01 2.827433E+01
       3.455752E+01 8.796459E+01 2.010619E+02)
      (3.141593E+00 9.424778E+00 1.570796E+01 2.199115E+01 2.827433E+01
       3.455752E+01 8.796459E+01 2.010619E+02)
      (6.283185E+00 1.884956E+01 3.141593E+01 4.398230E+01 5.654867E+01
       6.911504E+01 1.759292E+02 4.021239E+02)
      (6.283185E+00 1.884956E+01 3.141593E+01 4.398230E+01 5.654867E+01
       6.911504E+01 1.759292E+02 4.021239E+02)
      (6.283185E+00 1.884956E+01 3.141593E+01 4.398230E+01 5.654867E+01
       6.911504E+01 1.759292E+02 4.021239E+02)
de34   0.1000E-08  0.1000E-07  0.2500E-07  0.3600E-07  0.2510E-06
       0.6840E-06  0.1860E-05  0.5000E-05  0.1370E-04  0.3730E-04
       0.1010E-03  0.2750E-03  0.7490E-03  0.2030E-02
df34   0.4362E-10  0.1379E-10  0.8724E-11  0.7270E-11  0.2920E-11
       0.1780E-11  0.1090E-11  0.6560E-12  0.4000E-12  0.2330E-12
       0.1470E-12  0.8990E-13  0.5480E-13  0.3270E-13
c
f42:n    4 5 6 7 8 9 10 11 12 13 14 15 16 17
e42      4e-6  0.04  5
fs42   -23 -20 -26 -27 -28 -29 t
sd42   (3.141593E+00 9.424778E+00 1.570796E+01 2.199115E+01 2.827433E+01
       3.455752E+01 8.796459E+01 2.010619E+02)
      (3.141593E+00 9.424778E+00 1.570796E+01 2.199115E+01 2.827433E+01
       3.455752E+01 8.796459E+01 2.010619E+02)
      (3.141593E+00 9.424778E+00 1.570796E+01 2.199115E+01 2.827433E+01
       3.455752E+01 8.796459E+01 2.010619E+02)
      (3.141593E+00 9.424778E+00 1.570796E+01 2.199115E+01 2.827433E+01
       3.455752E+01 8.796459E+01 2.010619E+02)
      (3.141593E+00 9.424778E+00 1.570796E+01 2.199115E+01 2.827433E+01
       3.455752E+01 8.796459E+01 2.010619E+02)
      (3.141593E+00 9.424778E+00 1.570796E+01 2.199115E+01 2.827433E+01
       3.455752E+01 8.796459E+01 2.010619E+02)
      (3.141593E+00 9.424778E+00 1.570796E+01 2.199115E+01 2.827433E+01
       3.455752E+01 8.796459E+01 2.010619E+02)
      (3.141593E+00 9.424778E+00 1.570796E+01 2.199115E+01 2.827433E+01
       3.455752E+01 8.796459E+01 2.010619E+02)
      (3.141593E+00 9.424778E+00 1.570796E+01 2.199115E+01 2.827433E+01
       3.455752E+01 8.796459E+01 2.010619E+02)
      (3.141593E+00 9.424778E+00 1.570796E+01 2.199115E+01 2.827433E+01
       3.455752E+01 8.796459E+01 2.010619E+02)
```

```
      (3.141593E+00 9.424778E+00 1.570796E+01 2.199115E+01 2.827433E+01
       3.455752E+01 8.796459E+01 2.010619E+02)
      (3.141593E+00 9.424778E+00 1.570796E+01 2.199115E+01 2.827433E+01
       3.455752E+01 8.796459E+01 2.010619E+02)
      (3.141593E+00 9.424778E+00 1.570796E+01 2.199115E+01 2.827433E+01
       3.455752E+01 8.796459E+01 2.010619E+02)
      (3.141593E+00 9.424778E+00 1.570796E+01 2.199115E+01 2.827433E+01
       3.455752E+01 8.796459E+01 2.010619E+02)
de42   0.25300E-07 0.36000E-07 0.63000E-07 0.11000E-06 0.20000E-06
       0.36000E-06 0.63000E-06 0.11000E-05 0.20000E-05 0.36000E-05
       0.63000E-05 0.11000E-04 0.20000E-04 0.36000E-04 0.63000E-04
       0.11000E-03 0.20000E-03 0.36000E-03 0.63000E-03 0.11000E-02
       0.20000E-02 0.36000E-02 0.63000E-02 0.11000E-01 0.20000E-01
       0.36000E-01 0.63000E-01 0.82000E-01 0.86000E-01 0.90000E-01
       0.94000E-01 0.98000E-01 0.10500E+00 0.11500E+00 0.12500E+00
       0.13500E+00 0.14500E+00 0.15500E+00 0.16500E+00 0.17500E+00
       0.18500E+00 0.19500E+00 0.21000E+00 0.23000E+00 0.25000E+00
       0.27000E+00 0.29000E+00 0.31000E+00 0.33000E+00 0.35000E+00
       0.37000E+00 0.39000E+00 0.42000E+00 0.46000E+00 0.50000E+00
       0.54000E+00 0.58000E+00 0.62000E+00 0.66000E+00 0.70000E+00
       0.74000E+00 0.78000E+00 0.82000E+00 0.86000E+00 0.90000E+00
       0.94000E+00 0.98000E+00 0.10500E+01 0.11500E+01 0.12500E+01
       0.13500E+01 0.14500E+01 0.15500E+01 0.16500E+01 0.17500E+01
       0.18500E+01 0.19500E+01 0.21000E+01 0.23000E+01 0.25000E+01
       0.27000E+01 0.29000E+01 0.31000E+01 0.33000E+01 0.35000E+01
       0.37000E+01 0.39000E+01 0.42000E+01 0.46000E+01 0.50000E+01
       0.54000E+01 0.58000E+01 0.62000E+01 0.66000E+01 0.70000E+01
       0.74000E+01 0.78000E+01 0.82000E+01 0.86000E+01 0.90000E+01
       0.94000E+01 0.98000E+01 0.10500E+02 0.11500E+02 0.12500E+02
       0.13500E+02 0.14500E+02 0.15500E+02 0.16500E+02 0.17500E+02
       0.18500E+02 0.19500E+02 0.21000E+02 0.23000E+02 0.25000E+02
       0.27000E+02 0.29000E+02
df42   0.14906E-10 0.12626E-10 0.95326E-11 0.72163E-11 0.53570E-11
       0.39915E-11 0.30255E-11 0.22902E-11 0.17185E-11 0.13008E-11
       0.10200E-11 0.83822E-12 0.74959E-12 0.78283E-12 0.96992E-12
       0.13931E-11 0.22914E-11 0.39420E-11 0.67553E-11 0.11681E-10
       0.21001E-10 0.37503E-10 0.64423E-10 0.10871E-09 0.18933E-09
       0.31302E-09 0.48604E-09 0.57658E-09 0.60727E-09 0.62625E-09
       0.64523E-09 0.66321E-09 0.69460E-09 0.73741E-09 0.77801E-09
       0.81664E-09 0.85415E-09 0.88955E-09 0.92283E-09 0.95620E-09
       0.98633E-09 0.10165E-08 0.10608E-08 0.11171E-08 0.11662E-08
       0.12252E-08 0.12742E-08 0.13240E-08 0.13649E-08 0.14184E-08
       0.14663E-08 0.15349E-08 0.16689E-08 0.16906E-08 0.16548E-08
       0.17126E-08 0.17716E-08 0.18332E-08 0.18948E-08 0.19537E-08
       0.20022E-08 0.20624E-08 0.21142E-08 0.21695E-08 0.22364E-08
       0.23410E-08 0.25239E-08 0.25592E-08 0.25373E-08 0.26439E-08
       0.27315E-08 0.27787E-08 0.28538E-08 0.29648E-08 0.30038E-08
       0.31285E-08 0.31463E-08 0.32421E-08 0.32899E-08 0.34205E-08
       0.35717E-08 0.37110E-08 0.38390E-08 0.41820E-08 0.42670E-08
       0.43694E-08 0.43007E-08 0.44285E-08 0.44386E-08 0.46851E-08
       0.45749E-08 0.47860E-08 0.49020E-08 0.50300E-08 0.52379E-08
       0.55138E-08 0.54495E-08 0.54063E-08 0.55679E-08 0.56697E-08
       0.57173E-08 0.58403E-08 0.59787E-08 0.63920E-08 0.63770E-08
       0.66125E-08 0.68648E-08 0.70318E-08 0.70804E-08 0.72128E-08
```

```
       0.73173E-08 0.74422E-08 0.75855E-08 0.75641E-08 0.75124E-08
       0.75391E-08 0.74094E-08
c
f52:n  4 5 6 7 8 9 10 11 12 13 14 15 16 17
e52    4e-6  0.04  5
fs52  -23 -20 -26 -27 -28 -29 t
sd52  (3.141593E+00 9.424778E+00 1.570796E+01 2.199115E+01 2.827433E+01
       3.455752E+01 8.796459E+01 2.010619E+02)
      (3.141593E+00 9.424778E+00 1.570796E+01 2.199115E+01 2.827433E+01
       3.455752E+01 8.796459E+01 2.010619E+02)
      (3.141593E+00 9.424778E+00 1.570796E+01 2.199115E+01 2.827433E+01
       3.455752E+01 8.796459E+01 2.010619E+02)
      (3.141593E+00 9.424778E+00 1.570796E+01 2.199115E+01 2.827433E+01
       3.455752E+01 8.796459E+01 2.010619E+02)
      (3.141593E+00 9.424778E+00 1.570796E+01 2.199115E+01 2.827433E+01
       3.455752E+01 8.796459E+01 2.010619E+02)
      (3.141593E+00 9.424778E+00 1.570796E+01 2.199115E+01 2.827433E+01
       3.455752E+01 8.796459E+01 2.010619E+02)
      (3.141593E+00 9.424778E+00 1.570796E+01 2.199115E+01 2.827433E+01
       3.455752E+01 8.796459E+01 2.010619E+02)
      (3.141593E+00 9.424778E+00 1.570796E+01 2.199115E+01 2.827433E+01
       3.455752E+01 8.796459E+01 2.010619E+02)
      (3.141593E+00 9.424778E+00 1.570796E+01 2.199115E+01 2.827433E+01
       3.455752E+01 8.796459E+01 2.010619E+02)
      (3.141593E+00 9.424778E+00 1.570796E+01 2.199115E+01 2.827433E+01
       3.455752E+01 8.796459E+01 2.010619E+02)
      (3.141593E+00 9.424778E+00 1.570796E+01 2.199115E+01 2.827433E+01
       3.455752E+01 8.796459E+01 2.010619E+02)
      (3.141593E+00 9.424778E+00 1.570796E+01 2.199115E+01 2.827433E+01
       3.455752E+01 8.796459E+01 2.010619E+02)
      (3.141593E+00 9.424778E+00 1.570796E+01 2.199115E+01 2.827433E+01
       3.455752E+01 8.796459E+01 2.010619E+02)
de52   0.1000E-08  0.1000E-07  0.2500E-07  0.3600E-07  0.2510E-06
       0.6840E-06  0.1860E-05  0.5000E-05  0.1370E-04  0.3730E-04
       0.1010E-03  0.2750E-03  0.7490E-03  0.2030E-02
df52   0.4362E-10  0.1379E-10  0.8724E-11  0.7270E-11  0.2920E-11
       0.1780E-11  0.1090E-11  0.6560E-12  0.4000E-12  0.2330E-12
       0.1470E-12  0.8990E-13  0.5480E-13  0.3270E-13
c
f62:p  4 5 6 7 8 9 10 11 12 13 14 15 16 17
fs62  -23 -20 -26 -27 -28 -29 t
sd62  (3.141593E+00 9.424778E+00 1.570796E+01 2.199115E+01 2.827433E+01
       3.455752E+01 8.796459E+01 2.010619E+02)
      (3.141593E+00 9.424778E+00 1.570796E+01 2.199115E+01 2.827433E+01
       3.455752E+01 8.796459E+01 2.010619E+02)
      (3.141593E+00 9.424778E+00 1.570796E+01 2.199115E+01 2.827433E+01
       3.455752E+01 8.796459E+01 2.010619E+02)
      (3.141593E+00 9.424778E+00 1.570796E+01 2.199115E+01 2.827433E+01
       3.455752E+01 8.796459E+01 2.010619E+02)
      (3.141593E+00 9.424778E+00 1.570796E+01 2.199115E+01 2.827433E+01
```

```
       3.455752E+01 8.796459E+01 2.010619E+02)
      (3.141593E+00 9.424778E+00 1.570796E+01 2.199115E+01 2.827433E+01
       3.455752E+01 8.796459E+01 2.010619E+02)
      (3.141593E+00 9.424778E+00 1.570796E+01 2.199115E+01 2.827433E+01
       3.455752E+01 8.796459E+01 2.010619E+02)
      (3.141593E+00 9.424778E+00 1.570796E+01 2.199115E+01 2.827433E+01
       3.455752E+01 8.796459E+01 2.010619E+02)
      (3.141593E+00 9.424778E+00 1.570796E+01 2.199115E+01 2.827433E+01
       3.455752E+01 8.796459E+01 2.010619E+02)
      (3.141593E+00 9.424778E+00 1.570796E+01 2.199115E+01 2.827433E+01
       3.455752E+01 8.796459E+01 2.010619E+02)
      (3.141593E+00 9.424778E+00 1.570796E+01 2.199115E+01 2.827433E+01
       3.455752E+01 8.796459E+01 2.010619E+02)
de62   0.55E-01  0.30E+00  0.75E+00  0.15E+01  0.25E+01
       0.35E+01  0.45E+01  0.55E+01  0.65E+01
df62   7.42E-11  1.51E-10  3.82E-10  6.71E-10  9.63E-10
       1.21E-09  1.43E-09  1.64E-09  1.85E-09
nps    1000000
```

Appendix E

Multi–Fin Specific Temperature Rise Calculation (`flow.f`)

```
      program flow
*
      integer n
      real qold,qtotal,qaold,qb,qbold,qc,qcold,qd,qdold,qe,qeold,
     +     qf,qfold,hla,fa,fb,fc,fd,fe,ff,lda,ldb,ldc,ldd,lde,ldf,
     +     kentrance,kexit,kteebranch,kteeline,aa,ab,ac,ad,ae,af,
     +     g,qaold,rea,reb,rec,red,ree,ref,va,vb,vc,vd,ve,vf,nu,
     +     pr,ha,hb,hc,hd,he,hf,kf,dha,dhb,dhb,dhc,dhe,dhf,h1,h2,
     +     h3,h4,h5,h6,kcu,p1,p2,p3,p4,p5,p6,a1,a2,a3,a4,a5,a6,lfin,
     +     ml1,ml2,ml3,ml4,ml5,ml6,dtq1,dtq2,dtq3,dtq4,dtq5,dtq6,
     +     f1,f2,f3,f4,f5,f6,r(1001),f(1001)
*
      nu=1.00e-6
      kf=0.60574
      kcu=401.0
      g=9.81
      aa=2.31648e-5
      ab=2.31648e-5
      ac=2.31648e-5
      ad=2.31648e-5
      ae=2.31648e-5
      af=3.65479e-5
      a1=0.0015*1.34*.0254
      a2=0.0015*1.32*.0254
      a3=0.0015*1.25*.0254
      a4=0.0015*1.13*.0254
      a5=0.0015*0.93*.0254
      a6=0.0015*0.60*.0254
      p1=2.0*(0.0015+1.34*.0254)
      p2=2.0*(0.0015+1.32*.0254)
      p3=2.0*(0.0015+1.25*.0254)
```

```
      p4=2.0*(0.0015+1.13*.0254)
      p5=2.0*(0.0015+0.93*.0254)
      p6=2.0*(0.0015+0.60*.0254)
      lfin=0.01524
      f1=7.7233e-5/5.067075e-4
      f2=1.4991e-4/5.067075e-4
      f3=1.3528e-4/5.067075e-4
      f4=1.0631e-4/5.067075e-4
      f5=3.7981e-5/5.067075e-4
      f6=0.0
      lda=12.2823
      ldb=12.0834
      ldc=11.4675
      ldd=12.0104
      lde=12.1488
      ldf=14.5611
      dha=.002771
      dhb=.002771
      dhc=.002771
      dhd=.002771
      dhe=.002771
      dhf=.002771
      kentrance=0.5
      kexit=1.0
      kteebranch=3.0
      kteeline=0.9
*
      n=1
      do 900 i=1,200
      f(i)=real(i)/20.0
      q=f(i)*6.309e-5
      qold=q
      qaold=(2.31648e-5/1.523719e-4)*qold/2.0 ! Inital flow in A
*
 20   rea=1.196272e8*qaold
      call friction(rea,fa)
      hla=(fa*lda+kentrance+kexit)*qaold**2/2.0/g/aa**2
*
      qbold=qaold
      reb=1.196272e8*qbold
      call friction(reb,fb)
 40   qb=sqrt(2.0*g*ab**2*hla/(fb*ldb+kentrance+kexit))
      if (abs((qb-qbold)/qb).lt.1.0e-5) then
         go to 50
      else
         reb=1.196272e8*qb
         call friction(reb,fb)
         qbold=qb
         go to 40
      endif
*
 50   qcold=qb
      rec=1.196272e8*qcold
      call friction(rec,fc)
```

```
 90   qc=sqrt(2.0*g*ac**2*hla/(fc*ldc+2.0*kteebranch))
      if (abs((qc-qcold)/qc).lt.1.0e-5.or.m.eq.3) then
         go to 100
      else
         rec=1.196272e8*qc
         call friction(rec,fc)
         qcold=qc
         go to 90
      endif
*
 100  qdold=qc
      red=1.196272e8*qdold
      call friction(red,fd)
 140  qd=sqrt(2.0*g*ad**2*hla/(fd*ldd+2.0*kteebranch+2.0*kteeline))
      if (abs((qd-qdold)/qd).lt.1.0e-5) then
         go to 150
      else
         red=1.196272e8*qd
         call friction(red,fd)
         qdold=qd
         go to 140
      endif
*
 150  qeold=qd
      ree=1.196272e8*qeold
      call friction(ree,fe)
 190  qe=sqrt(2.0*g*ae**2*hla/(fe*lde+2.0*kteebranch+4.0*kteeline))
      if (abs((qe-qeold)/qe).lt.1.0e-5) then
         go to 200
      else
         ree=1.196272e8*qe
         call friction(ree,fe)
         qeold=qe
         go to 190
      endif
*
 200  qfold=qe
      ref=1.196272e8*qfold
      call friction(ref,ff)
 240  qf=sqrt(2.0*g*af**2*hla/(ff*ldf+6.0*kteeline))
      if (abs((qf-qfold)/qf).lt.1.0e-5) then
         go to 250
      else
         ref=1.196272e8*qf
         call friction(ref,ff)
         qfold=qf
         go to 240
      endif
*
 250  qtotal=2.0*(qaold+qb+qc+qd+qe+qf)
      if (abs((qtotal-qold)/qtotal).lt.1.0e-5) then
         go to 300
      else
         qaold=(q/qtotal)*qaold
```

```
         qold=qtotal
         n=n+1
         go to 20
      endif
*
 300  va=qaold/aa
      vb=qb/ab
      vc=qc/ac
      vd=qd/ad
      ve=qe/ae
      vf=qf/af
*
      pr=5.65
      ha=kf/dha*0.023*(rea**0.8)*(pr**0.4)
      hb=kf/dhb*0.023*(reb**0.8)*(pr**0.4)
      hc=kf/dhc*0.023*(rec**0.8)*(pr**0.4)
      hd=kf/dhd*0.023*(red**0.8)*(pr**0.4)
      he=kf/dhe*0.023*(ree**0.8)*(pr**0.4)
      hf=kf/dhf*0.023*(ref**0.8)*(pr**0.4)
      h1=ha
      h2=0.5*(ha+hb)
      h3=0.5*(hb+hc)
      h4=0.5*(hc+hd)
      h5=0.5*(hd+he)
      h6=0.5*(he+hf)
*
      ml1=sqrt(h1*p1*lfin**2/kcu/a1)
      ml2=sqrt(h2*p2*lfin**2/kcu/a2)
      ml3=sqrt(h3*p3*lfin**2/kcu/a3)
      ml4=sqrt(h4*p4*lfin**2/kcu/a4)
      ml5=sqrt(h5*p5*lfin**2/kcu/a5)
      ml6=sqrt(h6*p6*lfin**2/kcu/a6)
*
      dtq1=1.0/(sqrt(h1*p1*kcu*a1)*tanh(ml1))*1000.0
      dtq2=1.0/(sqrt(h2*2.0**2*p2*kcu*a2)*tanh(ml2))*1000.0
      dtq3=1.0/(sqrt(h3*2.0**2*p3*kcu*a3)*tanh(ml3))*1000.0
      dtq4=1.0/(sqrt(h4*2.0**2*p4*kcu*a4)*tanh(ml4))*1000.0
      dtq5=1.0/(sqrt(h5*2.0**2*p5*kcu*a5)*tanh(ml5))*1000.0
      dtq6=1.0/(sqrt(h6*2.0**2*p6*kcu*a6)*tanh(ml6))*1000.0
*
      r(i)=1.0/(1.0/(f1*dtq1)+1.0/(f2*dtq2)+1.0/(f3*dtq3)+
     +       1.0/(f4*dtq4)+1.0/(f5*dtq5))
 900  continue
*
      open(unit=13,file='mfflow.dat',status='unknown')
      write(13,*)
      do 920 i=1,200
         write(13,980) i,f(i),r(i)
 920  continue
      write(13,*)
      end


      subroutine friction(re,f)
```

```
*
      real re,f,fold
      fold=0.1
 50   f=1.0/(2.0*log10(re*sqrt(fold))-0.8)**2
      if (abs((f-fold)/f).lt.1.0e-5) then
         go to 100
      else
         fold=f
         go to 50
      endif
 100  return
      end
```

Appendix F

Heat Deposition Computational Method

Eq. 5.28 from Section 5.2 will use tabulated stopping power data in lithium and copper from Janni [44]. The mesh sizes will depend on lithium target thickness Δx_{Li} and incident proton energy E_{p_0}. In calculating a particular temperature drop $(\Delta T/I)_{stopping}$, E_{p_0} and E_{edge} are specified. Then the surface of the target is located at $x = 0$ and $E_p = E_{p_0}$, and a vector of N energy grid points ranging from E_{p_0} to 0 is established with E_{edge} corresponding to $i = M$. Another vector of length N is created in which the ith component is the stopping power corresponding to the ith position in the proton energy vector. For i between 1 and M, lithium stopping powers are used, and for i between M and N, copper is used. For certain energies that are not tabulated in [44], a linear fit to the inverse of the stopping power is used to interpolate stopping powers; this gives a very good ($r > 0.99$) fit, since the Bethe–Bloch formula for the stopping power varies as $1/E_p$, except for a slowly varying logarithmic term, on most of the range of interest. For all grid points,

$$x_{i+1} = x_i + \frac{(E_i - E_{i+1})}{(dE_p/dx)_i^{\mathrm{Li}}}, \qquad i = 2, M \tag{F.1}$$

$$x_{i+1} = x_i + \frac{(E_i - E_{i+1})}{(dE_p/dx)_i^{\mathrm{Cu}}}, \qquad i = M+1, N \tag{F.2}$$

The form of Eq. 5.28 is rather straightforward to solve numerically, since we only need to integrate twice. We will actually perform the first integration separately in the lithium and copper regions, and then adjust the relative magnitudes based on boundary conditions. Dividing each side of Eq. 5.28 by I to give a temperature variation per unit beam current, and using a trapezoidal integration approximation gives

$$\frac{1}{I}\left(\frac{dT}{dx}\right)_{i+1}^{\mathrm{Li}} = \frac{1}{I}\left(\frac{dT}{dx}\right)_{i}^{\mathrm{Li}} - \frac{(x_{i+1}-x_i)}{2E_{p_0}k_{\mathrm{Li}}A}\left[\left(\frac{dE_p}{dx}\right)_i^{\mathrm{Li}} + \left(\frac{dE_p}{dx}\right)_{i+1}^{\mathrm{Li}}\right], \qquad i = 2, M \tag{F.3}$$

$$\frac{1}{I}\left(\frac{dT}{dx}\right)_{i+1}^{\mathrm{Cu}} = \frac{1}{I}\left(\frac{dT}{dx}\right)_{i}^{\mathrm{Cu}} - \frac{(x_{i+1}-x_i)}{2E_{p_0}k_{\mathrm{Cu}}A}\left[\left(\frac{dE_p}{dx}\right)_i^{\mathrm{Cu}} + \left(\frac{dE_p}{dx}\right)_{i+1}^{\mathrm{Cu}}\right], \qquad i = M+1, N \tag{F.4}$$

where $(dT/dx)_1^{\mathrm{Li}}$ and $(dT/dx)_M^{\mathrm{Cu}}$, the first points in lithium and copper, respectively, are initally taken to be zero.

Before performing the next integration, boundary conditions for the problem should be discussed. Continuity of temperature is obvious, and should be applied at $x = \Delta x_{\mathrm{Li}}$ $(i = M)$ and $x = R$ $(i = N)$:

$$\left(\frac{T}{I}\right)_M^{\mathrm{Li}} = \left(\frac{T}{I}\right)_M^{\mathrm{Cu}} \tag{F.5}$$

$$\left(\frac{T}{I}\right)_{N,stopping} = \left(\frac{T}{I}\right)_{N,\mathrm{Cu}} \tag{F.6}$$

The other continuity equations of interest are heat flow at $i = M$ and $i = N$. At the lithium/copper interface, $q_{\mathrm{Li}} = q_{\mathrm{Cu}}$ implies

$$\frac{1}{I}\left(\frac{dT}{dx}\right)_M^{\mathrm{Li}} = \left(\frac{k_{\mathrm{Cu}}}{k_{\mathrm{Li}}}\right)\frac{1}{I}\left(\frac{dT}{dx}\right)_M^{\mathrm{Cu}} \tag{F.7}$$

Finally, a conservation of heat flow at the end of the proton stopping range gives

$$\frac{1}{I}\left(\frac{dT}{dx}\right)_M^{\text{Cu}} = -\frac{E_{p0}}{k_{\text{Cu}}A} \tag{F.8}$$

First, all values of $1/I(dT/dx)_i^{\text{Cu}}$ are adjusted by an additive factor so that Eq. F.8 is satisfied:

$$\frac{1}{I}\left(\frac{dT}{dx}\right)_i^{\text{Cu,new}} = \frac{1}{I}\left(\frac{dT}{dx}\right)_i^{\text{Cu}} - \frac{1}{I}\left(\frac{dT}{dx}\right)_N^{\text{Cu}} - \frac{E_{p0}}{k_{\text{Cu}}A}, \qquad i = M, N \tag{F.9}$$

The new value of $1/I(dT/dx)_M^{\text{Cu}}$ that this produces is used to determine a similar additive factor that is applied to the temperature gradients in the lithium target so that Eq. F.7 is also satisfied:

$$\frac{1}{I}\left(\frac{dT}{dx}\right)_i^{\text{Li,new}} = \frac{1}{I}\left(\frac{dT}{dx}\right)_i^{\text{Li}} - \frac{1}{I}\left(\frac{dT}{dx}\right)_M^{\text{Li}} + \left(\frac{k_{\text{Cu}}}{k_{\text{Li}}}\right)\frac{1}{I}\left(\frac{dT}{dx}\right)_M^{\text{Cu,new}}, \qquad i = 1, M \tag{F.10}$$

This is the final form of the spatial variation of the temperature gradient over the stopping region.

Now it only remains to calculate the temperature variation. Integrating the adjusted temperature gradients from Eqs. F.3 and F.4 gives

$$\left(\frac{T}{I}\right)_{i+1} = \left(\frac{T}{I}\right)_i + \frac{1}{2}(x_{i+1} - x_i)\left[\frac{1}{I}\left(\frac{dT}{dx}\right)_i + \frac{1}{I}\left(\frac{dT}{dx}\right)_{i+1}\right], \qquad i = 2, N \tag{F.11}$$

Note that Eq. F.5 is automatically satisfied. In Eq. F.11, $(T/I)_1$ is initially taken as zero for ease of computation; this is justified because we are looking for temperature RISE across the stopping region. At the end of the calculation, all temperatures are adjusted so that $(T/I)_N$ is zero, for convenience of presentation. The final $(\Delta T/I)_{stopping}$ is given by the difference $(T/I)_{max} - (T/I)_N$, which in all cases considered becomes $(T/I)_1 - (T/I)_N$. The calculation is complete.

Appendix G

Design of a Head Phantom for BNCT Beam Verification

An important aspect of the final design of the near–threshold CTU is the development of a head phantom to test the effectiveness of the neutron beam. A head phantom was designed and constructed to allow detailed measurement of the various dose components of the neutron sources under consideration. It was designed to meet the following criteria: be of a material similar in density and composition to a realistic combination of tissue, skull, and brain; be easy to fabricate and use; have a size and shape reasonably similar to an adult human head; and be rugged. In addition, emphasis was placed on developing a design that allows flexibility in the positioning of detectors within the phantom.

To meet these needs, cast acrylic was chosen as the phantom material. Acrylic consists of the same four principal elements that are common to tissue: hydrogen, carbon, oxygen, and nitrogen. The weight percentage of hydrogen, the main source of fast neutron and gamma doses in the phantom, is 8.05% in acrylic and 10.57% in brain tissue (see Table 4.2) [53]. The density of acrylic is 1.18 g/cm^3, higher than brain (1.047 g/cm^3) by 12.7%. Acrylic benefits from high strength, a reasonably high

Table G.1: Physical Properties of Body Parts and Phantom

Name	Volume (cm^3)	Density (g/cm^3)	Weight Percent (%)
Brain	1470	1.047	10.57
Skull	847	1.500	7.037
Neck	1357	1.000	10.00
Phantom		1.180	8.054

melting point, and low ductility. However, acrylic is not easy to machine, because the plastic tends to melt rather than cut if blades are not sharp enough or the cutting is too deep.

The cylindrical head phantom dimensions were chosen to be 6 inches (15.24 cm) in diameter and 8.5 inches (21.59 cm) long. Because the plastic supply houses used to purchase phantom materials sell items in inches, it was used as the unit of measure throughout. A cylindrical shape was chosen for ease of fabrication and similarity to the MCNP models developed in Chapter 4. The radial dimension was chosen to be similar to that of an adult human head. The length was chosen such that the neutron transport through the phantom is similar to that in the human head and neck. To this end, the total number of hydrogen atoms contained in the important parts of the human head and the phantom must be known. The important parts were determined to be the brain, skull, and neck. The volume, density, and weight percentage of hydrogen in each body part, as well as acrylic, are shown in Table G.1 [13, 89, 90].

It is not sufficient to simply choose the phantom length L such that the number of hydrogen atoms in the phantom is equal to the sum of the body parts listed in Table G.1. Since this object is being designed specifically to study the transport of BNCT neutrons, it is more reasonable to require that the sum of the products of the length and hydrogen density in each body part is equal to the total phantom length. This will lead to similar total amounts of neutron attenuation. Using values taken from Table G.1 gives phantom–to–body part length ratios of 1.1644 for brain, 1.1106

for skull, and 1.0522 for neck tissue.

Denoting the mass and length ratio of each component i by M_i and R_i, and the phantom radius and density by R_P and ρ, the phantom length is given by

$$L = \frac{1}{\pi \rho R_P^2} \sum_i M_i R_i \tag{G.1}$$

Inserting appropriate values gives a phantom length of $L = 21.515$ cm, or 8.47 inches. This value was rounded up slightly to 8.5 inches.

A schematic of the head phantom is shown in Figure G-1. A 1 inch (2.54 cm) wide slot was machined out of one end of the phantom cylinder to a depth of 3 inches (7.62 cm). Another slot was machined out parallel to the first from a depth of 4.5 inches (11.43 cm) to 6.5 inches (16.51 cm) to allow placement of detectors deep into the phantom. A bridge between the two slots was left to maintain the structural integrity of the phantom. The ends of the trenches were rounded to eliminate stress concentrations. Next, 1 inch (2.54 cm) wide, 6 inch (15.24 cm) long pieces of extruded acrylic of various thicknesses were constructed. The ends are rounded so that when placed in the slots of the phantom, the surface remains circular. Several of these "spacers" also have holes drilled through them. The hole diameters were chosen so that the various detectors used to measure neutron and gamma doses and thermal neutron flux can slide freely along this radial direction. Pieces of acrylic rod were also machined to different lengths. These rods can be placed inside the empty spaces of the detector holes so that most of the phantom is always acrylic. This design allows almost unlimited freedom of detector placement inside the phantom, so that the spatial resolution is only limited by detector size, spacer sizes, and experimental time constraints. Note that foils may also be placed between spacers for activation analysis, if desired.

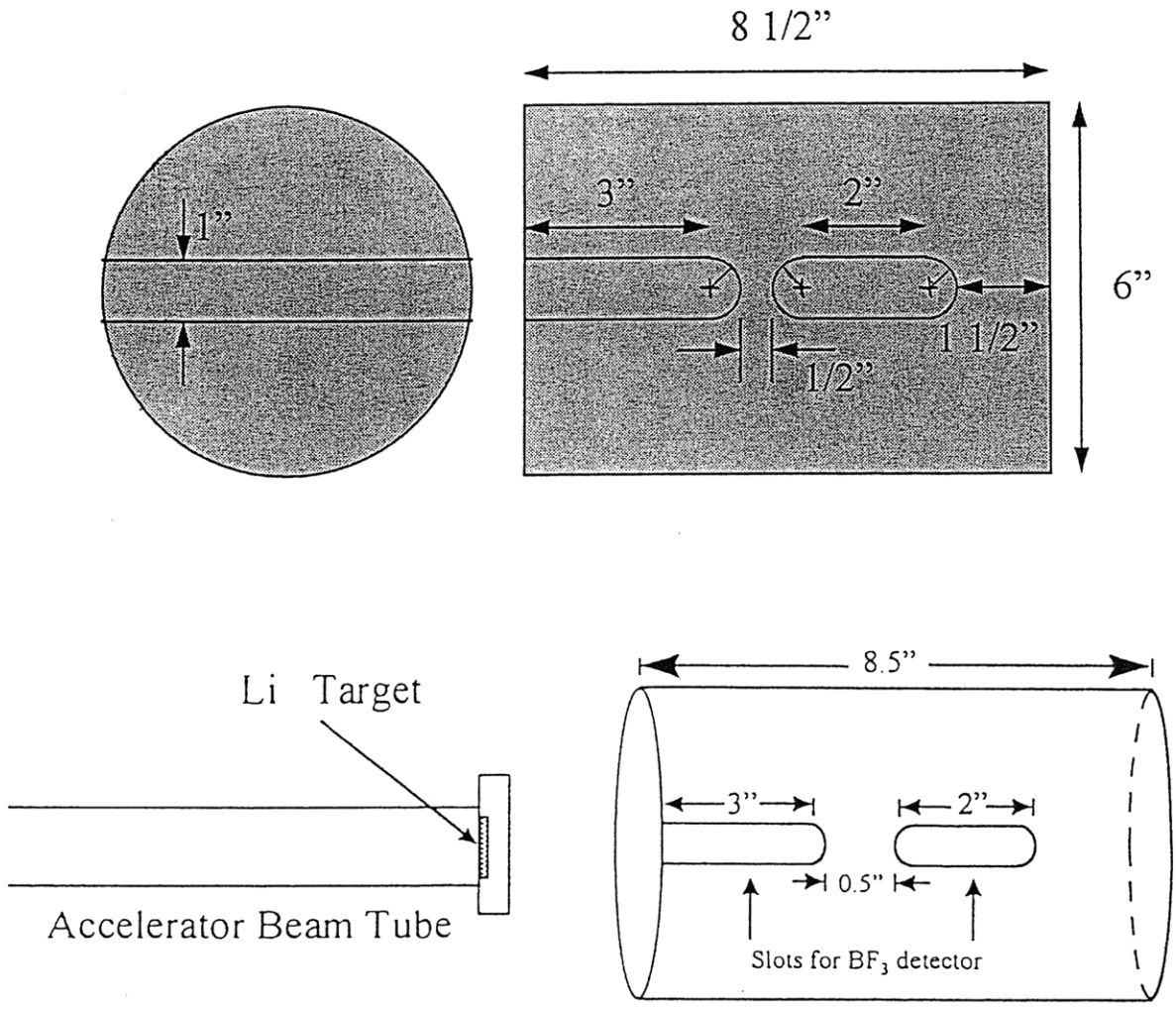

Figure G-1: Acrylic Head Phantom Design

Appendix H

Publications and Presentations

The following refereed papers, based on this research, have been published or are currently in peer review:

1. X.–L. Zhou and C. Lee, "Lithium Compounds as Targets for (p,n) Reactions," *Appl. Radiat. Isot.* **48**, No. 10-12, p. 1493 (1997).

2. X.–L. Zhou, C. Lee, J. Harmon, Y. Harker, and R. Hamm, "Analysis of Epithermal Neutron Production by Near–Threshold (p,n) Reactions," *Appl. Radiat. Isot.* **48**, No. 10-12, p. 1571 (1997).

3. C. L. Lee, X.–L. Zhou, J. F. Harmon, R. J. Kudchadker, and Y. D. Harker, "Thermal Neutron Flux Mapping in a Head Phantom," *Nucl. Instr. Meth. A*, accepted for publication May 1998.

4. C. L. Lee and X.–L. Zhou, "Thick Target Neutron Yields for the ^{7}Li(p,n)^{7}Be Reaction Near Threshold," submitted to Nucl. Instr. Meth. B, June 1998.

The following papers and posters, based on this research, have been presented or accepted for presentation:

1. C. L. Lee, X.–L. Zhou, J. F. Harmon, R. W. Bartholomay, Y. D. Harker, and R. J. Kudchadker, "Thermal Neutron Flux Mapping in a Head Phantom," 1998

Symposium on Radiation Measurements and Applications, Ann Arbor, MI, May 1998.

2. R. J. Kudchadker, J. F. Harmon, J. F. Kunze, R. Bartholomay, and C. L. Lee, "An accelerator based epithermal neutron source for BNCT," 6th International Conference on Nuclear Engineering (ICONE-6), San Diego, CA, May 1998.

3. C. L. Lee, X.–L. Zhou, J. F. Harmon, R. W. Bartholomay, Y. D. Harker, and R. W. Hamm, "Multi–Fin Heat Removal for Accelerator BNCT Targets," 8th International Symposium on Neutron Capture Therapy for Cancer, La Jolla, Ca, September 1998.

4. C. L. Lee, X.–L. Zhou, J. F. Harmon, R. J. Kudchadker, and Y. D. Harker, "Feasibility of Near–Threshold BNCT Based on Phantom Dosimetry," 8th International Symposium on Neutron Capture Therapy for Cancer, La Jolla, Ca, September 1998.

5. R. J. Kudchadker, C. L. Lee, F. Harmon, and Y. D. Harker, "Experimental Verification of Near Threshold Dosimetry for BNCT," 15th International Conference on the Applications of Accelerators in Research and Industry, Denton, TX, November 1998.

6. C. L. Lee and X.–L. Zhou, "Temperature Rise in Lithium Targets for Accelerator–Based BNCT Using Multi–Fin Heat Removal," 15th International Conference on the Applications of Accelerators in Research and Industry, Denton, TX, November 1998.

7. C. L. Lee, F. Harmon, Y. D. Harker, and R. Bartholomay, "Neutron Yield Benchmark Experiments for Near–Threshold Lithium Targets," 15th International Conference on the Applications of Accelerators in Research and Industry, Denton, TX, November 1998.

References

[1] H. Liskien and A. Paulsen, "Neutron production cross sections and energies for the reactions ^{7}Li(p,n)^{7}Be and ^{7}Li(p,n)^{7}Be*," *Atomic Data and Nucl. Data Tables.*, vol. 15, p. 57, 1975.

[2] R. J. Kudchadker, "A precision neutron detector for (p,n) reaction measurements," Master's thesis, Idaho State University, 1992.

[3] A. Z. Kiss *et al.*, "Measurements of relative thick target yields for PIGE analysis on light elements in the proton energy interval 2.4-4.2 MeV," *Journal of Radioanalytical and Nuclear Chemistry*, vol. 89, p. 123, 1985.

[4] J. H. Lienhard, *A Heat Transfer Textbook.* Englewood Cliffs, New Jersey: Prentice–Hall, Inc., 1981.

[5] M. C. Dobelbower, T. E. Blue, and K. Vafai, "Effect of duty factor and repetition rate on maximum target temperature for a proposed BNCT target assembly," in *Proceedings of the American Nuclear Society Topical Meeting on Nuclear Applications of Accelerator Technology*, (Albuquerque, NM USA), p. 516, 1997.

[6] A. H. Soloway *et al.*, "The rationale and requirements for the development of boron neutron capture therapy of brain tumors," *Journal of Neuro–Oncology*, vol. 33, p. 9, 1997.

[7] W. H. Sweet, "Early history of the development of boron neutron capture therapy of brain tumors," *Journal of Neuro–Oncology*, vol. 33, p. 19, 1997.

[8] R. L. Moss *et al.*, "The requirements and development of neutron beams for neutron capture therapy of brain cancer," *Journal of Neuro–Oncology*, vol. 33, p. 27, 1997.

[9] S. Sjöberg *et al.*, "Chemistry and biology of some low molecular weight boron compounds for boron neutron capture therapy," *Journal of Neuro–Oncology*, vol. 33, p. 41, 1997.

[10] R. G. Zamenhof, "Microdosimetry for boron neutron capture therapy: A review," *Journal of Neuro–Oncology*, vol. 33, p. 81, 1997.

[11] R. F. Barth, A. H. Soloway, and R. M. Brugger, "Boron neutron capture therapy of brain tumors: Past history, current status, and future potential," *Cancer Investigation*, vol. 14, no. 6, p. 534, 1996.

[12] J. C. Yanch, X.-L. Zhou, and G. L. Brownell, "A Monte Carlo investigation of the dosimetric properties of monoenergetic neutron beams for neutron capture therapy," *Radiat. Res.*, vol. 126, p. 1, 1991.

[13] X.-L. Zhou, "A design of an accelerator–based epithermal neutron beam for boron neutron capture therapy," Master's thesis, Massachusetts Institute of Technology, 1990.

[14] H. Cember, *Introduction to Health Physics.* Pergamon Press, 2nd ed., 1988.

[15] E. J. Hall, *Radiobiology for the Radiologist.* J. B. Lippincott Company, 3rd ed., 1988.

[16] T. E. Blue, T.-X. B. Qu, N. Gupta, and R. A. Gahbauer, "Effect of variations in

the RBE on the design of an AENIF for BNCT," *Advances in Neutron Capture Therapy*, p. 99, 1993.

[17] R. Zamenhof *et al.*, "Monte carlo–based treatment planning for boron neutron capture therapy using custom designed models automatically generated from CT data," *Int. J. Radiation Oncology Biol. Phys.*, vol. 35, no. 2, p. 383, 1996.

[18] C.-S. Yam, R. G. Zamenhof, and G. R. Solares, "Microdosimetric evaluations of boron compound efficacy," in *Transactions of the 1995 Winter Meeting of the American Nuclear Society*, (San Francisco, CA USA), 1995.

[19] W. Sauerwein *et al.*, "Update on the european clinical trials of boron neutron capture therapy for glioma," in *Transactions of the 1997 Winter Meeting of the American Nuclear Society*, (Albuquerque, NM USA), 1997.

[20] L. Wielopolski *et al.*, "Clinical trial of BNCT for glioblastoma multiforme," in *Transactions of the 1996 Winter Meeting of the American Nuclear Society*, (Washington, D. C. USA), 1996.

[21] T. H. Wu, R. M. Brugger, and J. F. Kunze, "Low energy accelerator–based neutron sources for neutron capture therapy," *Advances in Neutron Capture Therapy*, p. 105, 1993.

[22] C.-K. Wang, T. E. Blue, and R. Gahbauer, "A neutronic study of an accelerator–based neutron irradiation facility for boron neutron capture therapy," *Nucl. Technol.*, vol. 84, p. 93, 1989.

[23] D. A. Allen and T. D. Beynon, "A design study for an accelerator–based epithermal neutron beam for BNCT," *Phys. Med. Biol.*, vol. 40, p. 807, 1995.

[24] J. C. Yanch, X.-L. Zhou, R. E. Shefer, and R. E. Klinkowstein, "Accelerator–

based epithermal neutron beam design for neutron capture therapy," *Med. Phys.*, vol. 19, no. 3, p. 709, 1992.

[25] G. F. Knoll, *Radiation Detection and Measurement.* John Wiley & Sons, 2nd ed., 1989.

[26] D. R. Lide, ed., *The CRC Handbook of Chemistry and Physics.* CRC Press, 78th ed., 1997-1998.

[27] A. B. Chilton, J. K. Shultis, and R. E. Faw, *Principles of Radiation Shielding.* Prentice–Hall, Inc., 1984.

[28] R. J. Kudchadker, J. F. Kunze, and J. F. Harmon, "Accelerator designs that move close to the target and eliminate much moderator," in *Proceedings of the 7th International Symposium on Neutron Capture Therapy for Cancer*, (Zurich, Switzerland), 1996.

[29] Y. D. Harker, J. F. Harmon, and G. W. Irwin, "INEL and ISU BNCT research using a 2 MeV RFQ–based neutron source," *Nucl. Instr. Meth.*, vol. B99, p. 843, 1995.

[30] J. F. Harmon *et al.*, "Accelerator neutron sources for neutron capture therapy using near threshold charged particle reactions," in *Proc. 14th Int. Conf. on the App. of Accelerators in Research and Industry* (J. L. Duggan and I. L. Morgan, eds.), (Denton, Texas USA), 1996.

[31] J. F. Kunze, R. J. Kudchadker, and J. F. Harmon, "Accelerator designs that balance distance with energy and moderator dimensions," in *Transactions of the 1996 Winter Meeting of the American Nuclear Society*, (Washington, D. C. USA), 1996.

[32] X.-L. Zhou and C. L. Lee, "Lithium compounds as targets for (p,n) reactions," *Appl. Rad. Isotopes*, vol. 48, p. 1493, 1997.

[33] X.-L. Zhou, C. Lee, F. Harmon, Y. Harker, and R. Hamm, "Analysis of epithermal neutron production by near–threshold (p,n) reactions," *Appl. Rad. Isotopes*, vol. 48, p. 1571, 1997.

[34] R. J. Kudchadker, *Optimized Accelerator Based Epithermal Neutron Beams for Boron Neutron Capture Therapy.* PhD thesis, University of Missouri–Columbia, 1996.

[35] R. W. Bartholomay, "BNCT benchmark experiments for near lithium threshold target performance," Master's thesis, Idaho State University, 1998.

[36] A. I. M. Ritchie, "Neutron yields and energy spectra from the thick target Li(p,n) source," *J. Phys. D*, vol. 9, p. 15, 1976.

[37] H. H. Andersen and J. F. Zeigler, *Hydrogen: Stopping Powers and Ranges in All Elements.* Pergamon Press, 1985.

[38] H. W. Newson, R. M. Williamson, K. W. Jones, J. H. Gibbons, and H. Marshak, "Li^7 (p,n), (p,$p'\gamma$), and (p,γ) reactions near neutron threshold," *Phys. Rev.*, vol. 108, no. 5, p. 1294, 1957.

[39] J. H. Gibbons and R. L. Macklin, "Total neutron yields from light elements under proton and alpha bombardment," *Phys. Rev.*, vol. 114, p. 571, 1959.

[40] H. H. Barschall *et al.*, *Neutron Sources For Basic Physics and Applications.* Pergamon Press, 1983.

[41] J. B. Marion and J. L. Fowler, eds., *Fast Neutron Physics.* Interscience, 1960.

[42] K. K. Sekharan, H. Laumer, B. D. Kern, and F. Gabbard, "A neutron detector for measurement of total neutron production cross sections," *Nucl. Instr. and Meth.*, vol. 133, p. 253, 1976.

[43] V. N. Kononov, E. D. Poletaev, and B. D. Yurlov, "Absolute yield and spectrum of neutrons from the ^{7}Li(p,n)^{7}Be reaction," *At. Energ.*, vol. 43, p. 303, 1977.

[44] J. F. Janni, "Proton range–energy tables, 1 keV-10 GeV," *At. Data Nucl. Data Tables*, vol. 27, p. 147, 1982.

[45] G. N. Potetyunko, "Verifying the addition rule for the proton–retarding power of multicomponent materials," *At. Energ.*, vol. 52, p. 129, 1982.

[46] D. I. Thwaites, "Current status of physical state effects on stopping power," *Nucl. Instr. and Meth.*, vol. B12, p. 84, 1985.

[47] J. F. Zeigler and J. M. Manoyan, "The stopping of ions in compounds," *Nucl. Instr. and Meth.*, vol. B35, p. 215, 1988.

[48] M. M. Markowitz and D. A. Boryta, "Lithium metal–gas reactions: Interaction of lithium metal with air and its component gases," *J. Am. Chem. Soc.*, vol. 7, no. 4, p. 586, 1962.

[49] S. Yamaguchi, "An electron diffraction study on the corroded state of the alkali and the alkaline earth metals on exposure to air: Li, Na, K, and Ca," *Sci. Papers Inst. Phys. Chem. Res.*, vol. 37, no. 978, p. 424, 1940.

[50] S. Yamaguchi, "An electron diffraction study of the surfaces of alkali and alkaline earth metals exposed to air," *Nature*, vol. 145, p. 742, 1940.

[51] W. R. Irvine and J. A. Lund, "The reaction of lithium with water vapor," *J. Electrochem. Soc.*, vol. 110, no. 2, p. 141, 1963.

[52] A. F. Trotman-Dickenson *et al.*, eds., *Comprehensive Inorganic Chemistry*, vol. 1. Pergamon Press, 1973.

[53] J. F. Briesmeister, ed., *MCNP–A General Monte Carlo N–Particle Transport Code, Version 4A*. LA-12625-M: Los Alamos National Laboratory, 1993.

[54] R. G. Zamenhof, B. W. Murray, G. L. Brownell, G. R. Wellum, and E. I. Tolpin, "Boron neutron capture therapy for the treatment of cerebral gliomas. I: Theoretical evaluation of the efficacy of various neutron beams," *Med. Phys.*, vol. 2, p. 47, 1975.

[55] R. A. Brooks *et al.*, "Explanation of cerebral white – gray contrast in computed tomography," *J. Comp. Assist. Tomog.*, vol. 4, no. 4, p. 489, 1980.

[56] R. S. Caswell *et al.*, "Kerma factors of elements and compounds for neutron energies below 30 Mev," *Intl. J. Appl. Radiat. Isot.*, vol. 33, p. 1227, 1982.

[57] J. M. Blatt and V. F. Weisskopf, *Theoretical Nuclear Physics.* Dover Publications, 1979.

[58] D. R. Lide, ed., *Table of Isotopes.* CRC Press, 78th ed., 1997-1998.

[59] W. E. Sweeney, Jr. and J. B. Marion, "Gamma–ray transitions involving isobaric–spin mixed states in Be^8," *Phys. Rev.*, vol. 182, no. 4, p. 1007, 1969.

[60] G. A. Fisher, P. Paul, F. Reiss, and S. S. Hanna, "Giant $E1$ resonances in ^{8}Be from the reaction ^{7}Li$(p,\gamma)^8$Be," *Phys. Rev. C*, vol. 14, no. 1, p. 28, 1976.

[61] R. D. Evans, *The Atomic Nucleus.* McGraw–Hill Book Company, 1975.

[62] J. B. Marion and M. Wilson, "The ^{7}Li$(p,\gamma)^8$Be* reaction and single–particle levels in ^{8}Be," *Nucl. Phys.*, vol. 77, p. 129, 1966.

[63] O. K. Harling, K. A. Roberts, D. J. Moulin, and R. D. Rogus, "Head phantoms for neutron capture therapy," *Med. Phys.*, vol. 22, p. 579, 1995.

[64] N. Gupta, J. Niemkiewicz, T. E. Blue, R. Gahbauer, and T. X. Qu, "Effect of head phantom size on ^{10}B and ^{1}H[n,γ]^{2}H dose distributions for a broad field accelerator epithermal neutron source for BNCT," *Med. Phys.*, vol. 20, p. 395, 1993.

[65] M. C. Dobelbower and T. E. Blue, "A Monte Carlo analysis of the effect of increasing target diameter for an accelerator–based neutron source for BNCT," in *Proceedings of the American Nuclear Society Topical Meeting on Nuclear Applications of Accelerator Technology*, (Albuquerque, NM USA), p. 495, 1997.

[66] R. M. Brugger, G. Constantine, O. K. Harling, and F. J. Wheeler, "Rapporteurs' report," in Harling *et al.* [91], p. 3.

[67] H. Madoc-Jones, D. E. Wazer, R. G. Zamenhof, O. K. Harling, and J. A. Bernard, "Clinical considerations for neutron capture therapy of brain tumors," in Harling *et al.* [91], p. 23.

[68] K. S. Krane, *Introductory Nuclear Physics.* John Wiley & Sons, 1988.

[69] S. Tanaka, P. H. Stelson, W. T. Bass, and J. Liu, "Levels in ^{53}Mn, ^{58}Co, ^{63}Zn, and ^{70}Ga from the (p,n) reactions," *Phys. Rev.*, vol. C2, no. 1, p. 160, 1970.

[70] L. L. Lee, Jr. and F. P. Mooring, "Resonance detection of neutron energy groups from the ^{55}Mn(p,n)^{55}Fe reaction," *Phys. Rev.*, vol. 115, no. 4, p. 969, 1959.

[71] R. A. Chapman and J. C. Slattery, "(p,n) reactions in Mn^{55}, Co^{59}, Zn^{67}, and Zn^{68}," *Phys. Rev.*, vol. 105, no. 2, p. 633, 1957.

[72] P. Pietrzyk, K.-D. Büchs, E. Finckh, W. Fritsch, and B. Schreiber, "Study of ^{57}Co with the ^{57}Fe(p,n)^{57}Co reaction," *Z. Physik.*, vol. 262, p. 239, 1973.

[73] C. E. Weller and J. C. Grosskreutz, "Gamma rays from the proton bombardment of separated copper isotopes," *Phys. Rev.*, vol. 102, no. 4, p. 1149, 1956.

[74] M. A. Meyer, I. Venter, and D. Reitmann, "Energy levels of ^{28}Si," *Nucl. Phys.*, vol. A250, p. 235, 1975.

[75] F. Cvellbar, E. Betak, and A. Likar, "Pre–equilibrium and direct–semi–direct model calculations of proton radiative capture excitation functions near A=60," *J. Phys. G*, vol. 19, p. 1937, 1993.

[76] G. U. Din, I. A. Al-Agil, and A. M. A. Al-Soraya, "Reaction ^{52}Cr(p,γ)^{53}Mn from 1.66 to 2.91 mev," *Phys. Rev. C*, vol. 44, p. 972, 1991.

[77] N. Boukharouba, C. E. Brient, S. M. Grimes, V. Mishra, and R. S. Pedroni, "Low energy optical model studies of proton scattering on ^{54}Fe and ^{56}Fe," *Phys. Rev. C*, vol. 46, p. 2375, 1992.

[78] E. A. Skakun, V. G. Batii, Y. N. Rakivnenko, and O. A. Rastrepin, "Cross sections of (p,γ) reactions on ^{54}Fe, ^{112}Sn, and ^{114}Cd at proton energies up to 9 MeV," *Sov. J. Nucl. Phys.*, vol. 45, p. 384, 1989.

[79] J. G. Collier, ed., *Convective Boiling and Condensation.* New York: McGraw–Hill Book Company, 2nd ed., 1972.

[80] D. Q. Kern and A. D. Kraus, *Extended Surface Heat Transfer.* New York: McGraw–Hill Book Company, 1972.

[81] B. Gebhart, *Heat Transfer.* New York: McGraw–Hill Book Company, Inc., 1961.

[82] P. M. Gerhart and R. J. Gross, *Fundamentals of Fluid Mechanics.* Reading, Massachusetts: Addison–Wesley Publishing Company, 1985.

[83] Y. S. Touloukian, R. W. Powell, C. Y. Ho, and P. G. Klemens, "Thermal conductivity: Metallic elements and alloys," in *Thermophysical Properties of Matter*, vol. 1, New York: IFI / Plenum Press, 1970.

[84] H. Kremer, E. Buhr, and R. Haupt, "Heat transfer from turbulent free–jet flames to plane surfaces," in *Heat Transfer in Flames* (N. H. Afgan and J. M. Beer, eds.), (Washington, D. C.), Scripta Book Company, 1974.

[85] M. N. Özişik, *Heat Conduction.* New York: John Wiley & Sons, Inc., 1993.

[86] R. W. Hamm, "Model PL-2HC high current Linac for near threshold neutron production." Technical report for final report for University Research Consortium grant No. DE-AC07-94ID13223, 1997.

[87] R. E. Johnson, *Energetic Charged–Particle Interactions with Atmospheres and Surfaces.* New York: Springer–Verlag, 1990.

[88] H. H. Andersen and H. L. Bay, *Sputtering by Particle Bombardment.* New York: Springer–Verlag, 1981.

[89] E. Binello, R. E. Shefer, and J. C. Yanch, "Neutron beam design for boron neutron capture synovectomy," in *Proceedings of the 7th International Symposium on Neutron Capture Therapy for Cancer*, (Zurich, Switzerland), 1996.

[90] J. C. Yanch and M. L. Delfaus, "Boron neutron capture therapy for the prevention of restenosis," in *Transactions of the 1997 Winter Meeting of the American Nuclear Society*, (Albuquerque, NM USA), 1997.

[91] R. G. Zamenhof, S. D. Clement, O. K. Harling, J. F. Brenner, D. E. Wazer, H. Madoc-Jones, and J. C. Yanch, "Monte Carlo based dosimetry and treatment planning for neutron capture therapy of brain tumors," in Harling *et al.* [93], p. 283.

[92] W. S. Snyder *et al.*, "MIRD Supplement No. 3, Pamphlet 5," *J. Nucl. Med.*, vol. 10, p. 47, 1969.

[93] O. K. Harling, J. A. Bernard, and R. G. Zamenhof, eds., *Neutron Beam Design, Development, and Performance for Neutron Capture Therapy*, (New York), Plenum Press, 1992.